Study and modeling of the deuterium trapping in ITER relevant materials

Etienne Hodille

UNIVERSITE D'AIX-MARSEILLE

ECOLE DOCTORALE 352, Physique et Science de la matière
Spécialité : Energie, Rayonnement et Plasma

CEA Cadarache/Institut de Recherches sur la Fusion par confinement Magnétique

Thèse présentée pour obtenir le grade universitaire de docteur

par Etienne HODILLE

Etude de l'implantation du deutérium dans les composés face au plasma constituants du tokamak ITER

Soutenue le 03/11/2016 devant le jury :

Kalle HEINOLA	University of Helsinki	Rapporteur
François WILLAIME	CEA Saclay, DMN	Rapporteur
Charlotte BECQUART	Université de Lille, UMET	Examinateur
Khaled HASSOUNI	LSPM, CNRS	Examinateur
Yves FERRO	Université d'Aix-Marseille, PIIM	Examinateur
Jean-Marc LAYET	Université d'Aix-Marseille, PIIM	Directeur de Thèse
Christian GRISOLIA	CEA Cadarache, IRFM	Co-directeur de Thèse

Remerciements

Même si la rédaction d'un manuscrit de thèse est long et peut-être douloureux, la section la plus compliqué pour moi est sans doute les remerciements. Car il est peu probable qu'on puisse s'en sortir en résolvant une quelconque équation et ce n'est pas à souhaiter : ce serait trop simple. Voici donc ma tentative de remerciements.

Je tiens tout d'abord à remercier les deux co-directeurs de cette thèse sans qui, sachez le cher lecteur assidu de ce document sans doute trop long, ce travail n'aurait pas pu aboutir.
D'abord, M. Christian Grisolia qui m'a accueilli au CEA et m'a guidé durant ces trois années dans les méandres scientifiques que nous avons empruntés. Ça été un grand plaisir de travailler avec lui et de pouvoir profiter de ces connaissances (et ces termes à plusieurs sens). Et en plus de cela, il a parfois dû corriger les fautes de français ou d'anglais qu'il y avait sans doute en trop grand nombre dans mes rapports et papiers.
Ensuite, M. Jean-Marc Layet qui, comme il l'a dit à ma soutenance, était la caution académique de cette thèse. Mais je vous prie de croire qu'il a été plus que cela car, même si je ne le voyais pas forcément tous les jours car nos bureaux étaient séparés par une largeur de département, il m'a beaucoup aidé à avancer notamment lorsqu'il a fallu envisager l'après thèse.

Je souhaiterais ensuite remercier la région PACA pour avoir accepté de financer la moitié de cette thèse et le CEA pour avoir financé l'autre moitié.

Je souhaiterais également remercier Isabelle Bergoend et Eric Humbert de la société OPTIS pour avoir suivi cette thèse dans le cadre du co-financement région PACA/CEA. Même si le sujet de thèse n'était pas forcément lié aux problématiques traitées par OPTIS, ils se sont intéressés au sujet et je les remercie pour cela.

J'aimerais remercier M. François Willaime et M. Kalle Heinola pour avoir accepté d'être les rapporteurs de cette thèse. N'étant que jeune chercheur, je ne peux qu'imaginer la difficulté de ce travail. Je leur adresse donc ma gratitude pour l'avoir remplie et également pour avoir accepté de faire le déplacement jusqu'au sud de la France pour participer à ma soutenance en tant que membre du jury.

J'aimerais également remercier les autres membres du jury, M. Khaled Hassouni, Mme. Charlotte Becquart et M. Yves Ferro pour avoir accepté de faire le déplacement pour évaluer mon travail pendant les vacances de novembre alors qu'un pont de 4 jours se dessinait.

Je souhaiterais maintenant remercier Mme. Charlotte Becquart, M. Régis Bisson et M. Yves Ferro pour m'avoir prodigué de précieux conseils sur les différents points de la physique que j'ai dû aborder durant mon périple scientifique que ce soit sur la métallurgie, la physique de la surface et la physique du solide. Sans ces précieux conseils, il est évident que l'interprétation des résultats que nous avons obtenus serait appauvris.

Ensuite, je souhaiterais remercier les membres du groupes GP2B à l'IRFM qui travaille sur la physique du plasma de bord. Car même si j'ai quitté ce groupe un an avant la fin de la thèse du fait d'une réorganisation, je suis resté dans le couloir phare de ce groupe (508 et pas ailleurs).

Travaillé dans ce groupe m'a fait connaître des personnes formidables et j'espère que ce que j'ai pu faire leur sera utile.

Je souhaiterais également remercier les membres du groupe GPFCM à l'IRFM qui fut le groupe que j'ai rejoint à la suite de la réorganisation. Ça a été un plaisir d'être intégré à cette équipe et j'espère que j'ai pu apporter ma contribution.

J'aimerais aussi remercier la direction du service dans lequel j'ai évolué, d'abord le SIPP puis le SI2P. Le nom change mais les personnes sont les mêmes et elles ont été formidable avec moi, elles m'ont aidé dans toutes les situations et ça a été un plaisir d'évoluer dans ce service.

Après avoir remercié les groupes, puis les services dans lequel j'ai évolué, je voudrais maintenant remercier la direction de l'IRFM. Faire ma thèse au CEA au sein de l'IRFM, un laboratoire de première importance dans le domaine de la fusion, a été un immense plaisir et j'espère que j'ai pu apporter au laboratoire une petite contribution pour ses futurs projets.

J'aimerais aussi remercier l'ensemble des personnelles du laboratoire PIIM avec qui j'ai interagi. Car si j'étais basé au CEA à l'IRFM, j'ai beaucoup interagi avec le PIIM et ça a été un grand plaisir de participer au travail de ce laboratoire notamment à travers le projet WHISCI qui m'a beaucoup apporté d'un point de vue scientifique et humain.

Je souhaiterais désormais remercier l'université AMU. En effet, il ne faut pas oublier qu'un doctorant est aussi un étudiant ce qui, sans vouloir être mauvais esprit, apporte certain avantage lorsqu'il s'agit de se cultiver dans les salles obscures. Et même si parfois, l'organisation de l'université AMU peut paraître un peu floue, sans elle, les thésards seraient bien embêtés.

Viens maintenant le moment de remercier les doctorants, stagiaire(e)s, mes collègues de bureau, les « jeunes » en quelques sortent avec qui j'ai interagi pendant ces trois années. Ils ont été très sympathique et ont été réceptifs (de temps en temps) à mes élocutions qui n'avait parfois pas de sens. On pourrait penser que les doctorants entre eux ne parle que de science mais en fait ce n'est pas toujours le cas. D'ailleurs certains essaient justement de ne pas parler de science et ils ont raison. On a pu par exemple parler, à ma grande joie, des péripéties de certains en canoé, des randonnées dans les rochers qui ressemble soit à des courses d'obstacles soit à des explorations de jungle, des œuvres d'art en rouleaux cartonnés ou encore de la personnalisation des carottes.

Je voudrais aussi remercier la musique et le groupe d'abeille dans lequel je joue de la guitare. Même si notre carrière internationale n'a pas encore décollé, joue de la guitare dans un groupe a été et sera sans doute encore un temps une source d'inspirations.

Et enfin, je voudrais remercier ma famille qui a soutenu cette audacieuse entreprise d'entrer dans la physique. Leurs conseils et soutiens tout au long de ma thèse et bien avant n'ont pas été de trop pour m'amener à cette fin de phrase qui termine les remerciements.

Il y a sans doute beaucoup d'autres personnes que je devrais remercier et j'espère qu'ils savent que je les remercie vraiment même si ce n'est pas écrit ici.

Contents

Résumé substantiel

La production d'énergie est une question d'importance puisqu'elle est à la base du développement économique, social et culturel. Actuellement, les principales énergies primaires sont les énergies fossiles (gaz, pétrole, charbon) dont les coûts d'extraction sont de plus en plus élevés tandis que les sources ne cessent de diminuer. De plus, ces énergies sont de moins en moins populaires depuis que des problématiques environnementales liées à leurs utilisations ont été soulevées. Une redéfinition de ce qu'est une bonne source d'énergie peut donc être faite : c'est une source abondante, rentable et écologique. C'est dans ce cadre que s'inscrit la fusion thermonucléaire. Le chemin vers une filière énergétique bien qu'étant encore au stade de la recherche fondamentale semble bien défini avec le projet ITER, un projet de fusion international lancé officiellement en 2006 et actuellement en cours de construction en France. Le but de ce projet est de démontrer la faisabilité de la fusion contrôlée pour une utilisation civile.

La réaction envisagée pour produire de l'énergie par fusion nucléaire est la réaction deutérium (D) – tritium (^{3}H). Cette réaction a été choisie car elle offre la meilleure section efficace de réaction pour le minimum d'énergie injectée. La réaction D – ^{3}H est exothermique et produit un noyau d'hélium (He) portant 3,5 MeV et un neutron (n) portant 14,1 MeV.

Actuellement sur Terre, le confinement magnétique semble être le moyen le plus prometteur de contrôler la production d'énergie par fusion thermonucléaire. Et parmi les différentes configurations possibles, le tokamak est celle qui a été la plus explorée. Tokamak est l'acronyme russe de « toroïdalnaïa Kamera s magnitnymi katushkami » signifiant littéralement chambre toroïdale avec des bobines magnétiques. Dans un tokamak, un plasma chaud est confiné par un champ magnétique toroïdal généré par de puissantes bobines et par un champ magnétique poloïdal généré par la circulation d'un courant dans le plasma (figure 1.1).

Il est physiquement impossible de contenir un plasma à l'intérieur duquel de l'énergie est générée sans qu'une partie de cette énergie sorte du plasma confiné : en permanence, des particules constituant le plasma sortent de la région confinée du plasma et vont frapper les parois du tokamak. Dans le design actuel, pour éviter que l'intégralité des parois subisse de fortes interactions plasma-paroi (IPP), la majeure partie des particules sortant du plasma confiné sont dirigées vers les cibles du divertor (figure 1.2). Dans les tokamaks opérant actuellement comme le JET ou ASDEX Upgrade ainsi que dans les futurs tokamaks WEST et ITER, le matériau constituant les cibles du divertor est le tungstène (W). Ce matériau a été choisi pour ces propriétés thermiques et son faible taux d'érosion sous flux de D. Le flux de particules qui frappe les parois est majoritairement constitué d'isotopes d'hydrogène (IHs) mais également d'héliums issus des réactions de fusion et d'impuretés présentes dans le plasma.

Lors de l'interaction du plasma avec le mur en W, décrite sur la figure 1.3 du manuscrit, une partie du flux incident arrivant sur le matériau est réfléchie sous forme d'atomes chauds (avec de l'énergie cinétique) vers le plasma créant un flux de recyclage atomique. L'autre partie est implantée sous la surface à l'intérieur du matériau. L'implantation crée un gradient de concentration de particules qui amène spontanément les particules à diffuser afin d'homogénéiser la concentration. La diffusion est rationalisée par les lois de Fick qui fait intervenir le coefficient de diffusion des particules dans le W. Lors de leur chemin de diffusion, les particules peuvent rencontrer des défauts cristallins (lacunes, dislocations, joints de grains, amas de lacunes …) qui peuvent les piéger. Elles peuvent également diffuser vers la surface ce qui amène à une

désorption des particules du matériau vers le plasma. Cette fois, ce flux de recyclage est un flux de molécules froides (à la température du mur).
Durant les opérations d'ITER avec des réactions de fusion, en plus des particules provenant du plasma (IHs, He et impuretés), des flux important de neutrons irradieront les murs. Puisque ces neutrons ne sont pas confinés par le champ magnétique, ils frapperont les parois avec toute leur énergie cinétique c'est-à-dire 14.1 MeV. Avec une telle énergie, les neutrons vont endommager les parois en W et créer de nombreux défauts ce qui a un effet sur la quantité de particules pouvant être piégées dans les parois.

Deux problématiques sont posées par ces interactions entre le flux d'IHs venu du plasma et les composés Face au Plasma (CFP) en W :

- L'inventaire de tritium à l'intérieur de la chambre à vide d'ITER est limité à 700 g pour des raisons de sureté car le tritium est un élément radioactif (demi-vie de 12.3 années) qui se désintègre en ^{3}He via une désintégration β. Il faut donc être capable d'évaluer la quantité de tritium qui est retenue dans le divertor en W durant les plasmas d'ITER.
- Le dégazage des molécules froides du mur vers le plasma peut affecter la physique du plasma de bord puisque ce dégazage induit une source de particules qui peut affecter le plasma. Il est donc important de pouvoir estimer la quantité de particules dégazée mais aussi la dynamique du recyclage de molécules.

Pour apporter des éléments de réponse à ces deux problématiques, les propriétés de rétention des IHs du W doivent être déterminées. De plus, l'impact des neutrons de fusion sur ces propriétés doit être quantifié.

Pour traiter ces problématiques, les aspects expérimentaux et théoriques sont importants. Le premier pour déterminer les processus sous-jacents à la rétention des IHs et le deuxième pour les rationaliser mathématiquement et prédire les comportements dans un environnement de tokamak.
Mon projet de thèse a été dédié à la simulation d'expériences bien caractérisées afin d'obtenir ces propriétés de rétention des IHs pour :

- Prédire la rétention du tritium dans les CFPs en W d'ITER,
- Construire un modèle de mur qui permettra de calculer la partie moléculaire du flux de recyclage dans les codes de plasma de bords.

Les interactions des IHs avec le W peuvent êtres décrites par le diagramme d'énergie des interactions IH/W présenté sur la figure 2.2 (chapitre 2 de ce manuscrit). Ce diagramme présente plusieurs barrières de potentiel à la surface et dans le matériau positionnées entre différents sites stables. A la surface, le site stable est appelé un site d'adsorption et dans le matériau deux types de sites existent : les sites interstitiels et les sites de pièges. Les barrières d'énergies entre chacun de ces sites stables sont :

- E_C : la barrière qu'une molécule d'IHs doit franchir pour être dissociée afin que les IHs soient adsorbés sur la surface de W,
- E_D : la barrière qu'un atome adsorbé sur la surface de W doit franchir pour être dégazé. Pour cela, il faut que deux atomes se recombinent : l'énergie d'activation pour la désorption est $2 \cdot E_D$,
- E_A : la barrière qu'un atome adsorbé sur la surface doit franchir pour être inséré dans le matériau en position interstitielle,
- E_R : la barrière qu'un atome en position interstitiel doit franchir pour être relâché sur la surface dans un site d'adsorption,

- E_{Diff} : la barrière qu'un atome en position interstitiel doit franchir pour aller sur une position interstitielle voisine. Il est également supposé que c'est la barrière à franchir pour aller d'un site interstitiel à un site piégé,
- $E_{B,i}$: l'énergie de liaison d'un atome situé dans un site de piégeage i avec le W : pour sortir du piège i, la barrière à franchir est l'énergie de dépiégeage $E_{t,i} = E_{B,i}+E_{Diff.}$

Les fréquences $\nu_{1\to2}$ de saut d'un site stable 1 à un site stable 2 sont décrites par la théorie des états de transition : $\nu_{1\to2} = \nu_0^{1\to2} \cdot e^{-\frac{E_{1\to2}}{k_B \cdot T}}$ en s^{-1}. Dans cette formule, $\nu_0^{1\to2}$ est le facteur pré-exponentiel, $E_{1\to2}$ est la barrière d'énergie pour passer du site 1 au site 2, k_B est la constante de Boltzmann et T est la température du matériau.

Les modèles utilisés dans ce projet de thèse, basés sur ces expressions des fréquences de saut, sont des modèles monodimensionnels et ils peuvent être divisés en deux parties comme présenté dans le chapitre 3:

- La première partie traite les interactions des IHs avec le W à l'intérieur du matériau,
- La deuxième partie traite les interactions des IHs avec la surface du W.

La première partie considère le fait que les particules insérées dans le matériau peuvent diffuser de sites interstitiels à sites interstitiels mais aussi être piégées au niveau des défauts cristallins. Deux types de particules sont donc considérés :

- Les particules mobiles de concentration c_m,
- Les particules piégées de concentration $c_{t,i}$. Il peut y avoir plusieurs types de pièges indexés par i.

Deux types de modèles ont été utilisés pendant ce projet :

Le modèle classique considère une énergie de dépiégeage par piège. Il s'agit du modèle simplifié qui permet d'avoir les informations moyennes. Il est utilisé sans connaissance préalable des défauts présents dans le matériau. Les énergies de dépiégeage pourront ensuite être comparées à des calculs à l'échelle atomique comme les calculs DFT (density functional theory) afin d'estimer la nature des pièges. Ce modèle est implémenté dans le code MHIMS (Migration of Hydrogen Isotopes in MaterialS), décrit en détail dans la section 3.1.1.

Le modèle multi-piégeage considère qu'un piège peut contenir plusieurs IHs. Dans ce cas l'énergie de dépiégeage des IHs dépend du nombre d'IHs (ou taux de remplissage) dans le piège. il est motivé par les résultats des modélisations aux échelles atomiques comme la DFT : ces calculs DFTs donnent la distribution des énergies de dépiégeage pour un type de défaut particulier en fonction du taux de remplissage. Ainsi, en connaissant (ou en présupposant) la nature des pièges présents dans le matériau, il est possible de déterminer, par exemple, quel type de défaut piège efficacement les IHs ou si la quantité présente dans le matériau est constante ou évolue avec le temps. Ce modèle est implémenté dans MHIMS-R et décrit en détail dans la section 3.1.2.

Pour ces deux modèles, la diffusion des particules mobiles est traitée par les lois de Fick (équation 1.5) en une dimension. Il y a également une source volumique créée par l'implantation d'ions énergétiques. Finalement, l'échange entre particules mobiles et particules piégées est traité à l'aide de cinétique chimique avec des cinétiques de réaction exprimées grâce à la théorie des états de transition comme décrit plus haut.

La surface représente la condition aux limites du système d'équations pour les deux modèles. En dimension 1, il y a deux frontières (surfaces). Elles sont aussi traitées de deux manières différentes.

Le premier modèle de surface considère que la recombinaison des atomes d'IHs en molécules n'est pas un processus limitant dans le dégazage : les atomes restent très peu de temps sur la surface et sont instantanément soustraits du matériau. Ainsi cette condition aux limites peut s'exprimer comme une concentration de particules mobiles nulle sur les deux frontières (surfaces). Cette condition est utilisée lors des simulations d'implantations d'ions suffisamment énergétiques pour être implantés dans le matériau.
Dans le cas d'exposition avec atomes faiblement énergétiques, les expériences ont montré que les atomes étaient sensibles aux phénomènes de surface. De telles expositions étant simulées durant ce projet, un modèle de surface plus complexe a été mis en place prenant en compte les différents phénomènes de surface décrits plus haut (adsorption, désorption, absorption à l'intérieur du matériau depuis sa surface et relargage de l'intérieur vers la surface du matériau).

Par les simulations successives d'expériences faites sur des échantillons monocristallins, poly-cristallins non endommagés et poly-cristallins endommagés par des ions lourds, plusieurs caractéristiques du piégeage des IHs dans le W ont pu être dégagées. Ces résultats sont présentés dans le chapitre 4.

Dans le cas des simulations d'expériences sur les monocristaux, un modèle de création de pièges induits par la grande quantité d'IHs introduite dans le matériau pendant l'implantation est implémenté dans le code MHIMS-R. Cette formation de pièges induits par l'hydrogène est motivée par deux arguments :

- Les calculs thermo-statistiques qui montrent qu'après l'insertion d'une fraction $x=10^{-5}$ d'IH dans un W parfait, à 300 K, l'équilibre thermodynamique est atteint par la formation d'une fraction x/6 de lacunes. Cette formation de lacunes n'est présente qu'au-dessus d'une fraction insérée de $x \approx 5\times10^{-10}$.
- Les résultats expérimentaux qui montrent que pour une même fluence, la rétention des IHs augmente avec le flux incident à 300 K : la rétention varie d'un à deux ordres de grandeur quand le flux incident varie d'un ordre de grandeur. Au-dessus d'un flux incident d'environ 5×10^{17} $m^{-2}s^{-1}$, la quantité d'IHs retenus sature. Ce flux seuil correspond à une concentration de particules mobiles seuil de 5×10^{-10} identique à celle prédite par les calculs thermo-statistiques.

Les simulations menées semblent montrer que les pièges créés sont des lacunes avec des impuretés d'oxygène et de carbone contenant un ou plusieurs IHs (appelées VOH et VCH). Les énergies de dépiégeage des IHs de ces pièges sont données par les calculs DFT pour ces types de lacunes : pour le niveau de remplissage 1, l'énergie de dépiégeage est 1.5 eV et pour les niveaux supérieurs, elle diminue autour de 1.15 eV.
Comme prédit par les modèles thermo-statistiques, la création est déclenchée lorsque la concentration d'hydrogène est supérieure à 5×10^{-10}. Par ailleurs, la conclusion tirée des simulations est que la saturation de la concentration de pièges est liée à la quantité d'impuretés d'oxygène (O) et de carbone (C) présentes dans le matériau. L'origine de ces impuretés est double :

- Une faible partie est présente initialement dans le matériau à cause des procédés de fabrication et aux différents traitements subis par l'échantillon,
- Une partie vient du gaz résiduel et a été implantée lors de l'irradiation de l'échantillon par les ions IHs.

Pour ce deuxième point, il faut distinguer deux zones distinctes.

La première correspond à la zone d'implantation des ions O et C qui peuvent induire des lacunes par collision avec les W. Cette zone ne s'étend pas plus loin que quelques dizaines de nanomètres.
La deuxième zone s'étend entre 1 et 2 µm à 300 K et jusqu'à 6 µm autour de 500 K. La conclusion qui est tirée des simulations des résultats expérimentaux et que cette deuxième zone est attribuée à la diffusion thermiquement activée des impuretés de C et de O dans le matériau ce qui étend la zone de formation des pièges. Dans tous les cas, une loi est extraite des simulations pour estimer la profondeur à laquelle cette zone de création de piège s'étend en fonction de la température.

Les simulations d'expériences sur des poly-cristaux non endommagés montrent qu'en plus des pièges induits par l'implantation en grande quantité d'IHs, les défauts intrinsèques peuvent être représentés par deux pièges. Ainsi, 3 pièges sont utilisés dans ces simulations :

- Le piège 1 est un piège intrinsèque avec une énergie de dépiégeage de 0.85 eV. Il correspond principalement aux impuretés métalliques présentes dans le matériau comme le fer ou le cuivre. Pour les expériences simulées, la concentration de ce piège est autour de 0.1 pourcentage atomique.
- Le piège 2 est un piège intrinsèque avec une énergie de dépiégeage autour de 1 – 1.1 eV. Il correspond aux joints de grains et la distribution d'énergies peut être large suivant la diversité des joints de grains présents dans le matériau. Pour les expériences simulées, la concentration de ce piège est autour de 0.04 pourcentage atomique mais elle dépend de la taille des grains, de l'échantillon et du traitement pré-implantation.
- Le piège 3 est le piège extrinsèque induit par l'implantation d'une grande quantité d'IHs dans le matériau. Son énergie de dépiégeage est 1.5 eV. Comme dans le cas des simulations d'expériences sur les monocristaux, différentes zones sont considérées pour la création de pièges. Une première dans la zone d'implantation (~10-20 nm) des ions dans laquelle la concentration de pièges peut atteindre 10 pourcentages atomiques. Une autre jusqu'à quelques micromètres qui correspond à la zone de diffusion des impuretés d'O et de C. Dans cette zone, la concentration de pièges peut atteindre au maximum 1 pourcentage atomique.

Les paramètres dégagés de ces simulations reproduisent les résultats expérimentaux existant pour différentes températures d'implantation et différentes fluences. Ils semblent donc pertinent pour reproduire le comportement des PFC en W non-endommagé dans un environnement tokamak et ainsi estimer la rétention du fuel dans ces machine.
Les simulations montrent qu'avec de telles énergies, une température de 300 K est suffisante pour dégazer, après l'implantation, une partie des IHs initialement retenus durant l'implantation. Cela signifie qu'un dégazage pourra être observé lors des exploitations en tokamak entre les décharges et durant les arrêts d'opération pendant la nuit ou les week-ends. De plus, avec une énergie de dépiégeage maximale de 1.5 eV, seulement 700 K sont nécessaires pour désorber quasiment totalement tous les IHs retenus après l'implantation.

Les simulations d'expériences sur des poly-cristaux endommagés par des ions lourds (W^{6+} à 20 MeV) à 0.5 déplacements par atomes (dpa) permettent de déterminer trois nouveaux pièges liés à l'endommagement. En comparant les valeurs d'énergies de dépiégeage calculées par DFT avec les valeurs extraites des simulations, une nature a été attribuée à chacun de ces pièges :

- Le piège 4 a une énergie de dépiégeage de 1.65 eV. Il correspond au piégeage des IHs dans les crans des dislocations.

- Le piège 5 a une énergie de dépiégeage de 1.85 eV. Il correspond aux boucles de dislocations.
- Le piège 6 a une énergie de dépiégeage de 2.06 eV. Il correspond au piégeage des IHs dans les cavités et amas de lacunes suffisamment volumineux pour contenir de l'hydrogène sous forme moléculaire.

Des résultats expérimentaux montrent que la concentration de chacun de ces pièges sature pour un endommagement supérieur à 0.2 dpa. Pour les cas considérés, la zone endommagée s'étend entre 0 et 2 µm de profondeur. Ainsi, pour toute la zone endommagée, les concentrations de ces 3 pièges sont constantes. De plus, différents cas de recuits du matériau endommagé ont été testés expérimentalement et chacun de ces cas a été simulé : les concentrations des pièges dues à l'endommagement dépend de la température de recuit :

- Le piège 4 a une concentration entre 0.06 et 0.09 pourcentage atomique pour des recuits de 1 heure à 500 K et à 800 K. Il disparait totalement pour un recuit de 1 h au-dessus de 1000 K.
- Le piège 5 a une concentration qui diminue progressivement et continuellement pour des recuits de 1 h de 500 K à 1200 K. Elle passe de 0.28 pourcentage atomique à 0.05 pourcentage atomique.
- Le piège 6 à une concentration qui décroit lentement pour des recuits de 1 h entre 500 K et 1000 K passant de 0.08 pourcentage atomique à 0.02 pourcentage atomique. La concentration de ce piège augmente entre un recuit à 1000 K et un recuit à 1200 K et pour ce dernier recuit, la concentration est 0.04 pourcentage atomique.

Si l'hypothèse est faite que ces trois pièges créés par l'endommagement aux ions lourds sont une bonne estimation des pièges créés par une irradiation du W par des neutrons de fusion (14.1 MeV), ces paramètres de piégeage semblent pertinents pour estimer la rétention du fuel dans un tokamak dans lequel des réactions de fusion auront lieu entrainant un endommagement supérieur à 0.2 dpa.
Au vu des énergies de dépiégeage bien plus élevées que dans le cas d'un W non endommagé, la température de désorption des IHs d'un échantillon endommagé est supérieure à 1000 K.

A l'aide de ces paramètres de piégeage pertinents déterminés par la simulation de résultats expérimentaux, des simulations ont été faites pour estimer la rétention du tritium dans des CFPs W non endommagés et endommagés pendant des plasmas typiques de tokamaks. Ces résultats sont présentés dans le chapitre 5. Utilisant ces paramètres, des simulations de cycles de 1400 s, typiques des futurs plasmas d'ITER, sont effectuées.
Un cycle de 1400 s est défini en 4 étapes :

- une phase de démarrage du plasma de 20 s,
- une phase de plasma en état stationnaire de 380 s,
- une phase d'extinction du plasma de 40 s,
- une phase de repos sans plasma de 960 s.

Lors de la phase de démarrage, sur les CFPs, le flux incident de particule et de chaleur augmente de 0 à leurs valeurs nominales durant le plasma stationnaire (10^{24} $m^{-2}s^{-1}$ pour le flux incident de particule et 6.176 MW/m^2 pour le flux de chaleur).
Lors de la phase de plasma stationnaire, les flux de particules et de chaleur restent constant égaux aux valeurs décrites plus haut.
Lors de la phase d'extinction du plasma, les flux de particule et de chaleur décroissent progressivement.

Lors de la phase de repos, les flux sont nuls.
Les valeurs de flux de particules et de chaleur utilisées (à savoir un flux incident de particules de 10^{24} $m^{-2}s^{-1}$ et un flux de chaleur de 6.176 MW/m^2) correspondent à des valeurs typiques des flux subis par les cibles du divertor : c'est-à-dire une zone ou les IPPs sont particulièrement importantes.
Pour permettre de soutenir un flux de chaleur d'environ 6 MW/m^2 pendant 380 s, les CFPs en W doivent être activement refroidis par une boucle d'eau sous pression à 343 K (70 °C). Un gradient de température va donc s'établir entre la surface face au plasma recevant le flux de chaleur et la surface refroidie. Pour calculer ce gradient de température, un modèle de diffusion thermique simple en une dimension est utilisé. Ce modèle calcule qu'avec un flux de 6.176 MW/m^2, la température sur la surface face au plasma est 970 K pour un CFP d'environ 1 cm d'épaisseur.

Deux types de matériaux simulés sont considérés :

- le W non endommagé contenant les pièges 1, 2 et 3,
- le W endommagé contenant les pièges 1 à 3 ainsi que les pièges 4, 5 et 6.

Il est supposé que la concentration des pièges induits par l'endommagement ne varie pas au cours du temps. De plus, il est supposé que l'énergie des neutrons de fusion (14.1 MeV) est suffisante pour endommager de manière homogène toute l'épaisseur du CFP en W.

Après la simulation d'un cycle pour ces deux types de matériaux, il est observé que la rétention du tritium dans le W endommagé est 3 fois plus importante que dans le W non endommagé. Ceci est dû à la présence des pièges 4 à 6 qui retiennent efficacement le tritium même à haute température.
Pour les deux matériaux simulés, une soudaine augmentation de la rétention de tritium est observée pendant la phase d'extinction du plasma. Cette augmentation est due à la diminution de la température qui diminue la probabilité de dépiégeage alors que la probabilité de piégeage ne diminue pas puisque le flux n'est pas nul.

En simulant 40 cycles, il est observé que les IHs retenus pendant la phase d'extinction sont rapidement dégazés du matériau durant la phase de démarrage suivante.
Ensuite, la différence entre la rétention du tritium dans le W endommagé et dans le W non endommagé augmente par rapport à la simulation d'un seul cycle : après 40 cycles, il y a 10 fois plus de tritium dans le W endommagé que dans le W non endommagé. A partir des simulations, des lois d'extrapolations peuvent être faites afin d'estimer deux choses :

- la quantité de tritium retenu après N cycles,
- la profondeur atteinte par le tritium après N cycles.

De cette manière, la quantité maximale de tritium retenue peut-être estimée : c'est la quantité de tritium retenue lorsque la profondeur atteinte par le tritium sera 1 cm. Après cela, le tritium pourra potentiellement se déverser dans le liquide de refroidissement des CFPs.

- Dans le cas du W non endommagé, la quantité maximale de tritium retenue dans le CFP est 0.045 g/m^2 et cette quantité est atteinte en 320 cycles. Cela signifie qu'après 32 jours en considérant 10 cycles par jour, le tritium se déversera potentiellement dans le liquide de refroidissement.
- Dans le cas du W non endommagé, la quantité maximale de tritium retenue dans le CFP est 7.5 g/m^2 et cette quantité est atteinte en 65000 cycles ce qui équivaut à plus de 30 ans de fonctionnement en considérant 200 jours d'opération par an.

Les estimations actuelles de la surface du dépôt de chaleur et de particules est de l'ordre de 0.8 m^2. Cela donne une masse de tritium retenu de 0.036 g dans le W non endommagé et de 6.1 g dans le W endommagé. Ces quantités de tritium sont bien en dessous de la limite de sureté de 700

g de tritium. Cependant, seulement la partie du divertor qui est la plus exposée aux flux de chaleur et de particules a été traitée. Dans d'autres endroits du tokamak, où le flux de chaleur est moins important, la température des CFPs pourrait être bien plus faible permettant au mur de retenir bien plus de tritium. De plus, cette estimation ne considère que le tritium implanté et retenu dans le W. Or dans ITER, une partie du mur est faite de Béryllium. Ce Béryllium peut être érodé par le plasma et former des couches co-déposés retenant une certaine quantité de tritium. Pour évaluer la quantité de tritium dans toutes la machine, il est donc important de connaitre la quantité de tritium retenu dans ces matériaux Béryllium et ces couches co-déposés. Les simulations qui ont été effectuées durant ce projet de thèse montrent tout de même que la rétention du tritium dans les cibles en W du divertor est faible que le matériau soit endommagé ou non.

Durant le fonctionnement d'ITER, afin de contrôler la quantité de tritium retenu dans les matériaux et pour éviter que la limite de 700 g soit dépassée, plusieurs techniques sont envisagées pour récupérer le tritium piégé dans les parois comme par exemple le chauffage des surfaces par des lasers ou des lampes. Pour simuler cette technique de chauffage des surfaces, une simulation de 10 cycles a été faite afin de remplir le mur avec une certaine quantité de tritium. Après le chargement du mur en tritium, le chauffage est réalisé en augmentant le flux de chaleur en entrée (sans aucun flux de particules). Deux cas sont testés avec deux flux de chaleurs différents :

- Un flux de 7.5 MW/m^2. La température de surface monte jusqu'à 1145 K.
- Un flux de 10 MW/m^2. La température de surface monte jusqu'à 1532 K.

Le tritium sous la surface (jusqu'à environ 10 µm) est rapidement récupéré en quelques secondes/minutes. Cependant, afin de récupérer le tritium piégé en profondeur (~100 µm) plusieurs heures sont nécessaires. De plus, afin de permettre de récupérer plus de 90 % de tout le tritium retenu après 10 cycles, un flux de chaleur d'environ 10 MW/m^2 est nécessaire dans le cas d'un W endommagé, un flux de 7.5 MW/m^2 n'étant pas suffisant. Pour obtenir un tel flux de chaleur, des lasers focalisés doivent être utilisés ce qui implique un balayage de toutes les parois avec le laser nécessitant une longue période d'arrêt de la machine.

De plus, si le chauffage dure plusieurs minutes, bien que la majeure partie du tritium désorbe de la face chauffée, des particules piégées peuvent migrer vers le circuit de refroidissement ce qui peut induire une perméation du tritium jusque dans l'eau de refroidissement. Les simulations effectuées montrent que ce problème est principalement posé dans le cas du tungstène non endommagé : après seulement 40 min avec un chauffage à 10 MW/m^2, le tritium a atteint la surface refroidie.

Pour conclure sur l'efficacité de cette technique, les simulations montrent que si la volonté est uniquement de récupérer le tritium présent dans les premiers micromètres, un chauffage de quelques secondes suffit. Par contre, un chauffage avec un flux important est nécessaire pour récupérer efficacement tout le tritium retenu.

List of symbols

Roman symbols	
a_W	Lattice parameter of W (m)
c_m	Concentration of mobile particles (m^{-3})
c_m^{eq}	Concentration of mobile particles at the equilibrium (m^{-3})
c_m^{MAX}	Maximum value of the mobile particle concentration (m^{-3})
c_{surf}	Concentration of adsorbed particles (m^{-2})
c_{surf}^{eq}	Concentration of adsorbed particles at the equilibrium (m^{-2})
$c_{t,i}^{eq}$	Concentration of trapped particles at the equilibrium in the trap type i (m^{-3}) traps filled with i HIs (m^{-3})
$c_{t,i}$	Concentration of trapped particles in: the trap type i (m^{-3}) traps filled with i HIs (m^{-3})
c_{crit}^{HI}	Critical concentration of mobile HIs for the trap creation process (m^{-3})
D_H	Diffusion coefficient of H in tungsten (m^2s^{-1})
D	Diffusion coefficient of named HIs (deuterium or tritium) in tungsten (m^2s^{-1})
D_{LI}	Diffusion coefficient of light impurities (O and C) in tungsten (m^2s^{-1})
E_A	Activation energy for absorption process (eV)
$E_{B,i}$	Binding energy between W and HIs in: the trap type i (eV) traps filled with i HIs (eV)
E_C	Activation energy for HI molecule dissociation process (eV)
E_D	Half the activation energy for desorption process from the W surface (eV)
E_{des}	Activation energy for desorption process from the W surface (eV)
E_{Diff}	Activation energy for HIs diffusion in W (eV)
E_{inc}	Incident energy of HI ions impinging the W (eV/HI)

E_R	Activation energy for resurfacing process (eV)
E_S	Solution energy of HIs atom in W (eV)
$E_{t,i}$	Detrapping energy of HI trapped in: the trap type i (eV) traps filled with i HIs (eV)
f(x)	Spatial implantation distribution of ions for a given incident energy (m^{-1})
i	Index to name: the type of the considered trap (dimensionless) the number of HIs in a trap (dimensionless)
k_B	Boltzmann constant: $k_B \approx 8.6 \times 10^{-5}$ (eV/K)
L_0	Length of the one dimension simulation box (m)
l_m	Maximum number of HIs in a trap (dimensionless)
N_i	Concentration of traps containing i HIs (m^{-3})
N_i^{eq}	Concentration of traps containing i HIs at the equilibrium (m^{-3})
N_{trap}	Concentration of all the traps that contain between 0 and l_m HIs (m^{-3})
$N_{LI}(x)$	Concentration representing the space distribution of light impurities such as O and C
n_i	Concentration of traps for trap type i (m^{-3})
n_{TIS}	Concentration of Tetrahedral interstitial sites (TIS) (m^{-3})
n_{surf}	Concentration of adsorption sites (m^{-2})
$n_{a,max}$	Maximum concentration of created traps in the near surface layer (m^{-3})
$n_{b,max}$	Maximum concentration of created traps in the sub-surface layer (m^{-3})
P_r	Reflexion coefficient of incident HIs atoms on W (dimensionless)
r	Reflexion coefficient of incident HIs ions on W (dimensionless)
R	Recycling coefficient from the wall to the plasma (dimensionless)
R_d	Distance between R_p and the migration depth of HIs in the bulk at a given time (m)
R_p	Mean implantation depth of ions for a given incident energy (m)

$R_{trap,i}$	Equilibrium ratio for: the trap type i (dimensionless) traps filled with i HIs (dimensionless)
S_{ext}	Exterior source of particle due to ion implantation in the bulk ($m^{-3}s^{-1}$)
T	Temperature (K)
t	Time (s)
Tot_{trap}	Amount of trapped particles in all traps (for the simple analytical model) (m^{-2})
x	Spatial coordinate (m)
x_{diff}	Diffusion distance of O and C impurities (m) Depth up to which extrinsic traps are created (m)

Greek symbols

η_a	Creation rate of extrinsic trap in the near surface layer (dimensionless)
η_b	Creation rate of extrinsic trap in the sub-surface layer (dimensionless)
θ	Surface coverage (dimensionless)
θ^{eq}	Surface coverage at the equilibrium (dimensionless)
λ	Jumping distance of HI between two TIS (m)
λ_{abs}	Jumping distance between the first bulk TIS and an adsorption site (m)
λ_{des}	Jumping distance between 2 surface adsorption sites (m)
Γ_{atom}	Incident flux of HI atoms ($m^{-2}s^{-1}$)
Γ_{th}	Thermal flux hitting the divertor ($MW \cdot m^{-2}$)
ϕ_{atom}	Part of the incident atomic flux that is adsorbed on the surface ($m^{-2}s^{-1}$)
$\phi_{b\rightarrow s}$	Resurfacing flux ($m^{-2}s^{-1}$)
ϕ_{bulk}	Flux from the maximum-of-mobile-concentration depth to the bulk ($m^{-2}s^{-1}$)
ϕ_{des}	Desorption flux from the W surface ($m^{-2}s^{-1}$)
ϕ_{diff}	Diffusive flux ($m^{-2}s^{-1}$)

ϕ_{exc}	Flux associated to direct abstraction process ($m^{-2}s^{-1}$)
ϕ_{imp}	Part of the ion flux that is implanted below the W surface ($m^{-2}s^{-1}$)
ϕ_{inc}	Incident ion flux impinging the surface ($m^{-2}s^{-1}$)
$\phi_{s\rightarrow b}$	Absorption flux ($m^{-2}s^{-1}$)
ϕ_{surf}	Flux from the maximum-of-mobile-concentration depth to the surface ($m^{-2}s^{-1}$)
ρ_W	W atomic concentration (m^{-3})
σ_{exc}	Cross section associated to the direct abstraction process (m^2)
τ_m	Characteristic time for c_m^{MAX} growth (s)
ν_0	Pre-exponential frequency associated to the detrapping rate (s^{-1})
ν_0^{bs}	Pre-exponential frequency associated to resurfacing process (s^{-1})
ν_0^{d}	Pre-exponential frequency associated to desorption process from the W surface (s^{-1})
ν_0^{sb}	Pre-exponential frequency associated to absorption process (s^{-1})
ν_{bs}	Rate constant of the resurfacing process (m^1s^{-1})
ν_{crea}	Rate constant of the creation of trap creation process (s^{-1})
ν_{des}	Rate constant of the desorption process (m^2s^{-1})
ν_i	Rate constant of the detrapping process in: the trap type i (s^{-1}) traps filled with i HIs (m^{-3})
ν_m	Rate constant of the trapping process (m^3s^{-1})
ν_{sat}	Rate constant of the saturation of trap creation process (s^{-1})
ν_{sb}	Rate constant of the absorption process (s^{-1})

Sigle table

appm	Atomic part per million
at.fr.	Atomic fraction
at.%	Atomic per cent
D	Deuterium
DFT	Density Functional theory
dpa	Displacement per atom
ERDA	Elastic Recoil Detection Analysis
FIB	Focused Ion Beam
H	Hydrogen
^{3}H	Tritium
He	Helium
HI	Hydrogen Isotope
IBA	Ion Beam Analysis
KMC	Kinetic Monte Carlo
LI	Light Impurities
MD	Molecular dynamics
MRE	Macroscopic Rate Equation
MS	Molecular statics
NRA	Nuclear Reaction Analysis
PAS	Positron annihilation spectroscopy

PCW	Poly crystalline tungsten
PFM	Plasma Facing Material
PFC	Plasma Facing Component
PWI	Plasma Wall Interaction
QMS	Quadrupole mass spectrometer
SCW	Single crystalline tungsten
SEM	Scanning electron microscopy
SIMS	Secondary Ions Mass Spectrometry
SOL	Scrap Off Layer
SRIM	Stopping and Range of Ions on Matter
TDS	Thermal Desorption spectrometry
TEM	Transmission electron microscopy
TIS	Tetrahedral Interstitial Site
TST	Transition State Theory
VH	Vacancy with Hydrogen inside
VCH	Vacancy with Carbon and Hydrogen inside
VOH	Vacancy with Oxygen and Hydrogen inside
W	Tungsten

1. Introduction

1.1 Thermonuclear fusion

1.1.1 Global issues

The energy production is a global issue all around the world because it is the basis of economic, social and cultural development. Currently, the main primary energies are the fossil energies[2]. However, the fossil fuel sources are decreasing and their extractions are more and more expensive. In addition, these energies are less and less fashion since environmental concerns have been expressed in term of global warming. This issue is the point of research for new plentiful and environment-friendly energy sources. One of them is the energy at the origin of the star light: the thermonuclear fusion. Still at the fundamental research state, the path toward an exploitable industrial sector is quite well defined with the ITER project, an international fusion project launched officially in 2006 and currently being built in France, which intends to demonstrate the feasibility of controlled fusion for civil use.

1.1.2 Deuterium-tritium reaction

Two hydrogen isotopes (HIs) are involved in the fusion reaction foreseen to be used in a fusion reactor: Deuterium (D) and Tritium (^{3}H). They have been chosen because they offer the best cross section for the minimal amount of input energy [1, 2]. The exothermic D-^{3}H reaction produced a helium nucleus (α-particle) carrying 3.5 MeV and a neutron carrying 14.1 MeV following this equation:

$$ {}^{2}_{1}\mathrm{D}^{+} + {}^{3}_{1}\mathrm{H}^{+} \rightarrow {}^{4}_{2}\mathrm{He}^{+}(3.5\ \mathrm{MeV}) + {}^{1}_{0}\mathrm{n}(14.1\ \mathrm{MeV}) \quad (1.1) $$

Deuterium is a stable HIs with a natural proportion of 0.015%. It is so abundant in the water all around the globe that makes oceans a quasi-infinite source of fuel. However, Tritium is an unstable HIs with a life time of 12.3 years and its natural isotopic proportion is very low (only trace). The envisaged solution is to create Tritium in-situ using lithium blankets around the fusion device. The reaction of these blankets with the high velocity neutrons from fusion reactions (Eq. 1.1) generates tritium following the equations:

$$ {}^{6}_{3}\mathrm{Li} + {}^{1}_{0}\mathrm{n} \rightarrow {}^{3}_{1}\mathrm{T} + {}^{4}_{2}\mathrm{He} \quad (1.2) $$

$$ {}^{7}_{3}\mathrm{Li} + {}^{1}_{0}\mathrm{n} \rightarrow {}^{3}_{1}\mathrm{T} + {}^{4}_{2}\mathrm{He} + {}^{1}_{0}\mathrm{n} \quad (1.3) $$

According to Eq. 1.1, Eq. 1.2 and Eq. 1.3, the only ash of all the reaction are helium nuclei that are non-radioactive.

For the fusion reactions to occur, plasma with energy more than 10 keV (around 100 million degrees K) are needed in order to over pass the potential barrier and reach a sufficient reaction rate [1, 2]. In order to produce energy from fusion reactions without adding external heating sources, fusion reactions need at least to compensate all the energy losses. This condition called ignition is reached if the Lawson's criterion [1, 3] is verified:

$$ n_i \cdot T_i \cdot \tau_\epsilon > 5 \times 10^{21} \mathrm{keV.\,s/m^3} \quad (1.4) $$

Where n_i and T_i are the ion density and temperature in the plasma and τ_ϵ is the confinement time of the energy. There are three ways to satisfy the Lawson's criterion:

- A very high confinement time, a high density and a relatively low temperature: this occurs in star such as the Sun,

- A high density, a high temperature and a low confinement time: this is the principle of inertial confinement where high power ultra-short laser pulses hit and heat spherical micro D-^{3}H target,
- A high temperature, low density and relatively high confinement time: this is the principle of magnetic confinement where intense magnetic fields confine low density plasma inside a vacuum chamber.

In the following, we focus on magnetic confinement which seems to be the most promising way to achieve controlled fusion on Earth.

1.1.3 Tokamak and magnetic configuration

Among all the potential configurations to go to an industrial fusion reactor, the tokamak has been the most explored one. Tokamak is the Russian acronym for 'toroïdalnaïa Kamera s magnitnymi katushkami' which literally means toroidal chamber with magnetic coil: it is a toroidal device that uses powerful magnetic fields (from toroidal coil) to confine a hot plasma. Stable plasma equilibrium requires both a poloidal and a toroidal magnetic field. The toroidal magnetic field is directly produced by the toroidal coil and the poloidal one is the result of the toroidal plasma current induced by the central solenoid or the inner poloidal coil (Fig. 1.1).

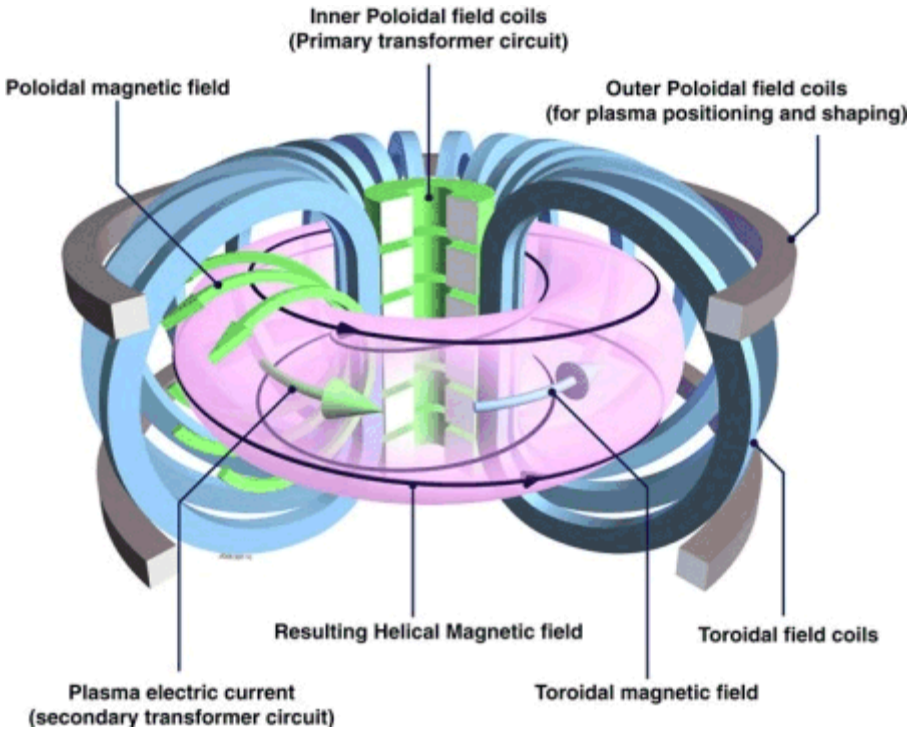

Figure 1.1. Tokamak configuration elements **[4]**

In order to achieve the confinement, the particle pressure has to be lower than the magnetic pressure generated by the magnetic field. This condition implies that the density of the plasma has to be 10^{-4} time lower than the atomic pressure: the inside of the tokamak is in a vacuum chamber.

The aim of magnetic confinement is to confine the ionized particles parallel to magnetic field lines inside a vacuum vessel. However, due to particle collisions and plasma instabilities, a

transport of particles appears perpendicularly to magnetic field line. This perpendicular transport tends to move out the particles from the confined plasma. They form the scrape off layer (SOL) plasma. Figure 1.2 presents a simple sketch of this perpendicular transport (large red arrow crossing the separatrix) in the case of a divertor configuration. Such configuration is currently equipping tokamaks (JET, ASDEX and soon WEST) and will equip ITER because it seems to be the best configuration to have high plasma performances. In this type of configuration, the confined plasma is delimited by the separatrix and the X point. Thanks to a small perpendicular transport in the SOL, the most part of the particles in this region are driven toward a specific part of the wall called the divertor. The components that receive these particles are called the divertor targets. Consequently, these targets will experience a particle flux (thin red arrow) creating interactions between the plasma and the wall or plasma-wall interactions (PWI).
This description is a very simple one that can explain how the divertor targets experience a flux of HI atoms. However, the reality is more complex because pure a D – ^{3}H plasma is not possible for different reason: a perfect vacuum is impossible, impurity injection is needed to mitigate transient event. In addition, the PWI are not experienced only on the divertor target and some particles can also hit the first wall. Finally, in future tokamaks in which a large amount of fusion reactions will take place, 3.5 MeV helium nuclei and 14.1 MeV neutrons will be created. The helium nuclei, which are confined by the magnetic fields, will be cooled down in the plasma contributing to its heating. The interactions of Helium with the wall can be described by the same way as it is done in figure 1.2. In the case of neutrons, they are not sensitive to the magnetic fields and so they will hit any part of the wall with their full energy.

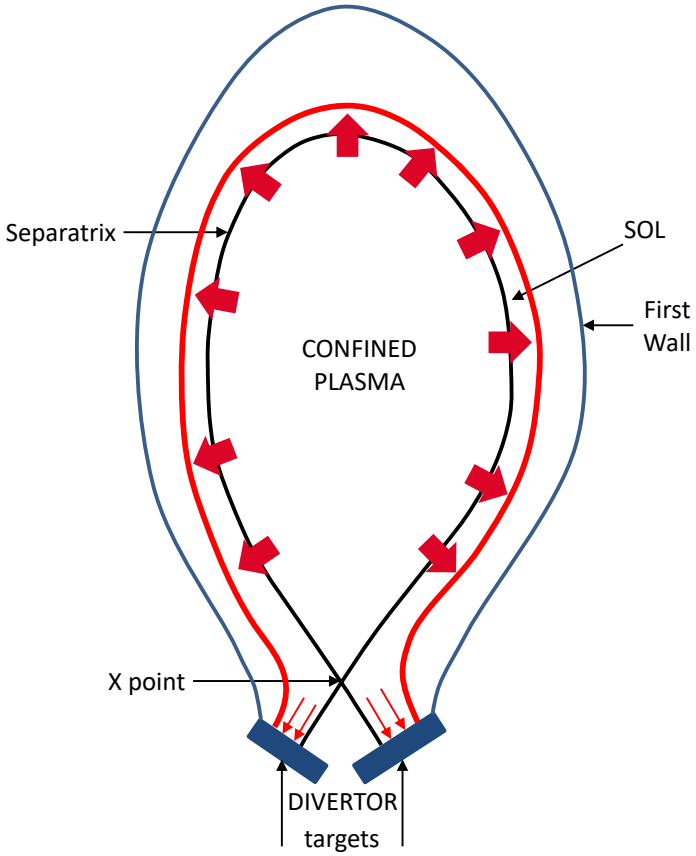

Figure 1.2. Sketch of the perpendicular transport from the confined plasma inducing the formation of the edge plasma called scrape-off layer. Here only a poloidal cross section is presented.

1.2 Choice of the plasma facing materials

According to figure 1.2, in a tokamak, a flux of diverse particles (mainly HI atoms/ions but also impurities, Helium and neutrons in the case of fusion tokamak) hit the plasma facing components (PFCs). These particles will deposit their energy on the PFCs: the incoming flux of particles induces a heating flux that increases the wall temperature. In current and future machines the heating flux is between 1 MW/m^2 and 10 MW/m^2.
Thus, the main considerations to choose an accurate material for the PFCs are:

- Good thermal properties: high temperature of fusion/sublimation to avoid complete destruction of the PFC. In addition, to sustain such high heat flux more than few seconds, the PFCs have to be actively cooled as they were in Tore Supra and as they will be in WEST, EAST, KSTAR and ITER. Thus, a high thermal conductivity is required.
- Electric conductibility. Indeed, since electrically charged particles are implanted and neutralized inside the plasma facing materials (PFMs), electric current need to be created to drive the electric charges away avoiding arcing that would destroy the PFCs,
- Good mechanical properties to hold the mechanical stress induced by thermal expansion or heavy transient such as disruption, edge localized modes (ELMs) …

– Low sputtering/erosion yield to avoid impurities in the plasma or/and low atomic number to reduce impurities impact on the core plasma and increase the life time of the PFCs.

To satisfy the first 3 points, the carbon based materials have been widely used since the 1980's in Tore Supra, JET and other tokamaks all around the world. The first advantage of this material is its sublimation temperature at more than 3800 °C which allows high heat loads without disturbing its mechanical integrity. In addition, it is a low Z material: the carbon impurities tolerance to have good plasma performance is high compared to other metal impurities such as iron (used in the first generation of tokamak). However, the main issue of carbon base PFC is the erosion. Indeed, due to chemical erosion, even at low energy of incident particles, the erosion of carbon is high [5] and it retains a lot of HIs in co-deposited layers [6] with HI/C ratio that can be greater than 0.4 [7].

The tritium is a 12.89 keV – β emitter with a half time period of 12.3 years. Thus, for safety issue the amount of tritium inside the vacuum vessel is limited to 700 g in ITER. It has been estimated that this amount would be reached in less than 100 discharges if the ITER divertor would be made of carbon materials [5].

For all these aspects, the carbon based materials have been put aside and the choice has been done to use tungsten (W) for the divertor of ITER. It main characteristics are summarized in table 1.1 [8].

Atomic number	74
Atomic mass	183.85
Melting point	3410 °C
Boiling point	5700 °C
Recrystallization temperature	1500 °C
Ductile-Brittle transition temperature	between 100°C and 450°C (brittle at room temperature)
Crystallographic structure	Body – centered cubic (bcc)
Lattice constant	316.5×10^{-12} m
Volumic mass density	19.253×10^{3} kg · m^{-3}
Atomic concentration	6.3×10^{28} m^{-3}

Table 1.1. Characteristics of metallic tungsten **[8]**.

Tungsten has been chosen because of its low expected erosion rate under deuterium irradiation. Indeed, the threshold of physical erosion of W by deuterium is around 200 eV [5] which is higher than the incident energy of Deuterium on the divertor target expected in ITER (around 20 – 30 eV/HI). The tungsten thermal properties are also very good since it is the metal with the highest melting point around 3410 °C (table 1.1).

However, as it can be seen on table 1.1, the ductile-brittle transition temperature is between 100 and 450 °C meaning that at room temperature, W is brittle. In addition, the recrystallized structure of W is fragile [9]: the temperatures of the W during the fabrication and the operation of such PFC have to be carefully controlled in order to prevent its destruction.

In order to test the accuracy of such material to be used as a PFC, many current tokamak such as JET, ASDEX-upgrade and soon WEST (the upgrade of the Tore Supra configuration) are equipped with W divertor.

In addition to the W divertor, ITER will be equipped with a Beryllium first wall that will experience lower heat and particle fluxes. In my PhD project, I only focus on the W divertor.

1.3 Problematic

The interaction between the incident fluxes of particles coming from the plasma with a metallic tungsten material can be summarized by figure 1.3.

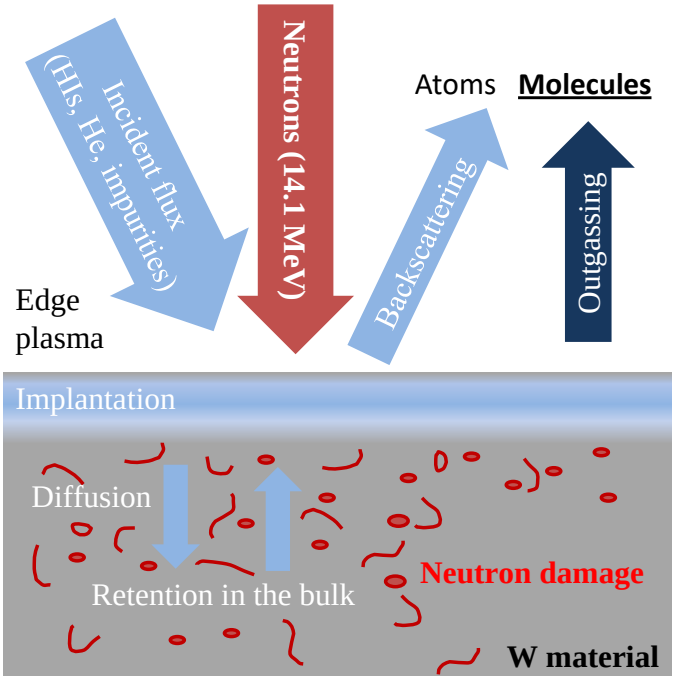

Figure 1.3. Sketch of the interaction between the incident flux of particles from the plasma and the W materials.

The incident energy of the ions is expected to be between 10 – 100 eV in ITER. Such particles can first be backscattered (reflected) by the PFC: the backscattered particles still have some kinetic energies and go back toward the plasma as atoms inducing a recycling flux of hot particles.

The incident particles can also be implanted in the wall. The distribution of the positions where the ions are stopped depends on the energy of the incident ion, the incidence angle, the target material and its surface topology. It can be calculated by the TRIM program (Transport of ions in matter) contained in SRIM® (Stopping and Range of Ions in Matter) software [10]. Once implanted, the particles are thermalized to the temperature of the wall. The concentration of the implanted particles is not homogenous so a concentration gradient appears that make the particles diffuse according to the Fick's diffusion laws: the concentration of particles A C_A in the material B can be described using the diffusion coefficient of A in B D_{AB} (equation 1.5):

$$\frac{\partial C_A}{\partial t} = \vec{\nabla} \cdot (D_{AB} \cdot \vec{\nabla} \cdot C_A) \quad (1.5)$$

The particles can both diffuse toward the surface and toward the bulk. In both cases, they may encounter defects such as vacancies or grain boundaries that can retain them as it will be shown in this manuscript. The implanted particles may also formed defects and change the surface morphology as He which agglomerates forming He bubbles in W [11, 12, 13] and formed on the

W surface very porous nano-tendril structure called fuzz [14]. Tritium is radioactive and decays creating ^{3}He: the trapping of tritium can lead to formation of helium bubble due to the tritium radioactive decay.
Arriving on the surface, they are outgassed and go back to the plasma inducing a first flux of recycling (figure 1.3, blue 'outgassing' arrow on the left). If the incident particles are HIs, they have to recombine to form HI_2 molecules: this outgassing flux is a flux of cold molecules.

Finally, The 14.1 MeV neutrons generated by fusion reactions lose their energy by collisions with the W atoms:

- Elastic collisions: the neutron gives a part of its energy to the W atom and the kinetic energy and the momentum of the couple neutron/W atom is conserved. It creates collision cascades inducing point defects (vacancies, self-interstitial), dislocations (lines and loops) and 3D defects (vacancy or interstitial clusters) [15]. Such damaging can be quantified by a physical quantity called displacement per atom or dpa.
- Inelastic collisions: the neutron reacts with the nucleus of the target atom and via nuclear reactions transmutes it into other chemical elements. The transmuted elements can be disintegrated through alpha decays inducing a production of Helium in the material.

By the end of ITER operation, it is expected that the W materials will receive a dose of 0.7 dpa [16] and the main transmutation products will be Rhenium (Re) and Osmium (Os) and Tantalum (Ta) with quantity around 10^{3}-10^{1} appm (atomic party per million) after 14 years [17]. Such changes of the microstructure will modify the retention properties of the W materials since new defects (vacancies, dislocations … in the case of elastic collisions and substitutional/interstitial atoms in case of inelastic collisions) will appear.

From this simple description of the interactions between the plasma and W, two issues can be stated:

- As explained already, the overall amount of tritium in ITER vacuum vessel (wall+dust+plasma) cannot be higher than 700 g. Thus, it is important to be able to evaluate the amount of tritium retained in the W divertor.
- The outgassing and reflection of HIs from the wall to the plasma can affect the edge plasma since it acts as a source of particles feeding the plasma edge. Thus, it is important to estimate the quantity of reflected and outgassed particles from the W wall as well as the dynamic of such recycling.

In order to answer these two open issues, the HIs retention properties in W have to be determined. In addition, the impacts of the fusion products and especially the impacts of the neutrons have to be evaluated and quantified.
Both experimental and theoretical/simulation aspects are important. The first one to determine the underlying physical processes that lead to HI retention and the second one to rationalize these processes and predict what will happen in tokamak environment.
In this PhD project, my purpose was to simulate well characterized experiments to obtain the HI retention properties and then:

- Predict the tritium retention in W PFC in ITER and future reactors,
- Give a wall model that will calculate the outgassing flux of molecules from the wall to the plasma in order to evaluate the molecular part of the recycling flux.

In this document, the state of the knowledge and the experiment that are simulated are presented in chapter 2. This chapter contains also a theoretical overview of the H/W interactions undertaken to understand the experimental results.

Then, chapter 3 presents the theoretical models used during this PhD project.
Chapter 4 shows the simulations of the experimental results presented in chapter 2 that allows to parametrize the wall model.
Finally, chapter 5 is dedicated to simulations of tritium retention during realistic tokamak cycles in order to estimate the tritium retention during tokamak operations.

2. State of the art - the H/W interactions

The physical processes which drive fuel retention and molecular recycling are mainly the interactions between electronic clouds of fuel particles and metallic tungsten inside tungsten material and at its surface. In that respect, the study of any HIs (hydrogen (H), deuterium (D) or tritium (^{3}H)) in tungsten would give useful data to answer these two problematics.

2.1 Simple description W/H interactions

There are two distinct places which play a role in the interaction between HIs and W: the surface and the bulk of the material. Figure 2.1 is a schematic representation of these interactions for the H that are not reflected on the W surface. The grey circles represent the tungsten atom of the crystal, the red circles represent the impurities that can exist on the surface or in the bulk and the blue circles stand for the H atoms. Three cases exist:

- H as molecules. The H_2 molecules dissociate so atoms can be adsorbed on the surface,
- Slow H atoms. The slow H atoms can also be adsorbed on the surface because they have not enough energy to be inserted directly in the metal,
- Energetic H ions/atoms. The fast H ions/atoms are directly inserted in the metal matrix. The depth at which they are stopped is distributed around a mean depth that depends on the energy of incident ions/atoms.

The atoms on the surface diffuse on that surface and can recombine if they meet each other. The recombination of H into molecules is the only way for H to be desorbed. They can also enter the bulk. In the bulk of the metal, H is present as atom and will diffuse in the perfect lattice between interstitial sites. They can be trapped in defects that are always present in real tungsten. There can be different sorts:

- 0 dimension defects: the interstitial atom (impurity …) and the mono-vacancy represented in figure 2.1,
- 1 dimension defects: the dislocation (screw, edge, loop …),
- 2 dimension defects: grain boundaries (GB) for polycrystalline W (PCW),
- 3 dimension defects: cluster of interstitial or void.

These defects can interact with the H atoms present in the bulk. They can trap them or provide preferred diffusion channels.

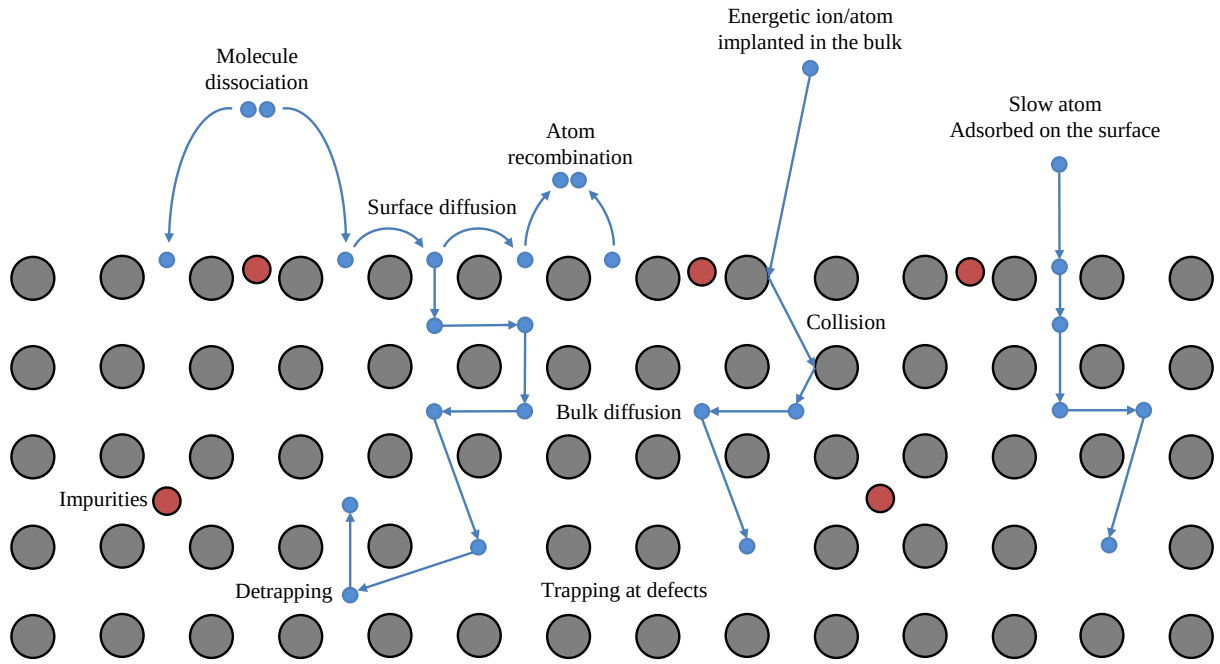

Figure 2.1. Schematic representation of interaction between W and H.

To describe the process exemplified in figure 2.1, the idealized energy diagram of hydrogen/tungsten interactions is commonly used [7, 18, 19, 20, 21]. It represents the evolution of the W/H interaction potential with the reaction coordinate (the distance between H and W atoms).

In this diagram, the interactions between H_2 molecules and the W surface is repulsive (dashed line): the H_2 molecules needs to dissociate to enter the bulk or to be adsorbed on the surface as explained figure 2.1. This process is associated to a first energy barrier E_C which corresponds to the crossing between the H atom/W potential interaction curve and the H_2 molecules/W potential interaction curve in figure 2.2. Once dissociated, the H atoms are adsorbed on the surface where they can diffuse. If an ad-atom (i.e. an adsorbed atom) meets another one, they can recombine and leave the surface (figure 2.1). For this entire process (surface diffusion + recombination), there is the energy E_D. A care has to be taken here. In this description, E_D is half the activation energy for the desorption of HIs: the total energy needed for recombination is $E_{des} = 2 \cdot E_D$ but the energy $E_D = E_{des}/2$ is used to get the solution energy [21]. E_D can be called the desorption energy per ad-atom and this notation is used in the following [21].

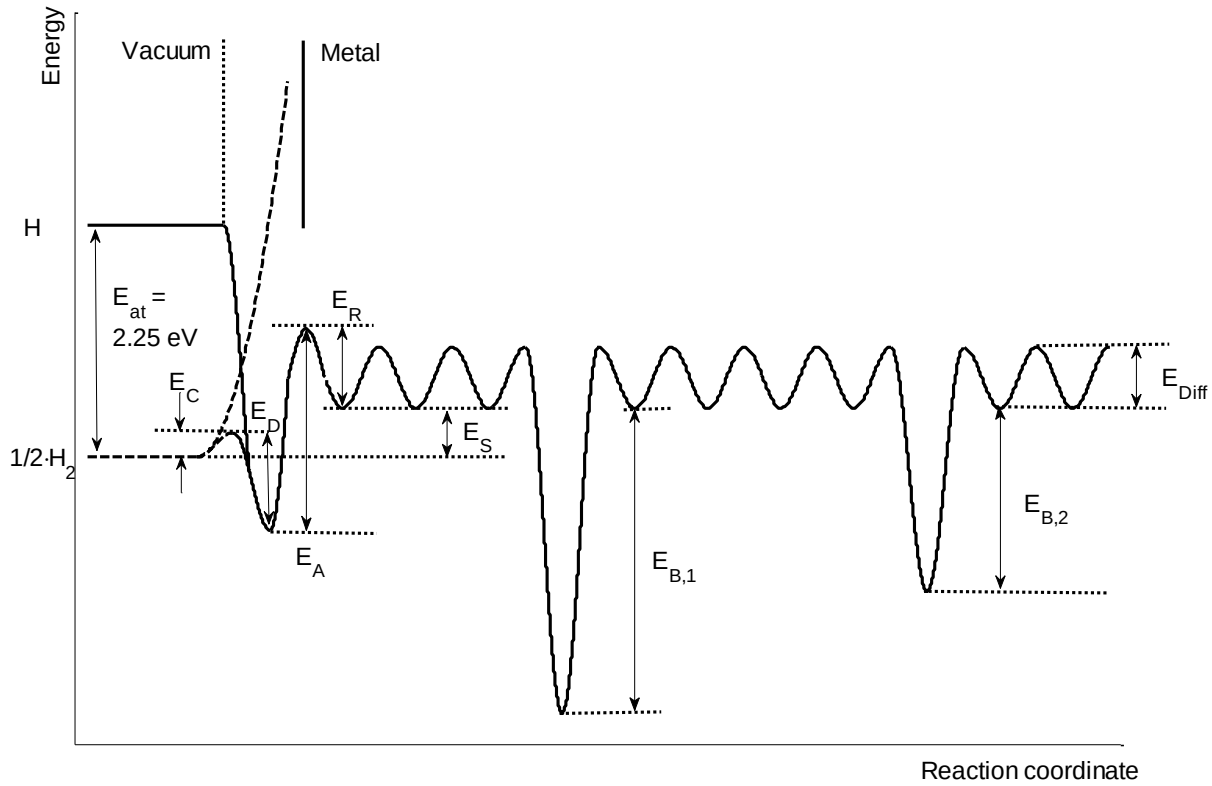

Figure 2.2. Schematic idealized energy diagram of H/W interactions. The solid line corresponds to the interactions between H atom and the metal and the dashed line correspond to the interaction between H_2 molecule and the metal.

The H ad-atoms can also enter the bulk from the surface (be absorbed) by overpassing the energy barrier E_A for absorption. Once in the bulk, H atoms can diffuse through interstitial site present in the lattice. For this process, the energy barrier is called E_{diff}.
The H atoms can diffuse toward the bulk or toward the surface depending on the H concentration gradient. If they diffuse toward the surface, they can overpass the energy barrier E_R to go from bulk to surface. This process is called the resurfacing process. During the diffusion process toward the bulk or the surface, H can be trapped at defects. To get detrapped, the energy barrier is $E_{T,i} = E_{B,i} + E_{diff}$. $E_{T,i}$ is called the detrapping energy and $E_{B,i}$ is called the binding energy which is the difference in term of energy between H in the trap i and H in an interstitial site. The value of $E_{B,i}$ can change depending on the nature of the trap (vacancies, grain boundaries, dislocation, void …). The potential profile can also be different from this simple picture plotted figure 2.2 as for example for dislocation [22].
From the four energy barriers E_C, E_D, E_A and E_R, the solution energy can be defined as $E_S = E_A - E_R - E_D + E_C$ [21] and expresses the thermodynamic equilibrium between H_2 gas phase and H in the metal. It gives the information about the affinity between H and the metals. If $E_S < 0$, the metal is exothermic: there is a chemical affinity between H and the metals. If $E_S > 0$, the metal is endothermic: energy must be added to introduced H inside the metal. As it can be seen on figure 2.2, there is a difference between the energy level for H atoms and H_2 molecules. This difference is $E_{at} \approx 2.25$ eV and is equal to half the bond-dissociation energy of H_2 molecules (this energy is slightly different for D_2 and T_2 molecules). If this value is higher than the solution

energy E_S, H atoms can possibly be inserted directly in the bulk without being affected by the surface barriers.

From the interaction potential diagram (figure 2.2), the kinetic of each process can be described using transition state theory (TST) [23]: the rate $\nu_{1\to2}$ (in s^{-1}) to go from a stable site 1 to another stable site 2 can be written with an Arrhenius law as Eq. 2.2:

$$\nu_{1\to2}(T) = \nu_0 \cdot e^{-\frac{E_{1\to2}}{k_B \cdot T}} \quad (2.2)$$

In this expression, ν_0 is called the pre-exponential factor (s^{-1}) and $E_{1\to2}$ is the activation energy (eV) to go from site 1 to site 2. $k_B \approx 8.6 \times 10^{-5}$ eV · K^{-1} is the Boltzmann constant and T is the temperature (K). Using TST to reproduce experimental measurements, both the value of the pre-exponential factor and the activation energy for the processes described in figure 2.2 can be determined. However, this does not give any indication on the type of defects involved in trapping, the type of trapping/diffusion site on the surface or the type of site through which H atoms diffuses. To answer these questions, calculations at the atomistic scales can be done such as density functional theory (DFT) or Molecular dynamics (MD). Because they simulate atomic scale processes, they require high computational time and are thus limited to the simulations of small times (few ns in case of MD) and space scale (few tens or hundreds of lattice constant).

In a multi-scale modelling approach, these calculations technics simulate at the atomic scale the interactions of H atoms with W in different configurations. They can provide activation energies for the different processes (diffusion, trapping, absorption, desorption, resurfacing …). Despite the fact that these technics simulate quasi ab-initio interactions between H and W, the results they obtained need to be look with a critical point of view. Indeed, in case of MD, the values obtained are strongly dependent on the type of interaction potential used. For DFT, the results can be impacted by the size of the simulated crystal, the approximation chosen for the exchange-correlation potentials…

These activation energies can be used in kinetic model (using rate defined by Eq. (2.2)) as Object Kinetic Monte Carlo simulation (OKMC) or Macroscopic Rate Equation simulation (MRE) in order to compare modelling and experimental measurements and discriminate the processes involved in H trapping in W.

In order to verify the accuracy of the models used, simulations of well-known experiments are mandatory. In that respects, the next section of this chapter presents the different experimental technics used to address these points.

2.2 Experimental technics

2.2.1 Sample preparation

The first step of any experimental procedures is to prepare the sample. The purpose of this preparation is to control the initial microstructure of the sample. It allows reducing the interference of artifact on the obtained experimental results and getting repeatable results. The standard procedure can be divided into two types that are: the polishing of the sample and the thermal preparation.

The purpose of the polishing is to provide a quasi-flat surface in order to remove artifact created by rough surface (increase of the adsorbed species …). The mechanical polishing can be used to remove the effect of past implantations if previous implantations have been done on the

sample. This polishing can be complete by electrochemical polishing in order to remove the residual stress on the surface induced by the previous mechanical polishing.

During the thermal preparation or annealing, the sample is heated to a temperature for a given time under a chose atmosphere to different purposes. Among them, the samples are heated before H loading to:

- outgas impurities and previously loaded H (under vacuum) [24, 25],
- reduce the residue of polishing [25, 26, 27],
- remove the residual stresses [25],
- remove the eventual oxide layer that can be formed (under H_2 pressure [25, 28, 29]),
- reduce the intrinsic defect concentrations through defects motion [25, 26, 27].

The temperature of the annealing varies across the literature. Between 743 K with a pressure of 1 atm of H_2 to reduce the oxide layer [28] to 2400 K under vacuum to recrystallized the sample and remove the dissolved impurities [29].

The impact of the sample preparation can be characterized by different characterization technics that are described in section 2.2.5. For example, Manhard et al. [30] annealed a polycrystalline tungsten (PCW) samples at 1700 K and 2000 K for 20 - 60 min. They looked at the STEM images before the annealing, after the annealing at 1700 K and after the annealing art 2000 K. Without any annealing, a large dislocation lines network is observed in the sample. This dislocation lines network is completely remove after the annealing at 1700 K meanings that samples that experienced an annealing at 1700 K do not have intrinsic dislocations.

In any case, the sample preparation is a key point in the analysis and comparison of the experimental data.

2.2.2 H loading in W sample

In order to study the interactions of H with tungsten at the surface or in the bulk, tungsten samples need to be load with H. The loading can be done using H_2 molecules, H atoms or ions (H^+ or H_2^+).

Using H_2 molecules, the amount of H that will interact with the surface/bulk material depends mainly on the temperature of the gas/metal and the H_2 pressure. To quantify the amount of molecules that interacts with- the metal surface, a quantity is defined which is called the exposure ϕ. Its unit is the Langmuir (L) and it is defined as: $\phi = t_{exp} \cdot P_{exp}$. Here, t_{exp} is the time of exposure and P_{exp} is the pressure. 1 L corresponds to the exposition of a surface to a gas pressure of 10^{-8} torr for 100 seconds. The H loading with gas is particularly accurate to study the interaction of H with W surface at low temperature (90 K in [31, 32]). To check that no HIs is entering the bulk, it is common to look for the amount of retained HIs as function of exposure [32, 33, 34]: if it saturates, it means all the surface sites are occupied by HI atoms and if it does not for long exposure, it means part of the HIs atoms are in the bulk. It can also be used to load W with H in the bulk by increasing the temperature [29] and can be used to study the interaction between W dust and T [28].

To study the H/W surface interaction, an H atom source can also be used. There is two main ways to create a flux of H atoms by breaking the H_2 molecules:

- Or the molecules are broken by a hot filament,
- Or the molecules are broken by a hot capillary source heated by electron bombardment.

According to [35], the second method provides a better characterized flux of H atoms and a lower amount of unbroken molecule on the W surface than with the first method. Thus, the

experimental conditions that will be inserted as input for the modelling are better characterized providing more relevant results.
With these two last technics, the atoms first stick on the surface and then can be absorbed inside the bulk. However, they can also stay on the surface and never enter the bulk depending on parameters such as sample temperature. The temperature that triggered the absorption of the adsorbed H is related to the energy barrier E_A.

The last technics to load sample with H is to use ions sources. The sources can be plasma sources or ion guns. In both case, the ions are created from H_2 gas that is ionized. The differences between the two types of sources are the energy range available, the amount of neutrals, the flux of particles… For example, in case of plasma implantation, very low energies of few eV/H are available but higher energies of tens of hundreds of keV/H are not. This is the opposite for ions guns. The purpose stays the same: implant ions directly in the bulk. In any case, the incident flux of H impinging the surface is obtained by recording the current of electrons that is created during the implantation: the incident ions are neutralized in the materials creating a local deficit of electrons inducing an electric current that is measured. The incident flux is obtained because the reflected H are also neutralized.

For the two last technics (atoms and ions sources), to quantify the amount of HIs that interact with the metal, two quantities are defined: the flux and the fluence. The flux stands for the amount of particles that hit the surface per unit of time and surface. It is expressed in particles/m^2/s. The fluence is the amount of particles that hit the metal surface per surface unit for a given time. It is expressed in particles/m^2.

2.2.3 Thermal desorption spectrometry

The principle of the thermal desorption spectrometry (TDS), also called thermal programmed desorption (TPD), is to measure quantitatively the gas that is desorbed form the sample during a well-controlled evolution of its temperature.
In practice, after the H loading, the W sample is inserted in a vacuum chamber with a very low background pressure (between 10^{-10} mbar to 10^{-8} mbar). The complete device is equipped with at least 6 components which are described below and in figure 2.3:

- A vacuum chamber which is continuously pumped (with primary pump and turbomolecular pump),
- A quadrupole mass spectrometer (QMS) which records over time the gas species that are present in the chamber,
- One or several pressure gauge which records the pressure inside the chamber,
- A gas injection line for QMS calibration,
- A heating system (tungsten filament, electron beam) which heats the sample,
- A Temperature monitoring device which is composed of a temperature sensor (thermocouple for example) for feedback of the heating system.

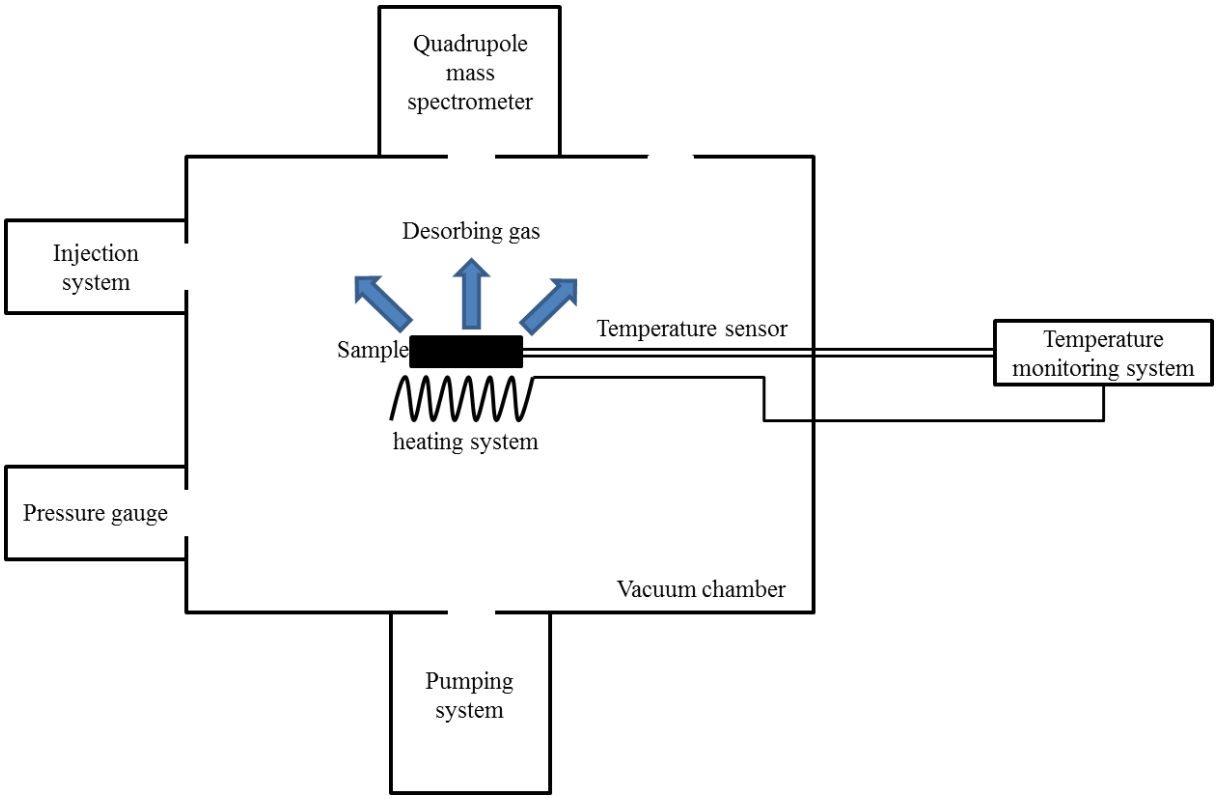

Figure 2.3. Schematic description of a standard TDS device.

There are two main purposes to this experiment:

- Measure the overall amount of HI retained inside the sample,
- Look for the triggering of desorption of HIs (which may be temperature).

To get the first point, the mass spectrometer is calibrated with the pressure gauge. The calibration consists on injecting well known gases (H_2, D_2 and N_2 for example) using the injection system (figure 2.3). During the injection, the pressure and the QMS signal are recorded. Thus, a correlation can be done between the spectrometer signal of a specific species (mass 2 for H_2 and mass 4 for D_2) and the partial pressure of these species in the gas present in the chamber. If the pumping speeds for these particular species are known, the partial pressures can be transformed into the production of each species per time unit i.e. the amount of each species that is desorbed with time from the sample and all the other surface of the vacuum chamber. In that respect, it is important to control the residual gas and the background level which determine the sensibility limit of the device. In order to have reliable measurement, a background pressure around 10^{-8} mbar is often used in the literature [25, 26]. However, the sensibility can be enhanced by pumping differentially the mass spectrometer [24] achieving very low background pressure (below 8×10^{-11} mbar). In any cases, the background gas is often composed of H_2 and other air component (N_2, O_2 and water). The signal of H_2 recorded by the mass spectrometer can be highly perturbed by the H_2 background gas making hard the determination of the amount of H_2 that desorbed from the sample [36]. To establish the amount of H_2 that is really desorbed from the sample, a procedure presented in [37] can be done that uses the value of HD and D_2 signal recorded by the mass spectrometer.

To control the evolution of the sample temperature during the heating, a temperature sensor (a thermocouple for example) is necessary to apply a feedback on the heating system. In standard TDS experiment, the temperature (T) increase linearly with time (t) from a starting temperature (T_0) with a certain heating rate (β): $T = T_0 + \beta \cdot t$. However, it is not mandatory and it can be imagined several evolution of temperature with time. For example, isothermal experiment or step by step… The temperature measurement and the control of the evolution of temperature with time is a critical point of the TDS technic because it guarantees the quality of the experimental data obtained. The accuracy of the temperature measurement can be affected on the type of method used to measure the temperature, the place where the temperature sensors take the temperature (on, in the sample or on the sample holder …). Different type of thermocouples or pyrometers can be used but the common accuracy of the temperature measurement can be around few tens of K which corresponds to an accuracy of around 0.1 eV on the detrapping energies that can be obtained by simulations.

To analyze the experimental measurements, the desorption rate (production per time unit) of the desorbed species (in our case molecules containing HIs) is plot versus the temperature of the sample and the obtained plot is called TDS/TPD spectrum. An example of TDS spectrum of D getting out from W sample is shown in figure 2.4 (taken from [24]). It shows the desorption rate of D atoms (in $m^{-2}.s^{-1}$) as function of the temperature that is recorded during a continuous increase of sample temperature of 1 K/s. The TDS is performed after D ion implantation at different fluences.

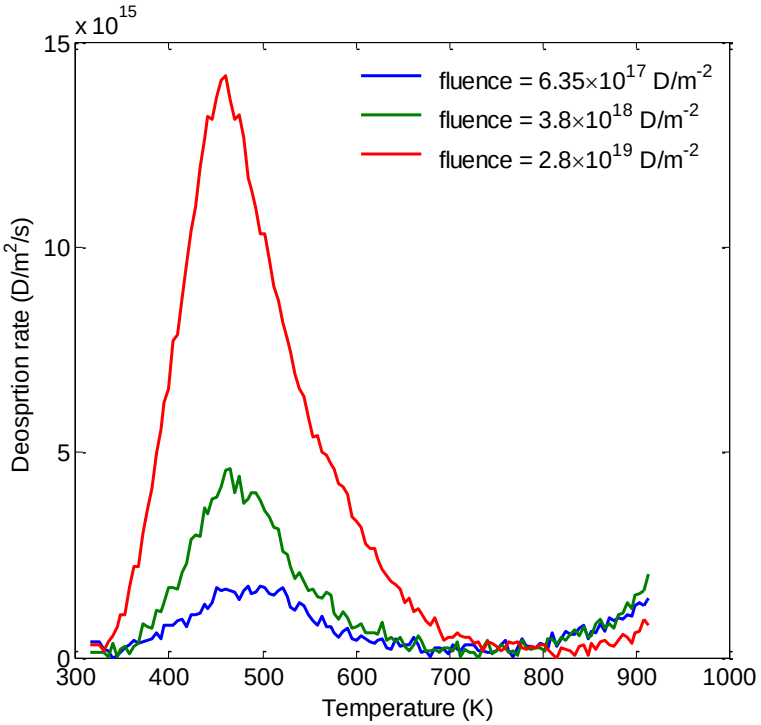

Figure 2.4. Experimental TDS spectra of D desorbing from W sample for different fluence **[24]**. The heating rate is 1 K/s.

A typical TDS spectrum, as those exposed figure 2.2, exhibit a desorption rate that peaks at certain temperatures. It has to be point out that the increase of the desorption rate at high

temperature is an artifact that may come from the desorbing species from all the part of the vacuum vessel. The position of this peak (here around 450 K) gives information on the desorption temperatures and so on the detrapping energies of the trapping site present in W. The overall amount of HIs retained can be measured from TDS spectrum by integrating the desorption rate over temperature (⇔ time in case of linear increase of temperature with time).
The TDS technic is one of the major technic used in the parametrization of the model developed in this work as it will be discussed later in Chapter 4. It gives information on the temperature of desorption (and so detrapping energies) from trapping sites. However, it gives global information and no information on the space distribution of the trapping sites can be extracted from TDS spectrum. In order to look for the distribution of HIs in the depth, ion beam analyses are used.

2.2.4 Ion Beam Analysis

Several Ion Beam Analysis (IBA) technics exist based on the same principle: launch energetic ions on a target sample and analyze particles (photon, ions, atoms, molecules …) that are emitted during the interactions between the target and the ion beam. For this technics, the ion beams need to be well characterized in energy that can varies from several hundreds of keV to several MeV. In that respect, the ions source used in IBA is mainly ion gun or particle accelerator (Van de Graaff, cyclotron …). An IBA device is composed with at least three parts presented below and in figure 2.5:

- A vacuum chamber inside which the sample to analyze is hold. In this chamber, a specific equipment can be added to monitored the position, the incident angle of the ion beam with the sample surface, the sample temperature.
- A line with the ion source,
- A line with the detector of particle emitted during the ion beam/sample interaction.

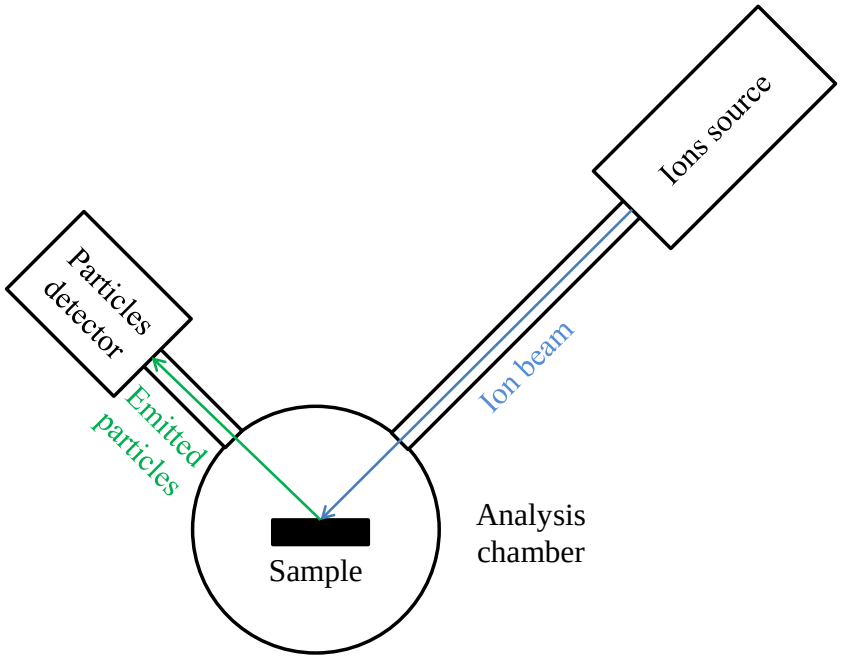

Figure 2.5. Schematic description of an IBA device.

Several IBA technics exist depending on the type and energy of ions that are launched on the target sample, the interactions that happen between the target and the ions, and the emitted particle that are detected. Here is a non-exhaustive list of IBA technics that can be used to characterize the presence of HIs in W:

- ERDA: Elastic Recoil Detection Analysis,
- NRA: Nuclear Reaction Analysis,
- SIMS: Secondary Ion Mass Spectrometry.

To probe the presence of light element inside W, ERDA can be used. In this case, the particle detected is the scattered target atom that is recoiled (or ejected) from the materials by the incident ions. This technic is especially suitable to detect the presence of light elements such as HIs inside materials as tungsten [38, 39]. In this case, the ions that are used are MeV-$^{7}Li^{2+}$ [38] and the maximal depth that can be probed using this technic is several hundred of nm. This technics is quantitative assuming that the cross sections of interaction are known and using the SIMNRA computer program [40] to obtain the evolution of concentration in depth. In the case of H/D detection in W, the sensitivity of the ERDA technic is below the sensitivity of the NRA (see below). However, one main advantage of the ERDA technic compared to the NRA technic is that it can record D and H (NRA can only detect D) [41]. In addition, the ERDA technic is sensitive to the surface process unlike NRA [41].

SIMS is another technic that can be used to detect the presence of H near the surface. In SIMS experiment, a heavy ion beam is launched on a sample with enough energy to sputter the surface of the sample. A part of the sputtered particles are ions. These ions are collected and directed to a mass spectrometer to be analyzed (the non-ionized particles are not analyzed). Several modes can be performed to get different type of information. In static mode, the ions flux that sputters the surface is low compare to the atomic surface density: only the surface is probe and no depth information is obtained. In dynamic mode, the ions flux sputtering the surface is higher: the atomic layers are eroded one after another and a depth profiling of the different species in the sample can be done. In case of W, the depth that is commonly reached is around 100 nm [42]. This technic is only qualitative. It can be calibrated using NRA (see below) or TDS measurements [43].

NRA is a technics based on the nuclear reaction between the incident ion and target nuclei. The result of this interaction leads to the creation of different type of particles (neutron, proton, photon …) that can be detected. A residual nucleus is also formed during the nuclear reaction but not detected. Depending on the species one want to detect and the nature of the materials in which this species is, different incident ions can be chosen.

In case of HIs presence in W, the reaction considered is described by equation 2.1 as follow [44]:

$$^{2}D + ^{3}He \rightarrow {}^{1}p + {}^{4}He \qquad (2.1)$$

This reaction, noted allows detecting the target atom of deuterium using incident $^{3}He^{+}$ ions between 0.5 MeV and 6 MeV. The detected particle can be a proton p or a helium nucleus ^{4}He. This technics is particularly suitable for determining quantitative D depth profile in a W sample. It requires the knowledge of cross section of reaction 2.1 and a deconvolution technique is necessary that can be done using the program SIMNRA [40]. Considering the stopping power of $^{3}He^{+}$ in W between 0.5 MeV and 6 MeV, the maximal depth that can be probed using this technics is around 7 µm and the depth resolution is 0.3 µm [44]. The detection limit of the technic is around 10^{-3} at.% (10^{-5} D atoms per W atoms) [45]. The accuracy of the concentrations obtained varies between 20 % to 100 % depending on the D concentration in the bulk relatively to the D concentration in the surface [44].

These three technics are particularly interesting to determine the distribution of HIs in the bulk and so the distribution of traps that retained HIs. This is especially the case of ERDA for the near surface and of NRA deeper in the bulk. In the other hand, SIMS can give quantitative measurements but it needs a calibration steps that requires more experimental device. However, SIMS can scan different species: the synergetic effect of impurities on HIs trapping can be obtained from SIMS measurements.

2.2.5 Sample characterization technic

The previously presented technics (TPD/TDS, SIMS, ERDA, NRA) are dedicated to the study of H/W interactions by directly probing the presence of HIs inside a sample. However, to help to interpret the results, several technics are dedicated to the sample characterization. These technics can provide very helpful information for example on surface or bulk composition (purity, oxide layer …) and morphology (mono or poly crystalline sample, dislocation or blister presence …). They are so used to look at the evolution of the sample microstructure from the sample preparation (in order to qualify the preparation) to the implantation to qualify the effect of H implantation on the sample. Here stands a non-exhaustive list of briefly described technics that can be used:

- XPS: X-ray Photoelectron Spectrometry. This technic, based on the interaction of X-ray photon with the core electrons of the chemical species on the sample surface, is particularly accurate to look for oxide layers [46, 47], carbon based impurity [47] or any other impurity on the sample surface.
- SEM/TEM: Scanning/Transmission Electron Microscopy. These both technics, based on the interaction of electron with the analyzed matter, are imagery technics. SEM and TEM are used to look at surface morphology, especially blister presence [47, 48, 49, 50], and bulk property such as grain boundaries, dislocations, voids, cracks [51, 49, 50, 52]. SEM is focus on scanning the surface which gives only the surface information. In another hand, TEM can be coupled with FIB (Focused Ion Beam) technic that is used to cut the sample and have access to bulk information [51, 49, 50, 52].
- PAS: Positron Annihilation Spectroscopy. This technics, based on the positron-electron annihilation allows probing the presence of defects inside W. These technics have been used to detect the presence of vacancy and vacancy cluster in W [53, 54, 55].

2.2.6 Summary

First the sample preparation is discussed explaining that polishing and thermal treatment are mandatory in order to have repeatable and accurate measurements by controlling the initial microstructure of the samples. Then, the H loading methods are divided into three branches: the gas/molecules loading, the atoms loading and the ions loading. Finally, the main experimental technics that probe the presence of HIs in the studied samples are described and the type of information obtained is discussed:

- The TDS technics gives information on the detrapping energy barrier as well as on the overall quantity of HIs trapped. It required a low background pressure, a calibration of the mass spectrometer and a good temperature control/measurement in order to obtain reliable data.

– The IBA technics give information on the distribution of HIs (of traps) in depth but also the synergetic effects effect on HIs trapping. It requires a calibration in case of SIMS and a computer program like SIMNRA to obtain quantitative information.

These two technics are extensively used to parametrize the wall models that include HIs trapping end release. Other technics are used to characterize the W sample without HIs (micro-structure, impurities content …). They are more briefly described here since they are not used extensively in the model parametrization.

2.3 Literature results on the H/W interactions

This section presented the experimental and theoretical results presented in the literature that are used in chapter 4 to parametrize the MRE models presented in chapter 3 and used in chapter 5 to estimate the retention and recycling in real tokamak condition.

2.3.1 Hydrogen on the W surface

i. Experimental overview

To study the H atoms on W surface, the surface coverage θ is defined. Calling $n_{surface}$ (in m^{-2}) the amount of available adsorption sites on the surface and $c_{surface}$ (in atoms.m^{-2}) the concentration of H atoms on the surface, the surface coverage is defined by Eq. (2.3).

$$\theta = \frac{c_{surface}}{n_{surface}} \tag{2.3}$$

If $\theta = 1$, the surface is saturated in H and if $\theta = 0$, the surface is free of any H.

To quantify the adsorption of H atoms on W surface from a source of molecules or atoms, the sticking probability is used and defined as $s = \frac{\phi_H}{\Gamma_H}$ with Γ_H being the incident flux of H (as molecules or atoms) and ϕ_H is the part of the flux that is really adsorbed. It is shown experimentally that, for H loading by gas (H as molecules), the sticking probability of H on clean W surface does not depend on the temperature (or by a weak dependence) [56, 57] but depends on the surface coverage [56, 57]. The sticking coefficient decreases as the coverage increases: as the adsorption sites are occupied, they cannot accept other H atoms. These results suggest that the dissociation energy $E_C \approx 0$ as proposed in [21]: the dissociation of H_2 on W surface is not thermally activated. It has also been recorded that impurities such as oxygen (O) have an impact on sticking coefficient of H on W surface: the sticking coefficient of hydrogen on (110) and (112) tungsten surface decreases as the surface coverage of pre-adsorbed O increases [31, 33]. The simplest interpretation of this result is that O inhibits H sticking on W surface by blocking the adsorption sites for H.

If H atoms are loaded on the sample using energetic atoms, it has been shown by MD simulations [58, 59] using the H-W potential developed by Juslin et al. [60] that the sticking probability depends on the incident energy of the atoms. From 0.01 eV to 1 eV, the sticking coefficient decreases quasi linearly from 0.5 to 0.1 and it is around 0.2 for an incident energy of 0.2 eV. Ogorodnikova et al. [59] explain this behavior by the large potential energy of the incoming atom (see figure 2.2 and E_{at}): the excess of energy is transferred to kinetic energy but can also be dissipate through internal state (vibration, rotation) as well as surface excitations (electron-hole pairs, phonons). The dissipation processes are efficient at low initial kinetic energy where the

sticking probability is high. As the initial kinetic energy of the atom increases, the dissipation processes are less and less efficient: the sticking probability decreases. Between 1 eV and ~10 eV, the sticking probability is constant and equal to 0.1. Then, it increases to around 0.6-0.9 at incident energy of 100 eV because in this range of temperature, the atom are implanted in the metal. This trends is observed in the simulation for three different surface orientations, W(110), W(001) and W(111) with a slightly higher sticking probability for W(111).

To study desorption of H from W surface, the samples are loaded with H_2 molecules at low temperature [32] to avoid any absorption of H inside the W bulk. Then, TDS is performed to estimate the energy of desorption of H from W surface. To calculate the desorption energy E_{des} from TDS spectrum in case of H adsorbed on a metal surface, the transition state theory (TST) described by Eq. 2.2 is used. The normalized desorption rate R_{des}(in s^{-1}) recorded during the TDS experiment is in fact the opposite time derivative of the surface coverage θ and can be explicitly expressed using TST by Eq. 2.4:

$$R_{des}(s^{-1}) = -\frac{\partial\theta}{\partial t} = \theta^n \cdot \nu \cdot e^{-\frac{E_{des}}{k_B \cdot T}} \tag{2.4}$$

In this equation, $E_{des} = 2 \cdot E_D$ is the activation energy for desorption of a molecule of H_2 and n is the order of the reaction. A first order reaction $n = 1$ corresponds to a direct desorption of the adsorbed species. A second order reaction $n = 2$ occurs when there is a recombination step between two adsorbed atoms during the desorption process. Since the H desorption from tungsten surface involves recombination, second order reaction is often used to analyze the experimental TDS spectra of H desorption from surface.

During the TDS, temperature and time are linked via the heating ramp $T = T_0 + \beta \cdot t$. Eq. 2.4 can then be rewritten replacing time by temperature in Eq. 2.5:

$$-\frac{\partial\theta}{\partial T} = \theta^n \cdot \frac{\nu}{\beta} \cdot e^{-\frac{E_{des}}{k_B \cdot T}} \tag{2.5}$$

As explain in section 2.1.2, TDS spectra show presence of desorption peaks. At the maximum of the desorption rate, $T = T_m$, we have the derivative of the desorption rate which is zero for $n \geq 1$: $\frac{\partial R_{des}}{\partial t}_{T=T_m} = 0 = -\frac{\partial^2\theta}{\partial t^2}_{T=T_m}$. From this, the formula proposed by Redhead [61] can be obtained to determine the desorption energy from TDS spectrum temperature position (Eq. 2.6):

$$\frac{\beta}{k_B \cdot T_m^2} = n \cdot \theta^{n-1} \cdot \frac{\nu}{E_{des}} \cdot e^{-\frac{E_{des}}{k_B \cdot T_m}} \tag{2.6}$$

According to Eq 2.6, for $n = 2$, the peak position also depends on the coverage. Depending on the initial coverage, the desorption peak has different temperature positions.

Using this methododlogy, desorption energy of H from different W surface have been extensively experimentally studied in the past [32, 33, 34, 56, 57, 62] and is recorded here in table 2.1.

From these studies, depending on the surface orientation, 2 to 4 surface desorption energies are recorded corresponding to 2 to 4 different adsorption sites. In reference [32, 56], only one desorption energy is found but which is decreasing as the surface coverage increased. It may be due to the fact that at low coverage, only the most stable adsorption sites are filled and as they begin to be saturated, the other sites, with lower desorption energy begin to be filled as observed by Tamm et al. [57].

W surface	Desorption energy per H_2 (E_{des} (eV))	Surface coverage	Technic used to load and desorb W sample	reference
(100)	0.91 1.65	$\theta > 0.46$ $\theta < 0.46$	Molecular beam technic, T = 190 K - 480 K	[56]
(100)	1.14 1.4	$\theta = 1$	Gas loading at low temperature (78 K) TDS, $\beta = 25\ K \cdot s^{-1}$	[34, 57, 62]
(110)	1.14 1.4	$\theta = 1$	Gas loading at low temperature (78 K) TDS, $\beta = 25\ K \cdot s^{-1}$	[34, 57, 62]
(110)	0.87 1.52	$\theta > 0.6$ $\theta < 0.6$	Gas loading at low temperature (90 K) TDS, $\beta = 2.5\ K \cdot s^{-1}$	[32]
(111)	0.61 0.91 1.14 1.4	$\theta = 1$	Gas loading at low temperature (78 K) TDS, $\beta = 25\ K \cdot s^{-1}$	[62]

Table 2.1. Summary of experimentally determined desorption energy per H_2 molecules $E_{des} = 2 \cdot E_D$.

The migration on HIs on the (110) W surface has also been studied experimentally in the temperature range of 130 K – 160 K [63]. In this temperature range, it is found that the diffusion is thermally activated with a migration energy between 0.18 eV for low coverage ($\theta = 0.1$) and 0.22 eV for higher coverage ($\theta = 0.9$). Below this temperature range, diffusion involving tunneling effects is observed and the diffusion is so no more thermally activated. Since in tokamak, no such low temperature will be observed, these tunneling effects will be ignored in the following.

ii. Theoretical overview

To complete these experimental studies and understand the processes involved in the H adsorption/desorption on/from W surfaces several DFT studies have been done recently [64, 65, 66, 67, 68] and reviewed in [69]. These theoretical studies calculate the migration and desorption energies of H on and from different W surfaces and are summarized in table 2.2 which also shows the experimental value for comparison. In this table, half the desorption energies per H atom $\frac{E_{des}}{2} = E_D$ are shown. In the DFT calculations, the adsorption of H atoms on the (100) surface leads to a surface reconstruction [66]. On the first layer, a displacement of 0.28 Å is calculated in [66] and the distance between 2 W atoms is 2.82 Å and 3.57 Å in [65]. Two adsorption sites are highlight in the calculation: short bridge (SB) and long bridge (LB), and the amount of SB sites is the same as the amount of LB sites. The energy barrier for the diffusion of H depends on the nature of the path followed by the H atom (SB to SB or SB to LB …). In the

same way, the desorption energy of H from W surface depends on the type of site in which the H atom is adsorbed.

Concerning the H migration on W(110), table 2.2 shows a very low energy barrier for diffusion from SB to SB. The calculated value for this path is in disagreement with the experimentally determined value (that cannot differentiate the path). However, the DFT calculations for the LB to LB migration are in a good agreement with experimental observation but only for a coverage of 0.5. It is probable that for higher coverage, the diffusion path may be more complex that only LB to LB migration or SB to SB migration.

Concerning the H desorption from any W surfaces, the values calculated by DFT agree relatively well with the experimental ones. For the desorption from W(100), two activation energies are calculated, one from LB and one from SB sites. This result agrees well with the experimental observations and the difference between the experimental values and the DFT values are less than 10 %. The same maximum relative error can be found between DFT and experimental values for H desorption from W(110). For the W(100), it can be noted that the calculated DFT desorption energies of H from SB sites is higher than from LB [65, 66]: at low coverage the H are preferentially on the SB sites (more stable site) and at high coverage, when all the SB sites are occupied, H are on both LB and SB sites. Since there are as many SB sites as LB sites, the coverage where LB sites should theoretically begin to be occupied is 0.5 and so for coverage higher than 0.5, the experimentally observed desorption energies should decrease and it is indeed observed [56]. These desorption energies are for clean W surface. It is reported that in case of pre-adsorption of O impurities on W(110), the desorption energy of H decreases as the coverage of H decreases and the coverage of O increases [31] (opposite trend compared to clean W surface). This result suggests that the presence of O impurities on surface weaken the H binding but authors do not conclude on the formation of a new binding state. No ab initio simulation has been performed yet to address this issue.

Concerning the absorption of H from surface to bulk, no experimental data are available since it is impossible to determine experimentally only this activation energy. Thanks to DFT calculations, values for the activation energy can be calculated and are reported in table 2.2. For the absorption of H from very different surface orientations to the bulk, the calculated energies range from 1.7 eV to 2.2 eV meaning that the absorption of H inside bulk is highly endothermic. It can be noted that in case of W(100), according to reference [65], H is much easily absorbed inside the bulk from a LB site than from a SB site.

Process	**DFT calculated activation energies (eV)**	**Experimental activation energies (eV)**
H migration on W(100)	0.43 from SB→SB [66] 0.65 from SB→LB [66]	
H migration on W(110)	0.05 from SB→SB ($\theta = 1$) [64] 0.31 from LB→LB ($\theta = 1$) [64] 0.10 from SB→SB ($\theta = 0.5$) [64] 0.22 from LB→LB ($\theta = 0.5$) [64]	0.23 ($\theta = 0.9$) [63] 0.21 ($\theta = 0.6$) [63] 0.18 ($\theta = 0.1$) [63]
H desorption from W(100) $E_D = \frac{E_{des}}{2}$	0.91/H from SB [66] 0.47/H from LB [66] 0.92/H from SB [65] 0.49/H from LB [65]	0.83/H for $\theta < 0.46$ [56] 0.46/H for $\theta > 0.46$ [56] 0.70/H [62] 0.57/H [62]

H desorption from W(110) $E_D = \frac{E_{des}}{2}$	0.87/H ($\theta = 0.25$ mono layer) [67] 0.68/H ($\theta = 1$) [64]	0.57/H [62] 0.7/H [62] 0.44/H for $\theta > 0.6$ [32] 0.76/H for $\theta < 0.6$ [32]
H absorption from W(100) surface to bulk	2.03 for SB→bulk [66] 2.13 for SB→bulk [65] 1.68 for LB→bulk [65] 2.36 [67] 2.16 [68]	
H absorption from W(110) surface to bulk	2.26 [67] (surface →2nd subsurface) 1.95 [68]	
H absorption from W(112) surface to bulk	2.13 [68]	

Table 2.2. Summary of DFT calculated activation energies for different surface processes involving H and W.

2.3.2 Hydrogen in the bulk: solubility and diffusion

i. Solubility constant

If H loading in the bulk is done by adsorbing first H atoms on the surface (gas loading), the amount of the H absorbed inside the bulk at a given temperature can be described by the Sieverts' law [70]. This law explains that, at the thermodynamic equilibrium, the concentration C_H of H inside the metal bulk can be expressed as a function of the pressure of H_2 gas as followed (Eq. 2.7):

$$C_H = \sqrt{\frac{P_{H_2}}{P_0}} \cdot S(T) \ \ (H/W) \qquad (2.7)$$

In this equation, P_0 is a reference pressure (often taken to 1 atm) and $S(T)$ is the solubility of H in W. This solubility can be expressed as $S(T) = S_0 \cdot e^{-\left(\frac{E_S}{k_B \cdot T}\right)}$ in (H/W). As explained in the description of H/W interaction diagram (figure 2.5), the solution energy E_S and so the solubility $S(T)$ expresses the affinity between a metal and H. In case of H/W system, the solubility has been measured between 2400 K and 1200 K to be $S(T) = 9.3 \times 10^{-3} \cdot e^{-\frac{1.04\ (eV)}{k_B \cdot T}}$ $(H/W \cdot atm^{-\frac{1}{2}})$ by Frauenfelder [29]. The solution energy of H in tetrahedral and octahedral interstitial sites has been calculated by DFT by different authors [65, 71, 72, 73]. They all observe that the solution energy is lower for H in tetrahedral interstitial sites (TIS) meaning that the preferable position of H inside pure W lattice is in TIS. The solution energy that is calculated varies between 0.86 eV and 0.95 eV. These value are close to the one extracted from the experimental measurements indicating that at high temperature, the H is positioned in TIS. Taking the solubility law from Frauenfelder, the concentration of H in W sample under a pressure of 1 atm of H_2 is $C_H(1200\ K) = 3.9 \times 10^{-7}$ H/W and $C_H(2400\ K) = 6.0 \times 10^{-5}$ H/W. These concentrations are low since the entering of H inside bulk W from the surface is endothermic ($E_S > 0$). However, at low temperature it has been observed experimentally that the apparent concentration of H, D or

^{3}H inside massive W sample, W coating and W dust is much larger than the one expected with the Frauenfelder solubility law [28, 46, 74, 75]:

- In [74], measuring the H_2 pressure in a chamber separated by a thin W sample from the molecular source (permeation of H through a W membrane), the measured H solubility is 6×10^{-7} H/W $\cdot$ atm$^{-\frac{1}{2}}$ for temperature between 673 K and 873 K for H inserted inside W+5% Re.
- In [75], measuring also permeation of H through a W membrane, the measured H solubility is 2.6×10^{-3} H/W $\cdot$ atm$^{-\frac{1}{2}}$ for a temperature of 400 °C (673 K) for H inserted inside W coating.
- In [28, 46], W dusts have been loaded with tritium (^{3}H) gas at 470 °C (743 K) with a pressure of $^3H_2$ around 1 atm. The ^{3}H activity measured after dissolution of the dust is in the range of 10 GBq/g which roughly correspond to a concentration of ^{3}H in the dust of 10^{-3} ^{3}H/W.

These experimental observations exhibit a trapping effect occurring at low temperature: H is notonly in TIS and the presence of numerous traps, open reactive surfaces or impurities (oxide layer, Re in [74] …) impact the apparent solubility.

To summarize the experimental and theoretical data existing on the solubility, it appears that soluble site of H in W is TIS of the bcc W lattice. At high temperature, H is effectively in this site and the solution energy is around 1 eV. At low temperature, due to presence of traps that can retain H, the effective solubility is higher than the one calculated by DFT for H in TIS or the one measured by Frauenfleder at high temperature and extrapolated to lower temperatures.

ii. Diffusion coefficient

Once in the bulk, H atoms interact with W in the bulk and, as described figure 2.1 and figure 2.2, these interactions can be divided into two main processes: the diffusion and the trapping. Concerning the diffusion of H inside W bulk, a lot of experimental and theoretical data are available and reviewed in different paper from Causey [7] and Skinner et al. [76] and Tanabe [77] for experimental data and in [69] for first principle calculation (DFT). In any case, the diffusion coefficient is presented with an Arrhenius law as followed (Eq. 2.8):

$$D(T) = D_0 \cdot e^{-\frac{E_{Diff}}{k_B \cdot T}} \ m^2 \cdot s^{-1} \qquad (2.8)$$

There are different experimental ways to determine the diffusion coefficient:

- Measuring the outgassing rate of hydrogen from W sample (generally with large dimension) [29, 78].
- Measuring the H_2 pressure or the ^{3}H radioactivity in a chamber separated by a thin W sample from a source of hydrogen (plasma or gas) containing a known concentration of ^{3}H. The permeation of H/^{3}H through the W sample is driven by gas driven permeation (GDP) or plasma driven permeation (PDP) depending on the source of H [79, 80, 74, 81].
- Measuring the distribution of tritium tracer at mm scale using tritium imaging plate (resolution of 25 µm) after implantation of H/^{3}H mixture in W with plasma [82, 83].

The diffusion coefficient is experimentally determined using analytical solution of the diffusion equation derived from Fick's laws. Reproducing the experiment over a large temperature range, the value of D_0 and E_{Diff} can be extracted.

The data considered to be the most relevant are Frauenfelder's data [29] since they have been measured on a large temperature range (2400 K – 1200 K) at high temperature preventing any

trap effects on the measured diffusion coefficient. In addition, in this experiment, the sample used is heated several times to 2400 K, alternatively in hydrogen (600 Torrs) and in vacuum in order to remove any impurities inside and on the sample guaranteeing a clean W surface. The measured diffusion coefficient for hydrogen is: $D(T) = 4.1 \times 10^{-7} \cdot e^{-\frac{0.39\ (eV)}{k_B \cdot T}}\ m^2 \cdot s^{-1}$.

Concerning the DFT calculations, many papers agree on the interstitial position of H in W and the diffusion path followed by H inside W [65, 71, 72, 84]. These papers show DFT calculations but with different computational methods. It is found that the H is preferentially in the TIS of bcc W lattice and the minimum energy path to diffuse inside W perfect lattice is by passing from a tetrahedral interstitial site to the next neighbor tetrahedral interstitial site. For these three papers, the energy barrier for going from a site to another is 0.42 eV [65], 0.21 eV [71], 0.2 eV [72] and 0.2 eV [84]. The difference between the different calculated energy barriers is due to different computational methods. Taking into account the distance between two TIS which is around 1.12 Å and using the harmonic transition state theory, the pre-exponential factor D_0 can be calulcated using the Wert and Zener's formula [85], the pre-exponential factor D_0 has been calculated in [65, 71, 72]. This allows a comparison between the experimental and theoretical work that is reported in figure 2.6.

Looking at the experimental data, and especially the ones of Frauenfelder [29], Zakharov et al. [81], Benamati et al. [74] and Esteban et al. [78], different regimes for the macroscopic diffusion can be seen. For temperature higher than 1500 K, the diffusion coefficients determined experimentally are in good agreement with the three DFT values from Johnson et al. [65], Heinola et al. [71] and Fernandez et al. [72]. For temperature below ~1500 K and for the experimental data cited above, a new regime is observed with an effective diffusion coefficient lower than the one theoretically calculated. The apparent diffusion barrier increased significantly and is about 1 eV as measured by Zakharov et al. [81]. This effect has been described theoretically by Fernandez et al. [72] and explained by the presence of trap such as mono-vacancies: the macroscopic diffusion is not driven by jumping from interstitial to interstitial site but by motion of H from trapping site to trapping site. According to Fernandez et al. [72], this effect is also present in Frauenfelder's data for temperature below 1500 K.

This trapping effects seems to be by-passed (or at least diminished) for plasma driven permeation as suggested by the experimental results from Otsuka et al. [82, 83] and Ikeda et al. [79, 80]. In these experiments, H plasma with ^{3}H tracers is used to implant H/^{3}H in the W sample. Then, the diffusion coefficient is extracted by measuring the amount of ^{3}H that permeate through the W sample or by profiling the ^{3}H in the sample with the tritium imaging plate. The measured diffusion coefficient is close to the Frauenfelder's one even if the measurements are done at much lower temperature. In similar measurement performed by Ikeda et al. [79] but using gas driven permeation, the diffusion coefficient is decreased by 2 orders of magnitude indicating a potential trapping effect just beneath surface that is avoid by plasma driven permeation. The same conclusion is taken from Otsuka et al. measurements [83] that exhibit a large ^{3}H concentration in the first 500 µm of the sample implanted with H plasma. However, care has to be taken with these data since the sample preparation (annealing, surface cleaning …) is not as rigorous as for the experiment done at higher temperature as the one done by Frauenfelder.

To summarize the experimental and theoretical data existing on the diffusion of HI in W, it can be said that the effective diffusion coefficient is characterized by different regime: a high temperature regime (>1500 K) defined by migration from interstitial sites to interstitial sites (TIS) and a low temperature regime defined by migration from defects to defects. In our modelling work, we considered the diffusion as a process of migration from interstitial sites to

interstitials sites. In that respects, the diffusion coefficient chosen is the one calculated by DFT by Fernandez et al. [72]: $D(T) = 1.9 \times 10^{-7} \cdot e^{-\frac{0.2\ (eV)}{k_B \cdot T}}\ m^2 \cdot s^{-1}$.

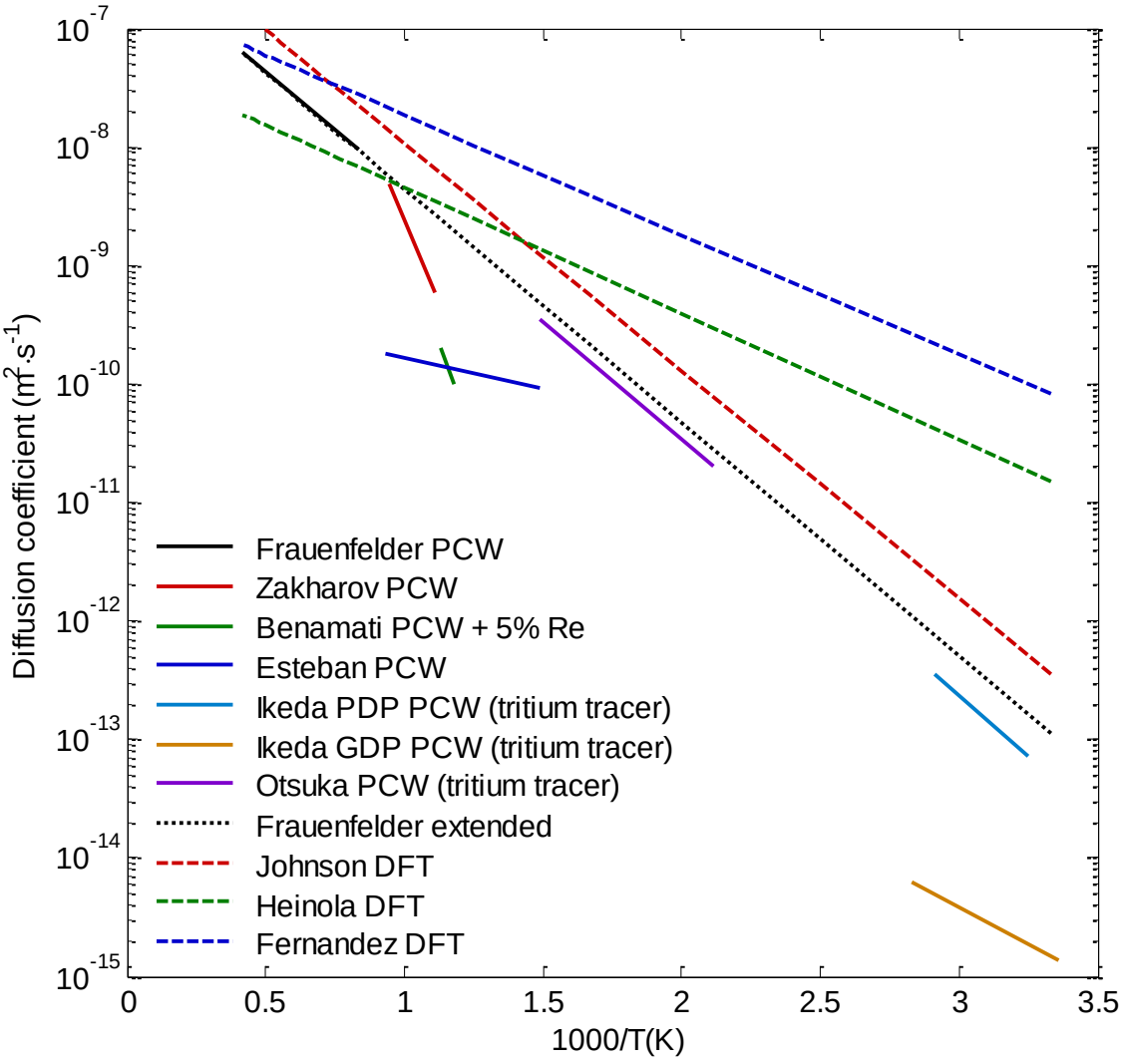

Figure 2.6. Temperature dependence of hydrogen diffusion coefficient in W. The solid lines correspond to experimentally determine diffusion coefficient from Frauenfelder **[29]**, Zakharov **[81]**, Benamati **[74]**, Esteban **[78]** Ikeda **[79, 80]** and Otsuka **[82, 83]**. The dotted line corresponds to the extension of Frauenfelder dependence assumed to be the most relevant experimental data. The dashed lines correspond to different theoretical DFT results from Johnson **[65]**, Heinola **[71]** and Fernandez **[72]**.

2.3.3 Trapping at defects: experimental overview

As explained in figure 2.1 and figure 2.2, HIs can be trapped inside W around different type of crystallographic defects such as vacancies, interstitials (impurities or self-interstitial), dislocation, grain boundaries and cavities (making hydrogen bubble). As explained in previous

section, these trapping sites can impact the different macroscopic properties of HIs inside the materials such as the diffusion coefficient and the solubility. As exemplified by figure 2.2, the trapping effect can be understood as the presence of sites where the energy of H in these sites is lower than the energy of H in interstitial sites (the difference is called binding energy): it is more stable for H to be in those sites than in interstitial positions.
The trapping characteristic i.e. the temperature of desorption and the amount of traps in the bulk of H in W can be experimentally determined for different types of W materials by first loading the materials with H (using ion/atomic beam or gas). TDS or IBA are then performed on the loaded sample in order to figure out the retention characteristics of a given sample. The desorption temperature can be obtained from the TDS measurements as well as the total quantity of D retained. The IBA depth profiles give also give an indication on the retention potential of a sample but they also give information on the depth distribution of the retained HIs i.e. near the surface, deep in the bulk…
In the following, the experimental results published in the literature are presented. They are separated into three different parts. The first part one presents the results obtained on single crystalline tungsten (SCW) samples that experienced only D ions irradiation after the sample preparation. The second part regroups the results obtained on polycrystalline tungsten (PCW) samples that only experienced only D irradiation after the sample preparation (annealing). The third and final part regroups the results of studies that look for the effect of the fusion ashes (He and neutron) on the D retention on PCW. Only the data that will be used in the model parametrization in chapter 4 are detailed in this section.

i. Results obtained on SCW

The team of Davis and Haasz at the University of Toronto Institute for Aerospace Studies published several papers about the D retention in SCW [26, 27, 42, 86, 87, 88, 45] and especially TDS measurement accompanied by NRA and SIMS measurements. In addition to these studies, NRA measurements of D in SCW can be found in papers by Alimov et al. [47, 89].

The data obtained by the team from Toronto have been recorded on W samples that experienced similar pre implantation treatment: several mechanical and electrochemical polishing steps separated by an annealing of at least 30 min in temperature ranging between 1500 K and 1800 K. The purposes of the polishing steps are to have a low roughness and remove the effect of previous implantations. The purposes of the annealing step are to remove the electrochemical polishing residues as well as remove dislocations, vacancies and impurities near the surface and in the bulk. According to Manhard et al. [30], annealing at 1700 K for 20 min allow removing the dislocations from the annealing samples (see section 2.2.1). Consequently, it can be said that there is initially no dislocation in these SCW samples after the annealing procedure.

Figure 2.7 presents two TDS spectra obtained by Toronto team (Poon et al. [26] and Quastel et al. [86]) showing the desorption of D from SCW implanted at room temperature (300 K).

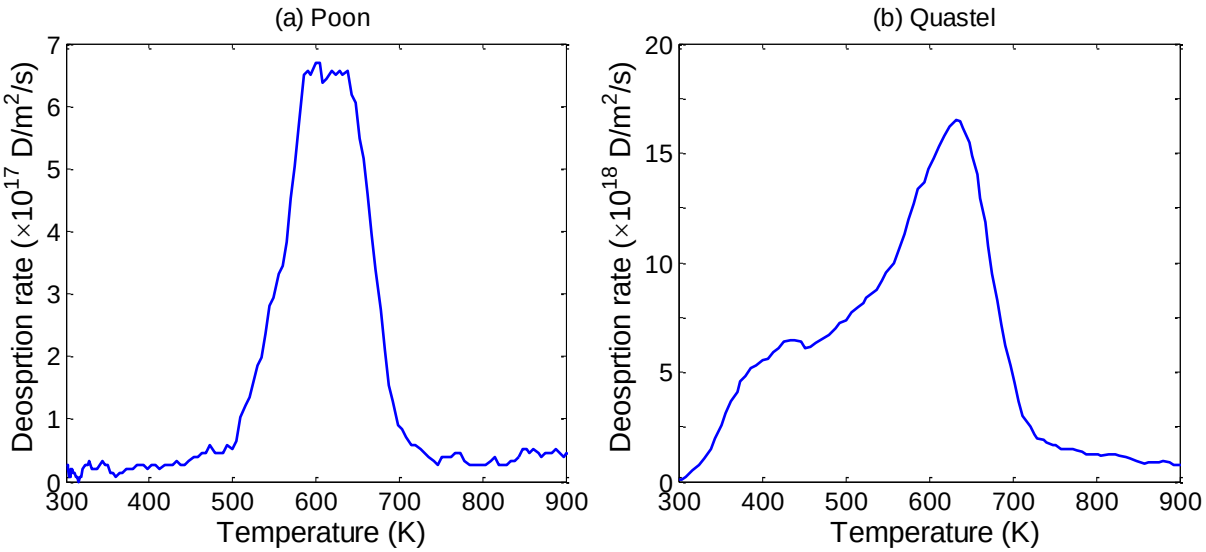

Figure 2.7. (a) TDS spectrum after irradiation of SCW at 300 K with D ions at 500 eV/D, flux = 10^{18} $Dm^{-2}s^{-1}$, fluence = 10^{21} D/m^2, heating rate = 4-6 K/s ,(by Poon et al. **[26]**).

(b) TDS spectrum after irradiation of SCW at 300 K with D ions at 500 eV/D, flux = 10^{20} $Dm^{-2}s^{-1}$, fluence = 10^{23} D/m^2, heating rate=5.1 K/s (by Quastel et al. **[86]**).

In case of data from Poon et al. [26] (figure 2.7 (a)), the incident flux is 10^{18} $D{\cdot}m^{-2}{\cdot}s^{-1}$, the energy of the ions is 500 eV/D and the fluence is 10^{21} $D{\cdot}m^{-2}$. The desorption spectrum exhibits a single peak at 600 K for a heating rate of 4 – 6 K/s. In case of data from Quastel et al. [86] (figure 2.7 (b)), the incident flux is 10^{20} $D{\cdot}m^{-2}{\cdot}s^{-1}$, the energy of the ions is still 500 eV/D and the fluence is 10^{23} $D{\cdot}m^{-2}$. As in the case of Poon et al., for a heating rate of 5.1 K/s a desorption peak around 600 K is observed but there is another peak around 400 K making the spectra wider. It has to be noted that in the experiment from Poon et al. [26], once the sample is loaded with D and placed in the TDS vacuum chamber, the vacuum chamber is baked at 400 K for about 1.5 hours. With similar procedure but baking at 360 K, Quastel et al. [86] shows that the peak at 400 K is suppressed and the desorption starts at 420 K instead of 300 K. Consequently, in Poon et al experiment, a peak at 400 K may have been removed by the baking at 400 K for 1.5 hours. The TDS spectra of D desorbing from SCW sample implanted by D ions at room temperature, published by the Toronto's team, show similar features: a predominant peak around 600 K and additional peak around 400 K or 500 K.

After implantation of SCW by 500 eV/D ions at 300 K, a reduction of the D inventory (measured by TDS) has been observed by Quastel et al. [86] after waiting 100 of hours at 300 K before the TDS starts. After waiting 1000 h, almost half of the initially retained D is outgassed. This outgassing at room temperature is followed by a large diminishing of the peak at 400 K. This observation of outgassing at 300 K after implantation at 300 K suggests the presence of weak binding states of H with W. These outgassing effects on long waiting storage time can have an effect on the analysis and modeling of such experimental results.

As discussed in section 2.2.3, the TDS spectra can be used to calculate the amount of D retained during the implantation and the evolution of D retention as a function of fluence. For SCW implanted around 300 K, it is shown that the D retention increases with fluence at low fluence and then seems to saturate for fluence above ~10^{23} $D{\cdot}m^{-2}$ [27, 45]. The retention is then

around 5-6×10^{20} D·m^{-2}. It has to be noted that the Toronto's team, with the same irradiation and TDS devices, reports also a saturation of the D retention in PCW at 300 K [87] which is not the case in other devices as it is discussed later on in section 2.3.3.ii.

The amount of D retained calculated by TDS can also be used to look at the evolution of D retention as a function of the incident flux at fixed fluence. Poon et al. [26] reported an increase of the D retention with the incident flux in SCW for irradiation at 300 K with 500 eV/D (figure. 2.8). For the lowest fluence the D retention is varying by 2 orders of magnitude as the flux does. This observation could be explained by a trap creation process that is efficient, at 300 K, for flux higher than 5×10^{17} D·m^{-2}·s^{-1} and less efficient for flux lower than this value. The incident flux 5×10^{17} D·m^{-2}·s^{-1} can be understood as the flux threshold for the trap creation process. The nature of the created traps could be first understood as displacement damaged induced by elastic collision between the incident ions and the W atoms. However, the threshold energy to create displacement damaged in W is 2050 eV/H [90] and 940 eV/D [91] which is above the energy of ions used here: the created traps cannot be considered here as displacement damages induced by D ions.

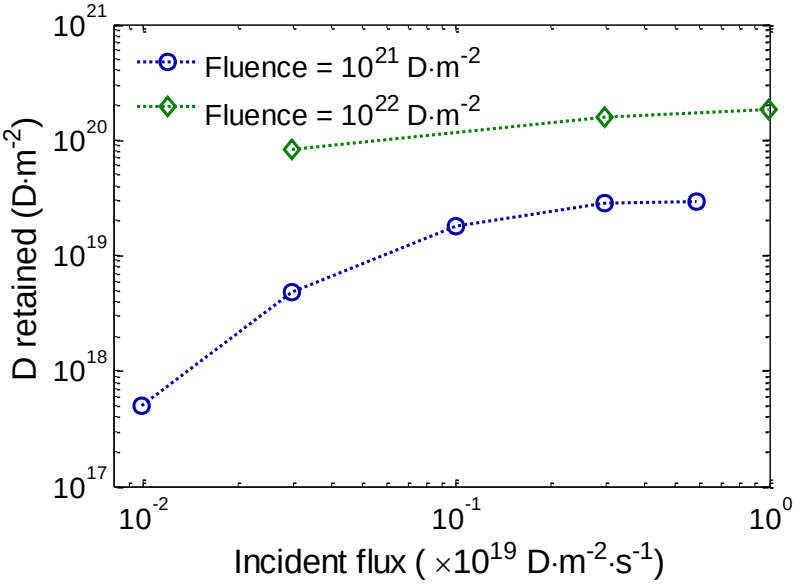

Figure 2.8. Evolution of D retention in SCW as function of incident flux **[26]**. The SCW is implanted with 500 eV/D at fluence of 10^{21} D/m^2 and 10^{22} D/m^2. During the implantation, a LN_2 cold trap is used to reduce the amount of impurities in the chamber for the blue data point (fluence = 10^{21} D/m^2). This LN2 cold trap is not used for the other set of data (fluence = 10^{22} D/m^2).

In addition to TDS spectra which give the evolution of retention with flux and fluence, near surface depth profiles of D and those of other impurities such as O and C and tungsten oxide (WO_2 and WO_3) are recorded by SIMS [27, 42, 43, 86] after and possibly before the D implantation at room temperature of SCW by 500 eV/D ions at various fluences. The SIMS measurements performed after the D implantation, that show the repartition of these species up to 60 nm deep, exhibit two distinct zones:

– A peak concentration of the D, O, C and tungsten oxide concentrations in the 20 first nm (the same shape for these species is observed).

– A constant D, O, C and tungsten oxide concentration in the zone deeper than the 10-20 nm.

To explain the presence of the peak near the surface, the authors concluded that O and C atoms have been inserted in the sample during the implantation due to their presence in the molecules of the background gases. This O and C impurities create defects that can trap D explaining the presence of the first zone with high D concentration. Instead of defects, the D can also be trapped forming tungsten oxide forming bronze (H_xWO_3, $x \leq 1$) [92, 93, 94]. The structure of this bronze is an oxide hydroxide $WO_{3-x}(OH)_x$ [93]. Thus, such structure can trap a lot of D (concentration reach 1-10 at.%) in pure WO_3 [92]. However, results from Bringans et al. [94] does not observed such bronze structure after H^+ implantation or H exposure on WO_3. Instead, they conclude to a loss of the oxygen from the surface. From these results, and since some WO_3 are present in the near surface zone after the D implantation it can be said that some bronzes are formed subsequently to the O insertion during the D implantation but it is not the main trapping site for D. In addition, comparing the O and C level before and after the D implantation, it is observed that the O and the C concentration increased in the deepest zone (deeper than 20 nm) by more than one order of magnitude in some cases [27, 42]. Poon et al. [27] proposed that the increase of the O and C impurities concentration after the implantation is induced by an irradiation-enhanced diffusion of the implanted O/C impurities deeper than the stopping range. The diffusion depth reached by these O/C impurities is not observed by the SIMS depth profile because this technics can only probe only up to ~100 nm.

In order to reduce the effect of these impurities on the D retention, a cold finger cooled with liquid nitrogen (LN_2) is used to reduce the partial pressure of background gases (H_2O, O_2, CO_2, CO …) during the implantation [26, 42, 86]. A significant reduction (factor 2) of the D retention in SCW at 300 K is observed indicating that the retention in the near-surface region is highly driven by the implanted impurities. Consequently, the SIMS results suggest that O/C impurities play a significant role in D trapping: O/C can behave as a site for D trapping. This assumption is strengthen by the studies of different SCW samples with different O and C native impurity content of 500 appm (atomic part per million $\Leftrightarrow 10^{-6}$ at.fr.) and 5000 appm [27]. It is shown that the sample in which the concentration of C and O is the highest retained far more D.

The analysis of D depth profile can be extended to 7 µm using NRA [45, 89]. The NRA D depth profile is recorded by Alimov et al. [89] after implanting a SCW sample at 300 K with 200 eV/D ions and an incident flux of $\sim 5\times10^{17}$ $D\cdot m^{-2}\cdot s^{-1}$ at different fluences. The results are presented in figure 2.9 that is taken from [89]. The SCW used in this case is manufactured by the same supplier as the one used by Toronto's team: the impurity content is the same. The samples were annealed at 1573 K for 3.5 h after mechanical and electrochemical polishing which is a similar pre-implantation treatment. The temperature of annealing is lower than the one used by Poon et al. [26] but the annealing time is higher.

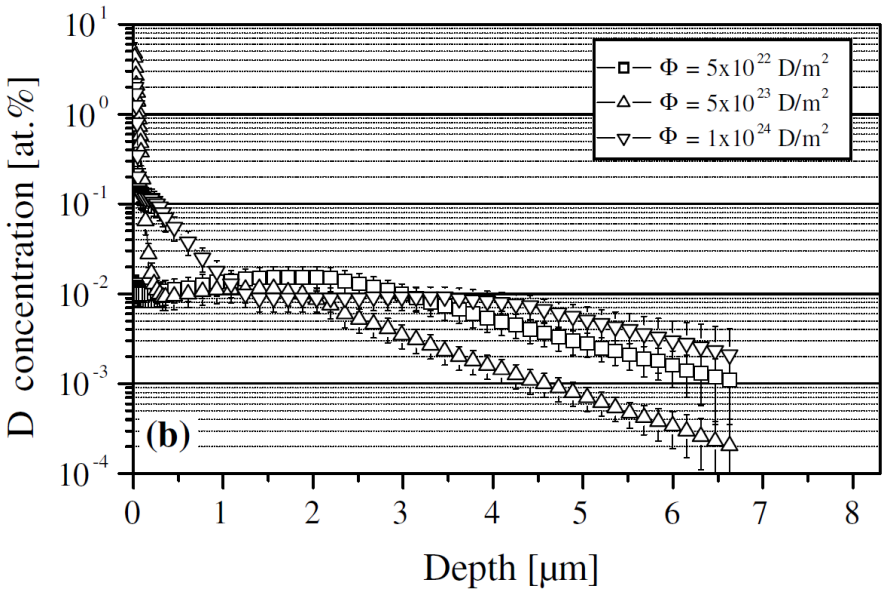

Figure 2.9. NRA depth profile of D in SCW irradiated with 200 eV/D ions with a flux of 1.8×10^{18} $D\cdot m^{-2}\cdot s^{-1}$ at 300 K. Figure taken from Alimov et al. **[89]**.

From this D depth distribution, the authors distinguished three different zones:

- The near surface layer (up to 200 nm) where high D concentrations are observed (up to 10 at.%),
- The sub-surface layer (from 200 nm to 2 µm) where D concentration is around 0.1 – 0.01 at.%,
- Bulk zone deeper than 2 µm where the D concentration is 0.01 – 0.001 at.% (the detection limit is 0.001 at.%).

The same three zone are observed by Roszell et al. [45] (Toronto's team) who use NRA to record the D concentration in SCW (same pre-treatment as Poon et al. and Quastel et al.) irradiated with 500 eV/D ions with an incident flux of $1\text{-}8\times10^{18}$ $D\cdot m^{-2}\cdot s^{-1}$ at a fluence of 10^{24} $D\cdot m^{-2}$. It is to not that Roszell et al. [45] reports a concentration of 1 at.% in the sub-surface layer up to 1 µm.
SIMS and NRA measurements suggest that there is a zone, near the surface where the D concentration is significantly higher (1-2 orders of magnitude) compared to D concentration deeper in the bulk. As suggested by SIMS measurements, this increase could be due to the insertion of O/C impurities during the implantation creating trapping site. Consequently, the trap creation exhibited by Poon et al. measurements at 300 K [26] (figure 2.8) may be due to the creation of trap in the first zone as described by Alimov et al. [89] (figure 2.9). In addition, the second zone corresponding to the sub-surface layer seems to growth as the fluence increases which is not the case of the third zone. It may then be concluded that the sub-surface layer is also a zone in which trap creation processes take place and the third zone seems to be only related to the intrinsic defects present in the metal.

The TDS spectra and NRA/SIMS observations reported up to now in this section have been recorded after implantation at 300 K. From the TDS spectra (figure 2.7), the desorption temperature of D from the traps present in the materials (created or intrinsic) is between 400 K and 600 K. Consequently, it could be thought that the SCW sample retains D for implantation temperature up to 600 K and for implantation temperature above 600 K, the D retention drops

because the detrapping of D is too high. However, experimental observations reported by Roszell et al. [88] and Poon et al. [27] exhibit a more complex evolution.
It is reported by Poon et al. [27] (figure 2.10 (a)) for implantation of 500 eV/D ions with a flux of 5-6×10^{19} D·m^{-2}·s^{-1} and a fluence of 10^{24} D·m^{-2} that the D retention decreases gradually staying above ≈2×10^{20} D·m^{-2} from 300 K to 500 K. For irradiation temperature of 600 K, the D retention drops of about one order of magnitude and for 700 K it drops again of one order of magnitude. This behavior is the same as the one that can be imagined from the TDS spectra (see paragraph above). However, a different evolution is reported by Roszell et al. [88] (figure 2.10 (a)) for implantation of 500 eV/D ion with a flux of 3×10^{18} D·m^{-2}·s^{-1} and fluence of 3×10^{23} D·m^{-2}. The D retention is the highest for implantation at 300 K (and in the same order of magnitude as for D retention reported by Poon et al. [27]) but it drops of about 2 orders of magnitude for temperature higher than 400 K and then remains almost constant for any higher implantation temperatures. The main differences between these two experiments are the incident flux since the samples are both SCW samples from the same manufacturer and the pre-implantation treatments are very similar (including several mechanical and electrochemical polishing steps as well as annealing at temperature above 1500 K for more than 30 min). As explain above from figure 2.8 and figure 2.9, trap creation processes limit the D retention in the near surface and sub-surface layers. At 300 K, the threshold flux for trap creation processes is around 5×10^{17} D·m^{-2}·s^{-1} [26] (figure 2.8). These observations of D retention at higher implantation temperatures suggest that the threshold flux for trap creation processes increases as implantation temperature increases. At 300 K, the flux of both experiment from Poon et al. and Roszell et al. are high enough to trigger the trap creation processes. For implantation temperature of 400 K - 500 K, the flux of experiment from Roszell et al. (3×10^{18} D·m^{-2}·s^{-1}) is below the threshold and the flux of experiment from Poon et al. (5-6×10^{19} D·m^{-2}·s^{-1}) is above: the threshold flux for trap creation in the range 400 K - 500 K is between this two value.

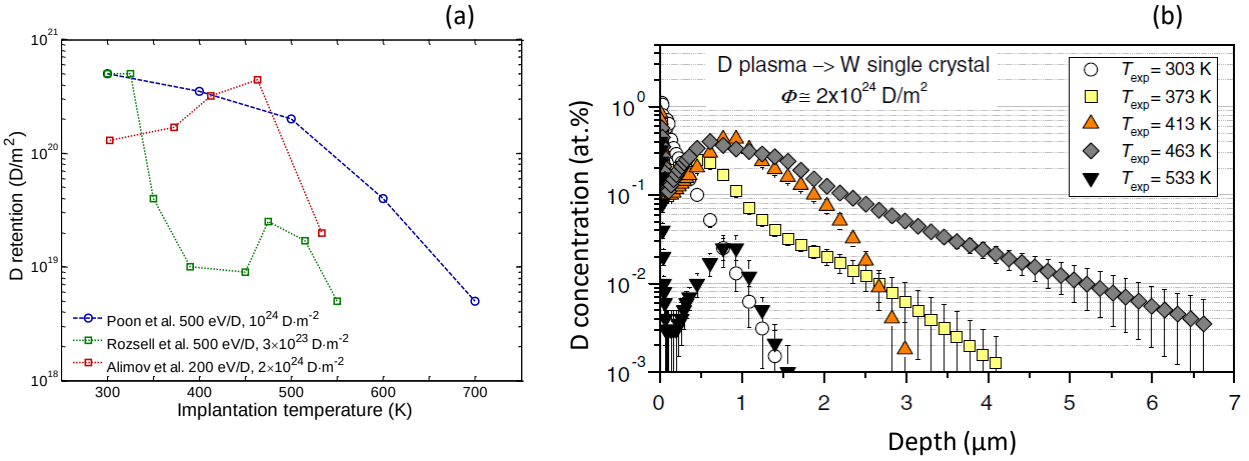

Figure 2.10. (a) Evolution of D retention with implantation temperature for SCW reported by Poon et al. **[27]**, Rozsell et al. **[88]** and Alimov et al. **[47]**.

(b) D depth profiles obtained by NRA after the implantation of 200 eV/D ions at 300 K with a flux of 10^{21} D·m^{-2}·s^{-1} and a fluence of 2×10^{24} D·m^{-2}·s^{-1} in SCW (figure taken from **[47]**).

Alimov et al. [47] also looked at the evolution of the D retention derived from NRA D depth profiles in SCW as a function of temperature. In the Alimov's experiment, the SCW sample is irradiated by a 200 eV/D plasma with a much higher flux of 10^{21} $D \cdot m^{-2} \cdot s^{-1}$ and with a fluence of 2×10^{24} $D \cdot m^{-2}$ (figure 2.10 (a)). In this experiment, the temperature range is between 303 K and 533 K. According to what is said above in this section, the flux used in this experiment is higher than the threshold value at least for implantation temperature between 300 K and 500 K: The D retention should not decrease drastically in this range of temperature. Indeed, the D retention does not decrease but in the opposite increases between the implantation at 303 K and the implantation at 463 K. This means that the number of traps created at 463 K is higher than at 303 K. If one looks at the D depth profile obtained by Alimov et al. [47] for these different temperatures (figure 2.10 (b)), one can clearly see that the increase of the retention is due to the extension of the sub surface layer from around 1 µm at 303 K to around 3 – 4 µm at 463 K. Thus, it seems that the zone were traps are created extended deeper at higher temperature making the trap creation processes increase from 300 K to 500 K.
From these experimental data it seems that the temperature and the flux have a coupled effect on the trap creation processes. It could be interesting to reproduce the experiment done by Poon et al. [26] at 300 K (i.e. the study of the evolution of D retention as a function of the incident flux) (figure 2.8) but at different implantation temperatures in order to determine the threshold values of the incident flux as function of the implantation temperature.

Summary:

- It is observed by TDS technics in SCW that the D trapped is release around 400 K and 600 K.
- Thanks to NRA D depth profile, the distribution of all the traps can be separated in three zones: the near surface layer, the sub surface layer and the bulk.
- From SIMS depth profiles of D and other impurities such as C, O and tungsten oxide, it can be said that the traps in the first two zones is limited by the trap creation processes.
- There is a flux threshold for triggering the trap creation processes that is around 5×10^{17} $D \cdot m^{-2} \cdot s^{-1}$ at room temperature.
- From the analysis of the evolution of retention with implantation temperature for two different fluxes separated by one order of magnitude, it can be suggested that the threshold flux that triggered the trap creation processes increases with increasing implantation temperatures.
- In the other hand, if the flux is higher than this threshold value, it seems that the efficiency of the trap creation processes is greater at 500 K compared to 300 K.

ii. Results obtained on PCW

In the literature, much more experimental data on the D retention in PCW samples can be found compared to data about SCW samples. Here, a non-exhaustive review of these results is made and only the data simulated in the next chapters are presented.
First, the implantation around 300 K is looked at and especially the TDS spectra obtained by Bisson et al. [24] and Ogorodnikova et al. [25] (figure 2.11).

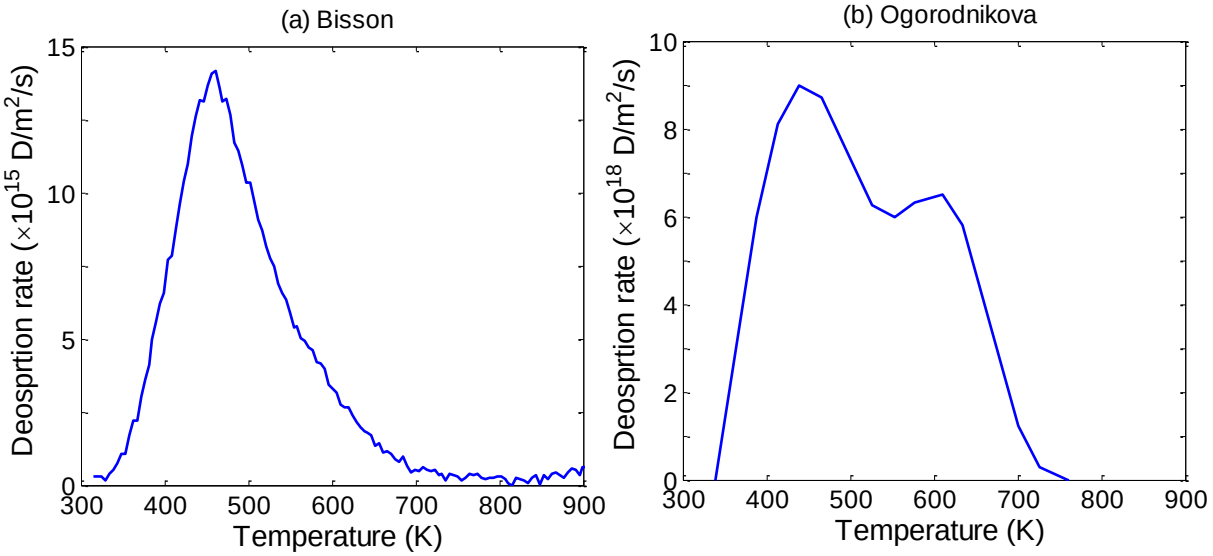

Figure 2.11. (a)TDS spectra obtained after irradiation of PCW at 319 K with D ions at 250 eV/D, flux = 2×10^{16} D/m^2/s, fluence = 2.9×10^{19} D/m^2, heating rate = 1 K/s (by Bisson et al. **[24]**).

(b) TDS spectrum obtained after irradiation of PCW at 300 K with D ions at 200 eV/D, flux = 2.5×10^{19} D/m^2/s, fluence = 10^{23} D/m^2, heating rate = 8 K/s (by Ogorodnikova et al. **[25]**).

In the experiment from Bisson et al. [24], the samples are delivered recrystallized (grain size around 30 µm) with a mirror finish obtained by mechanical polishing. An additional electrochemical polishing is done after delivery. Before the implantation, the sample is subject to at least two outgassing procedure (temperature increase up to 1300 K with a ramp of 1 Ks^{-1} followed by a plateau at 1300 K for 10 min). The TDS is performed with a heating rate of 1 Ks^{-1} after the implantation of a PCW samples by 250 eV/D ions with a flux of 2×10^{16} D·m^{-2}·s^{-1} and a fluence of 2.9×10^{19} D·m^{-2}. The obtained spectrum (figure 2.11 (a)) exhibits a single broad asymmetric desorption band centered around 450 K and with a tail at high temperature extending up to 700 K.

In the experiment from Ogorodnikova et al. [25], the samples experienced different pre-implantation treatments (outgassing at 1273 K for 10 min, eventual electrochemical polishing and heating at three different temperatures (1173 K, 1273 K and 1573 K)). During the heating at 1173 K, the samples are bombarded by 600 eV D_3^+ ions in order to remove the W oxide layer (see section 2.2.1). The TDS is performed with a heating rate of 8 Ks^{-1} after the implantation of PCW sample by 200 eV/D ions with a flux around 2.5×10^{19} D·m^{-2}·s^{-1} and a fluence of 10^{23} D·m^{-2}. The obtained spectrum (figure 2.11 (b)) exhibits two peaks positioned around 440 K for the highest intensity peak and at 600-650 K for the lowest intensity peak. The pre-treatment used in this case was the heating at 1573 K for 3 h. It is shown in Ogorodnikova's paper that the pre-implatation annealing has a strong impact on the TDS spectrum: the highest the annealing temperature is, the lowest the intensity of the TDS peak is. Manhard et al. [30] reported similar evolution of the D retention on PCW samples that experienced different pre-implantation treatment: the D retention in the PCW samples recrystallized at 2000 K (between 20 – 60 min) is almost two times lower than the D retention in the PCW not recrystallized or recrystallized at 1700 K. It means that the

annealing steps reduce the amount of intrinsic defects such as impurities, vacancies and dislocations (see section 2.2.1).
It is interesting to note that the positions of the TDS peaks are the same as the one observed by Quastel et al. [86] (figure 2.7 (b)) in the case of SCW samples but the relative intensity is reversed: the low temperature peak in case of PCW samples seems to be dominant according to Ogorodnikova's TDS spectrum. This would means that the traps present in PCW samples are similar to the one present in SCW samples but also that additional traps in PCW samples change the peak proportions.

The differences between these two experiments presented on figure 2.11 come mainly from the differences in the fluxes and fluences. The flux is higher by 3 orders of magnitude and the fluence is higher by 4 orders of magnitude in case of Ogorodnikova's experiments. In the case of the most gentle implantation by Bisson et al. [24], only one peak around 450 K is observed. In the case of the implantation with the highest flux and fluence by Ogorodnikova et al. [25], the peak around 450 K is still observed but an additional peak appear at 600 K. Considering that the trap creation processes observed on SCW samples (figure 2.8) is also present in PCW samples with the same threshold flux (5×10^{17} D·m^{-2}·s^{-1} at 300 K), it could be said that the peak present only in Ogorodnikova's TDS spectrum (at 600 K) corresponds to the created traps. Indeed, the ion flux in Ogorodnikova's experiment is higher than the threshold.
It has to be pointed out that many other TDS experiments performed by different groups have been done on PCW samples implanted at 300 K in various conditions. Here is a non-exhaustive list of papers showing the TDS spectrum [49, 88, 30, 95, 96, 97]. For all these papers the desorption temperatures range from 400 K to 700 K as the two spectra shown in figure 2.11.

After the implantation of D in PCW at 319 K, Bisson et al. [24], a reduction of the D inventory (measured by TDS) has been observed if one waits several tens of hours at 300 K before thermal desorption starts. More than 50 % of the initial retention is lost after waiting 135 h and the desorption can be characterized by an outgassing characteristic time of ~ 19 h. As explained in the SCW case, this shows the presence of weak binding state of D with W. Consequently, the necessary waiting /storage time has to be taking into account on the simulation of such experiments in order to obtain relevant modelling.

From the TDS spectra, Bisson et al. [24] and Ogorodnikova et al. [25] extracted the amount of D that have been retained during the implantation and they looked at the evolution of the D retention in their PCW samples as a function of the fluence. The fluence range used in the paper by Bisson is from ~6×10^{17} D·m^{-2} to ~10^{21} D·m^{-2} and the fluence range used in the paper by Ogorodnikova is from ~10^{21} D·m^{-2} to ~10^{24} D·m^{-2}. The data from Bisson et al. and Ogorodnikova et al. are complementary and by plotting both data on the same graph, a trend of the D retention as a function of fluence can be established over a wide range of fluence covering 7 orders of magnitude (figure 2. 12). For fluence higher than 10^{19} D·m^{-2}, the ratio D retention over D fluence decreases below the 10 %. By extrapolating both the data from Bisson et al. and the data from Ogorodnikova et al., it can be seen that the D retention at 300 K evolves as a power law of the fluence over a large fluence range: Retention$\propto$(fluence)$^{0.65}$. This power law, close to a square root law, exhibits a D retention processes that seems limited by the migration of D in the bulk. The small difference with the square root law could also suggest that the trap creation processes discussed above play an important role in the D retention in PCW.

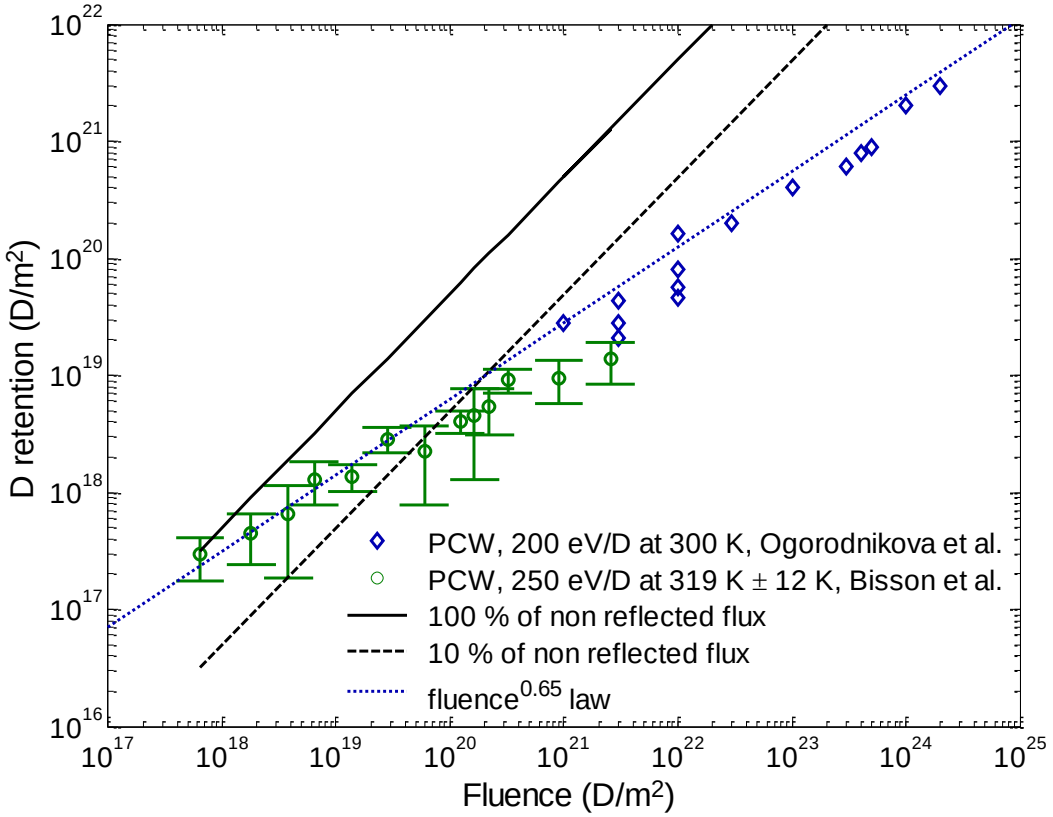

Figure 2.12. Evolution of retention calculated from TDS spectrum with fluence for D implanted into PCW. The data marked as'◊' are from Ogorodnikova et al. **[25]**. For these data, PCW are irradiated with D ions at 200 eV/D, flux = 2.5×10^{19} D/m^2/s. The data marked as '○' are from Bisson et al. **[24]**. For these data, PCW are irradiated with D ions at 250 eV/D, flux = 2×10^{16} D/m^2/s. The lines '100 % of non-reflected flux' and '10 % of non-reflected flux' has been calculated from the fluence using a reflection coefficient of 0.5 (typical reflection coefficient calculated by TRIM for irradiation with 200 eV/D or 250 eV/D).

The distribution of D, and so the distribution of the traps retaining D, has been extracted from NRA measurement performed by Alimov et al. [89] after implantation of 200 eV/D ions in the PCW with a flux of ~10^{18} D·m^{-2}·s^{-1} at different fluences. The results are presented in the figure 2.13 that is taken from [89]. As in the case of the D distribution in SCW samples shown on the figure 2.9, three different zones are defined by Alimov et al. [89] which are the same as already discussed: the near surface layer (up to 200 nm) where the D concentration reach 10 at.%, the sub-surface layer (from ~0.5 µm to ~2µm) in which the D concentration is around 0.1 at.% and the bulk part (deeper than 2 µm) where the concentration is around 0.001 at.% which is close to the detection limit of the NRA technic.

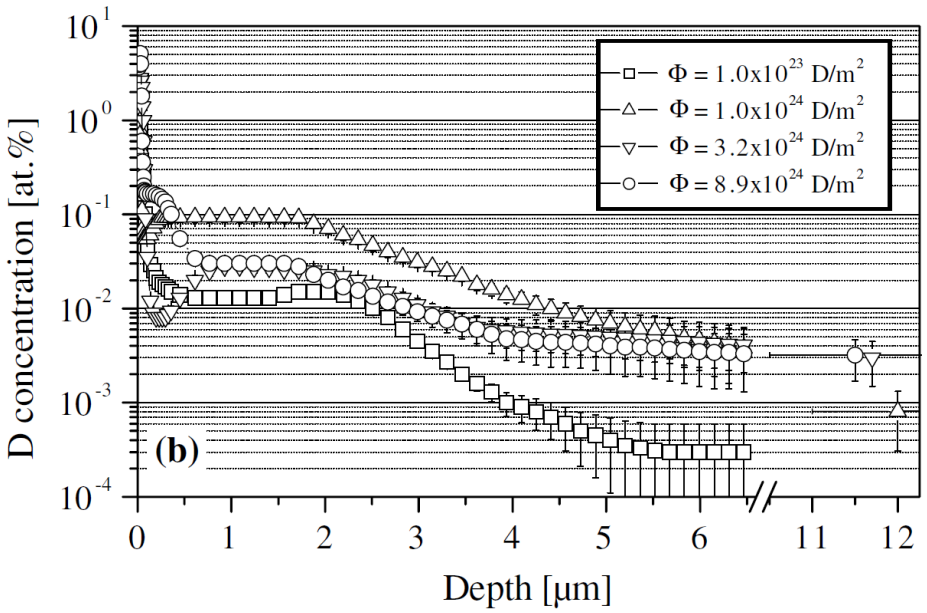

Figure 2.13. NRA depth profiles of D in PCW irradiated with 200 eV/D ions with a flux of 3.6×10^{19} $D\cdot m^{-2}\cdot s^{-1}$ at 323 K. Figure taken from **[89]**.

As explained in the case of the D depth profiles in SCW samples, the first two zones could be related to trapping of D in traps created during the D implantations and the third zones could be related to D trapping in intrinsic traps. And as for the SCW, the creation processes seems to be triggered by the flux and seems to increase with the fluence as suggested by Ogorodnikova et al. [25]. It has to be noted that after irradiation of PCW at 300 K at fluences higher than 10^{24} $D\cdot m^{-2}$, Alimov et al. [89] observed blisters on the surface of their samples. Similar blisters are observed by Manhard et al. [30] after irradiating non-recrystallized sample at 300 K at a fluence of 6×10^{24} $D\cdot m^{-2}$. Lindig et al. [98] as well as Alimov et al. [99] observed also this kind of blisters after the irradiation at 320 K and 360 K of PCW samples with 38 eV/D plasma at a flux of $\sim10^{22}$ $D\cdot m^{-2}\cdot s^{-1}$ and at a fluence of 10^{27} $D\cdot m^{-2}$. The observation of blisters strengthens the assumption of trap creation processes and the evolution of the amount of created traps as a function of the fluence: as the number of traps increases with the fluence, a threshold concentration of traps is reached inducing stresses that can create intra-granular cracks creating the blisters observed on the surface [98, 99].

So far, the experimental results shown here have been recorded after D implantation in PCW samples around 300 K. The study of the effect of the implantation temperature on the D retention in PCW has been also studied by Roszell et al. [88], Tian et al. [96] and Haasz et al. [100]. The evolution of the D retention versus the implantation temperature for each of these authors is reported in figure 2.14. According to these data, the D retention seems to be maximal in the range of 300 K – 550 K and drops at high temperature above 700 K.

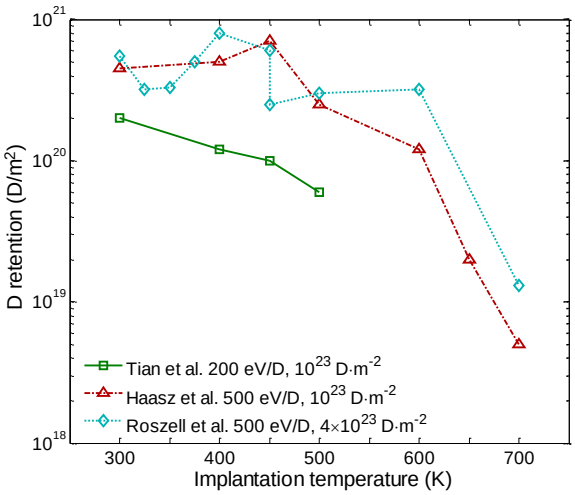

Figure 2.14. Evolution of D retention with implantation temperature for PCW reported by Roszell et al. **[88]**, Tian et al. **[96]** and Haasz et al. **[100]**.

In the experiment from Tian et al. and the experiment from Haasz et al., the flux is greater than 10^{19} D·m^{-2}·s^{-1} and in the experiment from Roszell et al., the flux is 3×10^{18} D·m^{-2}·s^{-1}. Unlike the experimental results from the SCW presented in figure 2.10 (a), the temperature, at which the D retention drops, seems not to be affected by the flux and remains around 500 K - 600 K. This could be due to the nature of the sample treated (PCW versus SCW). A possible explanation could be that the grain boundaries present in the PCW samples and not in the SCW samples retained D at high temperature. Even if no or a few amount of traps are created at low flux in the PCW samples (Roszell et al. experiment), the retention in GB masks this effect by retaining D at high temperature.

In the data from Haasz et al. [100], it can be observed that the maximum in the D retention is for an implantation at 500 K and the retention is around 1.5 times the retention obtained at 300 K. Similar increase of the D retention at 500 K compare to D retention at 300 K has also been reported by Alimov et al. [47, 99, 101], Lindig et al. [98] after implantation of different grade of PCW samples by D plasma at high flux (10^{22} D·m^{-2}·s^{-1}) and high fluence (10^{27} D·m^{-2}) compared to those already presented. This increase of retention at 500 K is correlated to an increase of the number of blisters and their size are more dispersed indicating both inter and intra granular cracks. Alimov et al. [99] and Lindig et al. [98] attribute the creation of these blisters to the stresses induced by the H oversaturation. These results suggest, as in the case of SCW samples already discussed, that the amount of traps created is increasing at 500 K.

Summary:

- It has been observed two different desorption temperatures on the TDS measurements around 400 K and around 650 K.
- From NRA depth profile, the same three zones as in the SCW case are observed i.e. the near surface zone up to 200 nm, the subsurface zone (up to 2 µm) and the bulk part. The two first zones seems to be related to creation processes and the bulk part to trapping of D in intrinsic defects present in the bulk and which can be reduced by annealing the samples.

- Analyzing the fluence dependence of the D retention over a 7 orders of magnitude large fluence range, it can be observed that the D retention at 300 K in PCW is limited mainly by the migration of D in the bulk.
- Looking at the evolution of the D retention with the implantation temperature, it can be said that the retention is maximum for temperature between 300 K and 500 K. above 500 K – 600 K, the retention drops by one or two orders of magnitude.
- In certain implantation circumstances, i.e. high flux (around or above 10^{21} $D \cdot m^{-2} \cdot s^{-1}$) and high fluence (above 10^{24} $D \cdot m^{-2}$) blisters are formed on the surface due to the presence of inter and intra granular cracks that may be due stresses induced by D oversaturation. The number of blisters is recorded to be higher for implantation at 500 K and their size distribution is broader at this temperature.
- In this high flux/fluence experiment, an increase of the D retention is also observed that may indicate that, as in the SCW case, the trap creation processes are more efficient at 500 K than at 300 K.

iii. Effect of the fusion ashes

As explain by (Eq 1.1), the ashes of the Tritium/Deuterium fusion reaction are a Helium nucleus of 3.5 MeV and a neutron of 14.1 MeV. For the model parametrization, only the damaged created by the neutron will be treated in this document. To briefly describe the effect of the He irradiation, bubbles are observed in W sample irradiated by He [51] and possibly fuzz (nano-tendril structure) on the W surface for specific condition of temperature (between 1000 °C and 2000 °C) and at high fluence. Concerning the D retention, it can be said that the simultaneous implantation of He and D reduces the D retention [102, 103, 104] but no additional trapping peak of D desorption are observed on the TDS spectra compared to pure D implantations.

The neutron is not affected by the magnetic confinement since it is not electrically charged. So, they will hit the wall with their full energy (14.1 MeV) creating displacement damaged inside the materials, transmutation and so possibly Helium creation via nuclear decay. Here, we focus on the effect of the damaged produced inside the materials. Testing the effect of 14.1 MeV neutrons on W is not an easy task for two main reasons. First, few 14.1 MeV neutron sources exists that are able to reach sufficient fluence to be consistent with fusion requirement. Then, the use of such sources requires specific equipment (hot cells …) since neutrons activate the irradiated materials by transmuting the elements inside. In order to test the impact of neutron damaging on the D retention properties, different proxy have been found. For example, neutrons with lower energy are easier to create and can be used to generate damage in W [97, 105] but hot cells are still required. Another and easier way to study the interaction of D with radiative damaged is to use heavy ions with high energy (typically tens of MeV) to damage the W samples [41, 52, 95, 106, 107, 108, 109, 110]. According to Ogorodnikova et al. [111], high energy heavy ions provide good proxy to simulate the damages created during neutron irradiation. However, it has to be noted that the irradiation such ions can created tracks very specific to this kind of irradiation if the electronic stopping power is much higher than the nuclear stopping power [112]. No tracks have been highlighted so far and if one looks at the value of the electronic/nuclear stopping power given by TRIM, it can be seen that both value are close to each other for 20 MeV W^{6+}. But it does not mean that such tracks are not present and the possible difference between heavy ions and neutron irradiation have to be kept in mind.

The zone damaged by the heavy ion can be calculated by the SRIM® software. The damaged zone is extended from the surface:

- up to 1 µm deep in case of 2.4 MeV Cu^{2+} [107],
- up to 0.8 µm in case of 5.5 MeV W^{2+} [110],
- up to 1.5 µm in case of 12.3 MeV W^{4+} [95],
- up to 2.4 µm in case 20 MeV W^{6+} [41, 52, 108].

The defects created by heavy ion irradiations are quantified by the dpa calculated with SRIM® that shows an inhomogeneous dpa distribution that seems to agree with the STEM observation of damage distributions for irradiation below 0.89 dpa [113]. However, from the NRA measurements after D atom exposure, it can be seen that the D concentration is quite homogeneous in the damaged layer for irradiation leading to 0.5 dpa [41, 52]. The D concentration in the damaged layer reach around 1 - 2 at.% for D implantation at 300 K [20, 59] which is one order of magnitude higher than the concentration in this range (1-2 µm) for undamaged W (figure 2.13). In addition, it is shown that the retention in self-damaged tungsten is saturating for about 0.2-0.3 dpa [95, 110]: on the damaged profile, if the damage level is higher than 0.2 dpa, no more traps will created and the trap concentrations will stay constant. Consequently, the distribution of the traps created by heavy ion irradiations is quasi uniformly distributed in the damaged zone.

After D atom exposure on self-damaged PCW samples at 500 K, Zaloznik et al. [52] observed that the D desorption appears around 700 K and 1000 K (figure 2.15). Similar desorption temperature are observed in case of ions or plasma implantations [95, 106, 107, 108, 109, 110].

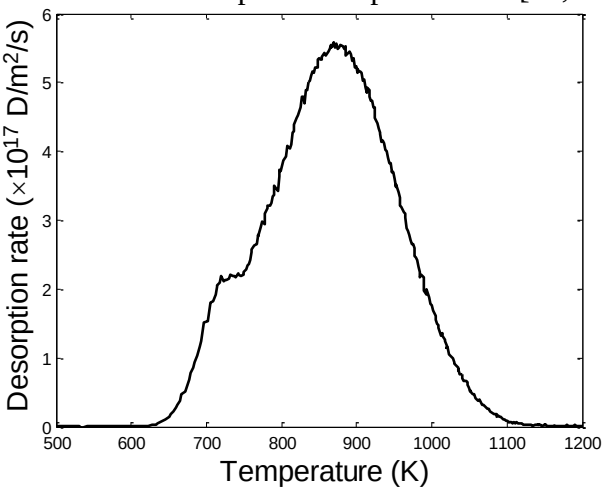

Figure 2.15. Experimental TDS spectra obtained with a heating rate of 15 K/min after the exposure on a self-damaged W sample. The damaging is obtained using 20 MeV W^{6+} ions and the samples are damaged at 0.5 dpa. These data are from Zaloznik et al. paper **[52]**.

These desorption temperatures are higher than for the undamaged W sample where peaks between 400 K - 600 K are observed. Consequently, W materials placed in a fusion tokamak damaged by neutrons will retain more D than the undamaged W during a typical plasma discharge during which the temperature can reach 1000 K.

The trap created by heavy ions or neutrons are related to trapping into irradiation defects created by collision cascades. As noted before, some of these defects such as dislocations, loops and cavities, can be observed in the damage layer using FIB followed by STEM [52, 107, 113]. By

annealing at different temperature the irradiated W sample, the evolution of these defects can be followed. According to Watanabe et al. [107] for annealing during 25 min. at 873 K, no significant changes can be observed except that the shape of the dislocation lines begins to change. They are gradually annihilated above 973 K. Similar observations are reported by Zaloznik et al. [52] which shows that the dislocation line density begins to decrease for annealing temperature around 800 K. Dislocation loops are also observed in STEM images [52, 107]. Watanabe et al. [107] reported that the loops are remarkably annihilate above 1173 K. Zaloznik et al. [52] reported a bit different observation on the annealing of the dislocation loops. Two annealing stages seem to appear with a first decrease of loop density for annealing temperature of 600 K. Then, the loops density stays constant and starts to decrease again for annealing temperature of 1000 K. In addition to dislocation lines and loops, Watanabe et al. reported the presence of nano-voids. These nano-voids grow for annealing temperature above 1073 K due to the migration of defects but their density is greatly decreased above 1273 K.

Summary:

- Heavy ion or neutron damaging changes drastically the fuel retention property of W by mainly creating traps that can retain D at higher temperature than the undamaged W.
- The created defects can be vacancies, dislocation lines and loops and nano-voids and in order to remove these defects, W has to be annealed higher than 1273 K.

2.3.4 Trapping at defects: theoretical overview

To analyze experimental data, investigate mechanisms involved in fuel retention or predict retention in different exposure conditions, theoretical studies can bring useful information. The detail of the information carried by theoretical analyzes depend on the technics used:

- DFT and MD simulate materials properties at atomic scale: they can be used to determine the binding states of H with different types of small defects such as mono-vacancies, interstitials or dislocations. DFT can also simulate trapping into grain boundaries but limited to symmetrical arrangement. In the opposite, MD which is able to simulate bigger structure can have a more general representation of the grain boundaries.
- OKMC simulate materials properties at crystal scale (from 100 nm to 1 µm). Such simulation can take as input DFT energy barrier and simulate kinetic motion of H atom into W matrix including diffusion and trapping. OKMC can simulate complete experiment such as TDS or realistic implantation. In any case, the jumping of H from a site to another is described by the thermally activated process (Eq. 2.2).
- MRE simulate materials properties at the sample scale (can reach cm scale) by not considering H atoms but continuous concentration of H atom or traps. The evolutions of each concentration are described kinetically using the rate as define by Eq. 2.2. The diffusion is described by the Fick's law. Since this manuscript will develop in more detailed this method of simulation, the equations will be described in detail in the next chapters.

The advantage of this last method is that it is quick to run and it can simulate big space and time scale (easily compared with experimental data). However, the nature of defects (vacancy, dislocation …) is replaced by their detrapping energies. If different defects have the same or similar detrapping energies, MRE cannot (or hardly) distinguish their natures.

i. Atomistic scale calculations

As already said in section 2.1, the results obtained by DFT and MD can be affected by the different hypothesis made (interaction potential, size of simulated crystals, method for the exchange-correlation …). In order to have a more global picture of the results, it is important to crosscheck simulation results obtained by different technics. From different DFT calculations, it is shown that a single trap such as a mono-vacancy can trap several HIs and the detrapping energy is dependent of the filling level of the traps. Figure 2.16 reports the detrapping energies from these DFT results for various types of defects. The binding energy $E_{B,i}$ as defined on figure 2.2 are calculated by DFT. In order to get the detrapping energies, we add the energy barrier for diffusion that is also calculated by DFT as being 0.2 eV [72, 84]. Figure 2.16 reports the results from:

- Kong et al. [114], the binding energies of H with light impurities of Carbon (-□-) and Oxygen (-□-) as well as the binding energies for H in a mono-vacancy (VH in -□-), in a mono-vacancy with an oxygen impurity inside (VOH in -□-) and in a mono-vacancy with a carbon impurity inside (VCH in -□-),
- Fernandez et al. [72], the binding energies of H in a mono-vacancy (-◊-),
- Heinola et al. [115], the binding energies of H in a mono-vacancy (-Δ-),
- You et al. [116], the binding energies of H in a mono-vacancy (-○-),
- Xiao et al. [117], the binding energies of H in a Σ3(111) tilt GB (-*-) as well as H in a stacking default to simulated dislocation loop (-+-),
- Zhou et al. [118], the binding energies of H in a Σ5(310)/[001] tilt GB with a vacancy in the grain boundary (-◊-)
- Terentyev et al. [119], the binding energy of H in a perfect dislocation (-☆-) and in a jogged dislocation at a jog (-×-)
- Becquart et al. [69], the binding energies of H with self-interstitial atom (W atom) (◊) and with different other metallic impurities such as Ni (○), Fe (□) and Cu (◊). Other impurities are reported from these calculations in [69] but for sake of clarity only few are shown here: the binding energyies for these not shown impurities are relatively low (<0.5 eV) compared to vacancy or other type of defects.

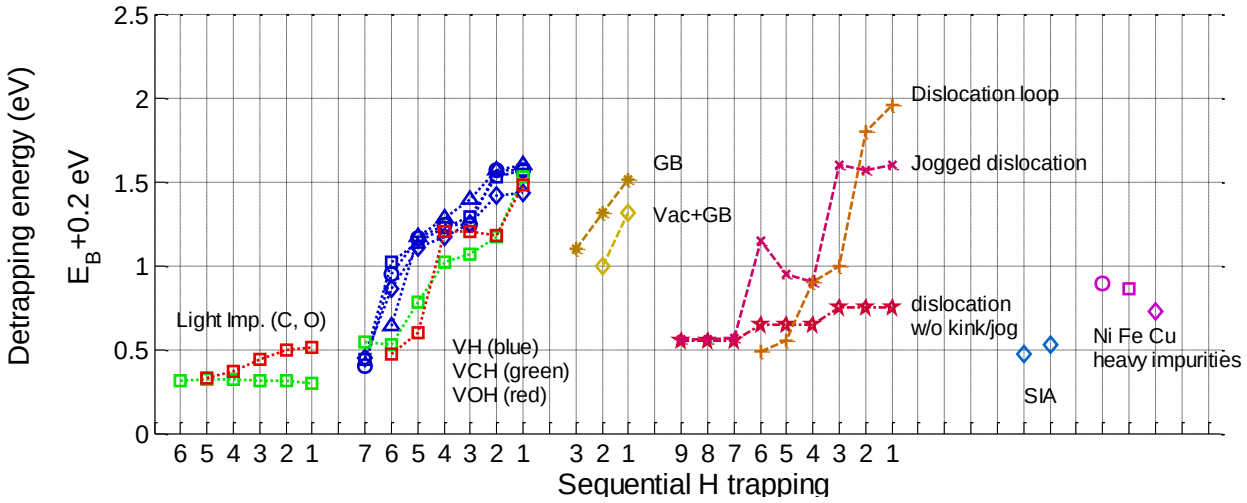

Figure 2.16. Non exhaustive overview of detrapping energies calculated by DFT for various types of defects: light C and O impurities, vacancy, Grain Boundary, different type of dislocation, self-interstitial atom and substitutional metallic atom. The sequential H trapping stands for the number of H that is trapped in defect.

A lot of DFT results are obtained for H trapped in mono-vacancy since it is a simple defect to create. The main observation that can be made from this plot is that many defects in W have very similar detrapping energies for H that range around 0.5 - 1.5 eV (except for the light impurities or self-interstitial atom that trap HI at much lower energy inducing a TDS peak at much lower temperature).

DFT can also be used to calculate the formation or migration energy of defects such as vacancies. For mono-vacancy in pure W, DFT results show that the formation energy is between 3.1 eV and 3.4 eV and the migration energy is around 1.7 eV [65, 72, 114, 115] (if the vacancy is empty of H atoms). With such high formation energy, the concentration of thermal vacancy is very low especially at 300 K ($<10^{-50}$ at.fr.) and they only can move for temperature higher than 500 K.

Kong et al. [114] calculated the formation energy of mono-vacancy filled with HI at different filling level (VH_n complex) as well as the formation energy of VOH_n and VCH_n complex. The formation energy of VH_n is lower than the one for empty mono-vacancy meaning that the presence of H ease the formation of mono-vacancy in W. However, it remains above 2 eV meaning that only few VH_n can be formed around 300 K ($<10^{-34}$ at.fr.).

In another hand, formation energy of VCH_n and especially VOH_n are considerably lower than formation energy of empty vacancy. In case of VOH_n, the formation energy is around 0.45 eV. Vacancies can be created by the simultaneous presence of H and O. This mechanism could explain the SIMS observation reported in section 2.3.3.i from the Toronto team [27, 42, 43, 86] which shows a similar repartition of D, O and C in SCW after implantation of D ions.

The amount of mono-vacancies in the presence of HIs can be calculated by thermo-statistical model [72, 120, 121]. Such models calculate, using the DFT results, the thermodynamic equilibrium between HIs in interstitial positions and HIs trapped in vacancies. Using a thermos-statistical model, Fernandez et al. [72] calculated that for an implanted HI fraction x_H of 10^{-5} at.fr. in interstitial positions, the amount of vacancies formed at the thermodynamic equilibrium is $\frac{x_H}{6}$. This implies that the presence of H eases the formation of

vacancies in W which are formed in order to reach the thermodynamic equilibrium. It is also reported by Ohsawa et al. [120] and Sun et al. [121] that there is a threshold of x_H for formation of superabundant vacancies which is around 10^{-10} at. fr. at 300 K [120, 121].

The hydrogen enhanced formation of vacancies has also been predicted by classical MD simulation reported by Liu et al. [122]. Using the Li et al. potential for W-H [123], they reported the formation of vacancies induced by hydrogen through mechanisms that associated hexagonal self-interstitial clusters and linear crowdion (an additional atom inserted within a row of atom).

The formation of superabundant vacancies induced by hydrogen insertion inside metal could explain the experimental observations of the NRA D depth profiles, the blistering and the cavity formations (by agglomeration of the vacancies) and the evolution of D retention with the D incident flux reported in section 2.3.3.

MD simulations by Piaggi et al. [124] show that the trapping and migration of H in GB is characterized by a broaden distribution of detrapping energies. These MD simulations have been undertaken using Li et al. potential for W-H [123]. They calculate an energy distribution centered on a detrapping energy of 2.6 eV. This value is close to the binding energy of H with vacancy calculated by MD simulations of Piaggi et al. [124]. The authors conclude that general GBs can trap H in the same range of temperature as vacancies. For specific GB and using the same potential from Li et al. [123], Yu et al. [125] calculated similar binding energy of H with GB of 2.5 eV and a diffusion barrier inside the GB of 1.65 eV. These two MD results suggest that GBs play an important role in H trapping. However, von Toussaint et al. [126], using Juslin et al. potential [60] calculated that the migration of H through Grain boundaries range between 0 and 4 eV. It has to be considered that the calculated migration of H in W (without GB) is 1 eV using this potential. Consequently, von Toussaint et al. [126] conclude that the GB can potentially provide preferential diffusion path for H in W which is in disagreement with previously reported MD results that say that GBs are trapping sites for H.

Finally, these different MD results suggest that GB, depending on their types, can either trap H or make it diffuse faster than in W crystal. It has to be point out that the effect of GB will only affect the fuel retention if grain size is lower than the migration depth of HIs that is changing with fluence.

Summary:

- The DFT calculations show that different types of defects (mono-vacancies, dislocations, grain boundaries …) can retain multiple HI. The detrapping energies of HIs are dependent on the filling level of the defects.
- The detrapping energies of HIs from many different types of defects is mainly distributed between 0.5 eV and 1.5 eV.
- Some DFT calculations shows that the formation energy of a vacancy containing an oxygen atom and multiple HIs is very low (0.45 eV) compared to the formation energy of an ampty mono-vacancy (<3 eV).
- Thermo-statistical model and MD calculations shows the possible formation of mono-vacancies if a high concentration of HI is inserted in perfect W.
- MD simulations show that grain boundaries can retain HIs with a wide distribution of detrapping energies. They can also provide some preferential diffusion path. It depends on the nature of the GBs (the orientation of the grain forming the GB).

As a remark:

The detrapping energies extracted from MD simulations using the H-W potential of Juslin et al. [60] or Li et al. [123] are very high compare to the ones extracted from DFT calculations.

ii. Kinetic Model: KMC and MRE

DFT and MD are very useful to understand how the HIs are trapped at particular defects (mono-vacancy, impurities, dislocations, grain boundaries …). However, they have access only to small scale due to the processes they look at. Consequently, these methods can hardly be compared directly with experiment. Larger scale modelling methods are so required such as Kinetic Monte Carlo (KMC) or macroscopic rate equation (MRE) methods.
KMC methods use the rate defined by Eq. 2.2 to calculate the probability that an object (for example an HI) has to go from a stable site to another stable site. Since the KMC methods calculate all the jumps including the quick jumps from a tetrahedral interstitial site (TIS) to another TIS, they are limited to small simulation box. However, long time scale can be simulated because the jump characteristic time is low compared to the characteristic time of the processes involved in the DFT or MD simulation.
Oda et al. [127] reported the effect of vacancies on the H macroscopic diffusion coefficient (called before the effective diffusion in section 2.3.2.ii). Using the DFT detrapping energy calculated by Oshawa et al. [128] that shows that the mono-vacancy can be filled with up to 12 H, Oda et al. [127] reported that the effective diffusion coefficient can be impacted by the presence of vacancies that can trap H. This trapping reduces the effective diffusion coefficient as already explain in section 2.3.2 below 1300 K. These results explain the measurements of diffusion coefficient made for a large range of temperature and reported figure 2.6 which show a decrease the activation barrier for diffusion for temperature below 1500 K. Oda et al. [127] explain this observation by the fact that for these temperature, H migrates from trap to trap (mono-vacancies in these KMC simulations).
Von Toussaint et al. [129] used KMC to simulate isotopic exchange of D by H implantation [130]. In order to reproduce qualitatively the experimental results, filling-level dependent detrapping energies have to be introduced in the model. Here, D stays in traps with detrapping energy of 1.4 eV. If another HIs (H or D) is trapped in an already-filled-with-one-HI trap, the detrapping energy decreases to 0.4 eV. The drop of the detrapping energies eases the desorption of any HI atoms trapped (H or a D) explaining the isotopic exchange observed experimentally at low temperature [130].

Another method of simulation that can be compared to experimental results is macroscopic rate equation (MRE). This technic, unlike KMC, treat the different processes considering continuous concentration of HI and traps. This method has been extensively used and developed in my PhD project and the equations will be presented in the next chapters. For the most works that compared MRE simulation to experimental data, the detrapping energies and the concentration of traps are used as a fitting parameter in order to reproduce the experimental data. In that aspect, TDS experiment is especially accurate to determine the detrapping energies and NRA depth profiles to determine the space distribution of traps. The optimum case is to get both TDS and NRA measurements on the same experiment. Table 2.3 reports the detrapping energies obtained by MRE simulations to reproduce experimental measurements (NRA or TDS) for different types of materials from well annealed SCW to hardly damaged PCW.

Experiment reproduced	Detrapping energies (eV)	Reference
TDS on PCW (implantation at 300 K) TDS/NRA on PCW (implantation at 300 – 700 K)	1.45 0.85	Ogorodnikova et al. [25] [131]
TDS on SCW (implantation at 300 K)	1.33-1.37 1.03-1.10	Poon et al. [43]
TDS on SCW (implantation at 500 K)	2.1 eV	Poon et al. [43]
TDS/NRA on PCW (implantation at 330 K)	1.2 0.9	Schmid et al. [132]
TDS/NRA on PCW [133] (implantation at 300 K)	1.35 1.25 1.17 1.07 0.97 0.85	Guterl et al. [134]
TDS on PCW (implantation at 473 K)	1.3 1.1	Shimada et al. [97]
SIMS depth profile on PCW implantation with 5, 15 and 30 KeV/D that created point defects (vacancies) [135]	1.56-1.54-1.37-1.26-1.16-0.61 (DFT data from [115] for H in W mono-vacancy)	Ahlgren et al. [136]
NRA depth profile PCW and SCW [47]	1.45 0.85	Hu et al. [137]
NRA and isotopic exchange in PCW [130]	1.41 – 0.79 (two filling levels) 1.41-0.95 (two filling levels)	Schmid et al. [138]
TDS/NRA on <u>self-damaged</u> PCW	2.4 2.2 1.85-1.9 1.45 0.9	Ogorodnikova et al. [20, 103]
TDS on <u>self-damaged</u> PCW	1.7-2.0	Gasparyan et al. [109]
TDS on <u>self-damaged</u> PCW	2.05 1.85 1.4 1.2	‘t Hoen et al. [106]
TDS on <u>neutron damaged</u> PCW	2.0 1.75 1.5 1.3 1.1 0.9	Shimada et al. [97]

Table 2.3. Detrapping energies calculated using MRE model to reproduced TDS, NRA or SIMS experiments. If no reference is set in the column "Experiment reproduced", it means that the reference contains also the experimental data.

As explain before, MRE is used to determine detrapping energies from TDS measurements. However, it does not give any indication on the nature of the defects involved. A way to overpass this difficutly is to run the simulation with the DFT detrapping energies as Ahlgren et al. did for their model [136] using the DFT data from Heinola et al. [115] as inputs. The main issue is that the detrapping energies for any kind of defects are very close to each other which leads to broad experimental TDS spectra especially for PCW samples. So, MRE simulations used to determine detrapping energies will give the "mean" detrapping energies of all the defects that trap HIs. Looking at these "mean" detrapping energies recorded in table 2.3, 3 values can be determined in case of undamaged W which are around 1.45 eV, 1.1 eV and 0.9 eV. If we compare these values to DFT values, it can be said that the 1.45 eV traps correspond to detrapping from vacancies type defect filled with 1 or 2 HIs (VH, VCH or VOH) or grain boundaries (if the migration depth is deeper than the typical grain size i.e. for high fluence). The detrapping energies 0.9 eV and the 1.1 eV could correspond to detrapping from vacancy with higher filling level (3-6), heavy impurities, grain boundaries or dislocation lines without kink/jog. According to DFT, the jogged dislocations and the dislocation loops have higher detrapping energies that range between 1.6 eV to 1.9 eV. No such detrapping energies are reported by MRE simulations for undamaged tungsten but they do in case of self-damaged damaged W: dislocation loops and jogged dislocations seem to trap D in the self-damaged W. Other traps with a detrapping energy around 2.1 eV can be determined in case of implantation of D at 500 K in SCW [43] or in any heavy ions or neutron damaged W. According to Ogorodnikova et al. [20], this detrapping energy is related to D trapped into void. To reach this conclusion, the adsorption model exposed by Gorodetsky et al. [139] has been used. This model considered that the detrapping energy of D with W in voids is the energy needed for an adsorbed D on W surface to go from the surface to the bulk.

Concerning the trap concentration associated to any of this detrapping energies, they are determined by adjusting the intensity of the simulated TDS spectrum with experimental TDS spectra or/and by reproducing the D depth profiles. As already discussed in section 2.3.3, three zones can be distinguished on D depth profiles recorded by NRA with the near surface zone and the subsurface zone possibly related to trap creation processes and the bulk zone related to intrinsic trapping. In order to reproduce these 3 zones, 2 solutions can be used:

- Set an ad-hoc profile in the near surface zone and sub-surface zone [43, 132] in order to mimic the enriched trap zone related to trap creation processes. The concentration of traps in the bulk is constant to simulate the intrinsic traps.
- Use fluence (time)-dependent trap concentrations in the near surface and sub-surface zone in order to simulate D induced trap [25, 137]. The concentration of traps in the bulk is also constant to simulate the intrinsic traps.

Schmid et al. [138] used a multi trapping model in order to simulate the isotopic exchange observed in W at low temperature [130]. This model is mandatory in order to reproduce the experimental data as already discussed for von Toussaint et al. KMC simulations [129]. In the MRE simulations, Schmid et al. [138] used 2 traps with 2 filling levels for each trap. The first has the detrapping energy of 1.41 eV (for 1 HI) and 0.79 eV (for 2 HIs) that is close to vacancy detrapping energies. This trap exists only in the near surface layer (up to 100 nm). The second

trap has similar detrapping energies: 1.41 eV (for 1 HIs) and 0.95 eV (for 2 HIs). These detrapping energies are still in the range of vacancy detrapping energies but also in the range of grain boundaries [117] and vacancy in grain boundaries [118] detrapping energies calculated by DFT.

Summary:

- Using the results from atomistic scale calculations, KMC simulations show that the presence of traps such as vacancy in the metal decrease drastically the effective diffusion coefficient as observed experimentally (section 2.2.3).
- Other KMC simulations show that the multi-trapping potential of defects in W allows understanding experimental observations on isotopic exchange.
- Considering MRE simulations, they are mainly used to determine the detrapping energies of HIs inside W by reproducing TDS, NRA or SIMS experiments.
- The nature of the defects that traps the HIs is not accessible from MRE simulations and MRE can provide only mean detrapping energies in case of complex system that includes numerous different trap types.
- The detrapping energies determined from simulations of experimental measurements are in the range of 0.5 – 1.5 eV for the SCW and PCW samples that only experienced D implantation (no damaging by heavy ions or neutrons).
- In case of PCW damaged by heavy ions or neutrons, higher detrapping energies are used to reproduce TDS peak at high temperature.

In this manuscript, we will deal with MRE simulations and we will try to add some understanding to the current knowledge presented in section 2. We will first try to simulate D retention in simple and well known SCW samples in order to reduce the different types of defects encountered. Thus, we might be able to make a bridge between ab-initio modeling and MRE simulations. Then, we will try to simulate the D retention in PCW in order to approach the real system that will be present in a tokamak. This methodology is the one used in the WHISCI project (W/H Interaction Studies: a Complete and Integrated approach) which is split into two main parts: experimental and theoretical studies. The experimental studies intend to provided experimental measurements (TDS, NRA, PAS …) from the simples SCW very well annealed to the complex PCW that will be install in the future fusions reactor. The theoretical studies intend to simulate the experimental results in a multi-scale approach from the DFT calculations to the MRE simulations passing by thermos-statistical models and OKMC simulations. During my PhD project, I was part of the project providing a part of the MRE calculations.
Finally, using these simulations to parametrize the W PFC in the tokamak, we will try to simulate and estimate the fuel retention under plasma exposures relevant to fusion devices.

3. Model presentation

This section presents the main features of the rate equation models used during this project. Each model can be divided in two parts:

- The bulk part that describes the interaction of H within W,
- The boundary conditions that describes the behavior of H on the W surface.

In this chapter, the bulk part is firstly described in section 3.1. Then, the different boundary conditions that can be use are described in section 3.2 as well as the situations in which these conditions are used. Finally, a simple analytical model is shown in section 3.3 that provides understanding on the behaviors of such models. In this manuscript, only mono-isotopic case is treated.

3.1. Bulk part

Based on the schematic description of H/W interactions (figure 2.5), two types of particles are considered in the bulk part:

- The mobile particles with a concentration c_m (in m^{-3}) that are subject to diffusion,
- The trapped particles with a concentration $c_{t,i}$ (in m^{-3}) that are trapped inside sites of type i.

The bulk part describes the time evolutions of these concentrations. To describe these time evolutions, two models have been developped.

The first model is the standard rate equation model that couple diffusion and trapping of HIs in metals that was first used in McNabb and Foster paper [140]. This model is widely used in the fusion community as well as in all the references in table 2.3 except for the model from Schmid et al. [138]. As discuss in section 2.2.5, this standard model provides good information on the mean retention parameters i.e. detrapping energies and trap concentrations: both of them are free parameters adjusted to reproduce experimental data. However, it is then difficult to attribute a detrapping energy to a particular defect. In order to face the difficulty, a second model has been developed.

This second model use DFT outcomes showing that a trap such as a mono-vacancy can trap several hydrogen atoms with detrapping energies depending on the filling level of the trap. The philosophy of this model is a multi-scale modeling approach: the detrapping energies obtained by DFT calculations are used as input parameters of the model that will be then compare with experimental data.

The choice of the used model depends on the type of information that we intend to look at. To have a general overview of the trapping parameters in order to provide a representative wall model for more complex application, the first model should be used: it gives the mean detrapping energies of a typical tokamak wall. To investigate more complex processes of trapping, the second model is used. In this last case, the experiment that are simulated are mainly experiment dealing with D trapping in well annealed SCW sample in order to reduce the complexity of the material structure (i.e. less grain boundaries, less dislocations …).

In our studies, the only space dimension considered is the direction orthogonal to the surface toward the bulk of the materials. If the flux of particles impinging the surface is homogeneous (or with low inhomogeneity), no gradient will appear in the directions parallel to the surface and no migration will occur toward these directions. So, the fuel retention is limited by migration toward the direction orthogonal to the surface. The space coordinate in this direction is called x.

3.1.1. Standard MRE model

The description of the standard model we use is done in one of our articles published in Journal of Nuclear Materials [141]. The following description is very similar to what it is presented in this article.

The equations of this standard model express the time evolution of the concentration of the mobile particles c_m (in m^{-3}) and the time evolution of the concentration of the trapped particles $c_{t,i}$ (in m^{-3}) as well as their evolutions in space. In this model, the index i corresponds to the type of trap considered. In this approach, one trap type has one single detrapping energy $E_{t,i}$ which does not depend on the number of HIs trapped inside: there is no direct connection between the different types of traps in the equations.

In the model, n_{TIS} (in m^{-3}) is the concentration of TIS which correspond to the maximum number of mobile particles that can be accommodated in the materials per unit volume. This quantity is constant with time and space. Similarly, n_i (in m^{-3}) is the concentration of traps of type i which correspond to the maximum number of trapped particles of type i per unit volume. This quantity can evolve with time and space. It is important to note that the concentration of particles (mobile or trapped) and the concentration of sites (TIS or trap) are in m^{-3} in the equation but it is convenient to normalize them to the atomic W concentration $\rho_W \approx 6.3 \times 10^{28}\ m^{-3}$. Thus, the concentration can be expressed as atomic fraction (at.fr.) which corresponds to an amount of particles/sites per W atom. The concentration can also be expressed as at.% which is the concentration in at.fr. multiplied by 100.

The evolution of the concentration of the trapped particle is driven by:

- The trapping of mobile particles inside traps of type i,
- The detrapping of trapped particles from these traps.

The following assumptions are made:

- A1: each trap site is surrounded only by TIS ($n_i \ll n_{TIS}$),
- A2: around each trapping site, there is at least one free TIS ($c_m \ll n_{TIS}$),
- A3: the trapping sites are immobile.

Since W crystallized in body-centered cubic structure, 6 TIS exist per W atoms. From the depth profiles reported by NRA (figure 2.9, figure 2.13 and figure 2.15 (a)), it can be said that the maximum concentration of H in the W is ~10^{-1} H per W which justifies the first two assumptions (the trap concentration n_i being similar to the concentration of trapped particles $c_{t,i}$ probe by NRA). Again, according to DFT calculations [72], the energy barrier for migration of a mono-vacancy is higher than 1.7 eV. This energy barrier becomes 2.52 eV if a HI is trapped inside: this makes the vacancy immobile around room temperature. They can migrate and annihilate around 500 K if they are empty [55] but if they are filled with HI, it is not possible. Concerning the dislocations, it is reported in section 2.3.3.iii that they begin to be annihilated above 800 K- 900 K. And concerning the GB, the recrystallization temperature is 1500 °C (table 1.1). Following this analysis, the third assumption can be justified for temperature below 900 K.

With these three assumptions, the time evolutions of mobile and trapped particles can be expressed by the following set of equation [142]:

$$\frac{\partial c_m}{\partial t} = \frac{\partial}{\partial x}\left(D(T) \cdot \frac{\partial c_m}{\partial x}\right) - \Sigma\left(\frac{\partial c_{t,i}}{\partial t}\right) + S_{ext}(x) \tag{3.1}$$

$$\frac{\partial c_{t,i}}{\partial t} = \nu_m(T) \cdot c_m \cdot \left(n_i - c_{t,i}\right) - \nu_i(T) \cdot c_{t,i} \tag{3.2}$$

The first term of the right hand side of equation (3.1) corresponds to the diffusion of mobile particles from TIS to TIS. This diffusion is described following the Fick's law for diffusion as explain section 1.3 by equation (1.5). As already presented in section 2.2.3, the diffusion coefficient of HIs D(T) (in m^2s^{-1}) evolves with temperature following an Arrhenius law (Eq. 2.8) characterized by a pre-exponential factor D_0 (in m^2s^{-1}) and the energy barrier for diffusion E_{Diff} (in eV): $D(T) = D_0 \cdot e^{-\frac{E_{Diff}}{k_B \cdot T}} (m^2 \cdot s^{-1})$.

The second term of the right hand side of equation (3.1) corresponds to the exchange between trapped particles (any types) and mobile particles through the trapping and detrapping processes.

The third term of the right hand side of equation (3.1) corresponds to a volume source term (unit $m^{-3}s^{-1}$) that simulates the implantation of energetic particles. This source term is not zero if HIs atoms are inserted directly in the bulk as in the case of energetic ions and it vanishes at the end of the implantation. It can be expressed by the following relation:

$$S_{ext}(x) = (1 - r) \cdot \phi_{inc} \cdot f(x) \tag{3.3}$$

In this relation, r is the reflection coefficient of the incident ions, ϕ_{inc} is the incident flux of ions that impinging the surface and f(x) is the space distribution of the atoms in the direction orthogonal to the surface. The quantities r and f(x) depends on the energy of ions and their incident angle. The source term is only in equation 3.1 because it has been considered that there are more TIS than trapping sites (assumption A1). Thus, the probability for an incident particle to stop in a trapping site is nearly 0.

Equation 3.2 can be understood as a balance between two "chemical" reactions:

- One mobile particle c_m and one free trap $(n_i - c_{t,i})$
- One trapped particle $c_{t,i}$ and one free TIS $(n_{TIS} - c_m)$.

The reaction between two free traps is not considered according to the assumption A1. And following the assumption A2, the free TIS is not the limiting reagent. The chemical system can so be express as following (with the concentration):

$$c_m + (n_i - c_{t,i}) \rightleftarrows c_{t,i} \tag{3.4}$$

The rate constant associated to the trapping of mobile particles in free traps (from the left to the right in equation 3.4) is $\nu_m(T)$ (in m^3s^{-1}). Thus, the increase of concentration of trapped particles due to trapping process (from the left to the right in equation 3.4) is written as: $\left(\frac{\partial c_{t,i}}{\partial t}\right)_{trapping} = \nu_m(T) \cdot c_m \cdot (n_i - c_{t,i})$. This is the first term of the right hand side of equation 3.2. It is assumed that the activation energy for a mobile particle to get trapped is E_{Diff} (figure 2.2). Following this statements, the rate constant for trapping can be expressed as:

$$\nu_m(T) = \frac{D(T)}{n_{TIS} \cdot \lambda^2} \tag{3.5}$$

Where λ (unit m) is the jumping distance between two TIS. According to DFT calculations [72], HIs diffuse in the bcc W lattice through TIS. The distance between 2 neighboring TIS is $\lambda = \frac{a_W}{2 \cdot \sqrt{2}} \approx 110$ pm with $a_W = 316$ pm the lattice constant of crystallographic W (table 1.1).

The rate constant associated to the detrapping of trapped particles is $\nu_i(T)$ (in s^{-1}). Thus, the decrease of concentration of trapped particles due to detrapping process (from right to left in

Eq. 3.4) is written as: $\left(\frac{\partial c_{t,i}}{\partial t}\right)_{detrapping} = -\nu_i(T) \cdot c_{t,i}$. This is the second term of the right hand side of equation 3.2. The activation energy for detrapping is $E_{t,i}$ as express figure 2.2. Thus, the rate constant for detrapping is described using transition state theory (equation 2.2) as follow:

$$\nu_i(T) = \nu_0 \cdot e^{-\frac{E_{t,i}}{k_B \cdot T}} \quad (3.6)$$

ν_0 is the pre-exponential factor (in s^{-1}) associated to the trapping process. It is commonly assumed that this value is in the range of 10^{13} s^{-1} [132, 143]. However, some authors express this quantity as a function of the jumping distance λ and the pre-exponential factor of diffusion coefficient D_0 as $\nu_0 = \frac{D_0}{\lambda^2}$ [142] which gives a pre-exponential factor between 10^{13} s^{-1} and 3×10^{13} s^{-1}. In fact, it depends slightly on the temperature and for H trapped inside a mono-vacancy, it has been calculated to be between 0.85×10^{13} s^{-1} and 1.45×10^{13} s^{-1} between 300 K and 1000 K [72]. In the next, it will be considered as constant with temperature and equal to 10^{13} s^{-1}.

The steady-state equilibrium of equation 3.2 is obtained when $\frac{\partial c_{t,i}}{\partial t} = 0$. In this case, it can be shown that the equilibrium concentration of trapped particles $c_{t,i}^{eq}$ is directly proportional to the concentration of traps n_i and this relation can be written as:

$$c_{t,i}^{eq} = R_{trap,i}(c_m, T) \cdot n_i \quad (3.7)$$

With

$$R_{trap,i}(c_m, T) = \frac{1}{1+\frac{\nu_i(T)}{\nu_m(T) \cdot c_m}} \quad (3.8)$$

The quantity $R_{trap,i}$ is called the equilibrium ratio of trap type i and it depend on the quantity of mobile particle c_m and the temperature T. It is a dimensionless quantity. For any temperature and for any concentration of mobile particles, this ratio is between 0 and 1. It exemplifies the competition between the detrapping and trapping processes described by the detrapping characteristic frequency $\nu_i(T)$ and the trapping characteristic frequency $\nu_m(T) \cdot c_m$. If the trapping process is faster than the detrapping process ($\nu_m(T) \cdot c_m \gg \nu_i(T)$), then $R_{trap,i} \approx 1$ which means that almost all the traps are filled with HIs. This is the case for low temperature ($\nu_i(T)$ is low) or/and for high mobile particle concentration. In the opposite, if the detrapping process is faster than the detrapping process ($\nu_i(T) \gg \nu_m(T) \cdot c_m$), then $R_{trap,i} \approx 0$ which means that almost no traps are filled with HIs. This is the case for high temperature ($\nu_i(T)$ is high) or/and for low mobile particle concentration.

This model is implemented in a code called MHIMS (Migration of Hydrogen Isotopes in MaterialS). The first version of MHIMS solves numerically the equation using a standard finite difference implicit Euler method. The code has been upgraded using the LSODE library [144, 145] which allows quicker calculations.

3.1.2. Multi-trapping model

The description of the multi-trapping model is done in an article that we published in Physica Scripta [146] and presented at the 15th international Conference on Plasma-Facing Materials and Components for Fusion Applications.

The multi-trapping approach is based on the DFT results summarized figure 2.14: a trap type (defect) can retained several HIs and the detrapping energy of one HI from this trap depends on the number of HIs that are inside it. To describe simply the model, we take the case where

there is only one type of defect. This trap type can retained between 0 and $l_m > 1$ HIs (if $l_m = 1$, the model corresponds to the standard model presented in section 3.1.1). The total concentration of traps is N_{trap} (in m^{-3}) and the concentration of traps filled with $0 \leq i \leq l_m$ is N_i (in m^{-3}). Thus, there is the equality: $\Sigma_{i=0}^{l_m} N_i = N_{trap}$. In this description, i is called the filling level of a trap. We considered that the concentration of trap N_{trap} can evolve in space but it is constant over time. In this model, $c_{t,i}$ (unit m^{-3}) is the concentration of HIs trapped in the traps filled with i HIs: $c_{t,i} = i \cdot N_i$. The equations of the model do not express directly the time evolution of the concentrations $c_{t,i}$ but the time evolution of the concentrations N_i.

As in the standard model, n_{TIS} (in m^{-3}) is the concentration of TIS which correspond to the maximum number of mobile particles that can be accommodated in the materials per unit volume. This quantity is constant with time and space. We make the same assumption as in the standard model:

- A1: each trap site is surrounded by only by TIS ($N_i \ll n_{TIS}$),
- A2: around each trapping site, there is at least one free TIS ($c_m \ll n_{TIS}$),
- A3: the trapping sites are immobile.

The equation describing the evolution of the concentration of mobile particles is the same as the standard model (Eq. 3.9):

$$\frac{\partial c_m}{\partial t} = \frac{\partial}{\partial x}\left(D(T) \cdot \frac{\partial c_m}{\partial x}\right) - \Sigma_{i=1}^{l_m}\left(\frac{\partial c_{t,i}}{\partial t}\right) + S_{ext}(x) \tag{3.9}$$

As explained in the standard model description, the first term of the right hand side of this equation corresponds to the diffusion of mobile particles rationalized by the Fick's law. The second term of the right hand side corresponds to the exchange with the trapped particle. Finally, the third term of the right hand side corresponds to the volume source of particle (Eq. 3.3).

As for the standard model, the time evolution of trapped particle concentrations is driven by trapping of mobile particles and detrapping of trapped particles:

- The rate constant associated to trapping of mobile particles is $\nu_m(T)$ (in $m^3 s^{-1}$) and its expression is the same as in the standard model (Eq. 3.5): $\nu_m(T) = \frac{D(T)}{n_{TIS} \cdot \lambda^2}$. The trapping rate constant is assumed to be the same for any filling level.
- The rate constant associated to detrapping of trapped particles in a trap filled with i HIs is $\nu_i(T)$ (in s^{-1}). Its expression is the same as in the standard model: $\nu_i(T) = \nu_0 \cdot e^{-\frac{E_{t,i}}{k_B \cdot T}}$. $E_{t,i}$ is the detrapping energy of one HIs from a trap filled with i HIs and for the same reason as for the standard model, it is set: $\nu_0 = 10^{13}\ s^{-1}$.

For $0 < i < l_m$, the evolutions of concentrations of traps N_i can be described by different reactions that couple the filling level i to the filling level $i + 1$ (Eq. 3.10) and the filling level $i - 1$ (Eq. 3.11). In this set of equations, the concentration of TIS does not appear since it is considered as an excess chemical reagent (assumption A2)

$$c_m + N_i \leftrightarrows N_{i+1} \tag{3.10}$$

$$N_i \leftrightarrows c_m + N_{i-1} \tag{3.11}$$

These notations allow seeing all the reactions in which the traps filled with i HIs (N_i) acts as a chemical reagent.

From equation 3.10, the evolution of N_i due to exchange with the population N_{i+1} can be written as:

$$\left(\frac{\partial N_i}{\partial t}\right)_{i\leftrightarrow i+1} = -\nu_m(T)\cdot c_m\cdot N_i + \nu_{i+1}(T)\cdot N_{i+1} \quad (3.12)$$

The first term of the right hand side of this equation corresponds to trapping of mobile particles in traps filled with i HIs: the filling level changes from i to $i+1$. The second term of the right hand side corresponds to detrapping of trapped particles from traps filled with $i+1$ HIs: the filling level changes from $i+1$ to i.

From equation 3.11, the evolution of N_i due to exchange with the population N_{i-1} can be written as:

$$\left(\frac{\partial N_i}{\partial t}\right)_{i\leftrightarrow i-1} = -\nu_i(T)\cdot N_i + \nu_m(T)\cdot c_m\cdot N_{i-1} \quad (3.13)$$

The first term of the right hand side of this equation corresponds to detrapping of trapped particles from traps filled with i HIs: the filling level changes from i to $i-1$. The second term of the right hand side corresponds to trapping of mobile particles in trap filled with $i-1$ HIs: the filling level changes from $i-1$ to i.

The evolution of concentration of traps filled with i HIs for $0 < i < l_m$ can be obtained by summing equations 3.12 and 3.13 which gives equation 3.15. The evolution of concentration of traps filled with 0 HIs and l_m HIs is based on the same basis but:

- In the case of empty trap ($i = 0$) no detrapping can occur from these traps. The evolution of N_0 is described by equation 3.14.
- In case of completely filled trap ($i = l_m$), no trapping can occur in these traps. The evolution of N_{l_m} is described by equation 3.16.

Therefore, the equations that described the evolution of any N_i are the following ones:

For $i = 0$:

$$\frac{\partial N_0}{\partial t} = -\nu_m(T)\cdot c_m\cdot N_0 + \nu_1(T)\cdot N_1 \quad (3.14)$$

For $0 < i < l_m$:

$$\frac{\partial N_i}{\partial t} = -\nu_m(T)\cdot c_m\cdot N_i + \nu_{i+1}(T)\cdot N_{i+1} - \nu_i(T)\cdot N_i + \nu_m(T)\cdot c_m\cdot N_{i-1} \quad (3.15)$$

For $i = l_m$:

$$\frac{\partial N_{l_m}}{\partial t} = -\nu_{l_m}(T)\cdot N_{l_m} + \nu_m(T)\cdot c_m\cdot N_{l_m-1} \quad (3.16)$$

With the set of equations 3.9, 3.14, 3.15 and 3.16 the model is fully described. As explain previously: $\Sigma_{i=0}^{l_m} N_i = N_{trap}$. Assuming that there is no trap creation over time, the concentration N_{trap} is constant with time: $\frac{\partial N_{trap}}{\partial t} = \Sigma_{i=0}^{l_m}\frac{\partial N_i}{\partial t} = 0$. This is verified by calculating the equation (3.14), (3.15) and (3.16). If a trap creation process, characterized by the function $F(t,x)$ (in $m^{-3}s^{-1}$), is present: $\frac{\partial N_{trap}}{\partial t} = F(t,x)$. In this case, the different components of that function characterizing the creation process has to be added to the right hand side of the equation 3.14, 3.15 or 3.16 depending on whether the created traps are filled or not. The simplest case is to assume creation of empty traps which means that the function $F(t,x)$ is added in the right hand side of equation 3.14.

In equation 3.9, the sum $\Sigma_{i=1}^{l_m}\left(\frac{\partial c_{t,i}}{\partial t}\right)$ can be replaced by $\Sigma_{i=1}^{l_m}(i\cdot\frac{\partial N_i}{\partial t})$. Using equations 3.14, 3.15 and 3.16 ones can obtain equation 3.17:

$$\Sigma_{i=1}^{l_m}\left(\frac{\partial c_{t,i}}{\partial t}\right) = \nu_m\cdot c_m\cdot\left(N_{trap} - N_{l_m}\right) - \Sigma_{i=1}^{l_m}\nu_i(T)\cdot c_{t,i} \quad (3.17)$$

The first term of the right hand side of this relation corresponds to the trapping of all the traps except the fully filled trapped (they cannot accommodate one more HI). The second term of this relation is related to the detrapping of HIs from all the traps that contain at least one HI. Consequently, these two right hand side terms represent all the exchanges possible between trapped and mobile particles.

As for the classical model, steady-state equations can be obtained from the equilibrium of equations 3.14, 3.15 and 3.16: $\frac{\partial N_i}{\partial t} = 0$. These steady-state equations established a relation between the local amount of mobile particles c_m and the concentration of traps at the equilibrium N_i^{eq}. Without trap creation, it can be demonstrated by induction that at the equilibrium, the following relations between N_i^{eq}exist:

For $1 \leq i \leq l_m$ $$\frac{N_i^{eq}}{N_{i-1}^{eq}} = \frac{\nu_m(T)\cdot c_m}{\nu_i(T)} \quad (3.18)$$

For $1 \leq i \leq l_m$ $$\frac{N_i^{eq}}{N_0^{eq}} = \frac{(\nu_m(T)\cdot c_m)^i}{\Pi_{j=1}^{i}\nu_j(T)} \quad (3.19)$$

For $0 \leq i \leq l_m - 1$ $$\frac{N_{l_m}^{eq}}{N_i^{eq}} = \frac{(\nu_m(T)\cdot c_m)^{l_m-i}}{\Pi_{j=i+1}^{l_m}\nu_j(T)} \quad (3.20)$$

For this multi-trapping model, the equilibrium ratio $R_{trap,i}(c_m, T)$ is defined as the ratio between N_i^{eq} and N_{trap} the total concentration of traps: $N_i^{eq} = R_{trap,i}(c_m, T) \cdot N_{trap}$. Using relations 3.18, 3.19 and 3.20 and the equality $\Sigma_{i=0}^{l_m} N_i = N_{trap}$, the equilibrium ratio of a given filling level i can be expressed as function of the rate constant and the local concentration of mobile particles as:

For $i = 0$ $$R_{trap,0} = \frac{1}{1+\Sigma_{k=1}^{l_m}\frac{(\nu_m(T)\cdot c_m)^k}{\Pi_{j=1}^{l_m}\nu_j(T)}} \quad (3.21)$$

For $1 \leq i \leq l_m$ $$R_{trap,i} = \frac{1}{1+\Sigma_{k=0}^{i-1}\frac{\Pi_{j=k+1}^{i}\nu_j(T)}{(\nu_m(T)\cdot c_m)^{i-k}}+\Sigma_{k=i+1}^{l_m}\frac{(\nu_m(T)\cdot c_m)^{k-i}}{\Pi_{j=i+1}^{k}\nu_j(T)}} \quad (3.22)$$

For $i = l_m$ $$R_{trap,l_m} = \frac{1}{1+\Sigma_{k=0}^{l_m-1}\frac{\Pi_{j=k+1}^{l_m-k}\nu_j(T)}{(\nu_m(T)\cdot c_m)^{l_m-k}}} \quad (3.23)$$

As for the standard model, the equilibrium exhibits a competition between the trapping process (frequency $\nu_m(T) \cdot c_m$) and the detrapping process (frequency $\nu_i(T)$). However, the relation is a bit more complex than in the standard model due to the coupling existing between the different filling levels. The equilibrium ratio can be used to calculate the value of N_i^{eq} for a given concentration of mobile particles c_m. By comparing the value of N_i^{eq} to the value given by the simulation, one can say if the traps are in the equilibrium or not with the mobile particles [146].

The multi-trapping model is implemented in a code called MHIMS-R (Migration of Hydorgen Isotopes in MaterialS-Reservoir). In its current version, the maximum value of l_m that MHIMS-R can deal with is $l_m = 12$ which is the maximal amount of HIs that a mono-vacancy can retain at 0 K according to DFT calculations [72]. In term of implementation, as for MHIMS, the first version of MHIMS-R solved the system of differential equation using a Euler implicit method but it has been upgraded with the LSODE Library.

3.2. Boundary conditions

3.2.1. Without surface processes taken into account

The simplest way to deal with the surface processes is to considered that they do not limit the HI desorption from W sample. In this case, they are neglected and not considered on the model. If $x = 0$ and $x = L_0$ represents the 2 boundaries of the 1D simulated material, the boundary condition that neglect the surface processes can be described by Dirichlet boundary conditions as follow:

$$\forall t\ c_m(x = 0) = c_m(x = L_0) = 0 \tag{3.24}$$

The physical meaning of such boundary conditions is that any mobile particle that arrives on the surface recombines immediately with another one and is desorbed as a molecule: the recombination of HIs in molecules is quick. Experimental measurements from Bisson et al. [24] suggest, that in case of ion exposure at low flux and fluence, the desorption of HIs from the surface is not the rate limiting step. In addition, the review paper from Causey [7] concludes that taking these boundary conditions for estimating the tritium retention in W would not underestimate the tritium retention. Based on this two points, these Dirichlet boundary conditions will be used in our studies with MHIMS [141] and MHIMS-R [146] to deal with ion implantations: when the ions are directly implanted in the bulk and do not need to pass through the surface processes to enter the bulk. Such boundary conditions are also used by Schmid et al. for ion implantation simulations [132, 138, 147].

3.2.2. Surface model: surface processes taken into account

As exposed before HIs atoms with low kinetic energy are subject to the surface process that can limit their penetration toward the bulk. In this work, some simulations will be done considering atom exposure and a surface model, acting as boundary condition, has to be used to describe the surface processes through which the atoms pass to get absorbed in the metal.
In this section, the surface model we proposed is described for the case of atomic exposure. It is based on the surface part of the energy diagram (figure 2.2) which is the interface between the "vacuum" and the "metal" part. In this model, two new quantities are introduced:

- c_{surf}: the concentration of adsorbed HIs on the W surface (unit m^{-2}),
- n_{surf}: the concentration of adsorption sites on the W surface (unit m^{-2}).

As a reminder, the surface coverage is $\theta = \frac{c_{surf}}{n_{surf}}$ (Eq. 2.3).
The surface model expresses the evolution with time of the concentration of adsorbed particles c_{surf} and the concentration of mobile particles just below the surface $c_m(x = 0)$. In the model, it is assumed that no incident atoms are directly implanted below the surface. In this case, the evolution of these two quantities is described by the balance of the different fluxes (unit $m^{-2}s^{-1}$) that are described figure 3.1 and can be rationalized by the following set of equations:

$$\frac{\partial c_{surf}}{\partial t} = \phi_{atom} - \phi_{exc} - \phi_{des} - \phi_{s\to b} + \phi_{b\to s} \tag{3.25}$$

$$\lambda \cdot \frac{\partial c_m(x=0)}{\partial t} = \phi_{s\to b} - \phi_{b\to s} - \phi_{diff} \tag{3.26}$$

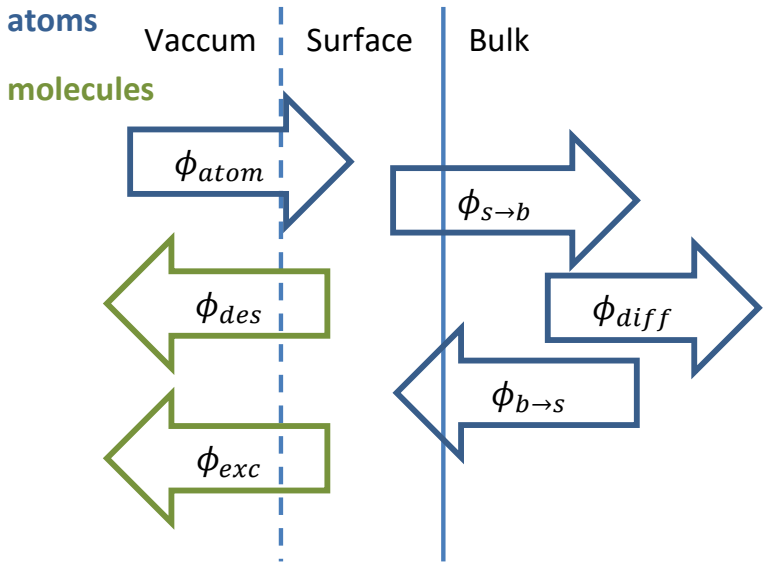

Figure 3.1. Explicative scheme of the flux balance on the surface. Blue arrows correspond to flux of atoms and green arrows correspond to flux of molecules.

The flux ϕ_{atom} corresponds to the part of the incident flux of atoms called Γ_{atom} (unit $m^{-2}s^{-1}$) that is adsorbed on the surface. It can be expressed as $\phi_{atom} = (1 - P_r) \cdot \Gamma_{atom} \cdot (1 - \theta)$. The term $(1 - \theta)$ implies that a fully covered surface prevents any incoming D atoms to be adsorbed. $(1 - P_r)$ is the sticking probability of D atom. It depends on the kinetic energy of the incident atoms [59].

The flux ϕ_{exc} corresponds to the direct abstraction i.e. the recombination of an incident D atom with an adsorbed atom on the surface [41]. It is characterized by the cross section σ_{exc} (unit m^2) and the flux is expressed as $\phi_{exc} = \Gamma_{atom} \cdot \sigma_{exc} \cdot c_{surf}$.

The flux ϕ_{des} corresponds to the desorption flux of adsorbed D atom from the surface as molecules. It can be expressed as $\phi_{des} = 2 \cdot \nu_{des}(T) \cdot c_{surf}^2$. In this expression, $\nu_{des}(T)$ (unit m^2s^{-1}) is the rate constant of the desorption process and it can be expressed using transition state theory as $\nu_{des}(T) = \nu_0^d \cdot \lambda_{des}^2 \cdot e^{-\frac{E_{des}}{k_B \cdot T}}$. Here, ν_0^d (unit s^{-1}) is the desorption pre-exponential frequency, $E_{des} = 2 \cdot E_D$ (unit eV) is the activation energy for HIs desorption from the W surface and λ_{des} (unit m) is the jumping distance between 2 surface adsorption sites. It can be estimated to be $\lambda_{des} = \frac{1}{\sqrt{n_{surf}}}$.

The flux $\phi_{s\to b}$ corresponds to the absorption of D ad-atom from the surface to the bulk (with the assumption of a low mobile concentration $c_m(x = 0) \ll n_{TIS}$). It can be expressed as $\phi_{s\to b} = \nu_{sb}(T) \cdot c_{surf}$. In this expression, $\nu_{sb}(T)$ (unit s^{-1}) is the rate constant of absorption process and it can be expressed using transition state theory as $\nu_{sb}(T) = \nu_0^{sb} \cdot e^{-\frac{E_A}{k_B \cdot T}}$. Here, ν_0^{sb} (unit s^{-1}) is the absorption pre-exponential frequency and E_A (unit eV) is the activation energy for HIs absorption from surface to bulk.

The flux $\phi_{b\to s}$ corresponds to the resurfacing flux of D mobile atoms from the bulk to the surface. It can be expressed as $\phi_{b\to s} = \nu_{bs}(T) \cdot (1 - \theta) \cdot c_m(x = 0)$. In this expression, $\nu_{bs}(T)$ (unit m^1s^{-1}) is the rate constant of the resurfacing process and it can be expressed using transition

state theory as $\nu_{bs}(T) = \nu_0^{bs} \cdot \lambda_{abs} \cdot e^{-\frac{E_R}{k_B \cdot T}}$. Here, ν_0^{bs} (unit s^{-1}) is the resurfacing pre-exponential frequency, E_R (unit eV) is the activation energy for resurfacing and λ_{abs} (unit m) is the jumping distance between the first bulk TIS and an adsorption site. It can be estimated to be $\lambda_{abs} = \frac{n_{surf}}{n_{TIS}}$. It can be noted that the surface gets inactive once it is fully covered by D atoms ($1 - \theta = 0$) meaning that the energy barriers are by-passed and the release of HIs from W as molecules is quick: the boundary condition express by Eq. 3.24 can be used.

The flux ϕ_{diff} corresponds to the diffusion of the absorbed D atom from the first bulk TIS beneath the surface ($x = 0$) to deeper in the bulk ($x > 0$). Following the Fick's law (Eq. 1.6) It can be expressed as $\phi_{diff} = -D(T) \cdot \left(\frac{\partial c_m}{\partial x}\right)_{x=0}$.

From different papers [41, 62, 148], the pre-exponential factor for desorption used to reproduced experimental measurements is $0.01\ cm^{-2} \cdot s^{-1} > \lambda_{des}^2 \cdot \nu_0^d > 0.001\ cm^{-2} \cdot s^{-1}$. For a value of λ_{des} of the order of 0.1 nm ($\sim \lambda$) and $\nu_0^d = 10^{13} s^{-1}$, there is $\lambda_{des}^2 \cdot \nu_0^d = 0.001\ cm^{-2} \cdot s^{-1}$. So in the next, the value $\nu_0^d = 10^{-13}\ s^{-1}$ is used. The value $\nu_0^{sb} = \nu_0^{bs} = 10^{13} s^{-1}$ are also used which is the order of magnitude of what is calculated for these adsorption and resurfacing processes [65].

In order to understand a bit more the model, the equilibrium of the equations 3.25 and 3.26 are studied: it is supposed $\frac{\partial c_{surf}}{\partial t} = 0$ and $\frac{\partial c_m(x=0)}{\partial t} = 0$. In addition, in order to simplify the approach, it is considered that the diffusive flux of particle from sub-surface to bulk ϕ_{diff} is negligible (i.e. $\left(\frac{\partial c_m}{\partial x}\right)_{x=0} = 0$). At the equilibrium, the concentration of mobile particles beneath the surface is called $c_m^{eq}(x = 0)$, the concentration of adsorbed particles is called c_{surf}^{eq} and the surface coverage is called $\theta^{eq} = \frac{c_{surf}^{eq}}{n_{surf}}$. The equilibrium of equation 3.26 shows a relation between $c_m^{eq}(x = 0)$ and c_{surf}^{eq}:

$$c_m^{eq}(x = 0) = \frac{\nu_{sb}(T)}{\nu_{bs}(T)} \cdot \frac{c_{surf}^{eq}}{1 - \theta^{eq}} \tag{3.27}$$

This relation implies that the equilibrium concentration of mobile particles below the surface does not depends on the value of E_A and E_B independently but on the difference $\Delta E = E_A - E_B$ since it is an equilibrium between absorption and resurfacing. The kinetic to reach this value will however depend on the value of E_A and E_B.

Using relation 3.27 and equation 3.26 in steady state, the following relation is obtained:

$$-2 \cdot \nu_{des}(T) \cdot \left(c_{surf}^{eq}\right)^2 - \omega_1 \cdot c_{surf}^{eq} + \omega_2 = 0 \tag{3.28}$$

With $\omega_1 = \Gamma_{atom} \cdot \left(\frac{1 - P_r}{n_{surf}} + \sigma_{exc}\right)$ and $\omega_2 = (1 - P_r) \cdot \Gamma_{atom}$. These quantities are introduced only to simplify the notations.

Solving equation 3.28, a simple relation can be established between c_{surf}^{eq}, the incident flux and the abstraction cross section (through ω_1 and ω_2):

$$c_{surf}^{eq} = \frac{\sqrt{\omega_1^2 + 8 \cdot \nu_{des}(T) \cdot \omega_2} - \omega_1}{4 \cdot \nu_{des}(T)} \tag{3.29}$$

If $\nu_{des}(T) \to 0$ (no desorption of molecules) of $\Gamma_{atom} \to \infty$ (high flux), the surface concentration is $c_{surf}^{eq} \to \frac{\omega_2}{\omega_1} = n_{surf} \cdot \frac{1 - P_r}{1 - P_r + \sigma_{exc} \cdot n_{surf}}$. In the case of an inactive or weak abstraction ($\sigma_{exc} \approx 0$),

the concentration of adsorbed particles is equal to the number of adsorbed site n_{surf}. If the abstraction is non-negligible, the maximum surface concentration is smaller than the surface site concentration n_{surf} depending on the efficiency of the direct abstraction process.

3.3. Simple analytical model

3.3.1. In case of ion implantation

In order to qualitatively understand the time evolution of the recycling coefficient (i.e. the flux of outgassed molecules divided by the implanted flux of particles), K. Schmid [147] proposed a simple analytical model. This model supposed that the profile of mobile particles generated by an implanted flux ϕ_{imp} (unit $m^{-2}s^{-1}$) of ions with mean implantation depth R_p has a triangular shape as shown by figure 3.2 (a) with the maximum of concentration of mobile particles (called c_m^{MAX}) at the depth R_p: $c_m^{MAX} = c_m(x = R_p)$. In this description, the boundary condition used is the one described in section 3.2.1 (Dirichlet Boundary condition, $c_m(x = 0) = 0$). This shape can be justified by simple a simulation.

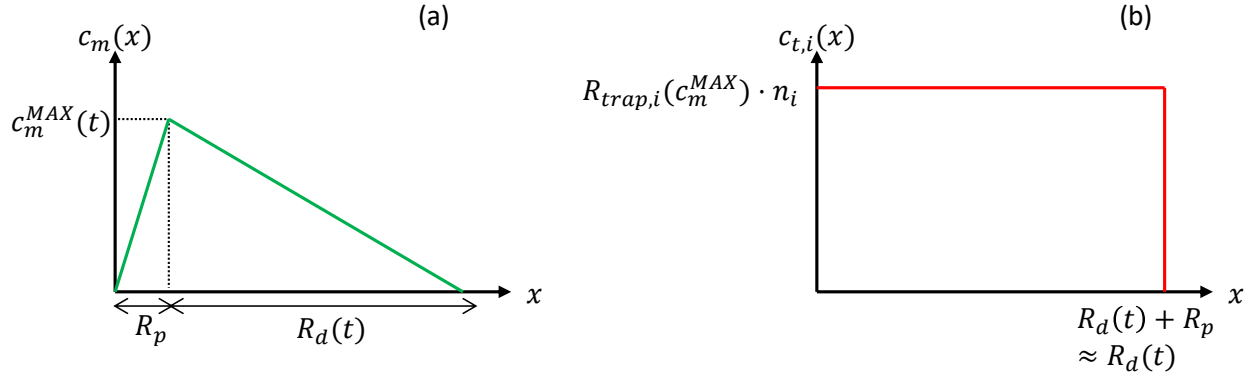

Figure 3.2. Simple analytical model describing the concentration of mobile particles (a) and the concentration of trapped particles (b) at a time t during an ion implantation.

The migration of the HIs from the implantation zone to the bulk is characterized in this simple model by the distance $R_d(t)$ as described in figure 3.2. As the implantation time grows, the HIs migrate deeper and deeper making $R_d(t)$ increase. This migration to the bulk comes from the gradient of mobile particle concentration between $x = R_p$ and $x = R_d(t)$ that generate the flux ϕ_{bulk} (unit $m^{-2}s^{-1}$) that can be written, following the Fick's law as $\phi_{bulk} = D(T) \cdot \frac{c_m^{MAX}}{R_d(t)}$. Also, in the other hand, the flux of particle desorbing from the W materials ϕ_{surf} (unit $m^{-2}s^{-1}$) can be expressed by Fick's law as $\phi_{surf} = -D(T) \cdot \frac{c_m^{MAX}}{R_p}$.

The balance between the implanted flux ϕ_{imp}, the desorbing flux ϕ_{surf} and the migration flux toward the bulk ϕ_{bulk}, can be written as:

$$\phi_{imp} = -\phi_{surf} + \phi_{bulk} \tag{3.30}$$

To calculate simply the concentration of trapped particles, the equilibrium ratio from the standard model is used (Eq. 3.8). Assuming that for all the traps considered $R_{trap,i}(c_m^{MAX}, T) \approx 1$, the

values of $R_{trap,i}$ evolve weakly with c_m. Then, it can be considered that $R_{trap,i}(c_m, T) \approx R_{trap,i}(c_m^{MAX}, T)$. In that case, and if the concentration of traps n_i is homogeneously distributed in space, the distribution of trapped particles can be described by figure 3.2 (b).
The amount of trapped particles, between the depth R_p and $R_d(t)$, in any kind of trap types for an implantation that last for a time t can be calculated as:
$Tot_{trap}(t) = R_d(t) \cdot \Sigma_i R_{trap,i}(c_m^{MAX}, T) \cdot n_i$.
In this region (between R_p and $R_d(t)$ the traps are filled by mobile particle diffusing due to the diffusive flux ϕ_{bulk} : $\frac{dTot_{trap}}{dt} = \phi_{bulk}$. This relation implies: $R_d(t) \cdot dR_d(t) = D(T) \cdot \frac{c_m^{MAX}}{\Sigma_i R_{trap,i}(c_m^{MAX},T) \cdot n_i} \cdot dt$. By integrating this relation between time 0 ($R_d(0) = 0$) and time t ($R_d(t)$), equation 3.30 is obtained.

$$R_d(t) = \sqrt{\frac{2 \cdot D(T) \cdot c_m^{MAX}}{\Sigma_i R_{trap,i}(c_m^{MAX},T) \cdot n_i} \cdot t} \quad (3.31)$$

For ions of several hundreds of eV/D, the typical implantation depth R_p is few nm. In the other hand, the migration distance $R_d(t)$ varies between several hundreds of nm (for low fluence) to several µm. Consequently, the migration depth $R_p + R_d(t)$ can be approximated to be $R_d(t)$. From equation 3.30, and using relation 3.31 to express ϕ_{bulk} as a function of time, the following equation is obtained:

$$0 = \frac{D(T)}{R_p} \cdot \left(\sqrt{c_m^{MAX}}\right)^2 + \sqrt{\frac{\Sigma_i R_{trap,i}(c_m^{MAX},T) \cdot n_i \cdot D(T)}{2 \cdot t}} \cdot \sqrt{c_m^{MAX}} - \phi_{imp}.$$

By solving this equation, the evolution of c_m^{MAX} with time can be obtained (eq. 3.32).

$$\sqrt{c_m^{MAX}} = \sqrt{R_p \cdot \frac{\phi_{imp}}{D(T)}} \cdot \sqrt{\frac{\tau_m}{t}} \cdot \left(\sqrt{1 + \frac{t}{\tau_m}} - 1\right) \quad (3.32)$$

In this relation, $\tau_m = \frac{R_p \cdot \Sigma_i R_{trap,i}(c_m^{MAX},T) \cdot n_i}{8 \cdot \phi_{imp}}$ is the characteristic time for the growth of c_m^{MAX}. Relation 3.32 implies that there is a limit value of c_m^{MAX} (figure 3.3) which is only dependent on the mean implantation range R_p, the diffusion coefficient D(T) and the implanted flux ϕ_{imp} (relation 3.32):

$$c_m^{MAX}{}_{t \to \infty} = R_p \cdot \frac{\phi_{imp}}{D(T)} \quad (3.33)$$

The evolution of c_m^{MAX} normalized to its limit value with the normalized time $\frac{t}{\tau_m}$ is shows figure 3.3.The limit value of c_m^{MAX} does not depend on the trapping parameters ($R_{trap,i}(c_m^{MAX}, T) \cdot n_i$). Indeed, relation 3.33 describes the equilibrium between the implantation of particle (ϕ_{imp}) in the implantation zone (characterized by R_p) and the diffusion of these particles from the implantation zone (D(T)): no trapping parameters are involved in this equilibrium. However, the kinetic to reach the equilibrium is depending on the trapping parameters (cf the definition of τ_m): the more traps there are, the slower the limit is reached since the mobile particles have to fill the free traps up to the equilibrium ratio first. Once this equilibrium reached, it can be said that the mobile particles are in equilibrium with the traps.
For $t = \tau_m$, the concentration of mobile particles reaches 17 % of its final value, for $t = 10 \cdot \tau_m$, it reaches 54 % of its final value and it is above 90 % of the final value only for $t = 400 \cdot \tau_m$: the evolution is quite slow compare to the response of a first order system to unit step (asymptotic exponential).

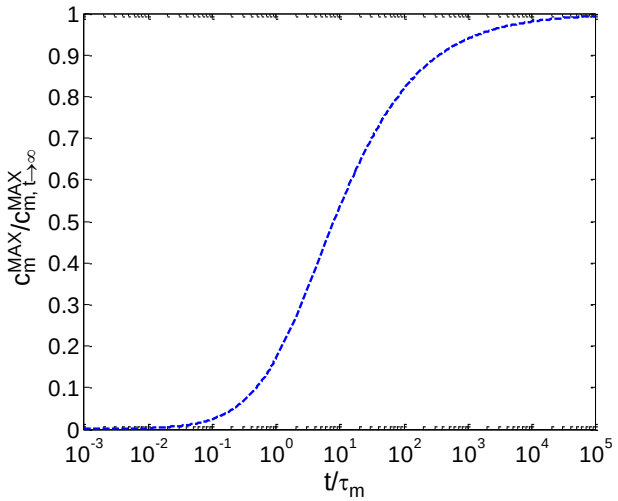

Figure 3.3. Evolution of c_m^{MAX} with normalized time t/τ_m.

However, the characteristic time τ_m is small for high flux, higher than 10^{18} $m^{-2}s^{-1}$. From deuterium depth profile in W shown figure 2.8 and figure 2.13, the value $\Sigma_i R_{trap,i}(c_m^{MAX}, T) \cdot n_i$ can be approximated to be $\approx 10^{-4} \cdot \rho_W$ with $\rho_W = 6.3 \times 10^{28}\ m^{-3}$ the tungsten atomic concentration (table 1.2). As presented in section 2.2.4, typical implantation of D ions in W are made using energy around 200 - 500 eV/D ($R_p \approx 5$ nm) and flux around $10^{18\text{-}20}$ $m^{-2}s^{-1}$. In this case, the value of τ_m varies from 4×10^{-2} s to 4×10^{-4} s. Compared to the experimental time of implantation, this value is several orders of magnitudes lower: during such implantations, the mobile particles are quickly in equilibrium with the traps. It is a bit different for implantation with low fluxes as the results presented by Bisson et al. [24]. In this case, the flux is ~10^{16} $m^{-2}s^{-1}$ and the energy is 250 eV/D ($R_p \approx 5$ nm): the value of τ_m is $\tau_m = 4$ s. The equilibrium is reached in time ($\approx 400 \cdot \tau_m = 1600$ s) which is the same order of magnitude as the implantation time: for the low fluence, the evolution of the retention would not be as the square root of time/fluence.

3.3.2. In case of an atom exposure

Similar simplified analytical model can be used to understand the migration of HIs in W under atom exposures. In case of ion implantation, the HIs are inserted directly in the bulk and the maximum value of the concentration of mobile particles is below the surface at the depth $x = R_p$. In case of an atom exposure, the atoms are adsorbed first on the surface and they can, after that, be absorbed in the metal lattice: the maximum of the mobile concentration is at the depth $x = 0$ and the simple analytical is described then by figure 3.4 with a source of particle at the depth $x = 0$ with a value of c_m^{MAX}.

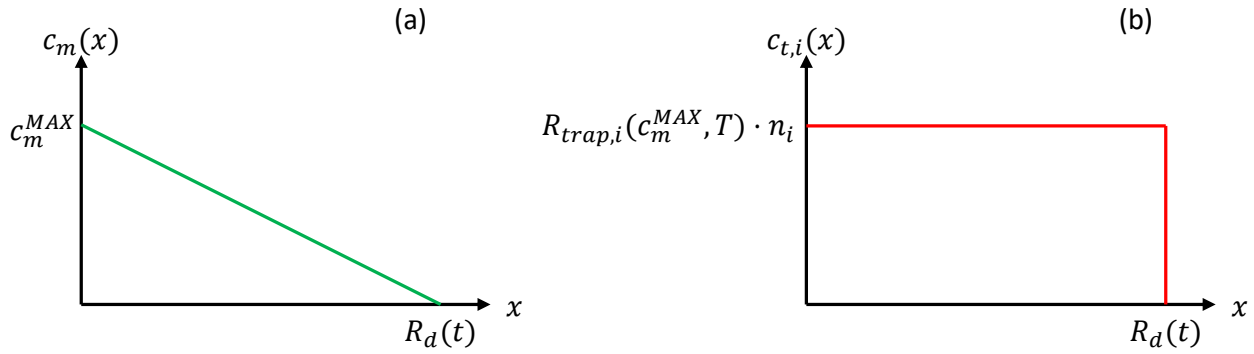

Figure 3.4. Simple analytical model describing the concentration of mobile particles (a) and the concentration of trapped particles (b) at a time t during an atomic exposure.

In this case, the value of $c_m(x = 0)$ is given by the surface model described in section 3.2.2. The limit value of c_m^{MAX} is then the value c_m^{eq} given by equation 3.27.
With this analytical model, it can be demonstrated with the same method as it has been done in section 3.3.1 that the evolution of $R_d(t)$ is the same as equation 3.31 and show here as reminder:

$$R_d(t) = \sqrt{\frac{2 \cdot D(T) \cdot c_m^{MAX}}{\Sigma_i R_{trap,i}(c_m^{MAX}, T) \cdot n_i}} \cdot t \quad (3.34)$$

This relation will be used when the simulation of atom exposure will be treated in Chapter 4 in order to evaluate analytically the energy barrier used in surface model presented in section 3.2.2. For this evaluation, the experimental depth profile and an evaluation of the concentration of adsorbed particles c_{surf}^{eq} is required. From the concentration of adsorbed particles c_{surf}^{eq}, the activation energy for desorption E_{des} can be estimated from relation 3.29. From the experimental depth profile, the value of $\Sigma_i R_{trap,i}(c_m^{MAX}, T)$ and $R_d(t)$ can be extracted for a given implantation time. Using relation 3.34, the value of the concentration of mobile particles c_m^{MAX} needed to reach $R_d(t)$ can be calculated. Considering $c_m^{MAX} = c_m^{eq}$ and using the estimation of the concentration of adsorbed particles c_{surf}^{eq}, the difference energy $\Delta E = E_A - E_R$ can be estimated analytically using relation 3.27.
The knowledge on n_{surf} is required for that analytical evaluation to be done. It can be obtained by loading atoms on the surface at low temperature which would likely saturate any adsorption sites. In [41], a self-damaged W sample has been exposed to D atoms at 380 K. The D surface concentration has been measured by ERDA to be10×10^{19} D·m^{-2} during the exposure in steady state. It will then be considered that this value is a good approximation of n_{surf}. It can be noted that with this value, $n_{surf} \approx 6 \times \rho_W^{\frac{2}{3}}$ meaning that there are 6 adsorption sites per W atoms on the surface. This is higher than the number of adsorption site derived from DFT calculations reported in section 2.3.1. It can be due to the fact that, in DFT calculations, perfect surfaces are considered with a single orientation. In the PCW that is used in the experiment, different surface orientations cropped on the surface (since it is a PCW sample) and the roughness may also play a role in the observed surface concentration.

3.4. Summary

In this Chapter, the two models describing the interaction between HIs and W in the bulk have been described:

- The standard model that gives the mean detrapping energies of all defects trapping HIs. It is particularly suitable for dealing with complex sample such as PCW sample presenting a various quantities of defects.
- The multi trapping that can be used to compare, in a multi-scale modelling approach, the DFT results with the experimental results. Mainly, this model is used to reproduce experimental results obtained with SCW samples annealed at high temperature in order to have the simplest possible structure (to avoid overlapping of desorption from different defects).

For each of this model, the boundary conditions traduce the interaction of HIs with the W surface. Two boundary conditions are described:

- The simplest one is a Dirichlet boundary condition: the concentration of mobile particle on the surface is zero which means that the desorption of HIs from the surface is not the limiting step. This boundary condition is used in the cases of implantations of ions directly in the bulk.
- The surface model that described the adsorption of HI atoms on the surface, the absorption from the surface to the bulk and the resurfacing from the bulk to the surface. These boundary conditions are used in case of atomic exposure at low energy of incident atom: the atom can be first adsorbed on the surface before entering the bulk.

The parameters of all the models described in this chapter (bulk models and surface model) are summarized in table 3.1. Some of these parameters are not free parameters and are taken from previous experimental results or DFT calculations. Others parameters are free parameters that can be determined by reproducing the experimental results, mainly TDS and NRA data. For the surface model, coupling the simple analytical model, the steady state equation of the model and the experimental observations on the depth profiles, the energy barriers can be analytically estimated.

Parameter	description	value	From
D(T)	Diffusion coefficient	For hydrogen (m^2s^{-1}): $1.9 \times 10^{-7} \cdot e^{-\frac{0.2(eV)}{k_B \cdot T}}$	DFT results [72]
a_W	Lattice constant of bcc W	316×10^{-12} m	[8]
ρ_W	Atomic concentration of W	6.3×10^{28} m^{-3}	[8]
λ	jumping distance between two TIS	$\sim110\times10^{-12}$ m	DFT results [72]
n_{TIS}	Concentration of TIS	6 at.fr. ($6 \cdot \rho_W$ in m^{-3})	DFT results [72]
n_{surf}	Concentration of adsorption sites	$\sim10^{20}$ m^{-2}	D surface concentration at 380 K [41]

λ_{des}	Jumping distance between two adsorption sites	$\frac{1}{\sqrt{n_{surf}}} \approx 100\times10^{-12}$ m	
λ_{abs}	Jumping distance between the first bulk TIS and an adsorption site	$\frac{n_{surf}}{n_{TIS}} \approx 250\times10^{-12}$ m	
ν_0 ν_0^d ν_0^{sb} ν_0^{bs}	Pre-exponential frequency factors for detrapping, desorption, absorption and resurfacing processes	10^{13} s^{-1}	[72] [41, 62, 148] [65] [65]
$E_{t,i}$	Detrapping energy from trap i	Free parameters (eV)	TDS results
n_i	Concentration of trap i	Free parameters (m^{-3})	NRA/TDS results
$E_{t,i}$	Detrapping energy from trap filled with i HIs	From DFT and adjustable to reproduce TDS results	DFT [72, 114, 115, 116]
N_{trap}	Concentration of traps that can contain l_m HIs	Free parameter (m^{-3})	NRA/TDS results
l_m	Maximum number of HIs in the traps	6 for mono-vacancy at 300 K	DFT [72]
E_{des}	Activation energy for desorption from W surface	Free parameter (eV)	Analytical estimation
E_R	Activation energy for resurfacing from the bulk to the surface	0.2 eV	DFT [66, 68]
E_A	Activation energy for absorption from the bulk to the surface	Free parameter (eV)	Analytical estimation
r	Reflection coefficient of HI ions on W	Depends on incident ion energy and angle	TRIM
f(x)	space distribution of the atoms in the direction orthogonal to the surface	Depends on incident ion energy and angle	TRIM
$1 - P_r$	Sticking probability of D atoms	0.19 for 0.3 eV/D atoms	[59, 60]
σ_{exc}	Cross section associated to the direct abstraction process	1.7×10^{-21} m^2	Isotopic exchange on surface [41]

Table 3.1. Summary of the parameters used in the different models.

4. Simulations of experimental measurements

This chapter is dedicated to the simulations of experimental measurements and results presented in section 2.3.3. The simulations are done using our home made codes MHIMS or MHIMS-R. It is divided into three parts.
The first one is dedicated to simulations of experiments performed on SCW reviewed in section 2.3.3.i. These simulations present the characteristics of D trapping in SCW which include a possible explanation of the trap creation processes and the nature of the traps that are created. In this part, the model used is the multi-trapping model implemented in MHIMS-R (section 3.1.2).
The second part of the chapter described the simulation of experiments done on PCW samples reviewed in section 2.3.3.ii. Because of the more complex structure of the PCW materials due to the presence of GB, the standard model (implemented MHIMS) is used in this part. However, the conclusions extracted from the simulation of SCW experiments, especially the trap creation processes induced by D irradiation, are included in these simulations. The purpose of this part is to parametrize the wall model to estimate the fuel retention in tokamak with a W divertor that is not damaged by neutrons.
The third and final part is dedicated to the simulations of PCW experiments that have been damaged by heavy energetic ions in order to mimic the defects induced by neutron irradiations. As explain in section 2.3.3.iii, the damaging by neutrons or heavy ions creates traps which change the retention properties of the W. The purpose of this part is to parametrize the wall model to estimate the fuel retention in fusion tokamak equipped with a W divertor during real operation.
It is reminded here that in all the simulations, the diffusion coefficient of H in W used is the one extracted from calculations of Fernandez et al. [72] for hydrogen. The diffusion coefficient of any other HIs is calculated from the diffusion coefficient of H which is divided by the square root of the atomic mass ratio between the considered HI and hydrogen ($\sqrt{2}$ for deuterium and $\sqrt{3}$ for tritium) to account for the larger mass of deuterium or tritium.

4.1. Simulations of SCW experiments

4.1.1. Trap creation model

It is observed by Poon et al. [26] that the D retention in SCW increases with the flux at a given fluence (section 2.3.3.i). This increase has been attributed to a trap creation process that becomes efficient for an incident flux higher than ~5×10^{17} D·m^{-2}·s^{-1}. As it has been reported in section 2.3.4.i, thermo-statistical calculations show that if H is inserted in a pure W crystal, mono-vacancies will be formed in order to reach the thermodynamic equilibrium [72, 120, 121]. According to the results from Ohsawa et al. [120] and the results from Sun et al. [121], two regimes of vacancy formation exist:

- At low concentration of H in pure W, few vacancies are formed per H inserted and a lot of the inserted H are outside the vacancies.
- Above a critical concentration of inserted H, the amount of formed vacancies increases so almost all the inserted H are trapped in vacancies. The calculation from Sun et al. [121] seems to show that the critical concentration is ~5×10^{-10} at.fr. at 300 K. This critical concentration is called c_{crit}^{HI}.

According to equation 3.33, the amount of inserted H during an ion implantation c_m^{MAX} is directly proportional to the flux. For 500 eV/D ions at normal incidence, the mean implantation depth is 7 nm and the reflection coefficient is around 0.5 (from TRIM). So the critical incident flux in order

to triggered the formation of vacancies predicted by the thermo-statistical model is $\phi_{crit}(c_m^{MAX} = c_{crit}^{HI})$ at 300 K. Using equation 3.33, one can obtain for the critical incident flux $\phi_{crit} \approx 5 \times 10^{17}$ D · m^{-2} · s^{-1}. This value corresponds to the threshold observed experimentally: the process predicted by thermos-statistical model seems to occur experimentally (section 2.3.3.i) which may mean that the created traps are mono-vacancies.

In order to check this assumption, simulations are done with the multi-trapping model adding a trap creation model and using the detrapping energies of H in mono-vacancy obtained from DFT calculations [72, 114, 115, 116] and reported in figure 2.16.

As discussed in section 2.3.3.i, the SIMS depth profile of D and O have the same shape with a concentration in the implantation zone (in the first 10 nm) of about one order of magnitude higher than deeper below the surface [27, 42, 43, 86]. From this observation, it has been decided to start the simulation using the detrapping energies of H in VOH_i complex (a mono-vacancy with an O atom inside that can trap H). The detrapping energies of H from VOH_i are very similar to the detrapping energies of H from VH_i or VCH_i (figure 2.16). They can be adjusted in order to reproduce with good agreement the TDS spectrum obtained experimentally (figure 2.7 (a)).

In order to reproduce the experimental observations, a trap creation model is needed. This model described the time evolution of the concentration of traps $\frac{\partial N_{trap}}{\partial t}$ and can be divided in 2 parts:

- A creation of traps driven by the amount of H inserted in TIS c_m as it is suggested by the thermo-statistical models. This creation is characterized by a creation frequency ν_{crea} (in s^{-1}).
- A saturation of traps that is driven by the amount of traps created. After reaching a certain value, the trap concentration stops growing. This saturation could be explained by the fact that all the O/C atoms that can form VO/CH_i are used to formed traps. This saturation process is characterized by a saturation frequency ν_{sat} (in s^{-1}).

The equation that described the time evolution of the concentration of traps has then two components as written in equation 4.1:

$$\frac{\partial N_{trap}}{\partial t} = \nu_{crea}(c_m) \cdot c_m - \nu_{sat}\left(\frac{N_{trap}}{N_{LI(x)}}\right) \cdot N_{trap} \quad (4.1)$$

N_{trap} (in m^{-3}) is the concentration of traps as in the description of the multi-trapping model (section 3.1.2). c_m (in m^{-3}) is the concentration of particle as described in chapter 3 and $N_{LI}(x)$ (in m^{-3}) is a concentration that represents the distribution of light impurities (mainly O and C). It is not directly the concentration of light impurities because the quantitative concentration is not available. It is just an input distribution used to reproduce the feature of the SIMS depth profiles. It is considered that the created traps are first empty and then filled by the trapping process described by the equations presented in Chapter 3.

The evolution of the creation frequency ν_{crea} with the concentration of mobile particles is described on figure 4.1 (a). The evolution of the saturation frequency ν_{sat} with the ration $\frac{N_{trap}}{N_{LI}}$ is shown on figure 4.1 (b). These evolutions have been parametrized in order to reproduce the experimental evolution of the D retention as a function of the flux as it will be described in section 4.1.2.i.

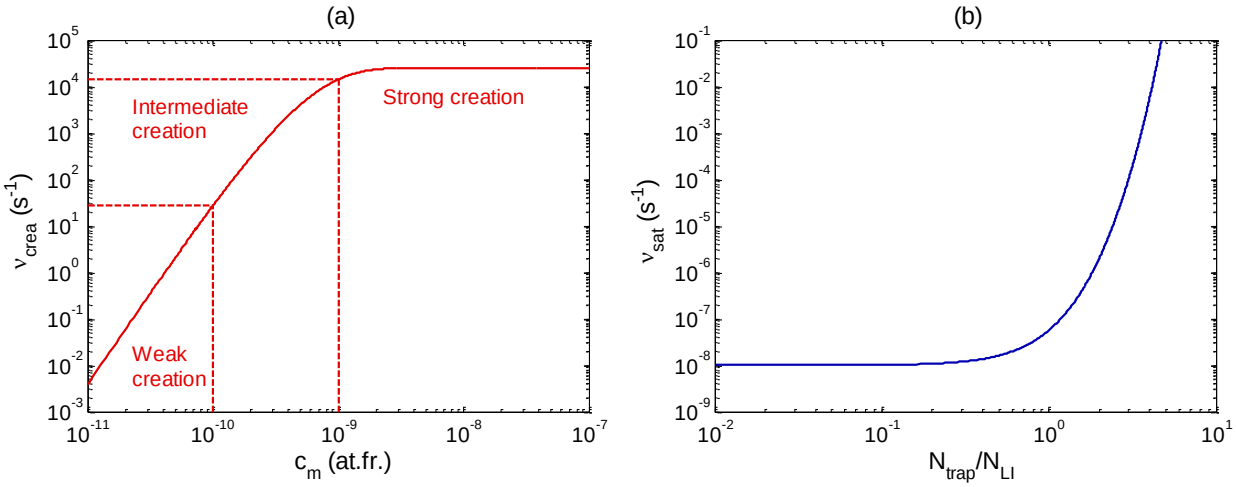

Figure 4.1. (a) Evolution of $\nu_{crea}(c_m)$ as a function of c_m.

(b) Evolution of $\nu_{sat}(N_{trap}/N_{LI}(x))$ as a function of N_{trap}/N_{LI}.

These two evolutions are used to simulate the creation of traps at 300 K.

The first term of the right hand side of equation 4.1 corresponds to the creation of traps. The thermo-statistical models suggest two things: the amount of created traps is proportional to the amount of mobile particles inserted during the implantation and a threshold value of around 5×10^{-10} at.fr. exists above which the creation process is efficient (at 300 K). Below this threshold, the creation is weaker. In the kinetic model, the coefficient of proportionality is the creation frequency $\nu_{crea}(c_m)$ and it evolves as shown in figure 4.1 (a). Three zones can be distinguished: the weak creation zone for mobile concentrations below 10^{-10} at.fr., an intermediate creation zone between 10^{-10} at.fr. and 10^{-9} at.fr. and a strong creation zone for concentrations above 10^{-9} at.fr..
The second term of the right hand side of equation 4.1 corresponds to the saturation of traps. As explained, the local saturation of the concentration of created traps can be explained by the fact that all the O/C impurities have been used to create traps. Thus, the saturation frequency ν_{sat} depends on the ratio between the concentration of created traps and the concentration of light impurities $\frac{N_{trap}}{N_{LI}}$ (see figure 4.1 (b)). From the SIMS measurements, two main zones have been identified in the O/C depth profiles: one near the surface up to 20 nm where the concentration of O/C is high and another one deeper (between 20 and 60 nm) where the concentration of O/C is lower by around one order of magnitude. Following this experimental repartition of O/C, the distribution of O/C impurities $N_{LI}(x)$ used in the simulations to reproduce these tendencies in the 60 nm zones is shown on figure 4.2.

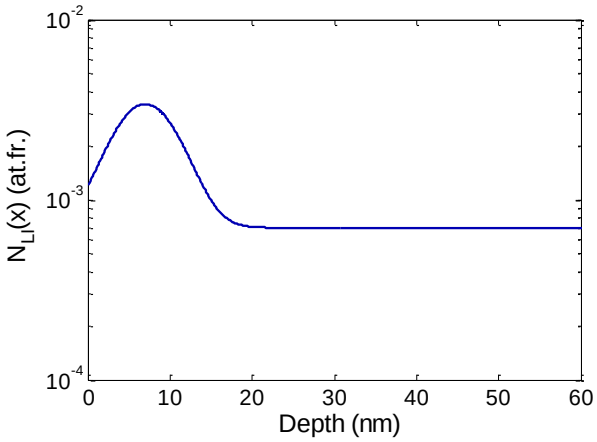

Figure 4.2. Distribution $N_{LI}(x)$ used in the simulation to represent the heterogeneous distributions of the light impurities O/C in the first 60 nm.

No experimental information is available on the concentration of O/C deeper in the bulk from the SIMS depth profiles. Consequently, in a first time, the second zone with the low C/O concentration, i.e. $N_{LI}(x) = 7 \times 10^{-4}$ at. fr. , is extended in all the bulk. Since the first simulations (section 4.1.2.i) intend to reproduce experimental measurements obtained after an implantation at a low fluence (10^{21} D·m^{-2}) at 300 K, this assumption does not affect the simulation results. Indeed, HIs does not migrate deeper than 1-2 µm for such fluence as it will be shown. However, a discussion will take place in order to improve the model for higher fluence implantations (section 4.1.2.ii).

4.1.2. Simulation of experimental results on SCW

i. Experiment at low fluence (10^{21} D·m^{-2})

In this section, we reproduce the results published by Poon et al. [31] and reported in figure 2.8. The samples used by Poon et al. are SCW samples mechanically and electrochemically polished. After each polishing, the samples are annealed at 1775 K under vacuum for 30 min. It is reminded here that Manhard et al. [30] observed a removal of the dislocations in samples annealed at 1700 K (section 2.2.1). Consequently, native dislocations are not a trap that would be considered here. The samples are then irradiated with 500 eV/D ions at normal incidence. After irradiation, the samples are kept for several hours at 300 K. Before the TDS measurement, the TDS device is baked for 1.5 h and during this baking step, the temperature of the samples reaches 400 K. The D retention is extracted from the TDS measurements done with a heating rate between 4 – 6 K/s. In the simulations, the heating ramp is 5 K/s. In order to get the most relevant simulations all these experimental steps need to be simulated. The outgassing during the baking step is far more important than the outgassing during the storage of the samples at 300 K. In that perspective, limited storage time is simulated (only one hour) in order to make the simulations shorter.

Simulation of the experimental results:

Using the trap creation model described in section 4.1.1, the evolution of the D retention with the incident flux is simulated by doing 5 simulations with the 5 different incident fluxes

used in the experiments. In these simulations, a reflection coefficient of 0.5 is used to simulate the reflection of 500 eV/D ions with normal incident on a W surface. The simulations are decomposed as in the experiment in 5 phases:

- The implantation at 300 K ($\phi_{inc} \neq 0$) with an incident fluence of 10^{21} D·m^{-2}
- A first storage time at 300 K for ~ 1000 s ($\phi_{inc} = 0$)
- A baking step at 400 K for 1.5 hours
- A second storage time at 300 K for ~ 1000 s
- The TDS between 300 K and 1300 K with a heating ramp of 5 K/s.

The simulations are done using MHIMS-R that uses the multi-trapping model (section 3.1.2) and the boundary conditions used are the one considering a quick surface recombination (section 3.2.1). The initial concentration of traps is 0: $N_{trap}(t = 0\ s) = 0$.

The comparison between the experimental results and the simulations are presented on figure 4.3 (a). Thanks to the evolution of $\nu_{crea}(c_m)$ and $\nu_{sat}\left(\frac{N_{trap}}{N_{LI}(x)}\right)$ presented in figure 4.1, the simulations reproduce quantitatively the experimental evolution of the D retention with the incident D flux.

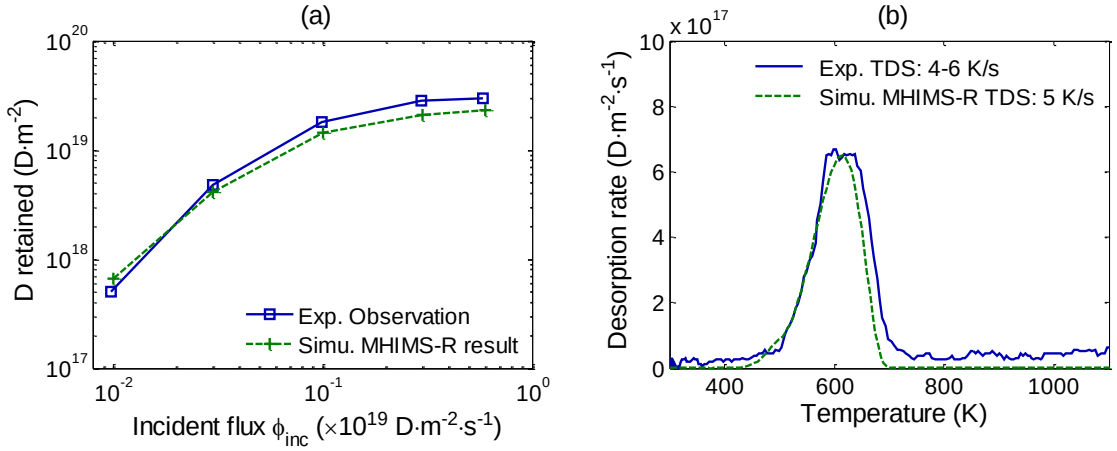

Figure 4.3. (a) Evolution of the D retention with the incident flux, comparison between experimental results and simulations.

(b) TDS spectrum for the case ϕ_{inc}=10^{18} D·m^{-2}·s^{-1}. The fluence is 10^{21} D·m^{-2} and the ions energy is 500 eV/D.

The TDS spectrum for the point obtained after an implantation with a flux of 10^{18} D·m^{-2}·s^{-1} is compared to the experimental one on figure 4.3 (b). As reported in section 2.3.3.i, only one peak is observed around 600 K. The simulated TDS spectrum also shows one peak. The shape and the position of the peak as well as its intensity are well reproduced by the simulation. The values of the detrapping energies used in these simulations to reproduce the TDS spectrum are discussed below.

Comparison between DFT calculated detrapping energies and MRE simulations:

Since it seems that oxygen plays a role in the D retention, to reproduced the TDS spectrum on figure 4.3 (b), we started from the detrapping energy distribution of VOH_i given by the DFT calculations of Kong et al. [114]. The detrapping energies are then slightly modified to reproduce the experimental TDS spectrum.

In the simulations, it has been considered that a trap can be filled with maximum 6 HIs ($l_m = 6$) and the final detrapping energy distribution is from the filling level 1 to the filling level 6: 1.5 eV, 1.13 eV, 1.10 eV, 1.05 eV, 0.60 eV and 0.47 eV. They are compared on figure 4.4 to the detrapping energies obtained from the DFT calculations by Fernandez et al. [72] for H trapped in VH_i and the ones obtained from the DFT calculations by Kong et al. [114] for H trapped in VH_i, VOH_i and VCH_i.

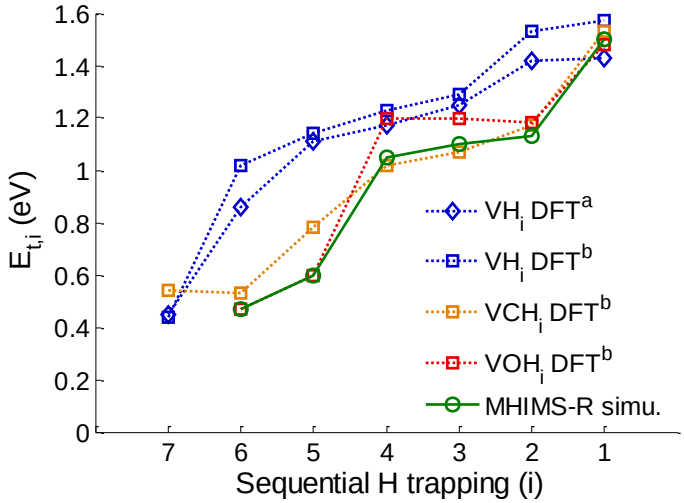

Figure 4.4. Detrapping energies as a function of the number of HIs trapped inside the trap. The detrapping energies used in the simulation are compared to detrapping energies calculated by DFT for H in VH, VOH and VCH. [a] **[72]**, [b] **[114]**.

As it can be seen on figure 4.4, the detrapping energies used in the MHIMS-R simulations are in good agreement with the detrapping obtained from the DFT calculations especially for VOH_i and VCH_i: we do not change too much the detrapping energies in order to reproduce well the experimental TDS spectrum which seems to confirm that the impurities have a strong impact on the HIs trapping and on the trap creation processes as it is suggested by the SIMS depth profiles. This interpretation is strengthened by the fact that the formation energies of VOH_i and VCH_i is very low (0.45 eV for $VOH_{1\leq i\leq 4}$) compared to the formation energies of VH_i as shown by DFT calculations by Kong et al. [114].

It is important to note that, in the simulations, the desorption peak simulated in figure 4.3 (b) is only related to the detrapping from traps filled with 1 HIs. Indeed, in order to get a relevant simulation, the baking step that follows the implantation is simulated: in the simulations, the temperature of the simulated W is kept at 400 K for 1.5 hours after the D implantation. Because of this baking step, HIs has been desorbed from the traps and only the traps filled with 1 HIs remains. The case of the simulation with an incident flux of 10^{18} $D{\cdot}m^{-2}{\cdot}s^{-1}$ is described in a bit further details.

Study of the baking in the case of an incident flux of 10^{18} $D{\cdot}m^{-2}{\cdot}s^{-1}$:

Figure 4.5 shows the evolution of the quantity retained in the traps filled with i D (integrated on all the simulated space) with $1 \leq i \leq 4$. The overall retention corresponding to all trapped and mobile particles (integrated in all the simulated space) is also shown. The time $t = 0$ s corresponds to the starting of the baking step and the time axis is in logarithmic scale in order to see the transient evolution at the beginning of the baking step.

At the beginning of the baking step, the main existing filling level is the filling level i = 4 even if the maximum number of HIs that can be trapped in the traps is $l_m = 6$. At the end of the baking step at 400 K for 1.5 hours, quasi only the filling level $i = 1$ remains.
To understand why the amount of traps filled with 5 and 6 D is low after the implantation and why the filling level 2 to 4 disappear during the baking step, the equilibrium ratio $R_{trap,i}(c_m, T)$ defined in Chapter 3 by equation 3.22 and equation 3.23 is a good tool. It is reminded that this equilibrium ratio gives the quantity of traps N_i as function of the total concentration of traps N_{trap} or simply: $N_i = R_{trap,i}(c_m, T) \cdot N_{trap}$. To do so, the mobile particles concentration first needs to be evaluated during the implantation and during the baking step.

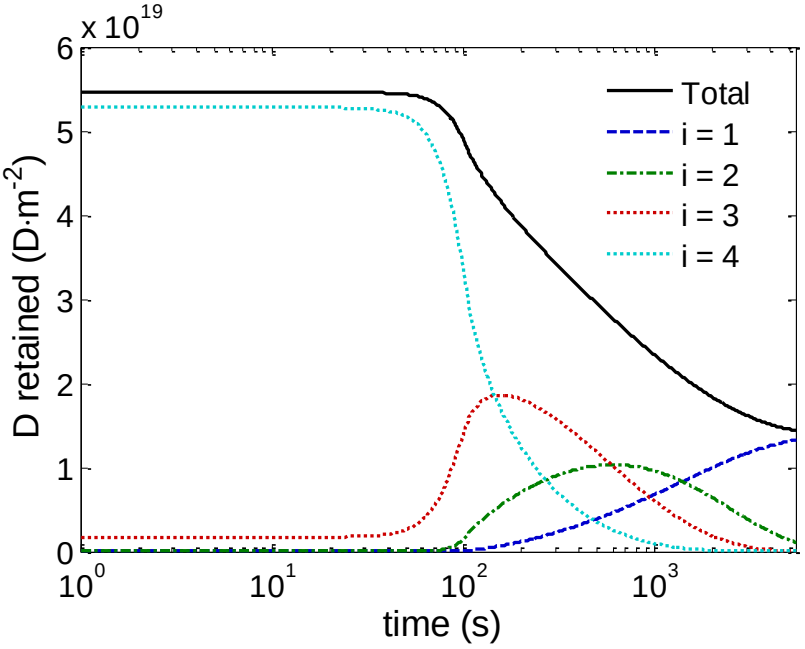

Figure 4.5. Evolution of the overall D retained (mobile + trapped) and evolution of the D retained in the traps filled with **i** D with $\mathbf{1 \leq i \leq 4}$ during a baking step where the temperature is 400 K for 1.5 h. The time t = 0 s corresponds to the starting of the baking step. The amount of mobile particles and the amount of D trapped in traps filled with 5 and 6 D are not shown because these quantities are too low to be seen.

In the simulation, during the implantation, the incident flux is 10^{18} D·m^{-2}·s^{-1} which corresponds to an implanted flux of 5×10^{17} D·m^{-2}·s^{-1} (reflection = 0.5). From equation 3.33, the maximum concentration of mobile particles equivalent to this implanted flux is $c_m^{MAX} \approx 9.6 \times 10^{-10}$ at. fr.. The equilibrium ratios for all the filling levels during the implantation phase are reported in table 4.1.
After the implantation, a period of 1000 s is simulated without implantation and without any temperature change: the temperature is 300 K. To calculate the equilibrium ratios during this period, a mean value of c_m^{MAX} given by the simulation in this period is taken. The equilibrium ratios for all the filling levels are also reported in table 4.1
After the storage period (no implantation, T = 300 K), the baking step at 400 K for 1.5 hours begins in the simulation. The value of c_m^{MAX} given by the simulation at the beginning of the baking step (t = 0 s), after 1000 s and at the end of the baking step (t = 5000 s) are used to estimate the equilibrium ratios for the different filling levels. The equilibrium ratios for all the filling levels at these three times during the baking step are reported in table 4.1.

	Implantation T = 300 K	Storage before baking T = 300 K	Baking t = 0 s T = 400 K	Baking t = 1000 s T = 400 K	Baking t = 5000 s T = 400 K
$\mathbf{c_m^{MAX}}$ (at.fr.)	9.6×10^{-10}	$\approx 1 \times 10^{-12}$	3×10^{-10}	2×10^{-11}	3×10^{-12}
Equilibrium ratio - $\mathbf{R_{trap,i}(c_m^{MAX}, T)}$					
i = 0	1×10^{-28}	3×10^{-16}	1×10^{-10}	2×10^{-6}	9×10^{-5}
i = 1	2×10^{-16}	3×10^{-7}	3×10^{-4}	0.17	0.83
i = 2	1×10^{-10}	2×10^{-4}	0.01	0.38	0.15
i = 3	3×10^{-5}	0.03	0.2	0.36	0.01
i = 4	0.999	0.96	0.8	0.08	2×10^{-4}
i = 5	9×10^{-4}	7×10^{-7}	6×10^{-6}	4×10^{-8}	7×10^{-12}
i = 6	5×10^{-9}	3×10^{-15}	1×10^{-12}	4×10^{-16}	7×10^{-21}

Table 4.1. Values of the equilibrium ratios $R_{trap,i}(c_m^{MAX},T)$ for the different filling levels during the implantation at 300 K with an implanted flux of 5×10^{17} D·m^{-2}·s^{-1}, the resting period at 300 K without implantation and during the baking step at 400 K. The values of the concentration of mobile particles used are reported in the first line. The main filling levels ($R_{trap,i}>0.1$) are surrounded by red line.

As it can be seen from table 4.1, the equilibrium ratio of the filling level 0 (empty trap) is very low in all the different steps: this means that almost all the traps contain at least 1 HI: the number of HIs in the traps during the different steps is discussed below.

During the implantation, it can be seen that the filling ratio i = 4 is dominant because the detrapping energies of the filling ratio 5 and 6 are too low to retain efficiently the HIs at 300 K with this flux. In addition, the filling level 4 is the highest filling level which has a high enough detrapping energy to retain HIs at 300 K: it dominates during the implantation.

During the storage period, no implantation exists to maintain the mobile particles concentration so the concentration drops around 10^{-12} at.fr. after ~ 1000 s. Thus, the equilibrium ratio of the filling level 4 decreases by few % and the one of filling level 3 increases by the same amount: some detrapping from traps filled with 4 HIs stands during this period. A part of the retained particles are desorbed from the simulated W transforming traps filled with 4 HIs in traps filled with 3 HIs.

During the baking step at 400 K, the filling level which has the highest equilibrium ratio shifts from the filling level 4 at the beginning of the baking to the filling levels 3 and 2 after 1000 s and finally to the filling level 1 at the end of the baking. At the beginning of the baking step, the temperature increases inducing a detrapping of HIs from the filling level 4. Thus, the equilibrium ratio of the filling level 4 decreases, increasing the equilibrium ratio of the filling level 3. This detrapping from the filling level 4 induces temporally an increase of the concentration of mobile

particles because the detrapped particles are not instantaneously desorbed from the simulated material. Thus, the drop of the filling ratio is not instantaneous: the trapping frequency $\nu_m(T) \cdot c_m$ increases at the beginning. After this initial increase, the concentration of mobile particles will tend to zero (the incident flux is 0). After 1.5 h the equilibrium ratio of the filling levels 4 and 3 are negligible and the filling level 1 dominates.
Finally, the desorption during the baking step removes a part of the HIs that have been trapped during the implantation and only the filling level 1 remains in the simulation: only one peak is observed related to the desorption of HIs detrapped from the filling level 1. Thus, only the detrapping energy of the filling level 1 is accurately determined by the simulation of the TDS spectrum and the detrapping energies related to the higher filling levels can only be indicative: their detrapping energies are below 1.15 eV. More relevant interpretation would require simulations of other experimental results without baking steps (section 4.1.2.ii).

Study of the D simulated depth profiles:

In section 2.3.3.i, it is explained that the experimental depth profiles reported by Alimov et al. [89] and Roszell et al. [45] exhibit three different zones where the HIs are trapped in the SCW:

- The near surface layer up to 200 nm where the concentration of HIs can reach up to 1-10 at.%
- The sub-surface layer extended to 1-2 µm where the concentration of HIs can reach 0.1-1 at.%
- The bulk zone deeper than 2 µm where the concentration of HIs can reach 0.01 – 0.001 at.%.

In another hand, the qualitative SIMS depth profiles show a peak of the retention in the first 10-20 nm and then an approximatively flat HIs concentration up to 60 nm.
The D depth profiles obtained after the five simulations of 500eV/D implantations with five different incident fluxes (from 10^{17} D·m^{-2}·s^{-1} to 6×10^{18} D·m^{-2}·s^{-1}) at a fluence of 10^{21} D·m^{-2} are reported in figure 4.6. These depth profiles are the one obtained in our simulations after the baking step and before that the TDS starts. The insert is a zoom of the D depth profiles between the surface and the 60 nm depth for the three highest fluxes.

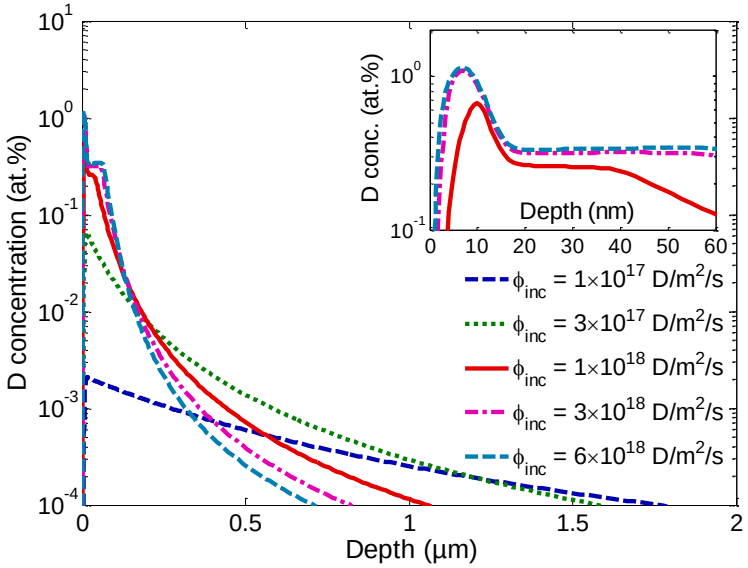

Figure 4.6. D Depth profiles obtained for the five simulations of 500 eV/D implantations with five different incident fluxes (from 10^{17} D·m^{-2}·s^{-1} to 6×10^{18} D·m^{-2}·s^{-1}) at 300 K. The fluence is 10^{21} D·m^{-2}. The depth profiles are the one obtained after the baking step and before the TDS starts.

For the lowest fluxes (10^{17} D·m^{-2}·s^{-1} and 3×10^{17} D·m^{-2}·s^{-1}), the simulated depth profiles exhibit a concentration of D which is maximum below the surface and decreases quasi linearly toward the bulk. The three zones observed experimentally are not presents in these two depth profiles because the fluxes are too low so the trap creation process is not efficient. Indeed, the fluxes for these two simulations are 10^{17} D·m^{-2}·s^{-1} and 3×10^{17} D·m^{-2}·s^{-1}. The value of c_m^{MAX} calculated using equation 3.33 is $\approx 9 \times 10^{-11}$ at.fr. for an incident flux of 10^{17} D·m^{-2}·s^{-1} and $\approx 3 \times 10^{-10}$ at.fr. for an incident flux of 3×10^{17} D·m^{-2}·s^{-1}. Reporting these values on figure 4.1 (a), one can see that the regimes of trap creation for these fluxes is the weak/intermediate regimes. Moreover, for this low fluence, there is not enough time to saturate the trap concentration: the trap profile and the D profile do not have the same shape as the concentration $N_{LI}(x)$ as it is for the simulations with the three others higher fluxes.

For the highest fluxes, three zones can be distinguished from the depth profiles:

- Zone 1: a high D concentration of ~ 1 at.% in the first 10 nm,
- Zone 2: a D concentration of ~ 0.3 at.% in a region that extended up to ~100 nm
- Zone 3: a decrease of the D concentration from 100 nm to deeper in the bulk.

Thanks to the shape of $N_{LI}(x)$ used in these simulations (figure 4.2), the first two zones described here (insert of figure 4.6) reproduce quite well the evolution that is observed in the SIMS D depth profiles [27, 42, 43, 86]. From the SIMS analysis, Poon et al. [42] explain that the peak at the surface is related to the implantation of O and C during the D irradiation (due to their presence in the background gas of the implantation chamber). They explain that the impacting 500 eV/D ions can transfer up to 200 eV to O and 250 eV to C. According to SRIM® simulations with a displacement energy of 90 eV, with such energy, O and C ions can create 0.4 vacancies per O and 0.3 vacancies per C [42]. The zone where these vacancies are created is zone 1. So, the vacancies created in zone 1 are classic displacement damaged due to elastic collision between O/C ions and W atoms. The amount of these created vacancies is so mainly driven by the fluxes of O and C

which depend on the amount of O and C in the background gas during the implantation. Thus, it is not directly driven by the D flux as suggested by the trap creation model. However, since the flux of C and O is not so easy to determine and since the amount of created trap in this area is quickly saturated (see the discussion below), it is not worth to add complexity to the current model. In addition, the main D retention is related to zone 2 and zone 3 that extend much deeper than zone 1 and the trap creation in these two zones is driven by the concentration of mobile D (⇔ D flux) as suggested by the trap creation model.

In zone 1 and zone 2, the trap concentration is (almost) saturated. To illustrate this saturation, figure 4.7 shows the evolution of the maximum of the trap concentration (in the zone 1) during the implantation phase for the simulation with the incident flux 6×10^{18} D·m^{-2}·s^{-1}. The fluence being 10^{21} D·m^{-2}, the implantation lasts for 167 s.

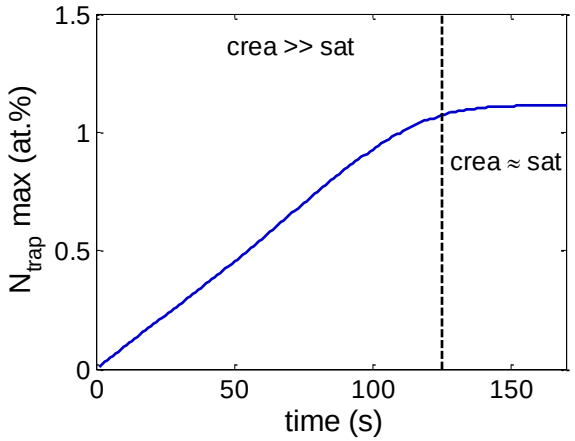

Figure 4.7. Evolution with time of the maximum trap concentration in the 10 nm zone during the implantation phase at 300 K. For this simulation, the incident flux is 6×10^{18} D·m^{-2}·s^{-1} and the fluence is 10^{21} D·m^{-2} (the implantation last 167 s).

In this figure, two regimes can be observed for the growth of the maximal concentration of traps:

- For time < 125 s, the concentration of traps increases linearly.,
- For time > 125 s, the concentration of traps saturates.

To explain these two regimes, the space distribution of the creation rate $\left(\frac{\partial N_{trap}}{\partial t}\right)_{crea} = \nu_{crea}(c_m) \cdot c_m$ and the saturation rate $\left(\frac{\partial N_{trap}}{\partial t}\right)_{sat} = \nu_{sat}\left(\frac{N_{trap}}{N_{LI}(x)}\right) \cdot N_{trap}$ of equation 4.1 can be compared for two times in these two regimes. This comparison is done on figure 4.8 for t = 25 s (a) and the t = 167 s (b).

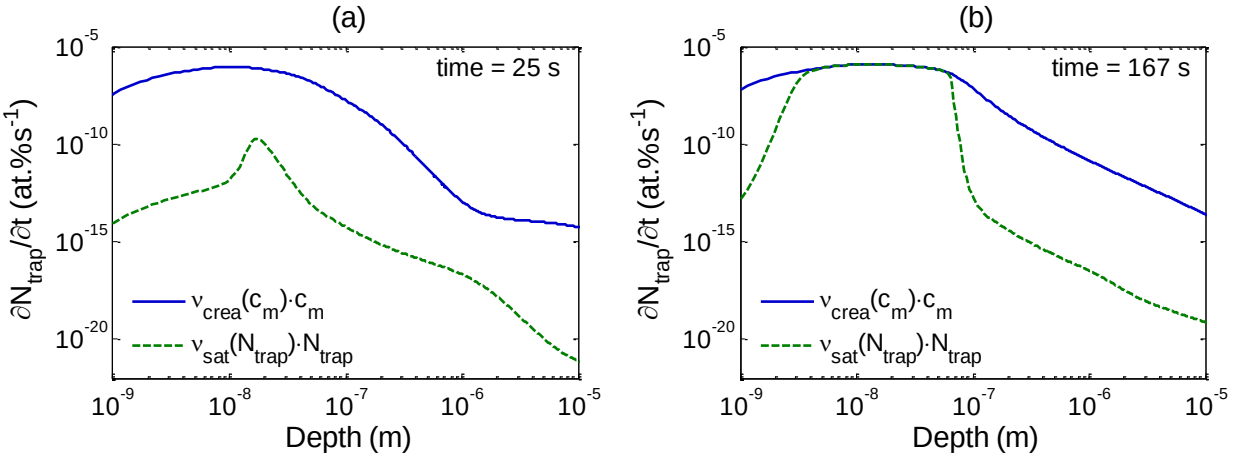

Figure 4.8. Depth distribution of $\nu_{crea}(c_m)\cdot c_m$ and $\nu_{sat}(N_{trap}/N_{LI}(x))\cdot N_{trap}$ at two different times. (a) at t = 25 s in the linear growth regime and (b) at t = 167 s in the saturated regime. The simulated incident flux is 6×10^{18} D·m^{-2}·s^{-1}and the fluence is 10^{21} D·m^{-2}.

In the linear growth regime, at time = 25 s (figure 4.8 (a)):

$$\nu_{crea}(c_m)\cdot c_m \gg \nu_{sat}\left(\frac{N_{trap}}{N_{LI}(x)}\right)\cdot N_{trap}$$

Thus, equation 4.1 can be simplified as followed:

$$\frac{\partial N_{trap}}{\partial t} \approx \nu_{crea}(c_m)\cdot c_m$$

As explained in section 3.3.1 by figure 3.3, the equilibrium concentration of mobile particles c_m^{MAX} is quickly reached for flux around 10^{18} D·m^{-2}·s^{-1}. Thus, the quantity $\nu_{crea}(c_m)\cdot c_m$ can be assumed constant.

It follows that the concentration of traps evolves linearly with time as:

$N_{trap}(t) \approx \nu_{crea}(c_m)\cdot c_m \cdot t$ explaining the first linear regime observed in figure 4.7.

In the saturated regime, at time = 167 s (figure 4.8 (b)):

$$\nu_{crea}(c_m)\cdot c_m \approx \nu_{sat}\left(\frac{N_{trap}}{N_{LI}(x)}\right)\cdot N_{trap}$$

Thus, equation 4.1 is locally at the equilibrium $\frac{\partial N_{trap}}{\partial t} = 0$. Then, the concentration of trap saturates to the value:

$N_{trap} = \frac{\nu_{crea}(c_m)}{\nu_{sat}\left(\frac{N_{trap}}{N_{LI}(x)}\right)}\cdot c_m$, explaining the second saturated regime in figure 4.7.

According to figure 4.8 (b), the saturated zone is between 2 nm and ~100 nm at the end of the simulation. This explains why the zone 1 and the zone 2 of the simulated depth profile are saturated.

Between the surface and 2 nm, the trap concentration is not saturated because the boundary conditions impose that $c_m(x = 0) = 0$: the creation in this zone is not as efficient as the creation at the ion implantation depth ($R_p = 7$ nm): the regime of creation in this zone is still in the linear regime.

Beyond 100 nm, in the zone 3, $\nu_{crea}(c_m)\cdot c_m \gg \nu_{sat}\left(\frac{N_{trap}}{N_{LI}(x)}\right)\cdot N_{trap}$. If the implantation had continued, the trap concentration would have increased linearly up to saturation. In addition, the mobile particles diffusing deeper and deeper would have increased the local concentration of mobile particles propagating the saturated zone 2 deeper and deeper toward bulk.

Consequently, if the distribution of the experimental depth profile reported by Alimov et al. [89] and Roszell et al. [45] are compared to the distribution obtained in the simulations, it can be concluded that:

- The zone 1 observed in these simulations corresponds to the near surface zone.
- The zone 2, for highest fluence would correspond to the sub surface (up to 1-2 µm).
- The zone 3 corresponds to the bulk zone.

However, in the current model, the distribution of light impurities, that drives the saturation, has only two zones (figure 4.2). If one wants to simulate very high fluence, the zone 2 will continue to extend in the bulk creating traps deeper and deeper as the mobile particles diffuse. Experimentally, it seems that at 300 K, the sub-surface stops around 1-2 µm. It means that the trap creation process is less efficient at these depths (ν_{crea} is lower) or that the saturation level is lower ($N_{LI}(x)$ drops around 1-2 µm). In the current simulations, since the migration of HIs does not extend deeper than 1 µm, it does not matter if such effects are taken into account or not. However, if higher fluences are simulated, these effects should be taken into account.

Summary of the low fluence (10^{21} D·m^{-2}) experiment in SCW:

These simulations show that, for a fluence of 10^{21} D·m^{-2}, the HI retention in SCW samples annealed at 1775 K seems to be limited by the trap creation process and the propagation of trap creation toward the bulk:

- The simulations reproduce quantitatively the experimental increase of the D retention with the flux at constant fluence.
- As suggested by the thermo-statistic model, the trap creation is weakened for concentration of mobile HIs below ~5×10^{-10} at.fr. which is equivalent to an incident flux of ~5×10^{17} D·m^{-2}s^{-1}.
- The experimental TDS spectrum obtained after the 500 eV/D ions implantation at 300 K with an incident flux of 10^{18} D·m^{-2}·s^{-1} is well reproduced. The detrapping energies used to simulate this TDS spectrum seems to be related to VOH_i and VCH_i.
- However, only the detrapping energy of the filling level 1 is accurately determined because of the baking step at 400 K that follows the implantation: during the baking step, the HIs trapped in filling level with a detrapping energy below ~ 1.15 eV are desorbed. To address the detrapping energies of the lower filling levels, simulations of SCW experiments without baking step needs to be done.
- Then, the study of the simulated D depth profiles allows defining three zones as in the experimental D depth profiles.

Two limits of the current creation model are pointed out:

- First, the fact that the first zone of trap creation up to 20 nm may related to collision between O and C ions that created traps. The creation of traps in this zone should be proportional to the incident fluxes of O and C ions. However, these fluxes are not easy to determine and depend on the amount of these light impurities in the background gas. So, it depends indirectly on the incident D flux. In addition, the D retained in this zone is not the major part of the D retained in the simulated materials (<1/4 in these simulations).
- Then, the space distributions of the different creation and saturation rates show that the trap creation zone can be extended in the bulk as the mobile particles diffuse deeper and deeper. This disagrees with the experimental depth profiles: the trap creation is somehow reduced for depth higher than 1-2 µm. This effect does not affect these simulations in which the maximum depth reached by D is below 1 µm. However, if higher fluences are

simulated, it is important to take the experimental observations into account and set a decrease of the trap creation efficiency in the simulations.

ii. Experiments at higher fluences

In this section, we try to reproduce two experimental TDS measurements obtained by Quastel et al. [86] (figure 2.7 (b)) and Roszell et al. [45]. These two TDS measurements have been obtained after the implantation of 500 eV/D ions in SCW with fluences higher than 10^{23} D·m^{-2}. In both case, the SCW samples come from the same supplier and they are annealed at temperature higher than 1500 K. In the case of the measurement from Roszell et al. [45], the NRA depth profile is also available.

Improvement of the trap creation model:

In the simulations of these experimental measurements, the evolution of $\nu_{crea}(c_m)$ and $\nu_{sat}(\frac{N_{trap}}{N_{LI}(x)})$ are the same as the ones presented on figure 4.1 (the value of c_{crit}^{HI} is 5×10^{-10} at.fr.). However, as discussed in section 4.1.2.i, the trap creation description needs to be slightly changed. Without any change, the simulated sub-surface zone in the D depth profile simulated would continue to extend in the bulk as the mobile particles diffuse deeper (as the fluence grows). Unlike the experimental depth profiles, this zone could reach higher depth than 1 – 2 µm. In that respects, it has been decided to reduce the efficiency of the trap creation process at depth higher than 1 – 2 µm. In order to do that, the distribution $N_{LI}(x)$ has been change at this depth as shown on figure 4.9. The distribution in the first 60 nm is the same as the one shown in figure 4.2.

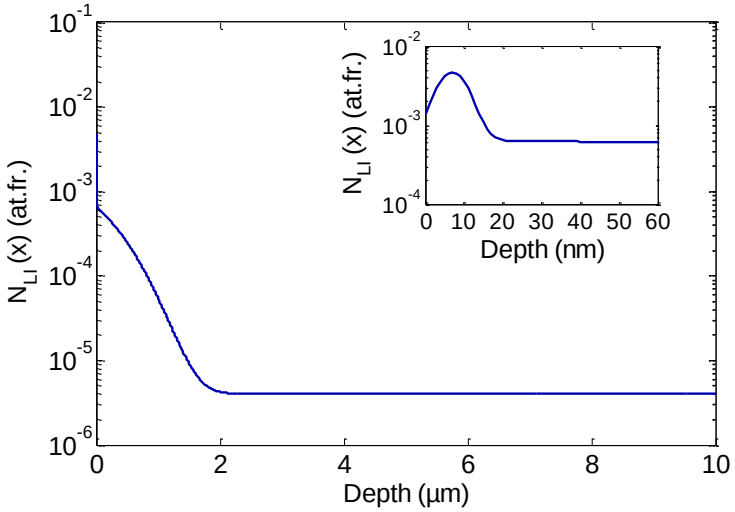

Figure 4.9. Distribution $N_{LI}(x)$ used in the simulation at high fluence to decrease the trap creation efficiency for depth higher than 1 – 2 µm. The distribution in the first 60 nm does not change compare to the figure 4.2.

It is reported in section 2.3.3.i that the concentration of C and O recorded by SIMS in the depth above 20 nm (deeper than the peak of C and O) up to 60 nm – 100 nm increases after the implantation of D compared to the concentration before the implantation [27, 42]. The authors suggest that this increase is due to an irradiation-enhanced diffusion of the O and C impurities deeper than the implantation zone (which corresponds to the peak of C and O around 10 nm) [42]. The depth where these impurities stop diffusing is not seen by SIMS depth profile since the

technic probe only up to ~ 100 nm. Thus, the reduction of the trap creation process at 1 – 2 µm may be explained by assuming that the C and O diffusion stops at 1-2 µm at the end of the D irradiation. In this simple approach, the distribution of light impurities $N_{LI}(x)$ is set as an ad-hoc distribution in the code. To be relevant with a diffusion limited distribution, an erfc function, which is the analytical solution of a pure diffusion equation [82], is chosen to shape the distribution $N_{LI}(x)$. Thus, the complete distribution can be divided into three parts as:

$$N_{LI}(x) = N_{LI,1} + N_{LI,2} \cdot \mathrm{erfc}\left(\frac{x}{X_{diff(T)}}\right) + N_{LI,3} \cdot f(x) \quad (4.2)$$

The first term of the right hand side of equation (4.2) corresponds to the native impurities content.

The second term of the right hand side corresponds to the diffusion of the light impurities to a depth up to x_{diff} (m). Since the diffusion of the impurities depends on the temperature, x_{diff} depends on the temperature. This dependence will be discussed in the section 4.1.2.iii. For both simulations of Quastel et al. [86] and Roszell et al. [45] measurements, the value of $x_{diff} = 0.8$ µm is taken to reproduce the NRA depth profile obtained by Roszell et al. [45] (see below).

The third term of the right hand side corresponds to the first zone observed on the SIMS depth profile with a peak of the D, C and O concentration in the first 20 nm.

In equation 4.2, the quantities $N_{LI,1}$, $N_{LI,2}$ and $N_{LI,3}$ set the intensity of the different part of the distribution $N_{LI}(x)$ shown in figure 4.9. $N_{LI,2}$ and $N_{LI,3}$ are function of the amount of O and C inserted during the D implantation: they depend on the O and C amounts in the background gas. $N_{LI,1}$ depends on the native concentration of O/C in the samples before the implantation: it depends on the initial concentration of O/C in the sample and on the pre-treatment experienced by the sample.

Simulation of implantation at high fluence (10^{23} D·m^{-2}): Quastel et al. measurements:

The TDS measurement by Quastel et al. [86] have been obtained after implanting 500 eV/D ions into a SCW sample with a flux of 10^{20} D·m^{-2}·s^{-1} and a fluence of 10^{23} D·m^{-2} at 300 K. Prior to the irradiation, the SCW sample experienced the same mechanical and electrochemical polishing steps as in the case of Poon et al. [26]. Between the different polishing steps, the sample is annealed around 1750 - 1800 K (between 5 and 15 min). The sample is finally annealed at 1750 - 1800 K before the implantation. Based on the observations of Manhard et al. [30] on samples annealed at 1700 K (see section 2.2.1), intrinsic dislocations in such annealed sample can be neglected. In this paper by Quastel et al. [86], the impacts of many experimental details (used of LN_2 cold finger, baking steps, storage times) on the D retention are investigated. In this section, the experimental TDS spectrum that we want to simulated has been obtained using the LN_2 cold finger during the implantation. In addition, the storage time between the implantation and the TDS measurement is 0.37 h = 1332 s. Therefore, all the experimental steps from the implantation to the TDS measurement have been done in-situ (the sample does not experience air exposure after the implantation). Finally, no baking steps have been done for the experiment we intend to simulate: thus, the lower trapping level may be accessible. The heating ramp during the TDS is 5.1 K/s. Thus, the simulation is divided into 3 phases as in the Quastel et al.'s experiments:

- The implantation at 300 K ($\phi_{inc} \neq 0$) for a fluence of 10^{23} D·m^{-2}
- A storage time at 300 K for 1332 s ($\phi_{inc} = 0$)
- The TDS between 300 K and 1300 K with a heating ramp of 5.1 K/s.

As for the previous simulations, the code MHIMS-R is used and the boundary condition use is the one considering a quick surface recombination (section 3.2.1). The initial concentration of traps is 0: $N_{trap}(t = 0\ s) = 0$.

Figure 4.10 (a) shows the comparison between the experimental and the simulated TDS spectrum. The simulated TDS spectrum agrees well with the experimental spectrum: the two peak around 400 K and around 600 K are well reproduced. In the simulation, the trap considered has a maximum filling level of 6. The distribution of the detrapping energies for this trap is shown on figure 4.10 (b). This distribution is compared to the detrapping energies extracted from DFT calculations [72, 114] for VH_i, VOH_i and VCH_i. These DFT detrapping energies are obtained by summing the binding energies with the migration energies (0.2 eV) far from the trap. However, Fernandez et al. [72] shows that the path to be detrapped from the vacancy can be a bit more complex. They calculated the energy barriers for HIs to go from the vacancy to the first neighbor TIS and these energies barriers are reported on figure 4.10 (b) as VH_i (v→s).

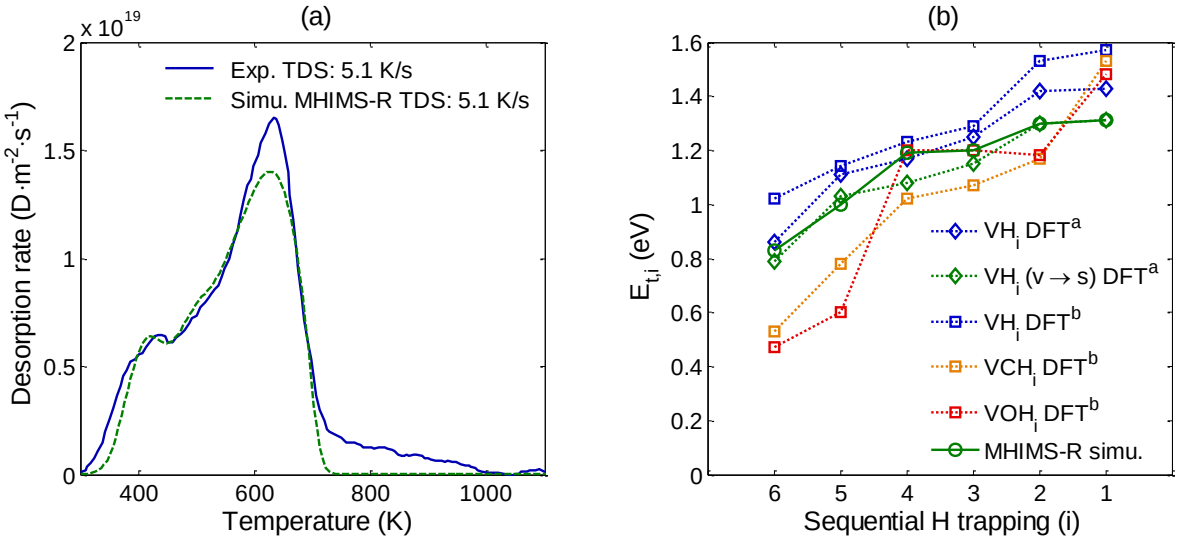

Figure 4.10. (a) Experimental (blue solid line) and simulated (green dashed line) TDS spectrum obtained after implantation of 500 eV/D ions in SCW with an incident flux of 10^{20} D·m^{-2}·s^{-1} and a fluence of 10^{23} D·m^{-2}. The heating rate is 5.1 K/s.

(b) Detrapping energies as a function of the number of HIs in the trap. The dashed lines are the detrapping energies extracted from DFT calculations for VH_i, VOH_i and VCH_i. The VH_i (v→s) is the energy barrier to go from the vacancy to the first neighbor TIS. The green solid line is the distribution used in the MRE simulations. [a] **[72]**, [b] **[114]**.

No baking have been done in the experiments so no baking is simulated which guarantees a better accuracy on all the detrapping energies used in the simulations especially for the higher filling level (low detrapping energy). A good agreement can be seen between the distribution of the detrapping energies among the filling levels used in the simulation and the distribution extracted from the DFT calculations. The agreement is particularly good for the distribution VH_i (v→s) which means that the traps involved in the D retention in this experiment seems to be vacancies.

The distribution of the detrapping energies used in this simulation is significantly different to the distribution used in the simulation of Poon et al. experiment at low fluence (section 4.1.2.i). On the simulation of Poon et al. experiment at low fluence (10^{21} D·m^{-2}), the

detrapping energy of the filling level 1 is 1.5 eV and it is accurately deduced from the simulation of the TDS spectrum. In the simulation of Quastel et al. experiment at higher fluence (10^{23} $D \cdot m^{-2}$), the detrapping energy of the filling level 1 is 1.31 eV. This indicates that the traps in the simulation of Poon et al. experiment at low fluence (10^{21} $D \cdot m^{-2}$) are not strictly the same as the traps in the simulation of Quastel et al. experiment a high fluence (10^{23} $D \cdot m^{-2}$). However, in both cases, it seems that the traps that are created are vacancy like defects (figure 4.4 and figure 4.10 (b)). The main difference between these two cases is that in the simulation at low fluence (section 4.1.2.i), the zone where traps concentration saturate does not exceed 100 nm. In the other hand, in the simulation at high fluence, the saturated zone is extended up to 1-2 µm with a concentration around 1 at.% . It seems that the vacancies initially created have been changed due to the high trap concentration in a thick layer. This mutation is for the moment not very well understood but some interpretation could be done such as:

- the trap – trap interaction due to the large amount of traps in a 1 µm thick layer,
- the stresses induced by the trap creation,
- the growth of some V_nH_i cluster favored by the large amount of vacancies.

For this last interpretation, Li et al. [149] performed molecular statics simulations, using the Li et al. W – H interatomic potential [123]. They calculated the binding energy of a vacancy, a self-interstitial atom (SIA) and H with a V_nH_i vacancy clusters.

They show that for a H/V ratio below 6, the binding energy of a vacancy with the V_nH_i cluster is less than the binding energy of a SIA with the same cluster (both are positive which means that it is energetically favorable): the V_nH_i cluster cannot growth. Above a H/V ratio of 6, this is the opposite: the binding energy of a vacancy with the V_nH_i cluster is the highest: the V_nH_i tends to grow if there are other vacancy available.

Their calculations show also that if the concentration of mobile H is low, the maximum H/V ratio is 5 because above, the binding energies of H with the V_nH_i cluster are negative. In the opposite, if the mobile concentration of H is high enough, the binding energies of H with the V_nH_i clusters are positive up to a H/V ratio of 10. Thus, at low H mobile concentration (i.e. at low flux), the V_nH_i cluster cannot evolve while they can at higher H mobile concentration (i.e. at high flux). In addition, for the same H/V ratio, the binding energies of H with clusters of several vacancies are similar (though a bit lower) as the binding energies of H with only one vacancy.

In the TDS measurement by Poon et al. [26] simulated in section 4.1.2.i, the flux is 10^{18} $D \cdot m^{-2} \cdot s^{-1}$ which is 2 order of magnitude lower than the one simulated here (10^{20} $D \cdot m^{-2} s^{-1}$). Thus, in the experiment simulated here, the traps may be vacancy clusters that are formed thanks to the process described by Li et al. [149] and the fact that a large amount of traps are created in a thick layer to feed this process. This mutation induces a slight change in the detrapping energies compared to the initially formed VOH_i.

It is to note that the difference in the detrapping energies could also come from the experimental uncertainty of the temperature measurements. Indeed, if the distribution of detrapping energies presented in figure 4.10 is used to make the simulation of the experimental measurement of Poon et al., the evolution of the D retention with the incident fluence is still reproduced and a single peak is observed on the simulated TDS spectrum. The difference would be that this peak is at 550 K – 560 K instead of 600 K. If the accuracy of the temperature position is around 40 K, the change of the distribution of detrapping energies could then be explained.

In any case, in both experiment, it seems that the trap created is initially VOH_i that can evolve in other type of defects if the amount of traps created is high and if a lot of HIs are trap into them (high H/V ratio).

Simulation of at high fluence (10^{24} D·m^{-2}): Roszell et al. measurements:

The TDS measurement reported by Roszell et al. [45] have been obtained after implanting 500 eV/D ions into a SCW sample with a flux of 8×10^{18} D·m^{-2}·s^{-1} and a fluence of 10^{23} D·m^{-2} at 300 K. Prior to the irradiation, the SCW sample experienced the same mechanical and electrochemical polishing steps as in the case of Poon et al. [26]. Between the different polishing steps, the sample is annealed around 1700 K for 5 min. The sample is finally annealed at 1500 K before the implantation for 2 h. s previously said above (Simulation of Quastel et al. measurements), based on the observation of Manhard et al. [30] on samples annealed at 1700 K (see section 2.2.1), it can be safely assumed that there are no intrinsic dislocations in such annealed SCW. After the implantation, the TDS vacuum chamber was baked at 400 K for 2 h. After this baking step, the sample is cooled down to room temperature and the TDS starts then up to 1473 K at a heating rate of 4 K/s. On one sample, the D depth profile has been measured by NRA. Thus, both TDS spectrum and NRA depth profile are available for the same implantation conditions on the same type of sample. Following this procedure, the simulation is divided into 5 phases as for the simulation of the Poon et al.'s experiments:

- The implantation at 300 K ($\phi_{inc} \neq 0$) for a fluence of 10^{23} D·m^{-2}
- A first storage time at 300 K for ~ 1000 s ($\phi_{inc} = 0$)
- A baking step at 400 K for 2 hours
- A second storage time at 300 K for ~ 1000 s
- The TDS between 300 K and 1300 K with a heating ramp of 4 K/s.

As for the simulation of the experimental TDS spectrum of Quastel et al., the adjusted distribution of light impurities $N_{LI}(x)$ (figure 4.9) is taken. In order to test the accuracy of the detrapping energies obtained from the simulation of Quastel et al. (figure 4.10), it is decided to keep this distribution. Figure 4.11 (a) shows the comparison between the experimental TDS spectrum and the simulated one. On both simulation and experimental TDS spectra, a single peak can be seen at 620 K. The difference in the position of the two peaks is below the uncertainty of the temperature measurements. Due to the baking step, the peak around 400 K is not present as discussed in section 4.1.2.i.

Figure 4.11 (b) shows the comparison between the experimental NRA D depth profile and the simulated one before the TDS. The simulated D depth profile is obtained using $x_{diff} = 0.8$ µm and the distribution of light impurities described on figure 4.9. A good agreement is observed between the simulation and the experimental D depth profile up to 7 µm. The NRA technic cannot probe deeper and it does not have the space resolution to probe the near surface layer at the nm scale. Thus, the insert window, which shows the simulated D depth profile in the first 60 nm can only be qualitatively compared to the SIMS depth profile in the first 60 nm. As in the case of the simulation of Poon et al.'s experiments, the insert shows the same 2 different zones with a peak in the first 20 nm.

This agreement of the experimental and simulated D depth profile validates the use and the value of x_{diff} taken for these simulations which represent the migration depth of light impurities at the end of the implantation. Indeed, as it can be observed, the zone deeper than 1-2 µm contain D (at around 0.01 at.%). It means that for such high fluence, the D migrates deeper than 1-2 µm. Consequently, in the simulations, if no decrease of the distribution of light impurities $N_{LI}(x)$ is introduced (figure 4.9), the trap creation process would have continued to extend deeper and deeper: the NRA depth profile and the simulated depth profile would not have matched.

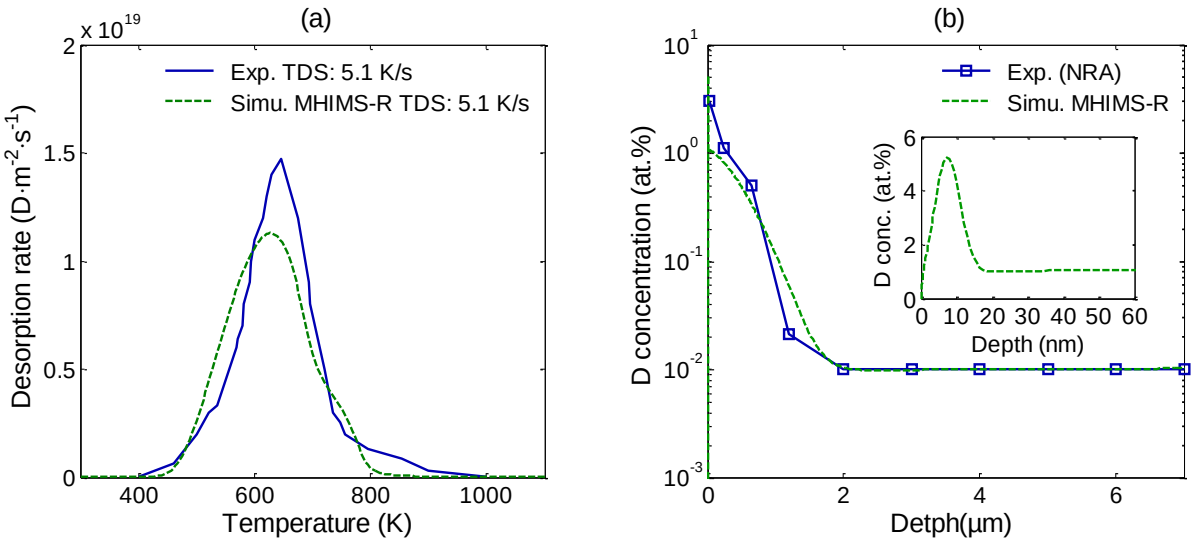

Figure 4.11. (a) Comparison between the experimental TDS measurements (blue solid line) and the simulated TDS spectrum (green dashed line).

(b) Comparison between the experimental NRA D depth profile (blue solid line and square) and the D depth profile before the TDS (green dashed line).

The flux is 8×10^{18} D·m^{-2}s^{-1}, the fluence is 10^{24} D·m^{-2}, the ion energy is 500 eV/D and the heating rate for the TDS is 4 K/s.

Summary:

To reproduce two experimental TDS spectra and a NRA D depth profile, for implantation of 500 eV/D at high fluence (> 10^{23} D·m^{-2}) at 300 K:

- The distribution of the detrapping energies has to be change. It indicates a possible mutation of traps (growth of blisters? Impact of trap-induced stresses?) or it could be due to the uncertainty on the temperature measurements during TDS experiment. This distribution is characteristic of a high number of traps created in a 1 µm thick layer and filled at the maximum filling level during the implantation.
- In any case, the distribution is still close to the distribution obtained by DFT for H trapped in vacancy like defects (VH_i, VOH_i, VCH_i, VH_i (v→s), V/H cluster).
- A change has to be done on the distribution of light impurities $N_{LI}(x)$ (figure 4.9). A decrease of $N_{LI}(x)$ is needed in order to reproduced the experimental D depth profile.
- This decrease could be explained by the stopping of the diffusion of O and C in the bulk at this depth at 300 K. To be relevant with a diffusion limited concentration, an erfc shape is used and the diffusion distance is $x_{diff} = 0.8$ µm in these simulations at 300 K.

iii. Experiment at different temperatures (fluence of 2×10^{24} D·m^{-2})

From the value of x_{diff}, a diffusion coefficient of O/C can be estimated. In order to obtain the activation energy of this diffusion coefficient x_{diff} has to be determined for different temperatures. Thus, in this section, we try to reproduce the experimental D depth profile in SCW for different implantation temperatures reported by Alimov et al. [47] (figure 2.10 (b)). In this experiment, SCW W sample electrochemically and mechanically polished are irradiated with 200 eV/D ions at an incident flux of 10^{21} D·m^{-2}·s^{-1} and a fluence of 2×10^{24} D·m^{-2}s^{-1}. The implantations temperatures are 303 K, 373 K, 413 K, 463 K and 513 K. The NRA measurements are done at room temperature so a cool down phase needs to be introduced in the simulations. No indication on the time to go back to room temperature is mentioned in the paper by Alimov et al. [47]. Then, it is chosen that the temperature decreases linearly with time from the implantation temperature to room temperature (300 K) in 300 s (for the highest temperature, this is equivalent to a decrease with a rate of ~ 1 K/s). Since the implantation is done at temperature ranging between 300 K and 533 K, it is estimated that the outgassing at 300 K that follows the cooldown does not have a strong impact on the depth profiles: no waiting phase at 300 K for a long time is simulated. For these simulations, the distribution of detrapping energies obtained from the simulation of the Quastel et al.'s experiment is used (figure 4.10 (b)).

As for the previous simulations, the code MHIMS-R is used and the boundary condition use is the one considering a quick surface recombination (section 3.2.1). The initial concentration of traps is 0: $N_{trap}(t = 0\ s) = 0$.

The NRA D depth profile reported by Roszell et al. [45] exhibits a zone where the D concentration is constant around 0.01 at.% between 2 and 7 µm (see figure 4.11). This zone is not observed on the NRA D depth profile reported by Alimov et al. [47] because it does not exist or because the D concentration is below 0.001 at.% (NRA detection limit) in this zone. The D concentration in this zone is given by the value of $N_{LI,1}$ in equation 4.2. So, it is decided to set a value of $N_{LI,1}$ to obtain a D concentration below the detection limit in this zone.

Figure 4.12 shows the comparison between the experimental and the simulated D depth profiles for the different implantation temperatures treated in the paper of Alimov et al. [47].

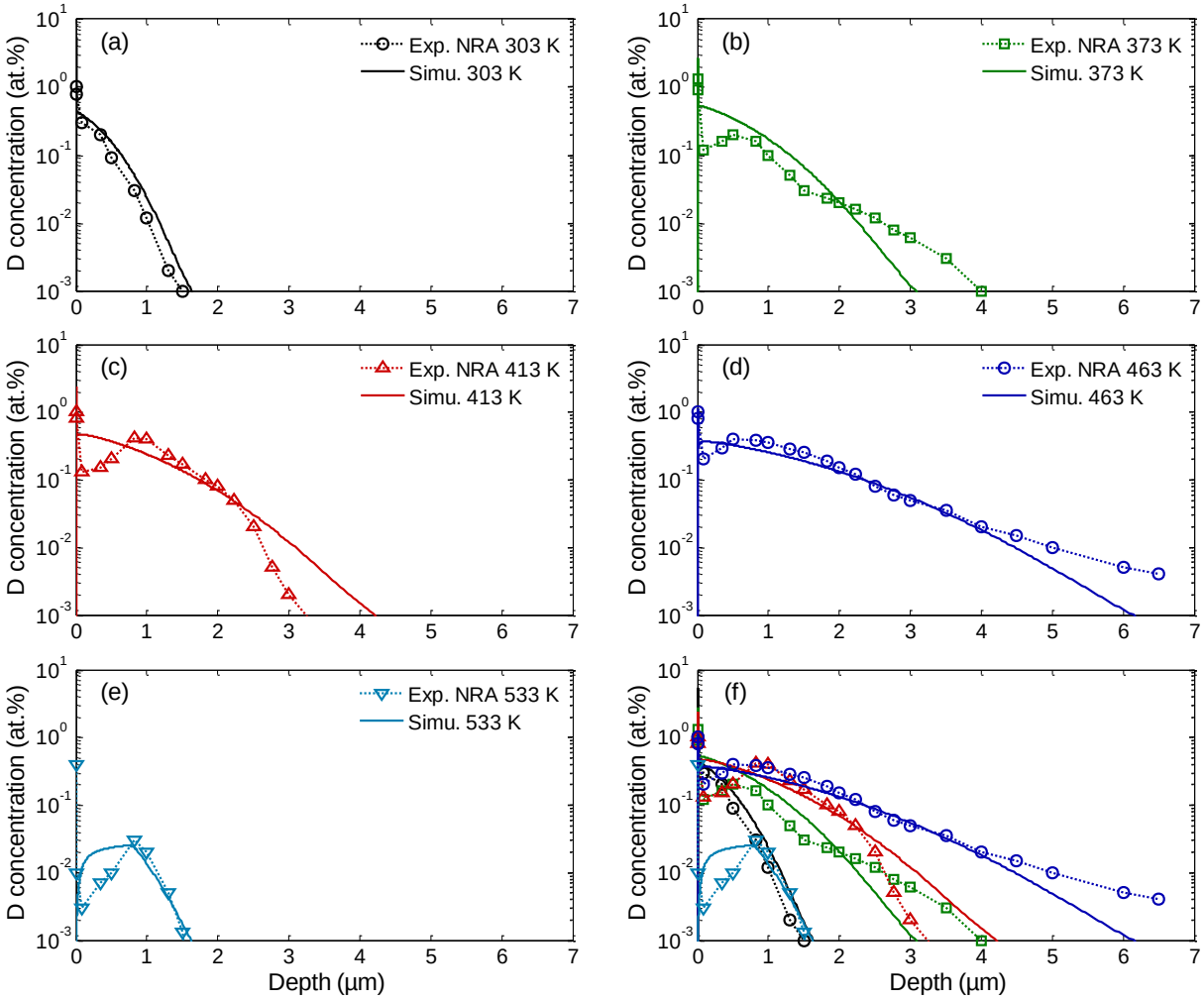

Figure 4.12. Experimental (NRA) and simulated D depth profiles obtained after implantation of 500 eV/D ions at an incident flux of 10^{21} D·m^{-2}·s^{-1} at a fluence of 2×10^{24} D·m^{-2} at different temperatures. (a) at 303 K, (b) at 373 K, (c) at 413 K, (d) at 463 K, (e) at 533 K and (f) for all temperatures.

On the experimental depth profiles, there is a peak in the near surface region (~ 200 nm) and there is a second peak in the D concentration observed in the sub surface layer around 1 µm for implantation temperature higher than 373 K. This peak is not reproduced in the simulation except for the simulation at 533 K but at a depth of 100 nm – 200 nm. To simulate this peak, Hu et al. [137] introduced in their MRE model a D diffusion enhanced by the presence of a stress field in the sub-surface region. In their interpretation, the stress field is generated by the implantation of hydrogen and by the trap creation in the near surface layer (first 200 nm).
In the simulation at 533 K, the peak around 1 µm is only due to an important outgassing of the near surface D during the cooling phase. Since we have to simulate a cooling phase that is probably not the true experimental one (no indication on the paper by Alimov et al.), the peak observed in the experimental D depth profile may be due only to the desorption during a cooling phase that is longer than the one simulated here. This point has not been studied in further

detailed for lack of time but it can be expected that the peak would be sharper for longer cooling phase.
Despite this peak, a pretty good agreement is observed between the experimental and simulated D depth profiles especially the falling tail of the D concentration deep in the bulk. To obtain this good agreement, only the critical concentration of HIs for trap creation c_{crit}^{HI} and the migration depth of light impurities x_{diff} have been changed. Their evolutions among the different temperature are reported on figure 4.13 (a) and 4.13 (b) respectively.

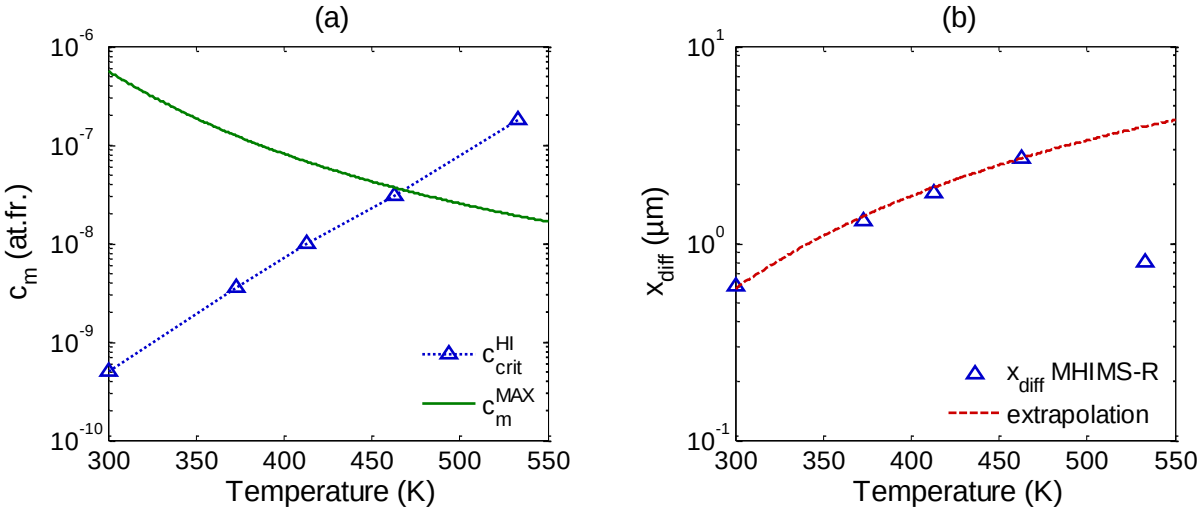

Figure 4.13. (a) Evolutions with the implantation temperature of c_{crit}^{HI} and c_m^{MAX} for the implantation of 200 eV/D with an incident flux of 10^{21} D·m^{-2}s^{-1}.

(b) Evolution with the implantation temperature of x_{diff}. An extrapolation of the 4 first points is done.

On figure 4.13 (a), the equivalent concentration of mobile particles for the implantation of 200 eV/D with an incident flux of 10^{21} D·m^{-2}·s^{-1} (equation 3.33) is also plotted. There are two cases:

- Below 500 K, $c_m^{MAX} > c_{crit}^{HI}$ which implies a strong trap creation and so a high D retention. It is confirmed by the experimental depth profile that shows a high D concentration in the sub surface layer which has a thickness of several µm (depending on the temperature).
- Above 500 K, $c_m^{MAX} < c_{crit}^{HI}$ which implies a weak creation and so a drop of the retention as observed experimentally by Alimov et al. [47] (figure 2.10 (a)). It has to be noted that the depth profile exhibits some creation because the fluence is high: even if the creation rate is note high, integrated on all the implantation time, some trap can be created.

In the simulations, the value of c_{crit}^{HI} increases with the temperature as suggested by the thermo-statistical model [121]. However, the values of c_{crit}^{HI} used in the simulation are lower than the one given by the thermos-statistical model for high temperature: in the simulation, $c_{crit}^{HI}(533\ \mathrm{K}) = 1.8 \times 10^{-7}$ at. fr and in the thermo-statistical model $c_{crit}^{HI}(533\ \mathrm{K}) < 2.7 \times 10^{-6}$ at. fr. [121]. It can be because ν_{crea}^{MAX}, which is the maximum value of $\nu_{crea}(c_m)$, increases with temperature with an Arrhenius law: $\nu_{crea}^{MAX}(T) = \nu_0^{crea} \cdot e^{-\frac{E_{crea}}{k_B \cdot T}}$. In these simulations, only the critical concentration changes which may underestimate the accurate value of c_{crit}^{HI}. To determine the activation energy E_{crea} and an accurate evolution of c_{crit}^{HI}, more experimental results are needed, i.e. the evolution

of the D retention with the incident flux as the one presented by Poon et al. [26] but at different temperatures and at a constant fluence (preferably low enough to see the evolution of the D retention).

On figure 4.13 (b), it can be seen that for the first 4 lowest temperatures, the value of x_{diff} increases with the temperature. This increase is coherent with a migration toward the bulk of the trap creation zone. Following the interpretation that we made, i.e. the creation is limited by the presence of light impurities, this migration may thus be explained by the diffusion of this light impurities which increases as the temperature increases. An extrapolation has been done on these first 4 points with the following formula:
$x_{diff} = 4 \times 10^{-5} \cdot e^{-\frac{0.11\ eV}{k_B \cdot T}}$ in m. The error on the values of x_{diff} can be estimated to be around 0.1 µm. Thus the error on the extrapolation of x_{diff} is 0.025 eV for the activation energy and 2×10^{-5} m for the pre-exponential factor.
In the simple case of a source of light impurities on the surface, the analytical solution of the standard diffusion equation given by the Fick's laws is:
$N_{LI}(x) = N_{LI,2} \cdot \mathrm{erfc}(\frac{x}{2\cdot\sqrt{D_{LI}(T)\cdot t}})$ with $D_{LI}(T)$ the diffusion coefficient of the light impurities and t the time. This relation corresponds to the second term of the right hand side of equation 4.2 that corresponds to the light impurities distribution with $x_{diff} = 2 \cdot \sqrt{D_{LI}(T) \cdot t}$. In this case, t = 2000 s corresponds to the implantation time to reach a fluence of 2×10^{24} D·m^{-2} with an incident flux of 10^{21} D·m^{-2}s^{-1}. It is thus possible to estimate the diffusion coefficient of the light impurities for the 4 temperatures considered:
$D_{LI}(T) = 4 \times 10^{-13} \cdot e^{-\frac{0.22\ eV}{k_B \cdot T}}$ in m^{2}s^{-1} with an error ~ 1×10^{-13} m^{2}s^{-1} on the pre-exponential factor and an error of ~ 0.05 eV on the activation energy based on the error on the values of x_{diff}. In [150], it is reported that the diffusion coefficient of oxygen in tungsten is $<10^{11} - 10^{-12}$ m^{2}s^{-1} at 1973 K. Using the value extracted from our simulations, one can obtain a diffusion coefficient of ~10^{-13} m^{2}s^{-1}. The difference could come from the fact that, as in the case of HI diffusion (section 2.3.2.ii), the trapping as an impact on the effective diffusion coefficient. In addition, this determination of the diffusion coefficient has been done in a very small temperature range (less than 200 K) and with a very indirect way. Moreover, this is really the diffusion coefficient of the light impurities in W only if the light impurities diffusion is the limiting process of the migration of the trap creation zone. Indeed, the extension of the trap created zone can also be due to the formation and the motion of dislocations in order to reduce the stresses induced by the creation of traps. The formation and the motion of dislocation would also increase with the temperature and is especially efficient for temperature higher than the DBTT (between 373 K and 743 K according to table 1.2). Such process would explain the surface morphology (blisters and etching pits) observed by Alimov et al. [47] on the SCW surface for temperature above 373 K. And of course, there could be a synergetic effect between the motion of dislocation and the diffusion of light impurities.

To answer this open issue more precisely, it could be interesting to look at the oxygen and carbon quantitative depth profiles after the implantation deeper than 100 nm (SIMS limitation). For example, NRA can probe the oxygen 18 using an energetic proton, Oxygen 16 using an energetic deuteron or carbon using an energetic deuteron. Then, the quantitative O/C depth profile can be compared to the D depth profile in SCW samples: if they are similar, it means that the interpretation made on this section is valid. If it is valid then, more complex simulation should be done including the diffusion+trapping/detrapping of HIs and O. In order to do such

simulations, the diffusion coefficient and the binding energy of O with VOH_i should be obtained from DFT calculations for example.

Concerning the last point at 533 K, the value of x_{diff} drops below 1 µm. It could be because at that temperature a trap mutation takes place that slow down the diffusion of the implanted light impurities. Indeed, Roszell et al. [88] and Poon et al. [27, 42] observed that for implantation of SCW at 500K with fluence higher than 10^{23} D·m^{-2}, a peak is observed around 800 K. They attributed the presence of this peak to a formation of D_2 nano-bubbles during the implantation at this high temperature and determined the detrapping energy to be 2.1 eV (table 2.3).

They propose the following process to explain the presence of such bubbles: the vacancies created during the implantation agglomerate into clusters that can be big enough to form D_2 molecule. In such traps, the D are detrapped from the void via the surface mechanism described in figure 2.2: The molecules are first dissociated, then D atoms are adsorbed on the nano-bubble surface and to enter the bulk and be detrapped, the D atoms have to reach the barrier E_A which is then the detrapping energy for such trap. According to DFT calculations (table 2.2), this energy to go from the surface to the bulk is around 2.0 – 2.3 eV.

Due to these trap mutations of the created vacancy the effective diffusivity could be change and slowed down. It has to be noted that even if the trap distribution used in our simulations does not take into account this trap mutation, the D depth profile is not affected. Indeed, a temperature of 533 K is not high enough to completely empty the trap with a maximum detrapping energy of 1.31 eV.

Summary:

In this section the simulations of implantations of 200 eV/D with a flux of 10^{21} D·m^{-2}·s^{-1} and a fluence of 2×10^{24} D·m^{-2} at temperatures from 303 K to 533 K have been done and compared to experimental results. From the results obtained, the following conclusions can be made:

- The H critical concentration of mobile particles for the trap creation process increases with the temperature. At 533 K, it is around 10^{-7} at.fr. which corresponds to a threshold incident flux around 10^{21} D·m^{-2}·s^{-1}.
- This results implies that for lower incident flux, the D retention drops at lower temperature.
- as the temperature increases between 300 K and 463 K, the zone where traps are created is extended toward the bulk.
- The experimental D depth profiles are well reproduced with the analytical solution of the standard diffusion equation: a diffusion coefficient can be extracted from the simulation. Following our interpretation of a trap creation limited by the light impurities implantation, this diffusion coefficient is the diffusion coefficient of the light impurities in W. But it can also be due to the formation and the motion of dislocations due to stresses induced by the high number of traps initially created.

4.1.3. Summary of the simulations on SCW samples

In this section, several simulations results have been shown. The simulations are done using the code MHIMS-R based on the multi-trapping model and are compared with success to experimental results obtained on SCW samples annealed at high temperature (low dislocation

concentration and no grain boundary) and implanted with different fluxes, with different fluence and at different temperatures. The simulation results obtained are show good agreements with the experimental results:

- The retention in well annealed SCW seems to be limited by a trap creation process at different temperatures. Such trap creation is predicted by thermo-statistical model. The traps are formed to reach the thermodynamic equilibrium. In this section, we propose a kinetic model for such trap formation process.
- Our interpretation is that the created traps are initially VOH_i (vacancy with oxygen and hydrogen trapped inside) or VCH_i (vacancy with carbon and hydrogen trapped inside). The traps can mutate into bigger vacancy clusters if a lot of traps are created in a µm-thick layer.
- In any cases, the maximum detrapping energy of the created traps is around 1.5 eV if few traps are created or if the creation zone is not thick (< 1 µm) and 1.3 eV if many traps are created in a zone with a thickness of about 1 µm and if the traps are fully filled.
- This trap creation process can be characterized by a creation frequency and a saturation frequency.
- The creation frequency is characterized by a critical concentration c_{crit}^{HI}. If the mobile concentration during the implantation is above this critical concentration, the trap creation is efficient and if the mobile concentration during the implantation is below the critical concentration, the trap creation efficiency drops by several orders of magnitude.
- This critical concentration increases with temperature as suggested by the thermo-statistical model. An evolution is proposed for temperature up to 533 K but it is lower than the one obtained from the thermo-statistical model. The reason proposed is an underestimation of c_{crit}^{HI} because the maximum value of the creation frequency stays constant with the temperature when it may follow an Arrhenius law.
- In our interpretation, the saturation frequency is dependent of the distribution of O and C impurities. These impurities are inserted during the implantation of D and present in the SCW samples. To reproduce the experimental NRA D depth profiles, three zones are defined for the distribution of O and C:
    - The first is related the implantation zone of the O and C impurities present in the background gas of the implantation chamber. These O and C impurities gain kinetic energy through elastic collision during the D implantation.
    - In our interpretation, the second zone, corresponds to the limited diffusion depth of the implanted O and C in W. From the simulations of the depth profiles at different temperatures, a diffusion coefficient for this impurities can be extracted indirectly: $D_{LI}(T) = 4 \times 10^{-13} \cdot e^{-\frac{0.22\ eV}{k_B \cdot T}}$.
    - The third zone corresponds to the native O and C impurities. In the samples considered, the native O and C impurities reached 0.05 at.% but it is reduced by the annealing of the samples.

The validation of the interpretation done in this section could be validated or invalidated by further experimental measurements such as:

- The evolution of the D retention with the incident flux at different temperature at fixed fluence. This would allow determining with accuracy the evolution of c_{crit}^{HI}.
- The experimental depth profile of D, C and O up to several µm deep. This would validate the interpretation of the second zone of the distribution $N_{LI}(x)$ used in our simulations.

In parallel, DFT results to obtain the diffusion and binding energies of O and C with VOH_i and VCH_i are also needed if one wants to simulate in a more accurate way this creation process.

4.2. Simulations of undamaged PCW experiments

After simulating the implantations of SCW samples, we saw that the D trapping in SCW is limited by the formation of H-induced vacancies (and eventually the mutation or formation of new traps induced by the large amount of formed vacancies). To go toward the relevant tokamak W materials, the study of PCW has to be done. In this case, the philosophy changes: First we reproduce the experiment and then we compared them to DFT or MD studies to determine the nature of the traps. In addition, it would be difficult to use MHIMS-R in such experiments. Indeed, in PCW samples, a large variety of different GBs exists and not only the symmetrical GBs that can be handle by DFT [117, 118]: it is impossible to obtain the distribution of detrapping energies for any GBs which are needed as input parameters for MHIMS-R. Then, the simulation of such PCW implantations will be done using the standard MRE model and the code MHIMS.

In this section, the simulations are focused on D implantation of PCW that are not damaged by neutrons or heavy ions.

The trap formation exhibits in the simulations of the SCW experiments also takes place in PCW experiment as discussed in section 2.3.3.ii. The first simulations that are presented in this section are simulations of PCW implantations at 320 K with flux lower than the critical flux of trap creation (5×10^{17} $D\cdot m^{-2}\cdot s^{-1}$) in order to see what are the effect of the microstructure changes on the D retention properties of W.

Then, simulations of D implantations in PCW at 300 K with a flux higher than the critical flux of trap creation are presented. These simulations intend to provide a simple description of the retention properties of W that are or will be installed in tokamaks. Such properties can be used as a wall model to describe the recycling of molecules in plasma edge codes (as SOLEDGE2D-EIRENE) or to estimate the fuel retention in tokamaks that do not experience neutron irradiation.

4.2.1. Simulations at low flux and low fluence

The experimental results that are simulated here are obtained by Bisson et al. [24] after implantations at ~ 320 K of 250 eV/D ions at an incident flux of 2×10^{16} $D\cdot m^{-2}\cdot s^{1}$ (below the critical flux for trap creation) and at an incident angle of 45° to the normal incidence. According to SRIM®, the reflection coefficient of 250 eV/D ions with an incident angle of 45° is 0.55: the implanted flux is 9×10^{15} $D\cdot m^{-2}\cdot s^{-1}$.

The PCW samples are mechanically and electro polished and they were subjected at least twice to a degassing procedure that starts by a linear increase of the temperature with 1 K/s up to 1300 K followed by a 10 min annealing at 1300 K. After the D implantation, the PCW samples are subjected to a storage time of at least 2 h under vacuum (base pressure < 10^{-9} mbar) around 300 K. The quantity of D retained during the implantation is quantify by a TDS measurement where the temperature increases with a rate of 1 K/s. After a storage of 2 hours, the TDS spectra exhibits one single asymmetric peak at 455 K ± 30 K for fluence higher than 1.4×10^{19} $D\cdot m^{-2}$ (figure 2.11). The asymmetry of the desorption peak is characterized by a tail at high temperature more pronounced than the tail at low temperature. For the lowest fluence, the peak is at higher temperature around 500 K.

The D retention increases with the fluence following a power law fluence$^{0.65}$ (figure 2.12). Finally, the D retention is also evolving with the storage time at 300 K: the D retention after a storage time of 135 h is only 40 % of the D retention after a storage time of 2 h for an fluence of 2.9×10^{19} D·m^{-2}.

In this section, we want to first reproduce this evolution of the retention with the storage time and then compared the simulated TDS spectra with the experimental ones. Since a single peak is observed, only a single detrapping energy is used. As in the experimental measurements, the simulations are separated into three steps:

- The implantation at 320 K with an incident flux of 2×10^{16} D·m^{-2}·s^{-1} and a fluence of 2.9×10^{19} D·m^{-2}.
- The storage time at 320 K for various times (between 2 h and 135 h),
- The increase of the temperature with a rate of 1 K/s (TDS).

The MHIMS code is used to do the simulations and the boundary condition use is the one considering a quick surface recombination (section 3.2.1).

Figure 4.14 (a) presents the evolutions of the simulated and experimental D retentions with the storage time. The following trapping parameters are used in the simulations:

- $E_{t,1} = 1.1$ eV,
- $n_1 = 0.13$ at. % homogeneously distributed in all the simulated space.

Figure 4.14 (b) presents the simulated and the experimental TDS spectrum for three different storage times (2 h, 15 h and 135 h).

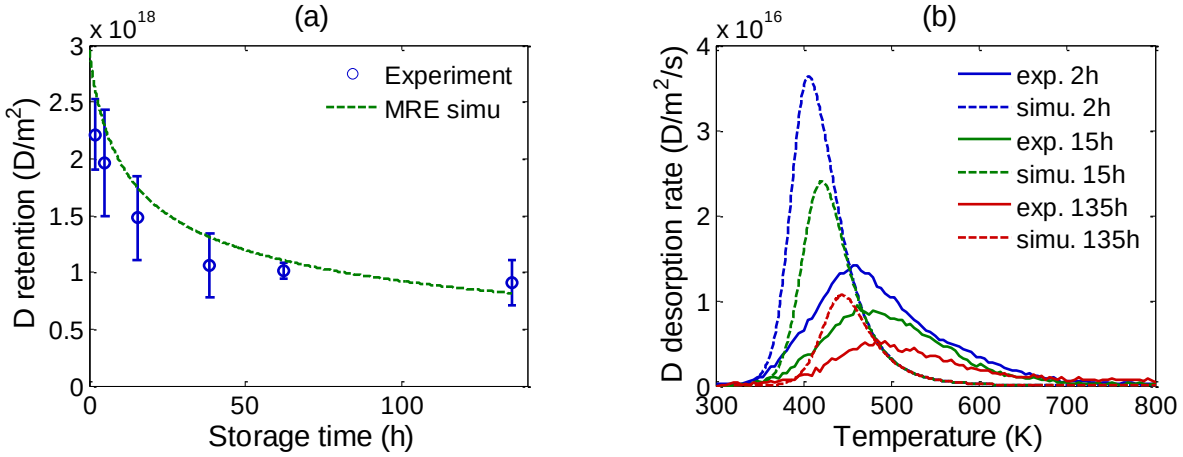

Figure 4.14. (a) evolution of the D retention as a function of the storage time at 320 K for the simulation with a single detrapping energy (solid line) and for the experimental measurements (data point).

(b) Simulated (dashed line) and experimental (solid line) TDS spectra for a storage time of 2 h, 15 h and 135 h.

The implantation is done with 250 eV/D ions at 320 K with an incident flux of 2×10^{16} D·m^{-2}·s^{-1} and a fluence of 2.9×10^{19} D·m^{-2}.

As it can be seen on figure 4.14 (a), the evolution of the D retention with the storage time at 320 K is well reproduced inside the experimental error bars with a detrapping energy of 1.1 eV. If one compares this 1.1 eV value with the DFT data (figure 2.16 and figure 4.25 in the summary of this chapter) it can be seen that such detrapping energy could be attributed to trapping in GBs,

dislocation jogs and vacancies. The vacancies cannot be thermal vacancies (formation energy of mono-vacancy > 3 eV) neither vacancies formed by the presence of H since the flux is too low to triggered the trap formation (section 4.1). Thus, vacancies are probably not the trapping sites for D in these experiments. Thus, the defects that can retain D are more likely GBs or dislocation jogs. Indeed, dislocations may have survived the annealing at 1300 K and GBs are presents in the samples since they are PCW samples.
On figure 4.14 (b), the simulated TDS spectra are compared to the experimental ones. First, the simulated peak as the same asymmetry as the experimental one: a tail at high temperature. In the simulations, such tail is observed because of two aspects:

- the presence of free traps beyond the zone where D stops diffusing at the end of the implantation + storage time,
- the diffusion and the retrapping of D in these free traps during the temperature ramping up.

In the simulations, as the storage increases from 2 h to 135 h, the TDS peak shifts from 405 K (for a storage time of 2 h) to 445 K (for a storage time of 135 h): the shift is 40 K for these two storage times. Experimentally, a shift is also observed: for a storage time of 2 h, the D desorption rate peaks at 455 K ± 30 K and for a storage time of 135 h, the D desorption rate peaks at 490 K ± 30 K. thus, the shift is 35 K ± 30 K for these two storage times: the experimental shift is quantitatively reproduced by the MRE simulations. However, the position of the simulated peak is 50 K less than the experimental one. In addition, the simulated TDS spectrum is thinner and higher than the experimental one.
The reason could be that there is more than 1 detrapping energy in such samples corresponding to a large variety of GBs as shown by the MD simulations reported in section 2.3.4.i. These MD simulations by Piaggi et al. [124] show that the trapping of H in general GB can be characterized by a broaden distribution of binding energies with a mean binding energies in the same range as the binding energy of H in mono-vacancy which range around 1.0 eV – 1.5 eV. Thus a mean binding energy of 1.1 eV is coherent with trapping in GBs. And a broaden distribution of binding energies may enlarge the simulated TDS spectrum.
In addition, from their MD simulations and making the assumption that the amount of D trapped in GB evolves as ~ 1/d (d = grain size), Piaggi et al. [124] estimated that the retention of D in GBs of 5 µm would be 0.035 at.% for a mean grain size of 5 µm. They also estimated that the amount of D retained in W with a high dislocation density of 10^{12} m^{-2} would be 4 orders of magnitude lower than that. The samples used by Bisson et al. are delivered with a typical grain size of ~30 µm but with also many gain with size in the 1 µm size: following the estimation of Piaggi et al., the amount of D that is trapped in such samples can reach ~ 0.1 at.% which is in the range of our trap density.

Summary:

- At low flux and low fluence, the desorption around 300 K in 135 h of 50 % of the initially trapped D can be reproduced using a single trapping energy of 1.1 eV.
- Both simulated and experimental TDS spectra exhibit a shift of the TDS peak of around 40 K between a storage time of 2 h and a storage time of 135 h.
- As in the experiment, the simulated TDS spectrum has a more pronounced high temperature tail.
- However, using a single detrapping energy does not allow reproducing the width of the experimental TDS spectrum. But, based on MD simulations, it is proposed that the D

retention in such samples is due to trapping of H in general GBs that is characterized by a broaden distribution of detrapping energy (inducing a wide TDS spectrum) centered around 1.1 eV.

4.2.2. Simulations at higher flux and higher fluence

In this section, the experimental results that are simulated are obtained by Ogorodnikova et al. [25] after the implantation at 300 K of 200 eV/D ions with normal incidence and a flux between 2.5×10^{19} – 4×10^{19} $D\cdot m^{-2}\cdot s^{-1}$. The PCW sample used in this experiment have been mechanically polished and outgassed at 1273 K. It has also been electrochemically polished and annealed at 1573 K for 3 h under vacuum. Initially, the grains size is in the range of 1 – 5 µm and they tend to grow during the annealing phase to be in the range of 5 – 15 µm. After the implantation at a fluence varying between 10^{21} $D\cdot m^{-2}$ and ~ 10^{24} $D\cdot m^{-2}$, the sample is kept for around 5 min under vacuum (in-situ measurements) at 300 K. After the 5 min storage time, the temperature increases linearly with time with a heating rate of 8 K/s and the outgassing flow of deuterium is recorded (TDS measurements). It is noted in Ogorodnikova's paper that the temperature of the sample was measured with an error of ± 50 K.

The simulation which is presented in this section is divided following the three parts described above: implantation, storage and TDS phases. The simulated fluence is 10^{23} $D\cdot m^{-2}$ and the experimental TDS spectrum obtained by Ogordonikova et al. after implantation at such fluence is presented figure 2.11 (b).

According to SRIM®, the reflection coefficient of 200 eV/D on a W surface with normal incidence is ~ 0.5. Thus, the implanted flux ranges between 1.25×10^{19} – 2×10^{19} $D\cdot m^{-2}\cdot s^{-1}$. In the simulation, an implanted flux of 1.25×10^{19} $D\cdot m^{-2}\cdot s^{-1}$ is taken. From the simulations on SCW presented in section 4.1, it has been shown that an incident flux higher than 5×10^{17} $D\cdot m^{-2}\cdot s^{-1}$ activates the creation of traps in the near surface layer (10 - 20 nm) and in the sub-surface layer (1 – 2 µm). Thus, in the simulation of an implantation with a flux of 1.25×10^{19} $D\cdot m^{-2}\cdot s^{-1}$, such trap creation has to be taken into account. The traps that are created are called extrinsic traps (vacancy traps as seen in section 4.1) comparatively to the intrinsic traps (grain boundaries, impurities for example) that are present before the implantation starts. To take into account the trap creation process, a simpler model than the one described in section 4.1 is used. Such model was first described by Ogorodnikova et al. [25] for the trap creation in the near surface layer. In this model the concenration of extrinsic traps is called n_3. The increase of n_3 during the implantation phase is described by the following equation:

$$\frac{\partial n_3(x,t)}{\partial t} = \phi_{imp} \cdot \left[\left(1 - \frac{n_3}{n_{a,max}}\right) \cdot \eta_a \cdot f(x) + \left(1 - \frac{n_3}{n_{b,max}}\right) \cdot \eta_b \cdot \mathrm{erfc}\left(\frac{x}{x_{diff}}\right)\right] \qquad (4.3)$$

In equation 4.3, the growth of n_3 is proportional to the incident flux. Thus, the total amount of created traps is proportional to the fluence as it is explained by Ogorodnikova et al. [25]. In the code, the trap creation process is switched on only if the incident flux is higher than 5×10^{17} $D\cdot m^{-2}\cdot s^{-1}$. There are two zones where traps can be created:

- In the near surface zone: it is expressed by the first term in the bracket of the right hand side of equation 4.3. The traps are created in the implantation zone via the implantation distribution of ions f(x) described in section 3.1.1.
- In the sub surface zone: it is expressed by the second term in the bracket of the right hand side of equation 4.3. The distribution of the created traps is the same as the one described

by the second term of equation 4.2: it corresponds to the extension of the trap creation zone possibly linked with the diffusion of the light impurities.

In this model, η_a and η_b (dimensionless) are the creation rates of the extrinsic traps in the near surface ($f(x)$) and the sub-surface ($\mathrm{erfc}\left(\frac{x}{x_{diff}}\right)$) respectively. As for the simulation of SCW presented in section 4.1, the value of x_{diff} is around 1 – 2 µm. The creation of traps stops when the trap concentration reaches the maximum amount of traps that can be created which are $n_{a,max}$ (in m^{-3}) in the near surface layer and $n_{b,max}$ (in m^{-3}) in the sub-surface layer. The parameters η_a, η_b, $n_{a,max}$ and $n_{b,max}$ are free parameters to reproduce the experimental TDS spectrum.

The simulations are done with the code MHIMS as in section 4.2.1 and the boundary condition use is the one considering a quick surface recombination (section 3.2.1).

Figure 4.15 (a) presents the comparison between the experimental and simulated TDS spectra. Figure 4.15 (b) presents the simulated D depth profile after the implantation and a period of 5 min of storage at 300 K.

The parameters that we used to reproduce the experimental TDS spectrum are summarized in table 4.2. Even if 2 peaks can be observed experimentally three different traps are required to match the experimental TDS spectrum: 2 intrinsic traps (trap 1 and trap 2) and one extrinsic trap (trap 3) with a concentration evolving during the implantation (equation 4.3). Indeed, the desorption peaks resulting from the detrapping from the different trapping sites are overlapped because the detrapping energies are close to each other. It is thus difficult to have a really precise distribution of detrapping energies: only the mean detrapping energies can be determined. On the simulated TDS spectrum, the peak around 400 K corresponds to the detrapping from trap 1, the peak around 650 K corresponds to the detrapping from trap 3. The desorption corresponding to detrapping from trap 2 occurs around 500 K.

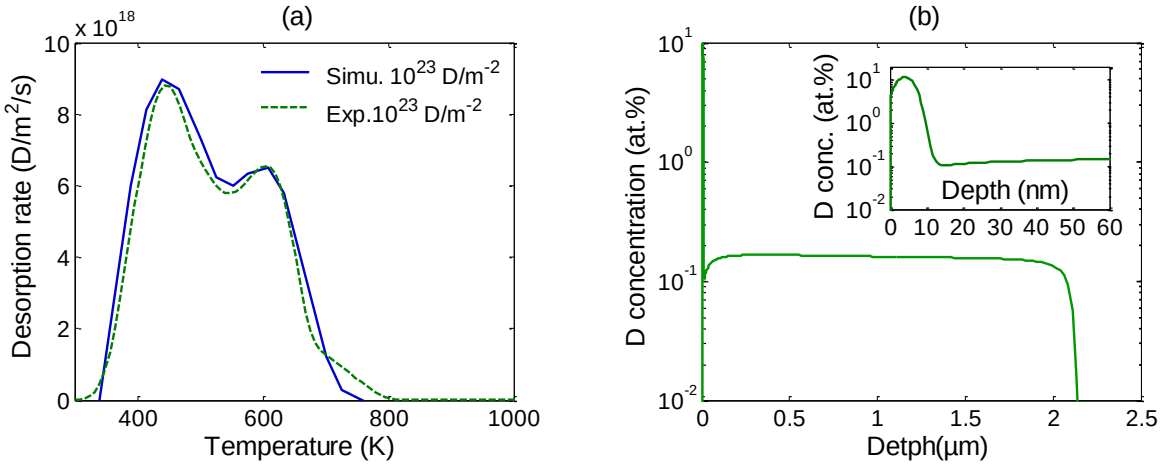

Figure 4.15. (a) Experimental (blue solid line) and simulated (green dashed line) TDS spectra.

(b) simulated D depth profile after the implantation and a period of storage of 5 min at 300 K. The insert is a zoom of the near-surface layer up to 60 nm.

The incident fluence is 10^{24} D·m^{-2}, the ion energy is 200 eV/D and the heating ramp is 8 K/s.

Discussion on the nature of traps:

Trap 3 has a detrapping energy of 1.5 eV and it is the extrinsic traps i.e. the one induced by the D irradiation. According to section 4.1, this trap can be interpreted to be vacancy with light impurities and HIs inside (VOH_i and VCH_i) which also has a detrapping energy around 1.5 eV.

Trap 2 has a detrapping energy of 1.0 eV which is close to the detrapping energy of 1.1 eV obtained from the simulation at low flux and low fluence. It is discussed in section 2.2.3 that an accuracy of temperature measurements during the TDS leads to an error on the determination of the detrapping energy of around 0.1 eV. Thus, the trap 2 can be interpreted to be GB or more precisely, the detrapping energy associated to trap 2 is the mean detrapping energy of all the GBs present in the samples. Ogorodnikova et al. [25] observed by SEM that the grain size before the implantation is in the range of 5 – 15 µm. The trap concentration used in the simulation is 0.035 at.% (table 4.2) which corresponds to a mean grain size of 5 µm according to the estimation of Piaggi et al. [124]. It strengthens the assumption saying that trap 2 corresponds to GBs.

Trap 1 has a detrapping energy around 0.85 eV. Looking at the detrapping energies calculated by DFT for various defects (figure 2.16 and figure 4.25 in the summary of this chapter), it can be said that a detrapping energy of 0.85 eV could correspond to detrapping from metallic impurities (Fe, Ni and Cu), dislocation lines and mono-vacancies filled with 6 HIs.

Since there are very few mono-vacancies (low formation energy), the trapping of H with mono-vacancy is only possible in the extrinsic vacancies created during the D irradiation. Thus, a small part of the first desorption peak at 400 K may be due to detrapping from this extrinsic traps. But in the simulation, the extrinsic traps are not the dominant traps so the detrapping from the created vacancies cannot be the only explanation.

A part of trap 1 can also be due to the intrinsic dislocation lines. It depends on the dislocation density that can be low because of the annealing steps. According to STEM images obtained by Manhard et al. [133], the dislocations are not completely removed in PCW annealing at 1500 K for 30 minutes. Thus, in the experiment simulated here, some dislocations could remain after a 3 h annealing at 1573 K.

Trap 1 can also be due to the metallic impurities present in substitutional sites. According to the DFT data available (figure 2.16) trap 1 could be Fe, Ni and Cu. Ogorodnikova et al. list the main impurity presents in the sample they used for their experiments. For the three elements listed above, only the concentration of Fe is given: ~0.0212 at.%. Thus, around 20 % of the intrinsic trap 1 could be interpreted as Fe in substitutional site. The content of Ni and Cu are not given but they also may have an impact on this desorption peak as well as other impurities.

Therefore, trap 1 can be interpreted as impurity (especially Fe), dislocation or the 6^{th} filling level of a mono-vacancy created during the irradiation. Because all these different defects have a similar detrapping energy, only the mean detrapping energy 0.85 eV is used with an homogeneous distribution in all the simulated material as an intrinsic trap.

At this point, one can ask why is trap 1 not observed experimentally for the low flux experiment at 320 K presented in section 4.2.1?

The implantation conditions of the experiment of Bisson et al. [24] simulated in section 4.2.1 are: a ion energy of 250 eV/D, an incidence angle of 45° and an incident flux of 2×10^{16} $D\cdot m^{-2}\cdot s^{-1}$ so an implanted flux of 0.9×10^{16} $D\cdot m^{-2}\cdot s^{-1}$.

For such implantation conditions at 320 K, the equivalent concentration of mobile particles given by equation 3.33 is $c_m^{MAX} = 6 \times 10^{-12}$ at. fr.. With this concentration of mobile particle, the equilibrium ratio of trap 1 is $R_{trap,1}(c_m^{MAX}, 320\ K) = 0.02$. Thus, during the implantation, such

trap cannot be filled because the flux is not high enough to guarantee that the trapping frequency $\nu_m(T) \cdot c_m$ is higher than the detrapping frequency $\nu_i(T)$: such trap cannot be observed in the experiment of Bisson et al. with a low flux. However, for a trap 2 (with detrapping energy between 1.0 and 1.1 eV), the equilibrium ratio is $R_{trap,2}(c_m^{MAX}, 320\ K) = 0.83 - 0.99$. So, during the implantation, almost all traps 2 are filled with H. It means that if one makes the simulations of the experiment of Bisson et al. with trap 1 and trap 2, it will obtain the same results as the simulation with only trap 2 presented in section 4.2.1.

Trap 1, **intrinsic** (impurities (Fe), dislocations)	$E_{t,1} = 0.85$ eV and $n_1 = 0.13$ at. %
Trap 2, **intrinsic** (GBs)	$E_{t,2} = 1.00$ eV and $n_2 = 0.035$ at. %
Trap 3, **extrinsic** (VOH_i, VCH_i)	$E_{t,3} = 1.5$ eV $\eta_a = 1.5 \times 10^{-3}$ and $n_{a,max} = 15$ at. % $\eta_b = 1.5 \times 10^{-4}$ and $n_{b,max} = 1$ at. % $x_{diff} = 1$ µm

Table 4.2. Trapping parameters and trap creation parameters used to reproduce the experimental TDS spectrum.

Discussion on the D simulated depth profile and impact of the storage time:

Here, we compare the simulated D depth profile (figure 4.15 (b)) to the experimental D depth profile obtained by Alimov et al. [89] (figure 2.13) after implanting 200 eV/D ions in PCW at 323 K. Experimentally, Alimov et al. observed 3 zones: the near surface layer (up to ~ 200 nm and a D concentration of 10 – 1 at.%), the sub-surface layer (up to 1 – 2 µm and a D concentration of 0.1 at.% – 0.01 at.%) and the bulk zone (up to 7 µm and a D concentration around the NRA detection limi 0.001 at.%).

In the simulated D depth profile (figure 4.15 (b)), at least two zone are observed:

- In the near surface layer, a high D concentration of ~10 at.% is observed,
- In the sub-surface up to a depth of 2 µm, a approximatively constant concentration of D around 0.1 at.%

There are two differences between the simulated depth profile and the experimental depth profiles reported by Alimov et al. [89] (figure 2.13):

- First, the bulk part (between 2 µm and 7 µm) with a low D concentration (around 0.001 at.%) is not observed.
- The concentration in the sub-surface is higher than in the experiments.

In the experiment of Alimov et al., the PCW sample has been prepared with the same procedure as in the Ogorodnikova et al.'s experiment: mechanically and electro-chemically polished and annealing at 1573 K for 3.5 h. In addition, in Alimov et al. experiment, the PCW sample is irradiated by 200 eV/D with a flux of $3.6 \pm 1.1 \times 10^{19}$ $D \cdot m^{-2} \cdot s^{-1}$ which is the same order of magnitude as the Ogorodnikova et al.'s experiment.

The first difference may come from the PCW samples used. In Ogorodnikova et al.'s experiment, it is explained that the grain size after the annealing is in the range of 5 – 15 µm. In Alimov et al.'s experiments, the grain size before the annealing is estimated by Alimov et al. to be in the range of 1 – 20 µm: after the annealing, the concentration of trap 2 may be lower in the experiment from Alimov et al. than in the experiment from Ogorodnikova et al..

The difference may also come from differences in the experimental condition: the implantation temperature in the Alimov et al.'s experiment is 323 K which may reduce the equilibrium ratio of trap 1. In addition, as it has been observed in section 4.2.1, D can be detrapped significantly in the 10 hours scale from trap 2 at 320 K. It is the same for trap 1 since the detrapping energy is even lower. In the paper from Alimov et al., no indication is given on the delay and the temperature between the implantation and the NRA measurements. Section 4.2.1 shows that the storage time has a significant impact on the D retention.

Here, the idea is to see if the storage time has a significant impact on the D depth profile. To be as close as the situation experienced in Alimov et al.'s experiment, an implantation of a 200 eV/D ion implantation at 323 K is simulated with a flux of 2.5×10^{19} $D\cdot m^{-2}\cdot s^{-1}$ and a fluence of 10^{23} $D\cdot m^{-2}$. After the implantation, a linear decrease of the temperature in 1000 is set from 323 K to 300 K. After the cooling phase, a long storage time of 395 000 s is simulated. The simulated depth profile is taken at the end of the implantation, after the cooling phase, after a storage time of 35 000 s (~ 10 h) and after a storage time of 395 000 s (~ 110 h). This 4 simulated D depth profiles are shown in figure 4.16 (a). On this figure, a significant decrease of the D concentration in the sub-surface layer can be seen from 0.1 at.% after the implantation to 0.05 at.% after a storage time of ~ 110 h. In addition, the D migration depth (when the D concentration drops) changes from ~ 2 µm after the implantation to ~ 4 µm after a storage time of 110 h.

Figure 4.16 (b) shows the evolution of the overall quantity of D retained in the simulated materials during the storage time (right after the implantation). The evolutions of the D trapped inside trap 1, trap 2 and trap 3 are also shown. It can be seen that the D retention decreases by about 30 % after a storage time of 110 h. The decrease is due to detrapping from traps 1 but all the D detrapped from traps 1 are not desorbed from the simulated materials. Depending on the gradient of mobile particle, a part of the detrapped particles will diffuse toward the surface and be desorbed and the other part will diffuse toward the bulk and be recaptured by trap 2 extending the depth profile as observed in figure 4.16 (a). As it has been seen in section 4.2.1, D can be detrapped from traps 2 around 300 K. Consequently, if one would have wait more than 110 h, all the traps 1 would be empty and D trapped in traps 2 would begin to be detrapped inducing a new phase of desorption.

Therefore, the storage at 300 K after implantation at 323 K has a significant impact on the TDS spectra (section 4.1.2) and on the D depth profile. Thus, the difference between the simulated D depth profile shown in figure 4.15 (b) and the experimental D depth profile recorded by Alimov et al. could be explain by the desorption during the storage time. Sadly, the information is not available in the Alimov et al. paper.

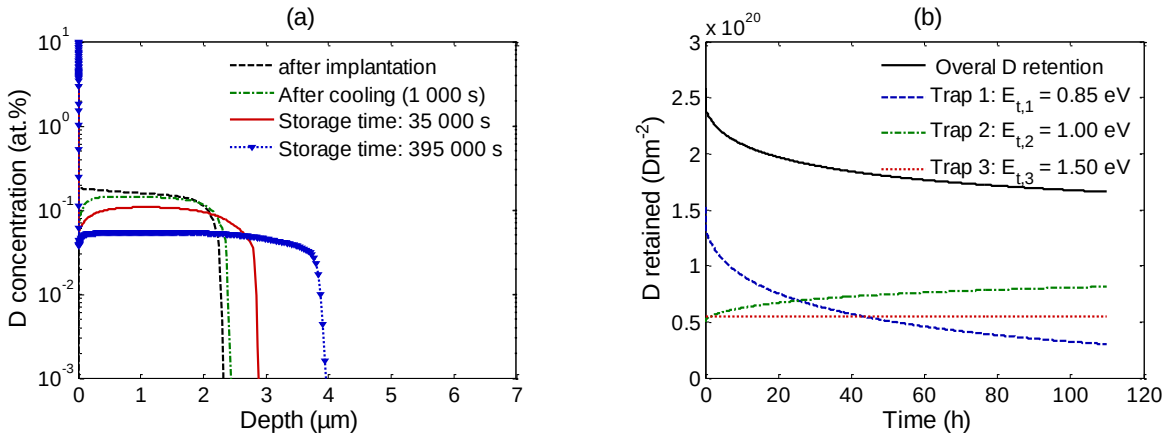

Figure 4.16. (a) Simulated D depth profile after the implantation, after a 1000 s cooling phase from 323 K to 300 K, after 10 h of storage at 300 K and after 110 h of storage at 300 K.

(b) Evolution of the overall D retained and the D retained in trap 1, trap 2 and trap 3 during the storage time.

The ions energy is 200 eV/D, the incident flux is 2.5×10^{19} D·m^{-2}·s^{-1}, the fluence is 10^{23} D·m^{-2} and the implantation temperature is 323 K.

Summary:

- The retention property of D in PCW can be described by 3 mean detrapping energies.
- Trap 1 with a detrapping energy of 0.85 eV is an intrinsic trap that may correspond to dislocations and impurities such as Fe.
- Trap 2 with a detrapping energy of 1.00 eV is an intrinsic trap that may correspond to GBs.
- Trap 3 with a detrapping energy of 1.5 eV is an extrinsic trap. It corresponds to the created trap exhibits in the simulation of SCW experiments (section 4.1) and seems to be related to VOH, VCH and VH.
- The simulation of the storage shows that it significantly affects the depth profile. A strong outgassing can be observed in a 10-hours scale.

The purpose is now to test if these trapping parameters presented in table 4.2 are valid to reproduce the evolution of the D retention as a function of the fluence and the temperature. If they are, they could then be used to estimate the retention of fuel in ITER like discharges without any damaging by neutrons.

4.2.3. Simulations at different fluences and temperatures

In this section, we try to reproduce the evolution of the D retention as a function of the fluence for two temperatures: at 300 K (figure 2.12) and at 473 K. Both experimental evolutions are taken from Ogorodnikova et al.'s paper [25]. For these simulations, the implantation parameters are the same as in the previous section: the incident flux is 2.5×10^{19} D·m^{-2}·s^{-1} and the ion energy is 200 eV/D. The fluence varies between 10^{21} D·m^{-2} and 10^{24} D·m^{-2}. The D retention is taken after a storage time of 5 min.

We also try to reproduce the evolution of the D retention as a function of implantation temperature (figure 2.14). For these simulations, the same implantation parameters are used. For a temperature higher than 300 K, a linear decrease of the temperature is simulated in ~100 s and the D retention is taken 5 min after the end of the implantation.
The trapping parameters used in these simulations are the same as the one presented in table 4.2 except for the value of x_{diff}: following the simulations done in SCW at different temperatures, (figure 4.13) the evolution extrapolated in section 4.1.2.iii is used: $x_{diff} = 4 \times 10^{-5} \cdot e^{-\frac{0.11\ eV}{k_B \cdot T}}$.

Evolution of the D retention as a function of the fluence:

Figure 4.17 shows the evolution of the D retention with the incident fluence in both simulations and experiments for implantations at 300K and 473 K.

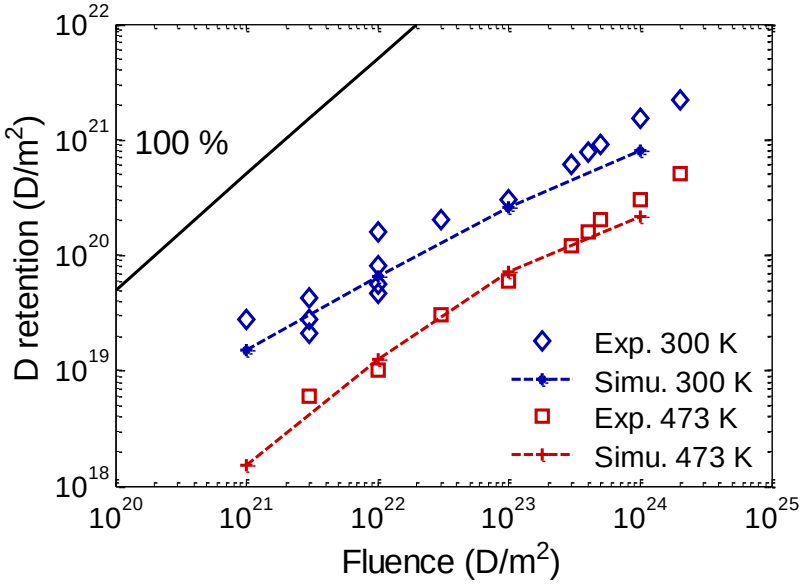

Figure 4.17. Evolution of the D retention as a function of the incident fluence for the simulations (dotted line) and the experiments (data points) at 300 K (blue) and at 473 K (red). The incident flux is 2.5×10^{19} D·m^{-2}·s^{-1} and the ion energy is 200 eV/D. The black solid line corresponds to a full retention of the incident fluence with a reflection coefficient of 0.5.

A good agreement for both implantation temperatures can be observed between the evolution of the D retention in the simulations and in the experiments. The only difference between the simulations and the experiments is that for the highest fluence (10^{24} D·m^{-2}), it seems that the simulation underestimate the retention by a factor of 2: 8×10^{20} D·m^{-2} in the simulation and 2×10^{21} D·m^{-2} in the experiment. This difference could be due to an underestimation of the trap creation process. It has been shown that x_{diff} evolves (section 4.1.2.iii) with the temperature but if it corresponds to a diffusion process of the light impurities (O and C) from the implantation zone to the bulk, it depends also on the implantation time and so increases with the fluence. It has also to be pointed out that for a fluence of 10^{24} D·m^{-2}, Tian et al. [96] reported a D retention of 4×10^{20} D·m^{-2} at 300 K with similar flux and the same ion energy: the simulation result still stays in the experimental error bars.
As pointed out in section 2.3.3.ii, for implantations at 300 K, it can be seen experimentally that the evolution of the D retention with the fluence is Retention~(fluence)$^{0.65}$. In the simulations, a

power law can also be extracted and it is seen that for implantation at 300 K Retention~(fluence)$^{0.57}$. The power law is similar to the experimental one (in the experimental error bars) and it is close to a square root indicating that the D retention is limited by the migration of the D toward the bulk as it can be anticipated from the simple analytical model section 3.3.1 and equation 3.31. The small deviation from the square root law is due to the trap creation model inducing a component of the D retention which evolves quicker than a square root law.
For implantation at 500 K, the simulated D retention also exhibits a power law: Retention ~ (fluence)$^{0.7}$. The deviation from the square root law is more pronounced because at this temperature, the main trap retaining the D is the extrinsic traps (with the highest detrapping energy) as it will be presented in the next on figure 4.18.
In both case, the evolution of the D retention with the fluence obtained in the simulations is in good agreement with the experimental evolution of the D retention for these two temperatures. For all this set of simulations, the only change has been the value of x_{diff} that evolves following the extrapolation made in section 4.1.2.iii. It means that the mean detrapping parameters obtained from the simulations of a TDS spectrum are consistent for estimating the D retention in PCW over a significant large range of fluence and for 2 implantation temperatures.

Evolution of the D retention as a function of the implantation temperature:

Here, we are interesting in reproducing the evolution of the D retention with the implantation temperature observed experimentally (figure 2.14). For all these experiments presented on figure 2.14, the PCW samples were mechanically and electro-chemically polished and annealed between 900 K and 1500 K for 1 h before the implantation. The incident fluence for these experimental data sets are around 10^{23} D·m^{-2} so the simulated incident fluence is also 10^{23} D·m^{-2}. The ion energy is 200 eV/D for Tian et al. [96] and 500 eV/D for Roszell et al. [88] and Haasz et al. [100]. The incident flux is varying from 3×10^{18} D·m^{-2}·s^{-1} to 9×10^{19} D·m^{-2}·s^{-1}. In our simulations, an ion energy of 200 eV/D is used as well as an incident flux of 2.5×10^{19} D·m^{-2}·s^{-1}. This incident flux is close to the one used in the experiment from Tian et al. [96]. Again, the trapping parameters (detrapping energies and trap concentrations) are not changed for these simulations. Only the value of x_{diff} increases with temperature as suggested from the simulations of SCW experiments.
Figure 4.18 (a) shows the evolution of the D retention as a function of the temperature for the different experiments listed above and the simulations. As it can be seen, the simulations reproduce well the global trends: the D retention decreases as the implantation temperature increases. The simulations reproduce especially well the evolution of the D retention reported by Tian et al. [96] for the same incident flux, the same ion energy and the same incident fluence. The quantitative difference between our simulations and the experimental results from Haasz et al. [100] and Roszell et al. [88] may be due to the fact that in these two works, the PCW used have been supplied by Rembar. The experiment on which the model is parametrized as well as the experimental results of Tian et al. [96] shown on figure 4.18 (a) have been done on PCW supplied by Plansee. In addition, Tian et al. [96] investigates the difference of the D retention in Plansee's PCW and in Rembar's PCW: the Rembar's PCW retained 2 to 3 times more D than Plansee's PCW. Despite this difference, which is probably due to different impurity contents and so different trap concentration amounts, the qualitative decrease of the D retention with the implantation temperature is reproduced. Thus, the trapping parameters determined in section 4.2.2 are suitable for reproducing the evolution of the D retention as a function of the implantation temperature.

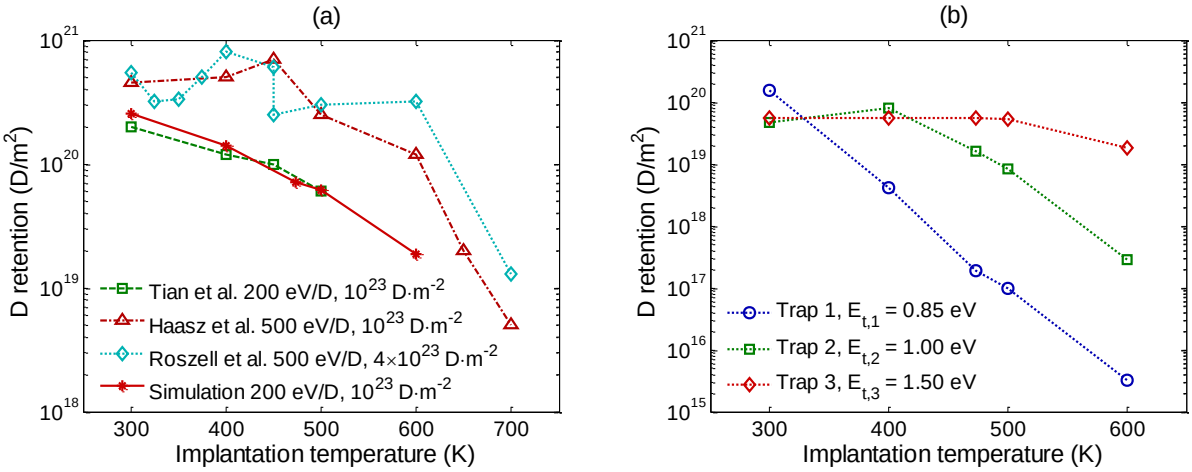

Figure 4.18. (a) Evolution of the D retention as a function of the implantation temperature for three different experiments and for the simulations.

(b) Evolution of the D retained in the different traps as a function of the implantation temperature for the simulations.

The implantation parameters of the simulations are an incident flux of 2.5×10^{19} D·m^{-2}·s^{-1}, an incident fluence of 10^{23} D·m^{-2} and an incident energy of 200 eV/D.

Figure 4.18 (b) shows the evolution of the amount of D retained in the different traps in the simulations for the different implantation temperatures. With this plot, the global trends of diminution of the D retention as a function the implantation temperature can be understood.
Concerning the evolution of trap 1, it can be seen that the amount of D retained in such trap decreases continuously as the implantation temperature increases. This continuous decrease can be explained by the drops of the equilibrium ratio as the temperature increases: at 300 K and for the considered incident flux, it is ~ 0.99 but at 400 K, it drops around 0.05.
Concerning the evolution of trap 2, it can be seen that the amount of D retained in this trap first increases between 300 K and at 400 K and then gradually decreases as the implantation temperature increases. For the considered flux, the equilibrium ratio at 300 K and 400 K is respectively 0.99 and 0.97. Thus, such trap can retain efficiently the D at 300 K and at 400 K. However, at 400 K, the total concentration of trapped particles $\Sigma_i R_{trap,i} \cdot n_i$ decreases compared to 300 K since trap 1 cannot trap D at 400 K. The depth reached by the D in the simulation can be estimated using the formula derived from the analytical model. It is according to equation 3.31:

$$R_d(t) = \sqrt{\frac{2 \cdot D(T) \cdot c_m^{MAX}}{\Sigma_i R_{trap,i}(c_m^{MAX},T) \cdot n_i} \cdot t}$$

According to equation 3.33, the product $D(T) \cdot c_m^{MAX}$ does not change between 300 K and 400 K. Thus, between these two temperatures, since $\Sigma_i R_{trap,i} \cdot n_i$ decreases, the depth at which the D migrates increases, increasing the amount of D trapped in trap 2 (equilibrium ratio almost equal to 1).
For temperature higher than 400 K, the equilibrium ratio of trap 2 drops (0.05 at 473 K for the incident flux used). Thus, the amount of D trapped inside trap 2 decreases.
Finally, it can be seen that the amount of D retained in trap 3 does not evolve for temperature below 500 K. For this trap and the incident flux considered, the equilibrium ratio is close to 1 up to 500 K. Thus, all the created traps are almost filled for temperature between 300 K and 500 K.

At 600 K, the equilibrium ratio of trap 3 is ~0.82: the amount of D trapped inside trap 3 begins to decrease. Since, the value of x_{diff} increases with the implantation temperature, the amount of D retained in trap 3 should increase with the temperature between 300 K and 500 K.
In fact, it does but slightly and it cannot be seen on the logarithmic scale on figure 4.18 (b). The reason is that the majority of the D retained by trap 3 is trapped in the near surface region (up to 10 nm) where the amount of trap is saturated because the creation rate η_a is high in this zone (table 4.2). However, in the sub-surface (up to ~x_{diff}), the creation rate η_b is one order of magnitude lower: at a fluence of 10^{23} D·m^{-2}, the amount of traps created is low in the sub-surface zone.
At higher fluence, the overall amount of trap created in the sub-surface layer would be higher and thus the amount of D retained in trap 3 would increase between 300 K and 500 K.
It is to note that such increase of the D retention at 500 K compared to the D retention at 300 K has been observed by Lindig et al. [98] and by Alimov et al. [47, 99, 101] after implantation of different grades of PCW by 38 eV/D ions at high fluxes (10^{22} D·m^{-2}·s^{-1}) and at high fluences (10^{26} – 10^{27} D·m^{-2}).

Summary:

- The detrapping parameters (detrapping energies and trap concentrations) determined from the reproduction of TDS spectrum allow reproducing the evolution of the D retention as a function of the fluence for two temperatures 300 K and 473 K.
- The same detrapping parameters allow reproducing the evolution of the D retention with the implantation temperature for a fluence of 10^{23} D·m^{-2}. For this fluence, the trend is that the D retention is maximum at 300 K and decreases. At 600 K, the D retention is one order of magnitude lower than the D retention at 300 K.
- In these simulations the value of x_{diff} increases with temperature as determined from the simulations of SCW experiments. This increase suggests that the D retention in trap 3 (created traps) will increase as function of the temperature for higher fluence as it is observed experimentally.

4.2.4. Summary of the simulations of undamaged PCW samples

In section 4.2, several simulations have been done of D implantation on PCW samples. These simulations have been compared to experimental results separated into two classes:

- The high flux implantations for incident flux higher than 5×10^{17} D·m^{-2}·s^{-1},
- The low flux implantations for incident flux lower than 5×10^{17} D·m^{-2}·s^{-1}.

From these simulations of experimental TDS, the conclusions that can be made are:

- For implantation around 300K in the case of a low flux implantation, a single mean detrapping energy of 1.1 eV is able to explain the desorption of D around 300 K. It also explained the shift of the TDS peak of 40 K toward the high temperature as the storage time increase from 2 h to 135 h. This trap with a detrapping energies of around 1.1 eV is attributed to GBs.
- The mismatching of the temperature position between the experimental measurements and the simulation can be caused by a broaden distribution of the binding energies of H with GB as shown by MD simulations.

- For implantation around 300 K in the case of a high flux implantations, three mean detrapping energies are needed to reproduce the experimental TDS spectrum. These traps are:
    - Trap 1 with a detrapping energy of 0.85 eV. It is an intrinsic trap. This trap is associated to dislocations and Fe impurity present in the PCW samples. This trap is not observed on the low flux experiment because of its low equilibrium ratio at 300K in case of a low flux implantation: the value of c_m^{MAX} is not high enough to guarantee that the trapping frequency is higher than the detrapping frequency.
    - Trap 2 with a detrapping energy of 1.0 eV. It is also an intrinsic trap. This trap is the same as the 1.1 eV determined in the case of a low flux implantation (the uncertainty being due to the uncertainty of the temperature measurements): it is thus attributed to GBs. Its trap concentration depends on the grain size: bigger the grains are, lower the grain boundaries surface is, reducing the concentration of trap 2.
    - Trap 3 with a detrapping energy of 1.5 eV. It is an extrinsic trap created during the D ion implantation through the process described in the simulations of SCW experiments. It is then attributed to VOH and VCH traps.
- Two area of trap creation can be defined as in the more sophisticated simulations of SCW experiments: near the surface (in the implantation zone up to ~ 10 nm) and in the sub-surface up to a depth x_{diff} (in the range of 1 µm at 300 K). As suggested by the simulations of SCW experiments, x_{diff} evolves with the temperature: $x_{diff} \propto e^{-\frac{0.11\ eV}{k_B \cdot T}}$. In the near surface, the trap creation is faster than in the sub-surface.

The impact of the storage time at 300 K (after an implantation at 300 K) on the D retention and the D depth profile has been investigated:

- At low fluxes, no or few D can be trapped in trap 1: only trap 2 is used in the simulations of the low fluxes experiments. During the storage time, the D retained in trap 2 can be easily detrapped since no D are trapped in trap 1. Around half of the initially retained D can be desorbed in 135 h after an implantation with an incident fluence of 2.8×10^{19} D·m^{-2}.
- However, at high fluxes D can be trapped in trap 1: during the storage time, the D is first detrapped from trap 1 before any D is detrapped from trap 2. Around 30 % of the initially retained D is lost in 110 h after an implantation with an incident fluence of 10^{23} D·m^{-2}.
- The detrapped D from trap 1 migrate toward the surface to be desorbed or toward the bulk to fill trap 2 that are not filled with D. This retrapping in trap 2 has an impact on the simulated D depth profile: the D depth profile after a long storage time (~ 110 h) shows that D migrate 2 µm deeper in the bulk than in the case of the D depth profile after a short storage time (~ 5 min).

To constraint more the mean detrapping parameters obtained in our simulations, it has been try to reproduce the evolutions of the D retention as a function of the incident fluence for two temperatures and the evolution of the D retention as a function of the implantation temperature:

- Using these 3 detrapping energy, the evolution of the D retention with fluence at 300 K and at 473 K is reproduced with a good agreement.
- At 300 K, in the simulations, the D retention evolves as fluence$^{0.57}$ which is close to a square root law: the D retention in this case is limited by the D migration.
- At 473 K, in the simulations, the D retention evolves as fluence$^{0.7}$ which is away from the square root law. Analyzing the amount of D retained in the different traps, it is shown that

the main trap retaining D at this temperature is trap 3 (1.5 eV): the D retention is limited by the trap creation process for a range of fluence around 10^{21} - 10^{24} D·m^{-2}.

- The evolution of the D retention as a function of the implantation temperature for a fluence of 10^{23} D·m^{-2} is also well reproduced: for this fluence, the amount of D retained tends to decrease as the implantation temperature increases.
- In the simulations, as it is suggested by the simulations of SCW experiments, the creation in the sub-surface is extended toward the bulk as the implantation temperature increase. The amount of trap 3 created, and so the amount of D retained by trap 3, increases with the temperature up to a temperature of ~500 K. However, this observation can only be made at fluences higher than 10^{23} D·m^{-2} since at this fluence, the main amount of trap 3 created is in the near-surface layer.

Finally, it can be concluded that the detrapping parameters determined in this section are relevant to estimate the tritium retention in divertor W target of tokamak that does not experience neutron irradiation.

4.3. Simulations of damaged PCW experiments

The simulation of D ion implantations in undamaged PCW allows us determining relevant detrapping parameters to explain the D retention in such samples. Such parameters are suitable to study the fuel retention and recycling during tokamak operation without any damage generated by the neutrons of the fusion reactions. However, in a fusion tokamak, the different PFCs and so the divertor will be irradiated by 14.1-MeV neutrons. Such energetic neutrons can damage the PFMs very deeply in the materials. Such damaged can change all the material properties and especially the fuel retention so it is important to study the effect of radiation damages on the D retention in the PFM and especially in our cases in the W materials.

However, 14.1 MeV neutron sources are scarce and a hot cell facility is required to deal with neutron-irradiated samples. A good proxy to simulate the damage induced during neutron irradiation has been found in MeV heavy ion implantation and especially MeV W ions: the latter irradiation resulting in the so-called self-damaged tungsten samples.

The purpose of this section is to determine the change of the D retention properties induced by the radiation damaged in such self-damaged W. Here, we use the MHIMS code to simulate the experimental results from two papers:

- The first one is a paper by Zaloznik et al. [52] in which recrystallized PCW (2000 K/2 min) were exposed to 20 MeV W^{6+} ions at room temperature at a fluence of 7.8×10^{17} W^{6+}·m^{-2}. After the self-irradiation, the samples were annealed for 1 h at different temperatures (600 K, 800 K, 1000 K and 1200 K) and one of the sample was not annealed. After the annealing, the samples were exposed to a beam of D atoms with a thermal energy of ~ 0.3 eV/D and an incident flux of 2.6×10^{19} D·m^{-2}·s^{-1} for 144 h. The sample temperature during the exposure was 500 K. Finally, the samples were analyzed by NRA and TDS with a temperature ramp up of 0.25 K/s.
- The second one is a paper by Markelj et al. [41] in which the PCW sample was also recrystallized (2000 K/2 min) and exposed to the same 20 MeV W^{6+} ions at room temperature with the same fluence. After damaging, the W sample was exposed to a D atom beam with a thermal energy of ~ 0.3 eV/D and an incident flux of 5.8×10^{18} D·m^{-2}·s^{-1} for 48 h. During the exposure, the D depth profiles were recorded *in situ*. After the D atom exposure, the sample was cooled down to room temperature and then re-heated and

maintained at 600 K to investigate isothermal outgassing. During the isothermal desorption at 600 K, the D depth profiles were recorded at 20 h and at 43 h after the beginning of the isothermal desorption.

In both cases, the thickness of the damaged layer induced by 20 MeV W^{6+} ions was calculated to be 2.4 µm and the irradiation at the damage peak was calculated to be 0.5 dpa using the full cascade option of the SRIM® 2013 software and displacement energy of 90 eV.

For the experimental results of Zaloznik et al., all the annealing case are simulated. For the experimental results of Markelj et al., the cooling phase between the end of the exposure and the beginning of the isothermal desorption and the re-heating at 600 K before the isothermal desorption are not simulated to simplify the simulation.

4.3.1. Determination of the surface energy barriers

To simulate both experiments, the code MHIMS is used. The exposure is done with low energetic D atoms: the boundary condition used is the surface model described in section 3.2.2. Indeed, it has been observed experimentally that the surface processes are limiting the entering of 5eV/D ions inside the PCW samples [106]. Thus, they would also limit the entering of 0.3 eV/D atoms.

The first step is then to determine the energy barriers on the surface using the procedure exposed in section 3.3.2 and summarized as followed:

1. Estimation from the experimental results of the surface concentration in steady state c_{surf}^{eq}. Using equation 3.29, it gives the value of the desorption energy per D atom, E_D.
2. Estimation from the experimental results of the migration depth $R_d(t)$ and the concentration of trapped particle $\Sigma_i R_{trap,i}(c_m^{MAX}, T) \cdot n_i$. Using equation 3.34, it gives the value of c_m^{MAX} needed to reach $R_d(t)$.
3. From the estimation of c_m^{MAX} and c_{surf}^{eq}, using equation 3.27, the difference $\Delta E = E_A - E_R$ can be estimated. Assuming the value of E_R, the value of E_A can be determined. In the next, it is assumed that $E_R = E_{Diff} = 0.2$ eV as shown by several DFT calculations [66, 68].

i. Desorption energy per D atom E_D

For exposure at 500 K :

No data on the surface concentration has been reported after exposure at 500 K in [52]. However, from *in situ* ERDA measurements of self-damaged W exposed to 0.3 eV/D atoms at 480K with an incident flux of 6.3×10^{18} D·m^{-2}·s^{-1}, it is observed, in steady state, that the surface concentration of D reaches 3×10^{19} D·m^{-2} [41]. To determine the value of E_D in these conditions, we plot on figure 4.19 (a) the evolution of c_{surf}^{eq} given by equation 3.29 as a function of E_D. From that plot, the value $E_D = 0.69$ eV at 480 K is deduced. The energy barriers at the surface should not change much between 480 K and 500 K so this estimated value of E_D will be used for the simulation of the D atom exposures.

With such desorption energy, the surface concentration in equilibrium c_{surf}^{eq} is 3×10^{19} D·m^{-2} in the implantation condition of Zaloznik et al. [52] (i.e. 500 K and an incident flux of 2.6×10^{19} D·m^{-2}·s^{-1}.

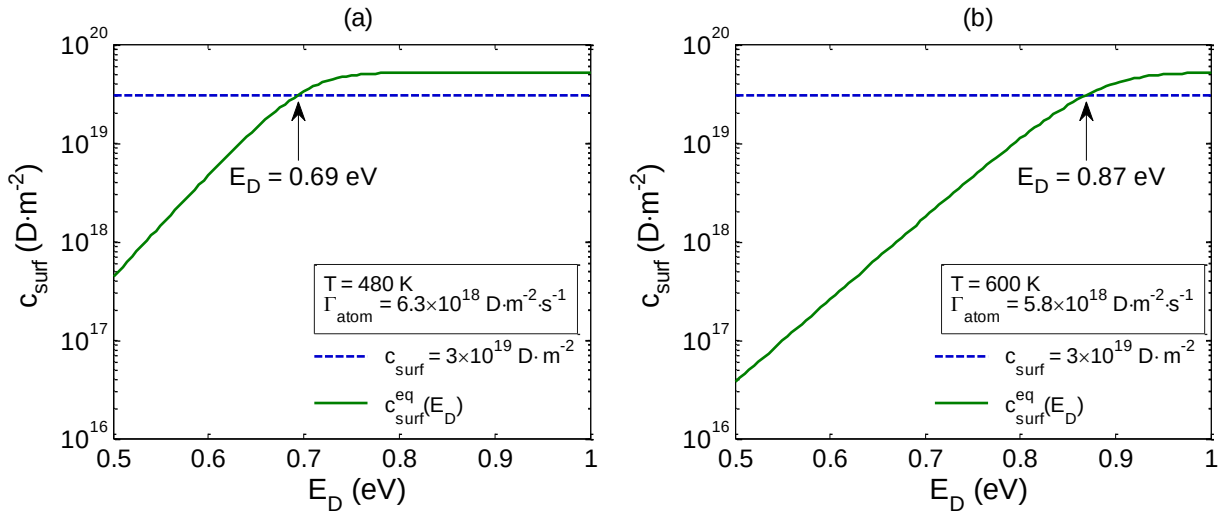

Figure 4.19. (a) Green solid line: evolution of c^{eq}_{surf} with E_D given by equation 3.29 for a temperature of 480 K and an incident flux of 6.3×10^{18} D·m^{-2}·s^{-1}, Blue dashed line: experimentally measured (ERDA) value of c_{surf} in **[41]** in the same conditions.

(b) green solid line: evolution of c^{eq}_{surf} with ED given by equation 3.29 for a temperature of 600 K and an incident flux of 5.8×10^{18} D·m^{-2}·s^{-1}, blue dashed line: value determine from experimental depth profiles **[41]** obtained in the same conditions.

For exposure at 600 K:

To estimate the energy E_D a 600 K, we look at the D depth profiles during the atom exposure (see figure 4.22) and the evolution of the D retention during the implantation (see figure 4.21). From the experimental depth profile obtained after a 2.5 h of exposure, the part of D retained in the bulk is ~ 5 – 6×10^{19} D·m^{-2}. In [41], the integrated amount of D (surface+bulk) is recorded to be ~ 5 – 9×10^{19} D·m^{-2} after 2.5 h of exposure at 600 K: it can be considered that during the atom exposure, the surface concentration reaches 3×10^{19} D·m^{-2}. Using equation 3.29 and plotting c^{eq}_{surf} as a function of E_D on figure 4.19 (b) for the exposure conditions used in the experiment (600 K and an incident flux of 5.8×10^{18} D·m^{-2}·s^{-1}) allows determining $E_D = 0.87$ eV for this value of surface concentration of D. This value is different from the one determined in the case of exposure at 500 K. The change can be explained by the presence of different adsorption sites present on the W surface as explained in section 2.3.1: the desorption energy determined is an average desorption energy on all the different adsorption sites present on the W surface.

ii. Absorption energy E_A

For exposure at 500 K:

According to the experimental D depth profile obtained by Zaloznik et al. after a 0.3 eV/D atom exposure of 144 h at 500 K with an incident flux of 2.6×10^{19} D·m^{-2}·s^{-1} on the non-annealed self-damaged PCW (figure 2.15), it can be estimated that:

- $R_d(144\text{ h}, 500\text{ K}) = 1.7$ µm,
- $\Sigma_i R_{trap,i} \cdot n_i \approx 0.42$ at. %.

According to equation 3.34, the concentration of mobile particles needed to reach this depth is $c_m^{MAX}(500\ K) = 1 \times 10^{-11}$ at. fr.. Using a surface concentration of 3×10^{19} D·m^{-2} obtained with the energy $E_D = 0.69$ eV, equation 3.27 gives $\Delta E = 1.13$ eV. As it is assumed that $E_R = E_{diff} = 0.2$ eV, the energy barrier to go from surface to bulk is $E_A = 1.33$ eV. Therefore, in the simulation we will use the following energy barriers: $E_D = 0.69$ eV, $E_R = 0.2$ eV and $E_A = 1.33$ eV.

For exposure at 600 K:

The experimental D depth profile obtained after a 0.3 eV/D atom exposure of 48 h at 600 K with an incident flux of 5.8×10^{18} D·m^{-2}·s^{-1} on a self-damaged PCW (figure 4.22) shows that:

- $R_d(48\ h, 600\ K) = 2 - 2.2$ µm,
- $\Sigma_i R_{trap,i} \cdot n_i \approx 0.33$ at. %.

Using equation 3.34, it is found that the concentration of mobile particles needed to reach this depth is $c_m^{MAX}(600\ K) = 1.4(\pm0.1) \times 10^{-11}$ at. fr.. Using the surface concentration of 3×10^{19} D·m^{-2} used previously to determine the energy barrier at the surface, equation 3.27 gives $\Delta E = E_A - E_R = 1.34 \pm 0.01$ eV. Thus, since it is assumed that $E_R = E_{diff} = 0.2$ eV, the energy barrier for absorption from the surface to the bulk is $E_A = 1.54 \pm 0.1$ eV. In the simulation, we use: $E_D = 0.87$ eV, $E_R = 0.2$ eV and $E_A = 1.55$ eV.

iii. Comparison with DFT and experimental values

The values that are used in the simulations are summarized in table 4.3.

	Simulations at 500 K	Simulation at 600 K
E_D (eV)	0.69	0.87
E_R (eV)	0.2	0.2
E_A (eV)	1.33	1.55

Table 4.3. Value of the energy barriers used in the simulations of 0.3 eV/D exposure at 500 K and at 600 K.

The theoretical and experimental determination of the desorption energy per H atom is summarized in table 2.2. Different desorption energy per H are determined depending on the surface orientation. In any case, at low coverage ($\theta < 0.5$) the desorption energy per H atom is $E_D = 0.7 - 0.91$ eV. The surface coverage at the equilibrium in both case studied here is low ($\theta \approx 0.3$). Thus, the desorption energies per H obtained from our analytical determination and that are used in the simulations agree well with the experimental and DFT values.

Concerning the values of E_A, no direct experimental determination of the value of this energy barrier exists. However, it is explained by 't Hoen et al. [106] that the insertion of 5 eV/D ions is also limited by surface processes. From the simulations of their results, they extracted an absorption energy around 1.6 eV which agrees well with our determined value (especially for the value at 600 K). However, it seems to be a bit low compared to the values calculated by DFT (table 2.2) which are between 2 – 2.4 eV [65, 66, 68, 67]. This low value of E_A has an incidence on the solution energy $E_S = E_A - E_D - E_R$ calculated from the values of table 4.3: the solution

energy is $E_S = 0.44$ eV at 500K and $E_S = 0.48$ eV at 600 K. Such values are much lower than the value of 1.04 eV determined experimentally by Frauenfelder [29]. The difference could come from the difference in sample preparation in the work of Frauenfelder and in the work from Markelj and Zaloznik [41, 52]. In the former, the sample was annealed at 2400 K for 10 hours in vacuum and then at 2400 K for 10 hours in H_2 atmosphere (600 Torr), while in the latter samples were annealed for 2 min at 2000 K. It is well known that tungsten oxide needs a temperature of 2400 K to be removed [151]. Thus, differences in surface oxide coverage are likely responsible for the different values of solution energy determined from Markelj and Zaloznik experiments and from Frauenfelder experiments. Other explanations could involve variation in tungsten crystals purity and subsequent surface segregation of contaminants or even grain boundary densities in the hypothesis that the latter would facilitate HIs insertion into the bulk.

4.3.2. Simulations of the experimental results

Using the energy barriers derived from the steady-state analysis and summarized in table 4.3, we are now able to simulate the experimental atom exposures at 500 K and at 600 K.

i. D atom exposures at 500 K

In the case of the atom exposures at 500 K, we simulated the exposures and TDS for all the annealing cases used in the experience of Zaloznik et al. [52], from the non-annealing case to the 1200K-annealing case. The simulations are separated in 4 phases:

- The D exposure at 500 K with an incident flux of 2.9×10^{19} D·m^{-2}·s^{-1} and an exposure time of 144 h,
- A cool down phase: the temperature decreases from 500 K to 300 K in 30 min.
- A storage time of 8 h at 300 K.
- The increase of the temperature to simulate the TDS experiments. The same evolution of the temperature as in experiment is used: at the beginning of the TDS (below a temperature of 700 K), the temperature does not evolve truly linearly. Above 700 K, the heating ramp is constant equal to 0.25 K/s.

During the atomic exposures, there are $c_{surf}^{eq} \approx 2.9 \times 10^{19}\ D \cdot m^{-2}$ and $c_m^{MAX} \approx 1.0 \times 10^{-11}$ at. fr. as expected from the steady-state study.

Simulations of the experimental D depth profiles and TDS spectra:

From previous section 4.2, three detrapping energies exists in the undamaged PCW samples: 2 intrinsic traps (trap 1 with a detrapping energy of 0.85 eV and trap 2 with a detrapping energy of 1.0 eV) and an extrinsic trap created by the ion implantation (trap 3 with a detrapping energy of 1.5 eV). In these simulations, the extrinsic trap 3 is not taken into account since D atom exposure is simulated and would not create such trap. The concentration of the two intrinsic traps (i.e. in all the materials) are around 0.01 at.% according to NRA results obtained on recrystallized PCW samples implanted at 320 K with D ions [130]. For these two intrinsic traps, the equilibrium ratios (equation 3.8) at 500 K and for $c_m = 1.0 \times 10^{-11}$ at. fr. are:

- $R_{trap,1}(500\ K, c_m = 1.0 \times 10^{-11}) = 1 \times 10^{-5}$
- $R_{trap,3}(500\ K, c_m = 1.0 \times 10^{-11}) = 2 \times 10^{-4}$.

Thus, these two traps retain very few D during the exposures and they do not impact the simulation results.

Figure 4.20 shows the comparison between the experimental and simulated D depth profiles (a) and the comparisons between the experimental and simulated TDS spectra (b) for the non-annealed case, the 800 K-annealed case and the 1200 K-annealed case (the other annealing cases are also simulated but not shown on the plot for sake of clarity).
The experimental D depth profiles and the experimental TDS spectra are well reproduced for the different annealing cases. In order to achieve a good agreement, three new traps have to be introduced in the simulations with three new detrapping energies: $E_{t,4} = 1.65$ eV, $E_{t,5} = 1.85 \pm 0.03$ eV and $E_{t,6} = 2.06 \pm 0.04$ eV. They will be referred in the following as trap 4, trap 5 and trap 6 respectively. On the TDS spectra, a main peak is observed at 875 K followed by a shoulder at 700 K and at 1000 K – 1100 K. In the simulations, the main peak (detrapping from trap 5) and the high temperature shoulder (detrapping from trap 6) are especially well reproduced. The presence of trap 4 induces a slightly more pronounced low temperature shoulder in the simulations than in the experiments. However, without trap 4, the low temperature shoulder would not appear in the simulations. Moreover, it will be shown in section 4.3.2.ii that the trap 4 is necessary to reproduce isothermal desorption at 600 K.

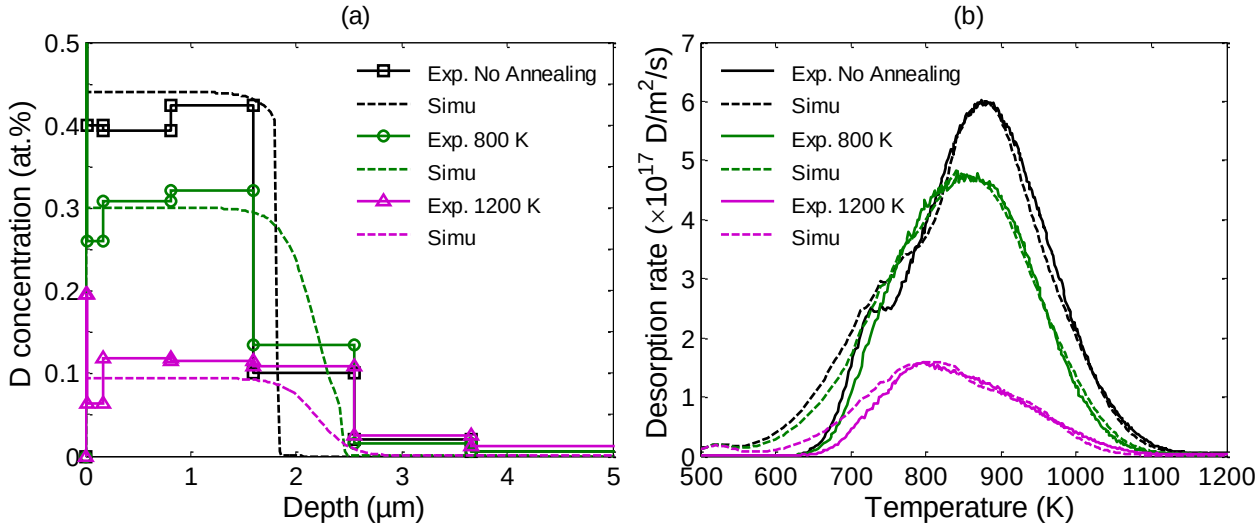

Figure 4.20. (a) Comparison between the experimental and simulated D depth profiles obtained after 144 h D atom exposure on self-damaged W samples with a flux of 2.9×10^{19} D·m^{-2}·s^{-1} at 500 K.

(b) Comparison between the experimental and simulated TDS spectra obtained after the same D atom exposure. The heating ramp is 0.25 K/s. Only the cases of non-annealed, 800 K-annealed and 1200 K-annealed samples are presented for sake of clarity.

To reproduce the D depth profiles, uniform distributions of traps for trap 4, trap 5 and trap 6 are used in the damaged layer up to depth around 2.2 µm. The trap concentrations then decrease between 2.2 µm and 2.4 µm. A uniform distribution of traps is not expected from the damaged profile given by SRIM®. However, it is observed by 't Hoen et al. [95] that the amount of D retained in self-damaged W saturates for damaging level of 0.2 dpa. It means that the primary defects induced during the irradiation have evolved into more complex defects. The amount of these defects saturated if the dpa level is higher than 0.2 dpa. In the considered experiments, the samples are damaged up to 0.5 dpa: the amount of defects is saturated and the concentration of traps in the damaged layer is uniform.

Evolution of the trap concentrations as a function of the annealing temperatures:
The concentrations of trap 4, trap 5 and trap 6 in the damaged layer used in the simulations are summarized in table 4.4 for all annealing cases. To obtain the overall amount of traps (for each different trap) present in the damaged layer, the trap concentrations used in the simulations are integrated in the entire damaged layer (between 0 and 2.4 µm). Figure 4.21 shows the evolution of this integrated amount of traps in the damaged layer as a function of the annealing temperatures. The point at 500 K corresponds to the non-annealed case.

Annealing case	**Trap 4 concentration** $\mathbf{E_{t,4} = 1.65 \pm 0.01\ eV}$	**Trap 5 concentration** $\mathbf{E_{t,5} = 1.85 \pm 0.03\ eV}$	**Trap 6 concentration** $\mathbf{E_{t,6} = 2.06 \pm 0.03\ eV}$
No annealing	0.09 at.%	0.28 at.%	0.08 at.%
1 h at 600 K	0.08 at.%	0.23 at.%	0.06 at.%
1 h at 800 K	0.06 at.%	0.19 at.%	0.05 at.%
1 h at 1000 K	0.00 at.%	0.15 at.%	0.02 at.%
1 h at 1200 K	0.00 at.%	0.05 at.%	0.04 at.%

Table 4.4. Concentration of the trap 4, trap 5 and trap 6 for the different annealing cases simulated.

On table 4.4 and on figure 4.21, it can be seen that the trap with the highest concentration is trap 5: detrapping from this trap is at the origin of the main desorption peak at 875 K. As the annealing temperature increases, the amount of trap 5 decreases gradually. It can also be seen that the amount of trap 4 decreases slowly between non-annealed (500 K) case and 800 K-annealed case but it completely disappears after annealing of 1 h at 1000 K or any higher temperature. Finally, it can be seen that the amount of trap 6 decreases also slowly between non-annealed (500 K) case and 1000 K-annealed case and it increases between the 1000 K-annealed case and the 1200 K-annealed case.
The evolution of the integrated trap amount with the annealing temperature and the value of the detrapping energies used in these simulations will be used to discuss the nature of the three traps created by the self-irradiation in section 4.3.3.

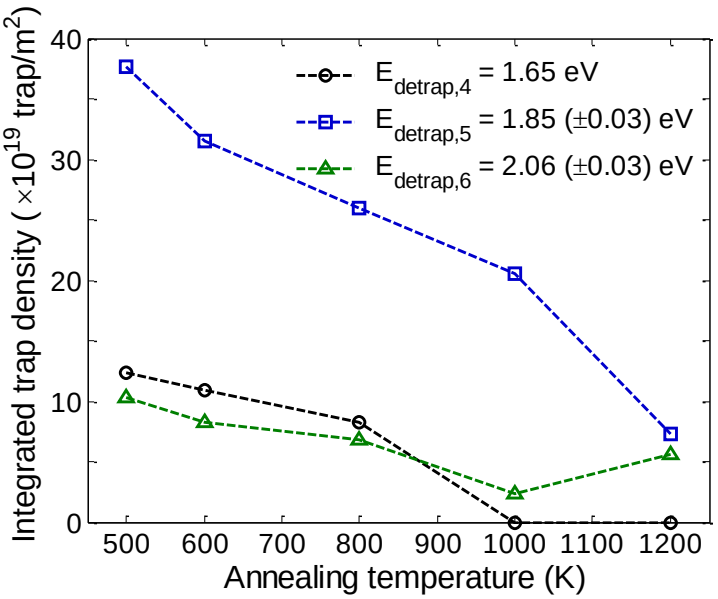

Figure 4.21. Integrated amount between 0 and 2.4 µm of the trap concentrations of slef-irradiation induced traps as function of the annealing temperature for the simulation of D atom exposure at 500 K. The point at 500 K corresponds to the non-annealed case.

Summary:

- To simulate accurately TDS spectra after atom exposure of self-damaged PCW at 500 K, 3 new traps with 3 new detrapping energies are needed:
  - Trap 4 with a detrapping energy of 1.65 eV,
  - Trap 5 with a detrapping energy of 1.85 eV,
  - Trap 6 with a detrapping energy of 2.06 eV.
- The evolution with the annealing temperature of the trap concentration for each of these traps shows that:
  - Trap 4 concentration decreases slowly between 500 K and 800 K and disappear around 1000 K,
  - Trap 5 concentration decreases gradually from 500 K to 1200 K,
  - Trap 6 concentration decreases slowly between 500 K and 1000 K and increases between 1000 K and 1200 K.

ii. D atom exposure at 600 K

In the case of the exposure at 600K, the simulation is separated in 2 phases:

- The exposure at 600 K with an incident flux of 5.8×10^{18} $D\cdot m^{-2}\cdot s^{-1}$ and an exposure time of 48 h,
- The isothermal desorption at 600 K for 43 h: during this period, the incident flux is 0.

The cooling step and re-heating step are not simulated to simplify the simulation. The energy barriers at the surface used in the simulations are the one presented in table 4.3. Using these energy barriers, during the atomic exposure, $c_{surf} = 3 \times 10^{19}\ D \cdot m^{-2}$ and $c_m^{MAX} = 1.3 \times 10^{-11}$ at. fr. as expected from the steady-state analysis.

Trapping parameters used in the simulations:

In this simulation, the detrapping energies used are the same as the ones obtained from the simulations of exposure at 500 K (section 4.3.2.i):

- There are the 2 intrinsic traps: trap 1 with a detrapping energy of 0.85 eV and trap 2 with a detrapping energy of 1.00 eV. Due to their low detrapping energies, the D retained in these traps during exposure at 600 K is negligible.
- The three new traps obtained from the simulations of the TDS spectrum: trap 4 (1.65 eV), trap 5 (1.85 eV) and trap 6 (2.06 eV).

In the simulation, the three self-irradiation induced traps have similar distributions in the damaged layer as in the simulations of D atom exposures at 500 K (section 4.3.2.i): uniform between 0 and 2 µm followed by a decrease between 2 and 2.4 µm. The trap concentrations for each trap in the uniform damaged layer are: is $n_4 = 0.19\,\text{at.}\%$, $n_5 = 0.16\,\text{at.}\%$ and $n_6 = 0.02\,\text{at.}\%$. These values are adjusted to reproduce the experimental depth profiles and the experimental evolution of the D retention during the exposure and the isothermal desorption at 600 K (see below).

Figure 4.22 shows the evolution for the experiment and the simulation of the total D retained (adsorbed D on the W surface + D in the bulk) as a function of time during the exposure (between 0 and 48 h) and during the isothermal desorption (between 48 h and 48 h + 43 h). The simulated amount of D retained in trap 4, trap 5 and trap 6 as well as the amount of D adsorbed on the surface is also shown.

Figure 4.23 shows the evolution of the simulated and experimental D depth profiles during the atom exposure at 600 K (a) and during the isothermal desorption at 600 K (b).

During the exposure at 600K:

The simulation reproduces very well the increase of the experimental D retention during the exposure presented in figure 4.22. In the simulation, during the exposure, the D retention evolves as the square root of the time as predicted by the simple analytical model (section 3.3.2). Looking at the comparison between simulated and experimental D depth profiles (figure 4.23 (a)), a good agreement can be seen: as the exposure time increases, the D migrates deeper and deeper in the bulk. This migration can be understood as a diffusion hindered by the presence of trap 4, trap 5 and trap 6 in the damaged layer. The corresponding effective diffusion coefficient can be roughly calculated as $D_{eff} = \frac{L_{mig}^2}{t_{exposure}}$ with L_{mig} the migration length observed in the simulation (figure 4.23 (a)) for a given exposure time $t_{exposure}$. From the simulation results presented figure 4.23 (a), there is $D_{eff} \approx 10^{-17}\ m^2 \cdot s^{-1}$ which is far lower than the diffusion coefficient from TIS to TIS used in the simulations (at 600 K, $D_H(T) = 3 \times 10^{-9}\ m^2 \cdot s^{-1}$).

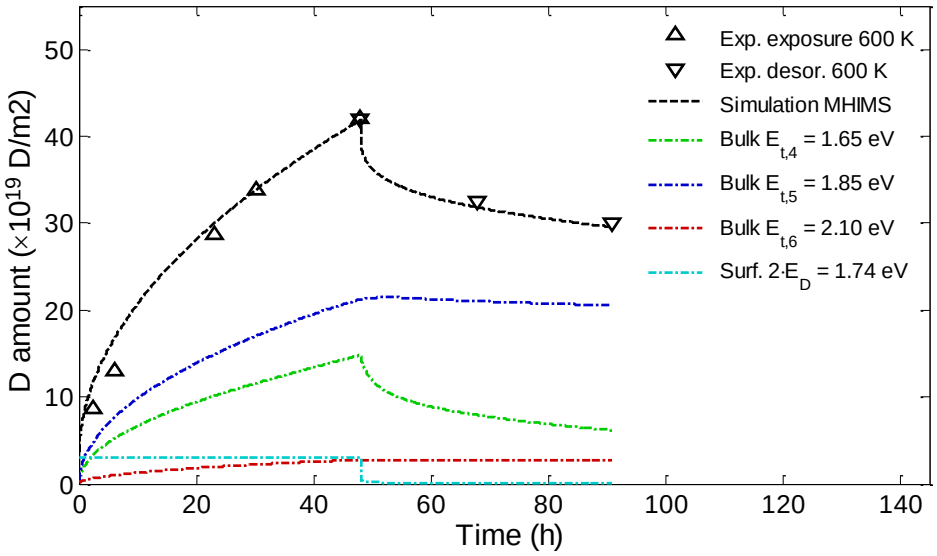

Figure 4.22. Comparison between the simulated and experimental evolutions of the D total amounts with time during a 48 h atomic exposure at 600 K with an incident flux of 5.8×10^{18} D·m^{-2}·s^{-1} followed by an isothermal desorption at 600 K for 43 h.

During the isothermal desorption at 600 K:

Looking at figure 4.22, it can be seen that the experimental decrease of the D retention during the isothermal desorption at 600 K is also well reproduced by the simulation. Analyzing the amount of D retained in the three self-irradiation induced traps as well as the amount of D adsorbed on the surface, it can be seen that during the isothermal desorption at 600 K, the amount of D adsorbed on the surface quickly (few minutes) falls to nearly zero: as no flux is present to maintain a high coverage on the surface, the surface concentration falls because at 600 K, the desorption of D_2 is quick with an activation energy of $2 \cdot E_D = 1.74$ eV.

After that first desorption, a slower desorption can be seen in the 10-hours scale: it is due to detrapping of D from trap 4 (with the smaller detrapping energies) in the bulk and diffusion toward the surface. A small amount of D trapped in trap 5 is also detrapped during the isothermal desorption but it is below 1 %. At the end of the 43 h isothermal desorption, 30 % of the initially retained D has been desorbed.

The detrapping of D from trap 4 induces a change in the simulated D depth profiles as it is observed experimentally (figure 4.23 (b)): the maximum concentration of D decreases from around 0.3 at.% to around 0.2 at.% and a shift of the maximum concentration from the surface to around 1.5 µm is observed as in the experiments. In addition, as in the experimental observations, the D concentration below the surface falls to around 0.15 at.% because the D trapped near the surface are the first to be desorbed.

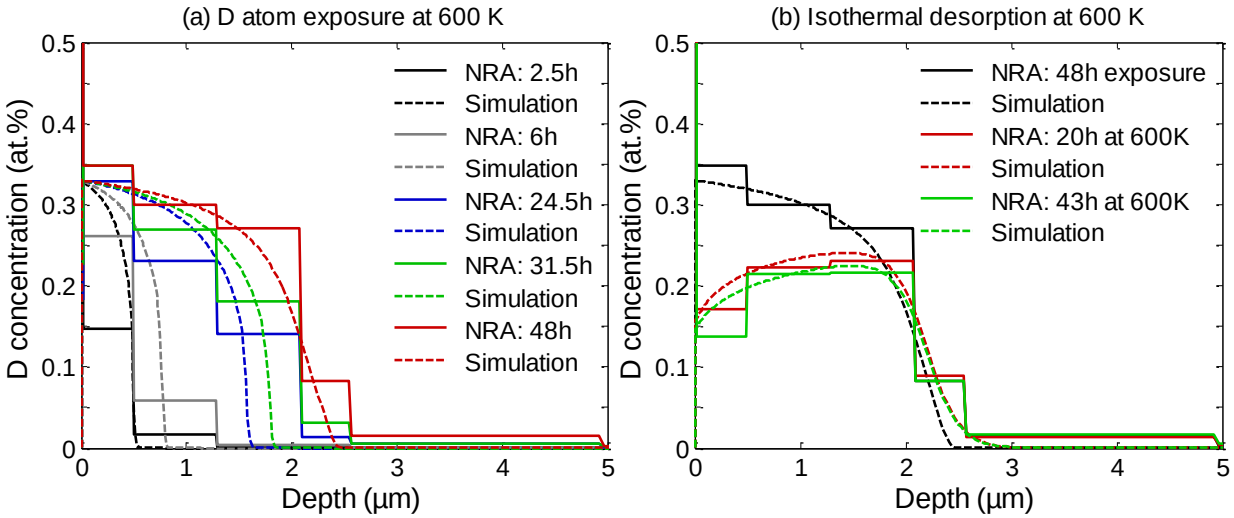

Figure 4.23. (a) Experimental and simulated D depth profiles during the D atom exposure at 600 K (maximum exposure time = 48 h).

(b) Experimental and simulated D depth profiles during the isothermal desorption at 600 K.

Summary:

- The three new traps derived from the simulations of exposures at 500 K (trap 4, trap 5 and trap 6) are robust to reproduce experimental D depth profiles obtained during an atom exposure at 600 K.
- They are also robust to reproduce the evolution of the D depth profiles and the D retention during an isothermal desorption at 600 K that follows the exposure at 600 K.

4.3.3. Discussion on the nature of the traps

The detrapping energy obtained from previous MRE simulations of retention/desorption from self-damaged [20, 106, 109] and neutron irradiated samples [97] are (table 2.3):

- Between 1.7-2.0 eV according to Gasparyan *et al.* [109] (self-damaged samples),
- 0.9 eV, 1.45 eV, 1.85-1.9 eV, 2.2 eV and 2.4 eV according to Ogorodnikova *et al.* [20] (self-damaged samples),
- 1.2 eV, 1.4 eV, 1.85 eV and 2.05 eV according to ‘t Hoen *et al.* [106] (self-damaged samples),
- 0.9 eV, 1.1 eV, 1.3 eV, 1.5 eV, 1.75 eV and 2.0 eV according to Shimada *et al.* [97] (neutron damaged samples).

Figure 4.24 compares these different detrapping energies with the detrapping energies for the 6 traps determined in our simulations of PCW experiments (damaged and undamaged). It can be seen on figure 4.24 that the detrapping energies observed in self-damaged PCW are similar (if not the same) as the detrapping energies observed in neutron damaged PCW. This indicates that MeV W ions are a good proxy to simulate radiation damaged induced by neutron irradiation.

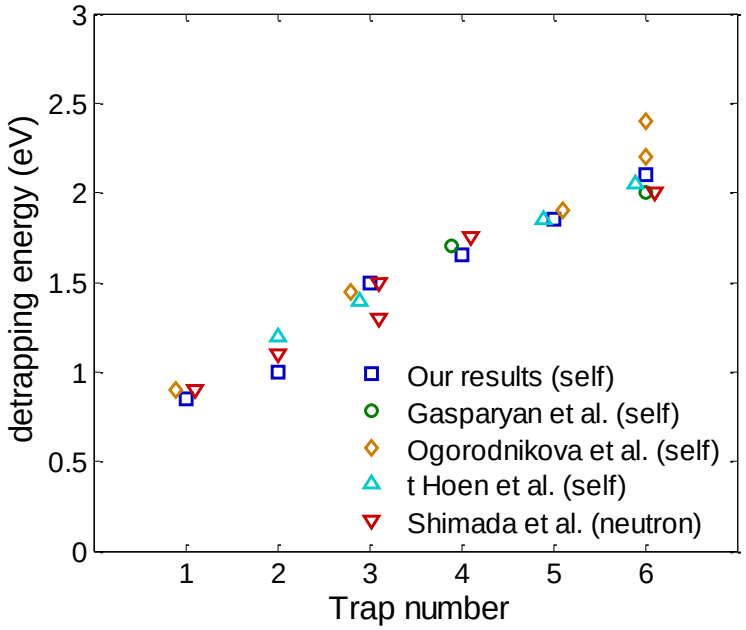

Figure 4.24. Detrapping energies obtained from different MRE studies in self-damaged (self) and neutron (neutron) damaged PCW experiments. For our results, the 6 detrapping energies are shown even if trap 3 is not used in our simulations of self-damaged PCW.

Trap 1 and Trap 2, intrinsic traps:

It can be seen on figure 4.24 that in the case of trap 1 and trap 2, other MRE simulations observed such traps. Ogorodnikova et al. observed trap 1 in undamaged PCW [25, 131] but the concentration of this trap increases in the case of the self-damaged PCW [20]. In addition, Shimada et al. [97] observed that trap 1 appears in their simulations of neutron irradiated PCW. In our simulations of self-damaged PCW, this increase cannot be observed because, as discussed, the amount of D retained in such traps at 500 K and 600 K are completely negligible.

Trap 3, mono-vacancies:

Considering trap 3, it can be seen on figure 4.24 that other studies observed this trap in both undamaged and damaged PCW. Ogorodnikova et al. [25] used this trap as a D ion induced trap as we do in the case of undamaged PCW (section 4.2). However, in addition to the D ion induced traps Shimada et al. [97],'t Hoen et al. [106] and Ogorodnikova et al. [20] used this traps in the damaged layer to reproduce a TDS peak around 600 K. In the TDS spectra simulated here, such peak is not present: thus this detrapping energy is not used in the simulation of the self-damaged PCW experiments. In the previous section (section 4.2.2), it has been suggested that trap 3 corresponds to mono-vacancy by comparing the obtained detrapping energies from the TDS simulations and the detrapping energies extracted from the DFT calculations (see figure 4.25 in the summary of this chapter). Mono-vacancy is the first possible defect created by self-irradiation. It would make sense to use it in the MRE simulations especially for exposure at 500 K since such traps can retained D at 500 K (figure 4.18 (b)). So, since the characteristic detrapping energy is not used to reproduce the TDS spectra after a D exposure at 500 K, it means that there is no mono-vacancy in the experiments we simulated.

To understand why trap 3 are absent in the simulations, we compare the experimental condition of ‘t Hoen et al.’s experiments after implantation of ion at 525 K and the experimental condition of the experiments we simulated:

- ‘t Hoen et al. implanted a self-damaged PCW sample with D ions at a high flux (~10^{24} $D \cdot m^{-2} \cdot s^{-1}$) for tens of seconds at 525 K,
- Zaloznik et al. (the experiments we simulated) exposed a self-damaged PCW sample with D atoms at a lower flux (~10^{19} $D \cdot m^{-2} \cdot s^{-1}$) for 144 h at 500 K.

Thus the loading time in the case of Zalzonik et al. is around 4 orders of magnitude higher than in the case of ‘t Hoen loading. It has been shown by PAS that mono-vacancies begin to anneal into vacancy clusters around 523 K for 1 h annealing [55]. Thus, in the experiment by ‘t Hoen et al., the implantation is not enough for all the mono-vacancies to be annealed. In the other hand, in the case of the experiments we simulated, the implantation is long enough for all mono-vacancies to be annealed and form nano-voids which explains the absence of vacancies.

Trap 4, jogged dislocation?

The nature of the traps created by neutron of heavy ion irradiations can be deduced from STEM [52, 107] or PAS [106]: on STEM images, dislocation lines, loops and nano-voids are observed and PAS analysis indicates the presence of voids or cavities.

Terentyev et al. [119] calculated with DFT the binding energy of H with jogged dislocation to be ~ 1.4 eV for 1 – 3 H trapped and 0.7 eV for 4 – 5 H trapped. Thus, the detrapping energy of H bound to such trap is 1.6 eV for 1 – 3 H trapped and 0.9 eV for 4 – 5 trapped (figure 2.16). Then, the increase of trap 1 reported by Ogorodnikova et al. [20] and Shimada et al. [97]could correspond to the trapping into jogged dislocations (seen by STEM) filled with 4 – 5 Hs and trap 4 could be related to D trapping into jogged dislocation filled with 3 – 1 H (figure 4.25 in the summary of this chapter).

Trap 5, dislocation loops?

Xiao et al. [117] calculated with DFT the binding energies of H with dislocation loop created by removing one layer in the 16-layers supercell in order to get a stacking defect. The binding energies of H with such a defect is between 1.6 – 1.76 eV for 1 – 2 H and fall down to 0.8 eV for a third H trapped. The detrapping energies from dislocation loops are then 1.8 – 1.96 eV and 1.0 eV. Thus, trap 5 could thus correspond to dislocation loops (see figure 4.25 in the summary of this chapter).

In addition, figure 4.21 and table 4.4 show that the trap with the highest concentration is trap 5. Experimental STEM images of the damaged layer show that the density of loops is higher than the density of dislocation lines [52]. Furthermore, the amount of trap 5 starts to decrease at 600 K as the evolution of loop density does on STEM images [52].

Trap 6, nano-void?

To calculate the detrapping energy of H in vacancy-cluster, one can consider H on a free surface as a good proxy as suggested by Gorodetsky et al. [139]. In this case, the D are detrapped from the void via the surface mechanism described in figure 2.2:

- First the molecules are dissociated,
- Then D atoms are adsorbed on the void surface
- To enter the bulk, they have to overcome the barrier E_A: the detrapping energy for such process is E_A.

Since internal surfaces of a bulk nano-void should be less prone to surface contamination as compared to a true gas/solid interface, we will not use the value of E_A used in the simulations (table 4.3). Instead, the detrapping energy of trap 6 is compared to the absorption energies from the literature [65, 66, 68, 67] reported in table 2.2 calculated with DFT : the energy E_A is ~ 2.0 – 2.3 eV. Thus, trap 6 could correspond to nano-void. In addition, Watanade et al. [107] observed experimentally the growth of nano-voids for annealing above 1073 K and the concentration of the nano-voids decrease only for annealing above 1273 K. In the simulations, trap 6 concentration increases between the 1000 K-annealed case and the 1200 K-case (figure 4.21 and table 4.4) which is another point to attribute trap 6 to nano-void: since the annealing temperature is not above 1273 K in the Zaloznik et al.'s experiments, the nano-void density do not decrease but the growth of nano-voids for annealing temperature above 1073 K induces an increase of the D trapped in nano-voids and so an increase of the concentration of trap 6.

4.3.4. Summary of the simulations of self-damaged PCW

The trapping characteristics of self-damaged PCW to 0.5 dpa exposed to 0.3 eV/D atoms have been investigated. Because the D atoms exposed to the W surface are sensitive to the surface process, a surface model has to be used and parametrized. From these simulations, the conclusions that can be made are:

For the parametrization of the surface model:

- The surface model can be fully parametrized using formula derived from the steady-state equation of the model.
- The obtained values of desorption energy per H, E_D, are in good agreement with the experimentally and theoretically determined desorption energies. The values are summarized in table 4.3),
- The obtained values of absorption energy, E_A disagree of about 0.5 eV with the value calculated by DFT. The difference is attributed to the presence of impurity and oxide on the W surface.

For the trapping characteristics of self-damaged PCW:

- Three new detrapping energies are needed to reproduce the experimental observations (depth profiles, TDS spectrum, isothermal desorption at 600 K). Comparing the DFT calculation and the obtained detrapping energies, a nature for each of these traps is proposed. These analysis is strengthens by STEM images.
- Trap 4 with a detrapping energy of 1.65 eV corresponding to jogged dislocations.
- Trap 5 with a detrapping energy of 1.85 eV corresponding to dislocation loops.
- Trap 6 with a detrapping energy of 2.06 eV corresponding to nano-voids.
- The trap concentrations in the damaged layer are uniform even if the damaged profile given by SRIM® is not. This can be explained by the experimental observation of the saturation of the D retention as a function of the damage level: above 0.2 dpa, the D retention is not increasing.
- The obtained detrapping energies are compared with other MRE simulations of other and independent experimental work. It is observed that the detrapping energies obtained in our simulations agree with the other MRE simulations of experiments done on self-damaged PCW and neutron irradiated PCW. This means that the traps created by neutron irradiation are similar to the traps created by self-irradiation.

Thus, the trapping characteristic of self-damaged PCW determined in this section can be used to estimate the tritium retention in the divertor W target during the burning phase of tokamak i.e. when fusion reaction will take place in the vessel generating 14.1 MeV neutrons that will irradiate the wall.

4.4. Summary

In this Chapter, several simulations of experiments are presented in the case of different samples structure. These simulations give some understanding of the HIs retention properties of W materials. They also allow a relevant parametrization of the wall model used for tokamak applications: dynamic recycling of fuel during plasma discharges for plasma edge code (as SOLEDGE2D-EIRENE) or estimation of fuel retention during tokamak plasma discharges.
The simulations presented start from the simplest microstructure of a SCW annealed at high temperature to remove the intrinsic defects to the self-damaged PCW.

Simulations of SCW experiments:

- The D retention is limited by the creation of traps that have been identified as vacancy like defects: vacancy with hydrogen (VH), vacancy with hydrogen and Carbone/Oxygen (VCH/VOH). Depending on the implantation conditions, the created traps can mutate into vacancy clusters.
- We proposed that the trap creation is limited by the amount of light impurities (O and C) present in the SCW sample. The origin of these light impurities is multiple:
    - A part is originally present in the sample as intrinsic impurities,
    - A part comes from the background gases of the implantation chamber. During the implantation, thanks to elastic collision between the energetic D incident ions and the background gases, O and C gain kinetic energy and are implanted in the material.
- The trap creation process, predicted by thermo-statistical models, is activated by the flux i.e. the amount of mobile particles inserted inside the materials during the implantation.
- Three zones of trap creation can be highlighted:
    - In the near surface layer (up to 20 nm): it corresponds to the damaged created by the incident O and C impurities coming from the plasma.
    - In the sub-surface layer (up to several µm): we proposed that the trap creation is limited by the diffusion of the O/C impurities that are implanted during the plasma interaction. Thus, the thickness of this sub-surface layer, characterized by the migration depth of the light impurities x_{diff}, evolves with the temperature as observed experimentally.
    - In the bulk: it corresponds to the intrinsic O and C impurities present before the implantation in the sample. The quantity of these impurities is reduced when the sample is annealed.

Simulations of undamaged PCW experiments:

- Three mean detrapping energies can be determined from the simulation of TDS obtained after the D ions implantation in undamaged PCW:
    - Trap 1, an intrinsic trap, with a detrapping energy of 0.85 eV,
    - Trap 2, an intrinsic trap, with a detrapping energy of 1.1 – 1.0 eV.

- Trap 3, an extrinsic trap induced by D ions irradiation as suggested by the simulations of SCW experiments, with a detrapping energy of 1.5 eV.

– Comparing these detrapping energies to detrapping energies extracted from previously reported DFT calculations (section 2.3.1.ii and section 2.3.4.i) on figure 4.25, a nature for these traps can be proposed:

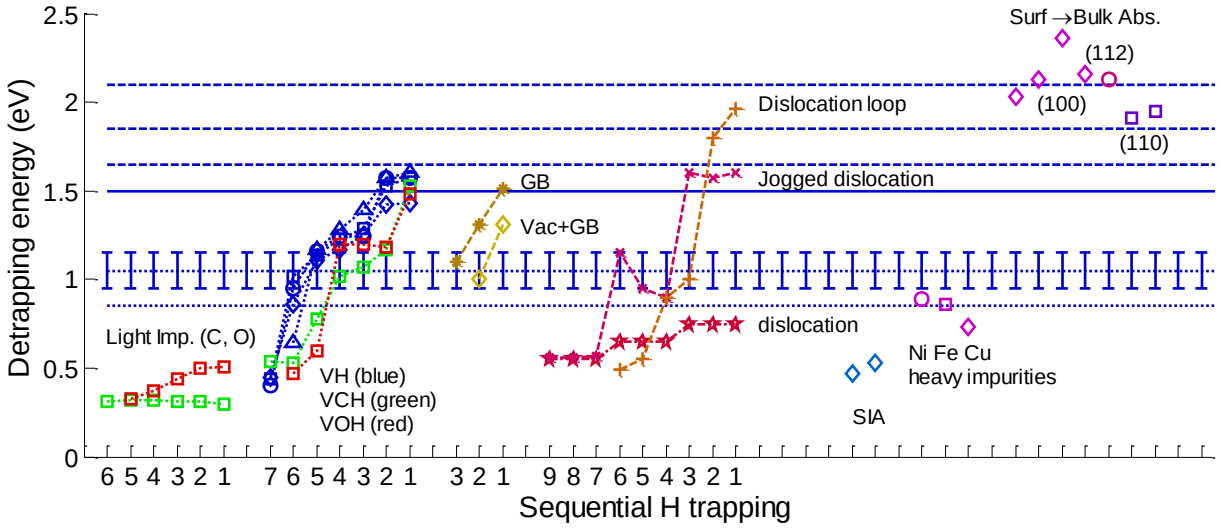

Figure 4.25. Comparison between the detrapping energies extracted from DFT ($E_{Binding}$ + 0.2 eV) for different defects and the detrapping energies obtained from the simulation of undamaged and self-damaged PCW experiments. The detrapping energies from voids with D_2 are the absorption energies from surface to bulk.

Blue dashed lines: traps from self-damaged PCW.
Blue solid line: D implantation induced traps.
Blue dotted line: intrinsic traps.

- Trap 1 may correspond to dislocation lines and Fe, Ni and Cu impurities that can be present at a high level in W.
- Trap 2 may correspond to grain boundaries: according to MD, they have a broaden distribution of binding energies which is shown on figure 4.25 by the error bar around the 1.0 eV detrapping energy.
- Trap 3, as suggested by the simulations of SCW experiments may correspond to vacancy like defects.

– The effect of the storage time after the D implantation is studied:
  - The experimental data available on that point in the literature are reproduced and they show that the storage at the 10 h scale have a big impact on the observed D retention: 50 % of the initially retained D is lost in 135 h.
  - In addition, our simulations show that the storage time has also a strong impact on the simulated D depth profiles: the D that is detrapped diffuse toward the surface and the bulk inducing desorption but also extension of the D depth profile.

– Using the set of trapping parameters obtained from the reproduction of one experimental TDS spectrum, we have been able to:

    - Reproduce the evolution of the D retention as a function of the fluence at two different temperatures,
    - Reproduce the evolution of the D retention as a function of the implantation temperature between 300 K and 600 K for a constant fluence,
    - Proposed a mechanism to explain the increase of the D retention between 300 K and 500 K as observed experimentally for fluence around 10^{26} $D \cdot m^{-2}$: as the implantation temperature increases, the zone where traps are created is extended toward the bulk (as suggested by the simulations of SCW experiments). Thus, the amount of trap created increases as the temperature rises.
- The detrapping energies obtained in these simulations seem to be able to reproduce the trapping characteristics of a non-neutron irradiated materials: they could be used to estimate the tritium retention in future tokamak with no fusion reactions.

Simulation of damaged PCW experiments:

- In addition to the three mean low detrapping energies determined in the case of undamaged PCW, three higher detrapping energies are determined from the simulations of self-damaged PCW. A nature for each of these traps is proposed based on the DFT calculations (figure 4.25) and the observation made on SEM images during the annealing of such damaged samples at different temperatures.
    - Trap 4 with a detrapping energies of 1.65 eV is attributed to jogged dislocations,
    - Trap 5 with a detrapping energies of 1.85 eV is attributed to dislocation loops,
    - Trap 6 with a detrapping energy of 2.06 eV is attributed to nano-voids and cavities.
- The concentration of each of these traps seems to be uniform throughout the entire damaged layer. It can be explained by the experimental observation of the saturation of the D retention as a function of the damage level. For damage levels above 0.2 dpa anywhere in the materials, the trap concentrations do not increase and is constant.
- The detrapping energies obtained in these simulations seem to be able to reproduce the trapping characteristics of a neutron irradiated materials: they could be used to estimate the tritium retention in future tokamaks with fusion reactions and so neutron flux damaging the wall.

5. Simulations of tokamak plasma discharges

In Chapter 4, relevant fuel retention properties have been determined reproducing several trends of SCW and PCW experiments. The purpose of this final chapter is to apply such outcomes in order to estimate the fuel retention and especially the tritium (T) retention during realistic tokamak thermal cycles. In that case undamaged and damaged actively cooled W plasma facing components are considered.
Throughout this chapter, a comparison is made between tritium retention in undamaged and damaged W. It is divided into 4 parts:

- The definition of the realistic tokamak thermal cycle,
- The simulation of the ^{3}H retention in the case of a single cycle,
- The simulation of the ^{3}H retention during 4×10 cycles,
- The simulation of a ^{3}H removal technic after 10 cycles.

In this chapter, the code MHIMS will be used to make the simulations with as boundary conditions, the one considering a quick surface recombination (section 3.2.1). Since in ITER, the PFC will be actively cooled, a thermal model is added to the current version of MHIMS to have a relevant temperature and temperature gradient inside the material.

5.1. Definition of a realistic tokamak thermal cycle

5.1.1. Input of the code: particle and thermal fluxes

As explain in Chapter 1, in a tokamak, there is a flux of particles that hit the divertor target. Considering that these particles are mainly D and ^{3}H with an incident energy of E_{inc}, the law that links the incident particle flux (ϕ_{inc}) and the incident thermal flux (Γ_{th}) is (equation 5.1):

$$\Gamma_{th} = \phi_{inc} \cdot e \cdot (E_{inc} + 13.6\ eV) \quad (5.1)$$

Here, $e = 1.6 \times 10^{-19}$ C is the elementary charge.
A cycle can be defined into 4 phases:

1. The plasma ramp-up,
2. The plasma burning phase,
3. The plasma ramp-down,
4. The resting time.

Each of this phases are defined by different evolution of ϕ_{inc} ($\Leftrightarrow$ different evolution of Γ_{th}).

During the plasma ramp-up phase, the energy of the confined plasma increases. Thus, the incident flux that hit the divertor target increases from 0 to its nominal value (the one of the plasma burning phase) in few seconds. In our simulations, it increases into 20 seconds.

During the plasma burning phase, the energy of the confined plasma is constant. The edge localized modes (plasma instability inducing a periodic increase of the particle/thermal fluxes with a frequency between some Hz to some 10 of Hz) are not considered. It remains constant even if the plasma is heated by external way (antenna, neutral beam …) or by internal way (nuclear fusion reactions). With the actively cooled divertor targets, it is expected that this phase last around 400 s during ITER operation. In our simulations, this phase will last 380 s. During this period, the incident flux of particles hitting the targets is constant.

During the plasma ramp-down phase, the energy of the confined plasma decreases gradually. In ITER, this phase will take tens of seconds. In our simulations, this decrease will last 40 s: during this phase, the incident flux goes from its nominal value during the plasma burning phase to zero.

During the resting times, there is no plasma in the tokamak vessel: the incident flux is zero. This period should last around 1000 s in ITER. In our simulations it lasts 960 s so the full cycle lasts 1400 s.
More detail on the described scenario can be found in the paper from Casper et al. [152].

We are interested here into the estimation of the ^{3}H retention in W materials constituing the divertor targets. In this area, during the burning plasma phase, the incident energy of the ^{3}H ions is ~ 25 eV and the incident flux is ~ 10^{24} HI·m^{-2}·s^{-1} [5]. Thus, during the 380 s burning plasma phase, the heating flux is $\Gamma_{th} = 6.176\ \mathrm{MW \cdot m^{-2}}$ according to equation 5.1. According to MD and TRIM® simulations [59], the reflection coefficient of 25 eV/^{3}H on W surface is around 0.7. Thus, 30 % of the incident flux is implanted and during the plasma burning phase, the implanted flux is 3×10^{23} HI·m^{-2}·s^{-1}.
In the simulation, it is not possible for the moment to treate different type of HIs: the incident flux is supposed to be purely a tritium flux. Thus, the diffusion coefficient of hydrogen given by DFT calculation and used in this work (table 3.1) is divided by $\sqrt{3}$ to account for the larger mass of tritium.
The evolutions of both implanted flux and thermal flux hitting the W divertor target during the first 3 phases described above are shown in figure 5.1. During the resting phases, both implanted particle flux and thermal flux are zero. These two evolutions are set as input parameters of the code MHIMS.

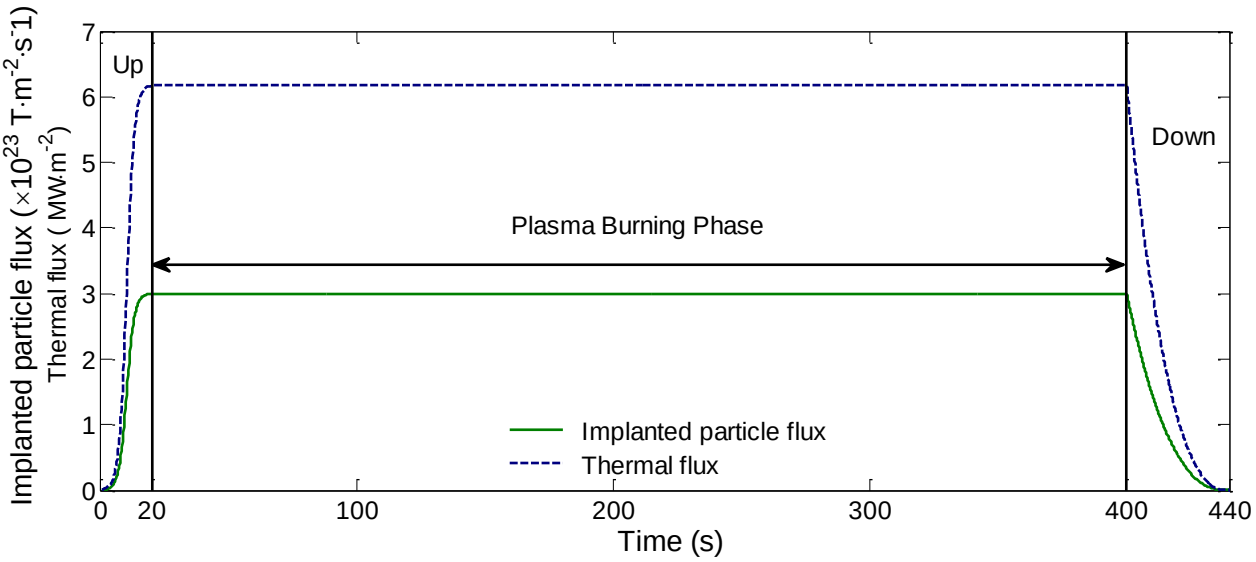

Figure 5.1.Evolution of both implanted particle and thermal fluxes hitting the W divertor target during the first 3 phases of a realistic ITER thermal cycle.

5.1.2. Thermal model of a plasma facing components

The W PFC is heated by a heat flux of 6.176 MW·m^{-2} on its plasma facing side. It is also cooled by liquid water on its other side. In the ITER design, there are three layers between the plasma facing surface and the heat sink: a W layer of around 6 mm thick, a copper layer of around 1 mm thick and a CuCrZr alloy layer of around 1.5 mm thick [153]. These two last layers are here to enhanced the heat transfer and cooled down the PFC more efficiently. However, we

just want to simulate simply the W PFC: only a 1 cm thick W PFC is considered. A simple description of the W PFC considered here is presented on figure 5.2.

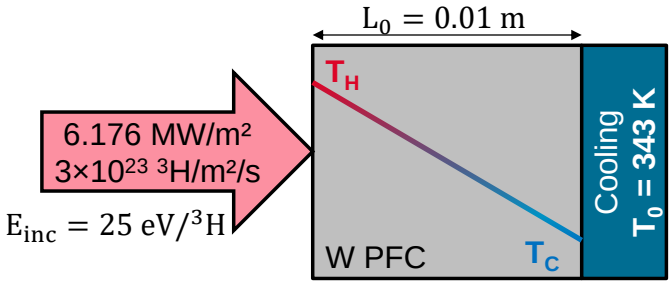

Figure 5.2. Simple description of the actively cooled 1-cm-thick W PFC experiencing a heat flux of 6.176 MW/m^2 and an implanted flux of 3×10^{23} ^{3}H·m^{-2}·s^{-1} of 25 eV/^{3}H ions and cooled at the back side by water at T_0 = 343 K. T_C is the temperature of the W PFC at the back side where it is cooled and T_H is the temperature of the W PFC where it receives the heat flux (hot temperature).

The temperature of the water in the cooling system is T_0 = 70 °C = 343 K. With such thickness and high flux, a temperature gradient will appear and in steady-state, the plasma facing surface will be hot at a temperature T_H and the cooled surface will be at a temperature T_C (figure 5.2). To calculate both T_C and T_H in steady-state as well as their evolution during the transient plasma ramp-down and ramp-down, a surface model need to be added to MHIMS. This model is based on the heat equation (equation 5.2):

$$\rho \cdot C_p \cdot \frac{\partial T}{\partial t} = \frac{\partial}{\partial x}\left(k(T) \cdot \frac{\partial T}{\partial x}\right) \tag{5.2}$$

With

$\rho = 19.253 \times 10^3$ kg · m^{-3} the volume mass density of W (table 1.2).

$C_p = 130$ J · kg^{-1} · K^{-1} the specific heat

$k(T) = \frac{1}{1.7\times10^{-6}\cdot T + 6.41\times10^{-3}}$ W · m^{-1} · K^{-1} the thermal conductivity

The numerical values of ρ and C_p are taken from [8] and the evolution of k(T) is taken from [154].

The boundary condition of the thermal model for the actively cooled W PFC are both Neumann boundary conditions defined by equation 5.3 and equation 5.4:

$$\left(\frac{\partial T}{\partial x}\right)_{x=0} = \frac{\Gamma_{th}}{k(T(x=0))} \tag{5.3}$$

$$\left(\frac{\partial T}{\partial x}\right)_{x=L_0} = h \cdot (T(x = L_0) - T_0) \tag{5.4}$$

$x = 0$ corresponds to the plasma facing surface and $x = L_0$ corresponds to the cooled surface. Equation 5.3 corresponds to the heating of the plasma facing surface ($x = 0$) with a thermal flux of Γ_{th} and equation 5.4 corresponds to the cooling of the heat sink that is characterized by a heat transfer coefficient h (in W·m^{-2}·K^{-1}). Its value is $h = 77940$ W · m^{-2} · K^{-1} [153]. Due to the boundary condition used, the temperature T_C is not equal to the temperature of the cooling system.

The initial condition is $T(x, t = 0) = T_0$.

This simple thermal model will be use to described the temperature evolution over time in all the simulated material. This model is implemented in a version of MHIMS. The equations are numerically solved using a standard finite difference implicite Euler method.

Figure 5.3 shows the evolution of the temperature of the cooled surface ($T_C = T(x = L_0)$) and the temperature of the plasma facing surface ($T_H = T(x = 0)$) given by the thermal model during the 3 first phases of the thermal cycle (section 5.1.1) with as input parameters the evolution of the thermal flux described figure 5.1.

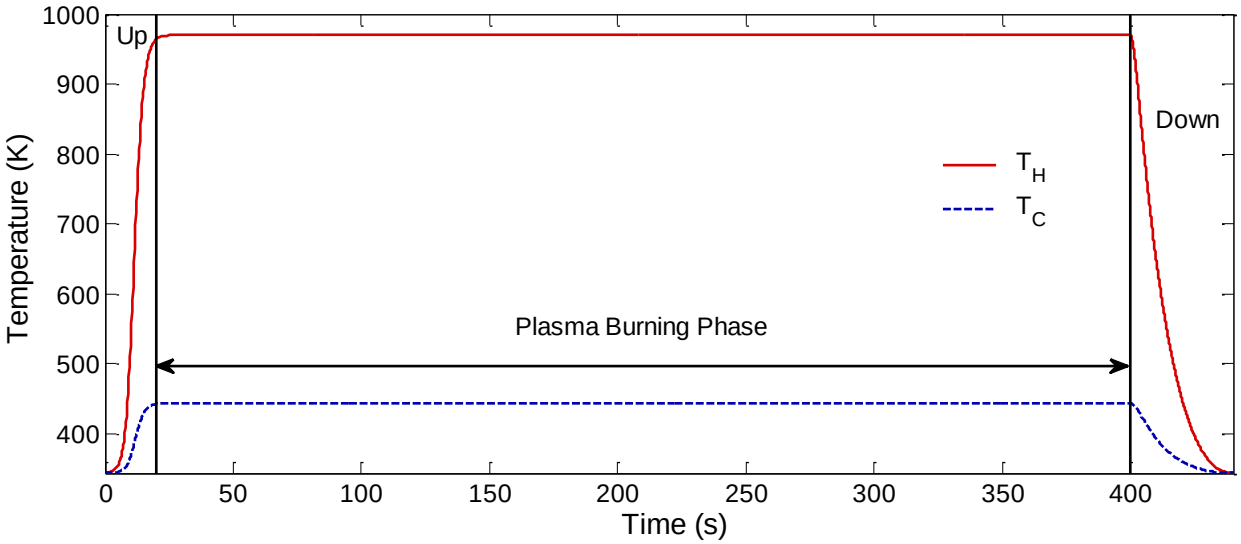

Figure 5.3. Evolution of the temperatures of the plasma facing surface (T_H) and the cooled surface (T_C) during the first three phases (ramp-down, plasma burning, ramp-down).

According to Denis et al. [153], the times response of the wall to a step of thermal flux is ~1 seconds in the divertor: the temperature on both surface is quick to be established in comparison to the length of the cycle. The maximum temperatures on both sides are observed during the plasma burning phase. It reaches 970 K on the plasma facing surface and 443 K on the cooled surface. If one compares these temperatures to the desorption temperature of D from undamaged and damaged PCW, it can be anticipated that in the case of undamaged W, very few ^{3}H will be retained since D is released below 800 K (figure 4.15). In the other hand in the case of damaged W, D is released below 1100 K so ^{3}H can be efficiently retained in such W.

5.2. Simulations of one cycle of tokamak operation

5.2.1. Trapping input parameters

In this section, a single cycle is simulated. Two cases are considered:

- The case without the traps induced by 14.1 MeV neutrons called undamaged W. Only trap 1, trap 2 and trap 3 are used in this case.
- The case with the traps induced by 14.1 MeV neutrons called damaged W. Trap 1, trap 2, trap 3, trap 4, trap 5 and trap 6 are used in this case.

For this last cases, it is supposed that the 14.1 MeV neutrons create the same 3 traps as previously determined in section 4.3 (trap 4, trap 5 and trap 6). From now, these traps are called neutron-induced traps. It is also supposed that the amount of neutron-induced traps saturates as in the case of self-damaged W [95] and that the neutrons damage the 1 cm thick W PFC in all its thickness:

the concentration of neutron-induced traps is constant in all the simulated materials. In addition, the concentrations of neutron-induced traps are in the same range as the concentration used in the simulations on self-damaged PCW samples (section 4.3). The values chosen for the simulations are summarized in table 5.1.
For both cases, the trap creation process induced by ^{3}H ions is switch on and the value of the depth up to which traps are created (x_{diff}) is given by the extrapolation done in section 4.1:

$$x_{diff} = 4 \times 10^{-5} \cdot e^{-\frac{0.11\ eV}{k_B \cdot T}}$$

At 970 K, there is $x_{diff} = 10\ \mu m$.
Table 5.1 presents the trapping parameters used in the simulations presented below. For the undamaged W, the neutron-induced traps (trap 4, trap 5 and trap 6) are not used.

Trap 1, **intrinsic** (impurities (Fe), dislocations)	$E_{t,1} = 0.85$ eV $n_1 = 0.13$ at. %
Trap 2, **intrinsic** (GBs)	$E_{t,2} = 1.00$ eV $n_2 = 0.035$ at. %
Trap 3, **^{3}H ion-induced** (VOH_i, VCH_i)	$E_{t,3} = 1.5$ eV $\eta_a = 1.5 \times 10^{-3}$ and $n_{a,max} = 15$ at. % $\eta_b = 1.5 \times 10^{-4}$ and $n_{b,max} = 1$ at. % $x_{diff} = 10\ \mu m$
Trap 4, **neutron induced** (jogged dislocations)	$E_{t,4} = 1.65$ eV $n_4 = 0.1$ at. %
Trap 5, **neutron induced** (dislocation loops)	$E_{t,4} = 1.85$ eV $n_4 = 0.2$ at. %
Trap 6, **neutron induced** (cavities)	$E_{t,4} = 2.06$ eV $n_4 = 0.05$ at. %

Table 5.1. Trapping parameters used in the simulations. For the undamaged W, the neutron-induced traps (trap 4, trap 5 and trap 6) are not used.

For both plasma facing surface and cooled surface, the boundary condition of the MRE model are the same: $c_m(x = 0, L_0) = 0$. Thus, if ^{3}H migrate up to the cooled surface, it will be release out of the materials simulating a release of ^{3}H in the water of the cooling system.

5.2.2. Simulation results: damaged W versus undamaged W

Figure 5.4 (a) shows the evolution of the ^{3}H retention in both undamaged and damaged cases during one full 1400 s cycle and Figure 5.4 (b) shows the ^{3}H depth in both cases at the end of the cycle (t = 1400 s).

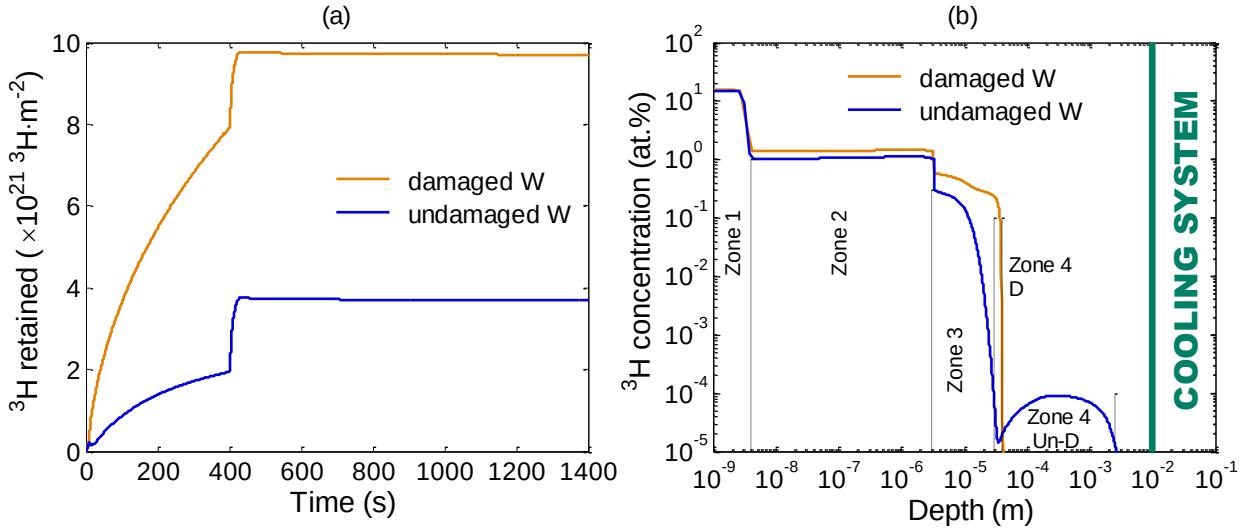

Figure 5.4. (a) Evolution of the ^{3}H retention during one full 1400 s cycle in the undamaged (blue) and damaged (orange) cases.

(b) ^{3}H depth profile in the undamaged (blue) and damaged (orange) case at the end of the 1400 s cycle: t = 1400 s.

The first thing that can be observed on figure 5.4 (a) is that the ^{3}H retention in undamaged W is 3 times lower than in damaged W after 1 cycle. This difference was expected since, in the case of damaged W, high energy traps are present with high trap concentrations (table 5.1).
The other remarkable observation that can be made on figure 5.4 (a) is that during the plasma ramp-down, between 400 s and 440 s, the ^{3}H retention increases by 1.8×10^{21} ^{3}H·m^{-2} which is about 50 % of the total ^{3}H inventory at the end of the cycle in the case of undamaged W and 20 % in the case of damaged W. This increase is due to the fact that during the plasma ramp-down, the temperature decreases progressively from 970 K to 343 K and the implanted flux also decreases progressivelly: at low temperature, the trapping is more favorable than the detrapping explaining this sudden increase of the ^{3}H retention. This point will be discussed in more detailed a bit further.
At the end of the plasma ramp-down, a small outgassing stands during the resting time. A negligible part of the retained ^{3}H (2% for undamaged W and 0.8 % for damaged W) is released from the simulated material.

Looking at the ^{3}H depth profiles (figure 5.4 (b)), one can distinguish four zones in both cases:

- Zone 1: between 0 and 4 nm. The ^{3}H concentration is around 10 at.%.
- Zone 2: between 4 nm and ~ 3 µm. The ^{3}H concentration is 1.44 at.% for the damaged W and 1.10 at.% for the undamaged W.
- Zone 3: between 3 µm and up to ~ 30 µm. The ^{3}H concentration is about 0.6 – 0.5 at.% for the damaged W and 0.3 at.% for the undamaged W.
- Zone 4:
    - between 10 µm up to 40 µm for the damaged W (Zone 4 D). The ^{3}H concentration is about 0.2 at.%.
    - between 10 µm and 2.5 mm for the undamaged W (Zone 4 Un-D). The ^{3}H concentration is about 10^{-4} at.%.

The zone 1 corresponds to the near-surface zone where trap 3 is created in a high amount ($n_{a,max} = 15$ at. %).
Both zone 2 and zone 3 are related to the sub-surface layer where trap 3 is created up to x_{diff}. However, during the ramp-down phase, the implanted ^{3}H stop migrating at a depth of 3 µm: there is a step delimiting zone 2 and zone 3 at 3 µm (see below for the explanation).
Finally, zone 4 is related to ^{3}H trapping in the traps that are present in all the materials i.e. the intrinsic traps (trap 1 and trap 2) in the case of undamaged W and intrinsic + neutron-induced traps (trap 1, trap 2, trap 4, trap 5 and trap 6) in the case of damaged W.
In the case of undamaged W, the shape of the zone 4 with a peak of ^{3}H concentration around 500 µm is due to the outgassing of ^{3}H from trap 1 during the resting time. Indeed, trap 1 can be easily released at 343 K if no particle flux is present to fill these traps. Thus, particles are detrapped and diffuse toward the surfaces to be desorbed explaining this shape with a peak: the near surface particles are desorbed first.
In the case of damaged W ,the depth up to which ^{3}H has migrated during the plasma phases (ramp-up, plasma burning, ramp-down) is 40 µm which is 2 order of magnitude lower than in the case of undamaged W (2.5 mm). This is due to the fact that in damaged W, there are traps with high detrapping energies that can retained ^{3}H at this high temperature slowing down the migration of ^{3}H toward the bulk.

Retention during the plasma ramp-down:

To understand why there is this sudden increase of ^{3}H retention during the plasma ramp-down phases, the evolution of the maximum concentration of mobile particles c_m^{MAX} given by the simulations is plotted on figure 5.5 (a). Since during the plasma ramp-down phase the temperature decreases, the temperature for different times is also reported on the plot. The maximal value of concentration of mobile particles is at a depth of about 1 nm so the temperature at this depth is the same as the temperature of the plasma facing surface.

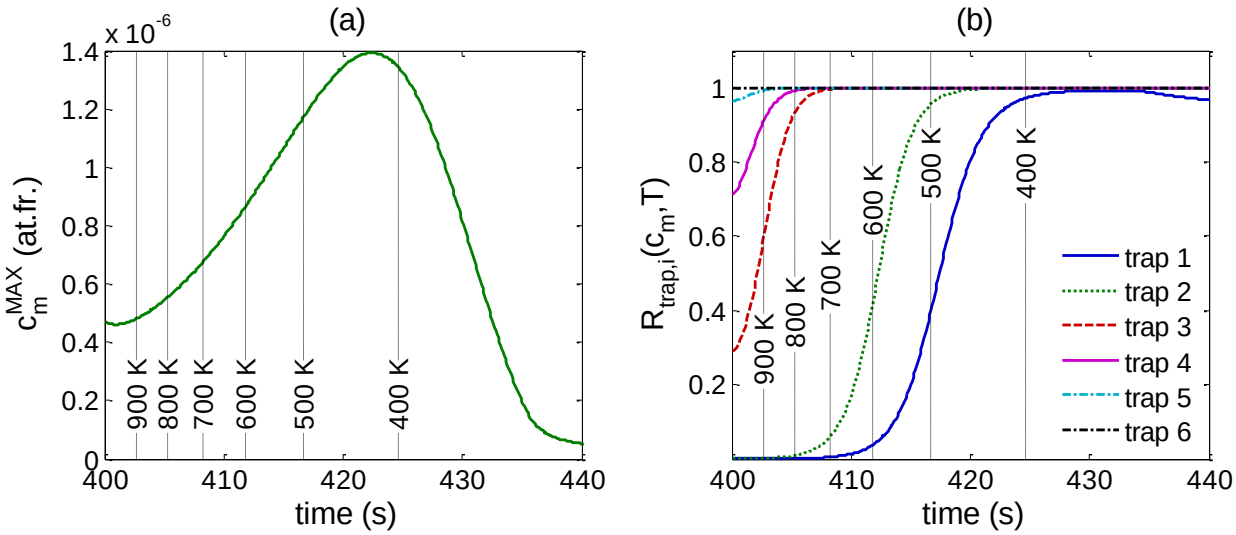

Figure 5.5. (a) evolution of the maximum of the concentration of mobile particles (given by equation 3.33) during the plasma ramp-down phase.

(b) evolution of the equilibrium ratio during the plasma ramp-down phase.

On figure 5.5 (a), two phases can be observed on the evolution of c_m^{MAX}:

- Between 400 s (970 K) and 422 s (420 K): c_m^{MAX} increases from 4.5×10^{-7} at.fr. to 1.4×10^{-6} at.fr..The diffusion coefficient decreases by a factore of 23 and the implanted flux by only a factor of 8. Since $c_m^{MAX} \approx {c_m^{MAX}}_{t\to\infty} \propto \frac{\phi_{imp}}{D(T)}$ (equation 3.33), c_m^{MAX} increases by a factor of 3.
- Between 422 s (420 K) and 440 s (343 K): c_m^{MAX}decreases to 5.3×10^{-8} at.fr.. The diffusion coefficient decreases only by a factor of 4 which is not enough to compensate the decrease of the flux.

Using this evolution of c_m^{MAX}, the equilibrium ratio $R_{trap,i}(c_m, T(t))$ given by equation 3.8 can be calculated for the 6 traps (figure 5.5 (b)). It is reminded that the equilibrium ratio is used in equation 3.7 to calculate the concentration of trapped particles as:

$c_{t,i} = R_{trap,i} \cdot n_i$

On figure 5.5 (b) it can be seen that, except for trap 6 which has an equilibrium ratio equal to 1 during all the ramp-down phase, the equilibrium ratios for all traps increase as the temperature decreases:

- The equilibrium ratio of trap 5 is 1 below 900 K,
- The equilibrium ratio of trap 4 is 1 below 800 K,
- The equilibrium ratio of trap 3 is 1 below 700 K,
- The equilibrium ratio of trap 2 is 1 below 430 K,
- The equilibrium ratio of trap 1 is 1 below 360 K.

Thus, the amount of ^{3}H retained in these traps increases during the ramp-down phase explaining the sudden increase seen on figure 5.4 (a).

After being equal to 1 at ~ 430 s (360 K), the equilibrium ratio of trap 1 decreases at the end of the ramp-down phase: the concentration of mobile particles is not high enough to guarantee $\nu_i(T) < c_m \cdot \nu_m(T)$ so ^{3}H is detrapped from such trap. This explains the small outgassing observed during the resting phase.

Now, the depth reached by the ^{3}H during this ramp-down phase ($R_d^{rd}(t)$ with 'rd' standing for ramp-down) is estimated. It is considered that the temperature is constant between the surface and the depth $R_d^{rd}(t)$. If $R_d^{rd}(t)$ is of the order of 10 µm, this assumption is fine.

In section 3.3.1 with a simple analytical model, a simple formula exists to obtain $R_d(t)$ (equation 3.33) but it is for a constant temperature with time and a constant concentration of mobile particles with time. To obtain the formula of $R_d^{rd}(t)$ for a time evolving temperature and mobile particle concentration, we go back to how equation 3.33 is obtained: the total amout of trap HIs particles during the ramp-down Tot_{trap}^{rd} phase can be written as (figure 3.2):

$Tot_{trap}^{rd}(t) = R_d^{rd}(t) \cdot \Sigma_i R_{trap,i}(t) \cdot n_i$

The trapped are filled thanks to a diffusive flux $\phi_{diff}^{rd}(t) = D(T(t)) \cdot \frac{c_m^{MAX}(t)}{R_d^{rd}(t)}$.

Thus, the evolution of Tot_{trap}^{rd} is given by $\frac{dTot_{trap}^{rd}}{dt} = \phi_{diff}^{rd}(t)$ which implies:

$R_d^{rd}(t) \cdot dR_d^{rd}(t) = D(T(t)) \cdot \frac{c_m^{MAX}(t)}{\Sigma_i R_{trap,i}(t) \cdot n_i} \cdot dt$

We get then:

$$R_d^{rd}(t) = \sqrt{2 \cdot \int_{400\ s}^{t} D\big(T(t)\big) \cdot \frac{c_m^{MAX}(t)}{\Sigma_i R_{trap,i}(t) \cdot n_i} \cdot dt}$$

It is supposed that the ^{3}H migrate far deeper than zone 1 (0 – 4 nm) as seen on figure 5.4 (b). In the simulations, the concentration of trap 3 between 4 nm and 5 µm is around 1 at.%. So, for the estimation of R_d^{rd}, $n_3 = 1\ \text{at.}\%$ is taken. In this case, with the evolution of $c_m^{MAX}(t)$ given by figure 5.5 (a) and the evolution of $R_{trap,i}(t)$ given by figure 5.5 (b), we obtain at the end of the ramp-down phase:

- $R_d^{rd}(t = 440\ \text{s}) = 3.1\ \mu\text{m}$ in the case of damaged W,
- $R_d^{rd}(t = 440\ \text{s}) = 3.8\ \mu\text{m}$ in the case of undamaged W. For this last case, there are not trap 4, trap 5 and trap 6 so $\Sigma_i R_{trap,i}(t) \cdot n_i$ is lower.

These value of $R_d^{rd}(t = 440\ \text{s})$ agree very well with the end of zone 2 (~ 3 µm) observed on the simulated depth profiles (figure 5.4 (b)). The small difference between the undamaged and damaged W can also be seen on the simulated depth profiles. Thus, as explaiend previously, zone 2 observed on the simulated ^{3}H depth profile corresponds to ^{3}H trapped during the plasma ramp-down phase. The sharp frontier between zone 2 and zone 3 is due to the fact that the ^{3}H trapped during this ramp down phase stop migrating at around 3 µm.

5.2.3. Summary

After one 1400 s cycle that includes plasma ramp-up, burning plasma, plasma ramp-down and resting time, it has been seen that:

- The ^{3}H retention in damaged W is 3 times higher than in undamaged W,
- During the plasma ramp-down, a sudden increase by about 1.8×10^{21} ^{3}H·m^{-2} of the ^{3}H retention is observed. It corresponds to 50 % of the final ^{3}H inventory in the case of undamaged W and 20 % in the case of damaged W.
- This increase of the retention during the plasma ramp-down is due to a decrease of the temperature while the implanted flux is not zero: the equilibrium ratio for each traps increases during this period.
- The implanted ^{3}H during the plasma ramp-down phase stop migrating at 3 µm.
- 4 zones can be distinguished on the simulated D depth profiles for both damaged W and undamaged W:
    - Zone 1: near the surface up to 4 nm with a concentration of ^{3}H of about 10 at.%. It corresponds to the ions-induced trap 3 in the 25 eV/^{3}H ion implantation zone.
    - Zone 2: up to 3 µm with a concentration of ^{3}H of about 1 at.%. It corresponds to the part of the sub-surface layer where ions-induced trap 3 is created (between 0 and x_{diff}) and where the implanted ^{3}H during the plasma ramp-down phase are trapped.
    - Zone 3: between 3 µm and 10 µm. It correspond to the part of the sub-surface layer where ions-induced trap 3 is created and where the implanted ^{3}H do not migrate during the plasma ramp-down phase.
    - Zone 4: it corresponds to the trapping of ^{3}H beyond the zone where trap 3 is created ($x > x_{diff}$). It gives the maximal depth reached by the implanted ^{3}H during the full cycle.
- Due to the presence of neutron-induced traps with high concentrations in damaged W, the maximal depth reached by the ^{3}H during the full cycle is only 40 µm but the ^{3}H concentration in zone 4 is high (0.2 at.%).

– Due to the low detrapping energy of intrinsic traps, the maximal depth reached by the implanted ^{3}H during the full cycle is 2.5 mm but the ^{3}H concentration in zone 4 is low (10^{-4} at.%).

5.3. Simulations of 4×10 cycles

After having simulated one 1400 s cycle and seeing the different features of the ^{3}H retention during such cycle, several cycles are simulated. In this section, a total of 40 cycles are simulated. Between each group of 10 cycles, a long resting period of 40 000 s (~ 11 h) is simulated to simulate an overnight operation break: there are 4 group of 10 cycles and 4 long resting periods. The trapping parameters used in these simulations are presented in table 5.1.

5.3.1. Simulation results

T retention as a function of the fluence (time):

Figure 5.6 shows the evolution of the ^{3}H retention during the 4×10 cycles as a function of the fluence. The fluence is used for this figure since it is more convenient to extract extrapolation law. However, since during the resting time, the implanted flux is zero, the fluence does not increase: the outgassing during the resting time cannot be observed on that plot. It does not really matter since this outgassing is negligible (maximum few % of the ^{3}H retained per cycle). On figure 5.6, the ^{3}H retention is expressed in two units: ^{3}H·m^{-2} on the left and gram of ^{3}H/m^{-2} (g/m^2) knowing that 1 gram of ^{3}H is 2×10^{23} ^{3}H.

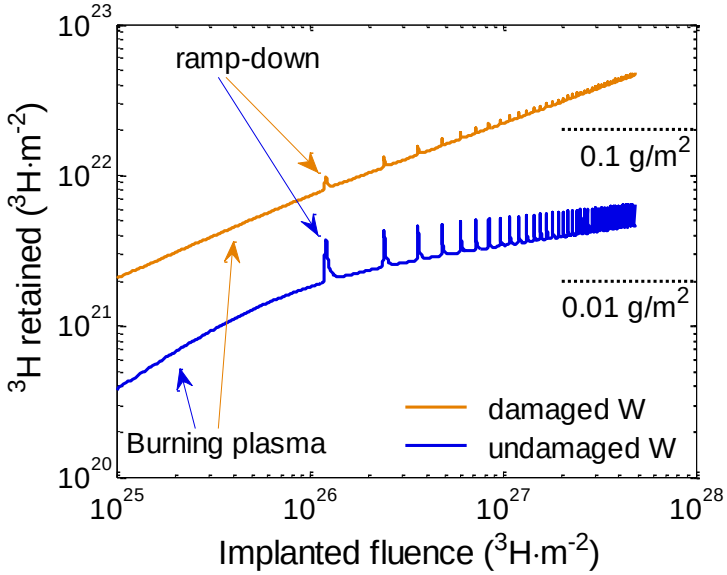

Figure 5.6. Evolution of the ^{3}H retention as a function of the implanted fluence during 4×10 cycles in the undamaged (blue) and damaged (orange) cases.

After one single cycle, the ^{3}H retention is 3 times higher in damaged W than in undamaged W (figure 5.5 (a)). The difference increases with the number of cycle (or the fluence) as it can be seen in figure 5.6: after 40 cycles, there are 10 times more ^{3}H retained in damaged W (0.24 g/m^2) than in undamaged W (0.023 g/m^2).

For both undamaged and damaged W, thin peaks can be observed on the evolution of the ^3H retention with the implanted fluence. These peaks correspond to the sudden retention during the plasma ramp-down discussed in section 5.2.2. When a new burning plasma phase starts, the peaks quickly disappear and the ^3H retention came back to the ^3H retention there was at the end of the previous burning plasma phase: because the temperature rises again from 343 K to 970 K during the plasma ramp up, almost all the ^3H trapped during the plasma ramp-down phase are remove from the W PFC (damaged or undamaged). The intensity of the peak are for any cycle the same: ~ 1.8×10^{21} $^3H\cdot m^{-2}$. It means that it is always the same ~ 3 µm thick zone below the surface that is filled with always the same amount of ^3H during the plasma ramp-down phase.

T depth profiles as a function of fluence (time):

Figure 5.7 shows the simulated ^3H depth profiles after 10 cycles, 2×10 cycles, 3×10 cycles and 4×10 cycles in both damaged and undamaged W. The evolution in the depth of the diffusion coefficient for tritium $D_T(T)$ is also shown in red.

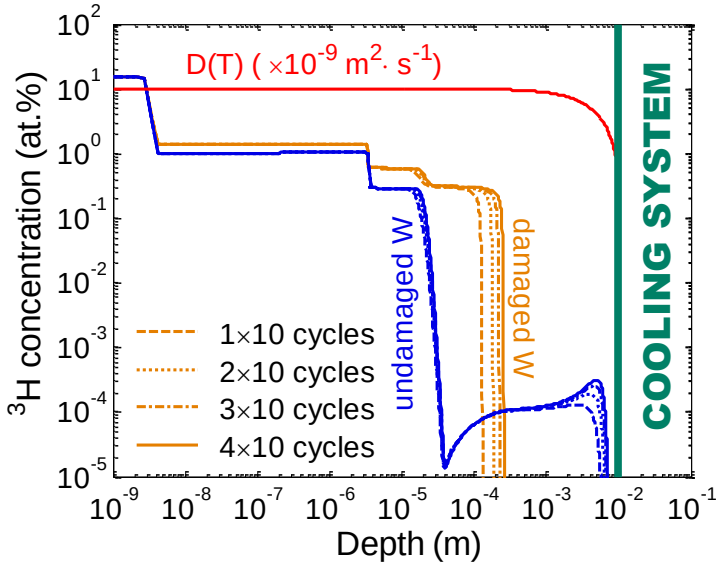

Figure 5.7. Simulated ^3H depth profiles for undamaged (blue) and damaged (orange) W at the end of each group of 10 cycles. The evolution of the diffusion coefficient with depth is also shown in red.

The same four zones defined in section 5.2.2 can be distinguished on figure 5.7:

- Zone 1 (up to 4 nm) corresponds to the near-surface layer where ions-induced trap 3 is created (in the implantation zone),
- Zone 2 (up to 3 µm) corresponds to the sub-surface layer where ions-induced trap3 is created and where the ^3H implanted during the plasma ramp-down phase is trapped.
- Zone 3 (up to 40 µm) corresponds to the sub-surface layer where ions-induced trap 3 is created and where the implanted ^3H do not migrate during the plasma ramp-down phase.
- Zone 4 corresponds to the trapping of ^3H beyond the zone where trap 3 is created. It starts around 40 µm.

In both undamaged and damaged W, zone 1, zone 2 and zone 3 are similar. In this zone, the more present trapping site is the created trap 3. It has a high enough detrapping energy to

retain ^{3}H significantly at 970 K: the equilibrium ratio of this trap is ~ 0.3 during the plasma burning phase and 1 during the plasma ramp-down phase (figure 5.5).
The difference in zone 1+2 between undamaged and damaged W is 0.35 at.% which is exactly the concentration of neutron-induced traps: the equilibrium ratio is 1 in this zone after the plasma ramp down phase (figure 5.5). The difference in zone 3 between undamaged and damaged W is 0.3 at.% which corresponds to $\Sigma_{i=4}^{6} R_{(trap,i)} \cdot n_i$ with the equilibrium ratio during the plasma burning phase (figure 5.5).

The amount of created traps increases with fluence and saturates at a certain fluence. On figure 5.7, it can be seen that zone 1, zone 2 and zone 3, which are related to creation of traps does not change so much as the number of cycles (the fluence) increases: after 10 cycles, the amount of trap 3 is nearly saturated. Consequently, the increase of the ^{3}H retention shown on figure 5.6 is not due to the increase of the number of traps created but to the migration of ^{3}H toward the bulk: the zone 4 is evolving as a function of the number of cycles as seen on figure 5.7. In the next, the depth where ^{3}H stops migrating after N_{cycle} is called $R_d^C(N_{cycle})$. In practice, this value is the depth at which the total concentration of ^{3}H drops below a given value (in this case 10^{-5} at.%).
Two different behaviors of ^{3}H trapping can be observed in zone 4:

- In case of damaged W, the ^{3}H concentration is almost constant in zone 4.
- In case of undamaged W, the ^{3}H concentration is not constant in zone 4. The zone 4 between 30 µm and 2 mm is similar to the one seen in the case of a single cycle (figure 5.4 (b): there is a hole between 40 µm and 100 µm and then it is almost constant. This evolution is explained by the ^{3}H outgassing during the resting phase. However, there is a peak of the concentration between 2 mm and R_d^C which is not present for the single cycle case.

In the case of damaged W, the ^{3}H concentration is almost constant in zone 4 because R_d^C is between 100 µ (for 10 cycles) and 266 µm (for 40 cycles): the diffusion coefficient is constant in all the zone 4 between 40 µm and R_d^C (red line on figure 5.7). The reason is that the temperature in this interval of depth is very close to the temperature at the surface (the temperature difference is below 20 K). Thus, the trapping frequency $\nu_m(T) \cdot c_m$ does not change much since both ν_m and c_m are a function of the diffusion coefficient. In addition, since the temperature does not change, the detrapping frequency $\nu_i(T)$ is constant: the equilibrium ratio $R_{trap,i}$ are the same in all this interval of depth and so is the ^{3}H concentration.
In the case of undamaged W, there is a peak of ^{3}H concentration between 2 mm and R_d^C in zone 4 because R_d^C is between 5 mm (for 10 cycles) and 7 mm (for 40 cycles): the difference of temperature between a depth of 2 mm and R_d^C is 310 K. Thus, as it can be seen on figure 5.7, the diffusion coefficient varies by almost one order of magnitude in this interval. It implies that, at a depth of R_d^C the concentration of mobile particle c_m and the trapping frequency for the intrinsic traps $\nu_m \cdot c_m$ increase compared to a depth of 2 mm. In addition, the temperature passing from around 840 K to 530 K, the detrapping frequency of the intrinsic traps $\nu_i(T)$ decreases in this interval of depths. Consequently, the equilibrium ratios $R_{trap,i}$ of the intrinsic traps are higher near the cooling system (at a depth of R_d^C) than near the plasma facing surface (at a depth of 40 µm). It would not affect so much the ^{3}H depth profile if the equilibrium ratios were close to 1 (for high detrapping energies as in the case of damaged W). However, since the detrapping energies of intrinsic traps are low (table 5.1), the equilibrium ratios near the plasma facing surface (at 40 µm) are very low. So, as the ^{3}H migrate toward the cooling system, the equilibrium ratios of the

intrinsic trap significantly increase explaining the peak of ^{3}H concentration observed between 1 mm and R_d^C.

Summary:

- The difference between the simulated ^{3}H retention in damaged W and in undamaged W increases as the number of cycle (the fluence) increases: after 40 cycles, the ^{3}H retention in damaged W is 10 times higher than in undamaged W.
- The ^{3}H implanted and trapped during a plasma ramp-down phase is removed during the next plasma ramp-up phase. Thus, the amount of ^{3}H retained during the plasma ramp-down phase is always the same (1.8×10^{21} ^{3}H·m^{-2}) and during this phase, the ^{3}H is always trapped in the same 3 µm thick layer.
- The simulated ^{3}H depth profiles after different numbers of cycles show the same 4 zones as described in section 5.2.
- For a number of cycle higher than 10, the ^{3}H retention seems to be limited by the ^{3}H trapped beyond the zone where trap 3 are created: it is limited by the migration of ^{3}H toward the bulk and toward the cooled surface:
    - In case of damaged W, the migration of ^{3}H stops at 266 µm after 40 cycles.
    - In case of undamaged W, the migration of ^{3}H stops near the cooling loop at 7 mm after 40 cycles. Between 2 mm and 7 mm, there is a strong gradient of the diffusion coefficient: the trapping is more efficient near the cooled surface inducing a peak of ^{3}H concentration near this surface.

5.3.2. Extrapolation to high numbers of cycles

To estimate the ^{3}H retention for higher numbers of cycles without making simulations, extrapolation laws of ^{3}H retention as a function of N_{cycles} can be extracted from the simulations results (figure 5.6). If only the ^{3}H retention at the end of plasma burning phases is considered (since the ^{3}H implanted during a plasma ramp-down is removed during the next plasma ramp-up), thus the following extrapolation laws can be obtained between the ^{3}H retention (Ret in ^{3}H·m^{-2}) and the number of cycle N_{cycle}:

- $Ret(N_{cycles}) = 8.2 \times 10^{21} \cdot (N_{cycles})^{0.472}$ for the damaged W,
- $Ret(N_{cycles}) = 2.1 \times 10^{21} \cdot (N_{cycles})^{0.214}$ for the undamaged W.

The power law in the case of damaged W is close to the square root law since the diffusion coefficient in the zone where ^{3}H stops does not change to much. In the opposite, the power law in the case of undamaged W is far from the square root law because of the gradient of diffusion coefficient discussed previsouly (section 5.3.1).

Of course, these power laws are valid to estimate the ^{3}H retention if the value of $R_d^C(N_{cycles})$ (depth where ^{3}H stop migrating) is below the thickness of the W PFC i.e. in our case if $R_d^C(N_{cycles}) < L_0 = 1\ cm$. So if $R_d^C(N_{cycles}) = 1\ cm$, the ammount of ^{3}H retentained cannot grow anymore. It will saturate (figure 5.8) and some ^{3}H can be released in the water cooling system.

Scaling laws of $R_d^C(N_{cylces})$ are extracted from the simulation results presented on figure 5.7. To obtain $R_d^C(N_{cycles})$ from the simulated ^{3}H depth profiles, the maximum depth at which the ^{3}H

concentration is higher than 10^{-5} at.% is taken. The following laws are obtained that express the depth at which ^{3}H stop migrating R_d^C as a function of the number of cycles N_{cycles}:

- $R_d^C(N_{cycles}) = 4.3 \times 10^{-5} \cdot (N_{cycles})^{0.493}$ for the damaged W,
- $R_d^C(N_{cycles}) = 3.9 \times 10^{-3} \cdot (N_{cycles})^{0.168}$ for the undamaged W.

As for the ^{3}H retention and for the same reason, the depth $R_d^C(N_{cycles})$ evolves close to a square root law for the damaged W. Similarly, in the case of undamaged W, this evolution is not close to a square root law due to the temperature/diffusion coefficient gradient.

Figure 5.8 (a) shows, for both undamaged and damaged W, the evolution of $R_d^C(N_{cycles})$ as a function of the number of cycles (simulations and extrapolation laws). Similarly, for both undamaged and damaged W, figure 5.8 (b) shows the evolution of the ^{3}H retention as a function of the number of cycles (simulations and extrapolation laws). On figure 5.8 (b), the ^{3}H retention is express in two units: ^{3}H·m^{-2} on the left and g/m^2 (1 gramm of ^{3}H is 2×10^{23} ^{3}H).

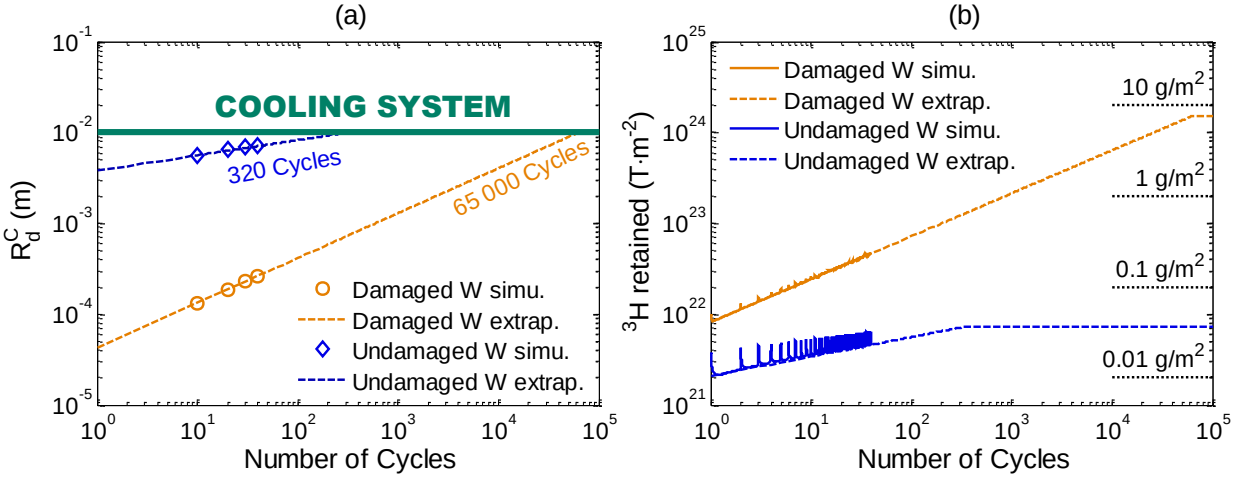

Figure 5.8. (a) evolutions of the depth $R_d^C(N_{cycles})$ with N_{cycles} for undamaged (blue) and damaged (orange) W. The marker corresponds to the value extracted from the simulations and the dashed line corresponds to the extrapolation laws obtained.

(b) evolutions of the ^{3}H retention with N_{cycles} for undamaged (blue) and damaged (orange) W. The solid lines are the simulation results and the dashed lines are the extrapolation laws.

Using the extrapolation laws obtained from the simulations results, it can be seen that the ^{3}H will reach the cooling system after:

- 320 cycles for the undamaged W. The mass of ^{3}H retained is small around 0.04 g/m^2 (or 0.045 g/m^2 if one add the ^{3}H retention during the plasma ramp-down phase).
- 65 000 cycles for the damaged W. The mass of ^{3}H retained is about 7.6 g/m^2.

Due to the presence of the neutron-induced traps with a high concentration and a high detrapping energy, the migration of ^{3}H in damaged W is slow but the maximal ^{3}H retention is high.

In undamaged W, because the neutron-induced traps are not presents, the maximal ^{3}H retention is 160 times lower than in the case of damaged W but the ^{3}H migrate quickly toward the cooling system and a possible release of ^{3}H in the water of the cooling system can be expected after only 320 cycles.

It has to be noted that in case of the damaged W, the extrapolation laws for the ^{3}H retention and the migration depth of ^{3}H can be discussed. Indeed, it is possible that when ^{3}H migrate to very high depth (few mm), the extrapolation law will change: due to the diffusion coefficient gradient, the migration may be slowed down. To check if the extrapolations laws are accurate, simulation of more than 65 000 cycles should be done which was not possible during this PhD project. In any case, if the migration is slowed down, the estimation of 65 000 cycles to reach the cooling system is a lower margin: it is the worst case scenario for the ^{3}H migration (the fastest migration). It has also to be noted that these simulations (and so the extrapolation laws for the ^{3}H retention) consider only pure tritium implantation. In a real fusion tokamak, there will be a mixture of deuterium and tritium (1/2 of D and ½ of ^{3}H): the estimation made here could be roughly divided by 2 to obtain the amount of tritium retained in such mixe deuterium tritium plasma. In addition, 65 000 cycles corresponds to 30 years of operation (10 cycles per day and 200 day per year): the ^{3}H retained during the first cycles have decayed into Helium (half time decay of 12.3 years) that may change the amount of ^{3}H retained in the material and the ^{3}H retention properties.
From the scaling law of the width of the scrap-off layer obtained by Eich et al. [155] from the results of current machines, it can be estimated that the area exposed to the thermal/particle fluxes on one W divertor target will be ~1 cm in ITER. The major radius of ITER is 6.2 m and there are two targets (inner divertor and outerdivertor), so the total surface exposed to the thermal/particle fluxes during a plasma discharge is $S = 2 \cdot (2 \cdot \pi \cdot 6.2) \cdot 0.01 = 0.8\ m^2$. In that case, the maximal amount of ^{3}H retained in the W tagret of ITER divertor is 0.032 g for undamaged W and 6.1 g for damaged W: this is very low compared to the safety limit of 700 g. Thus, the retention of tritium in the W divertor targets are not an issue since the amount of tritium remains low. However, the possible release of tritium in the cooling water is a concern which will have to be handled during ITER operation. In case of damaged W, it would not cause so much trouble since 65 000 cycles correspond to 30 years of operation (10 cycles per day and 200 day per year). However, in the case of undamaged W, 320 cycles corresponds to 32 day of operation so the permeation of tritium may quickly become an issue.

5.3.3. Summary

- After 40 cycles, the amount of ^{3}H retained in damaged W is 10 times higher than in undamaged W: the difference between damaged W and undamaged W increases with the number of cycles.
- The ^{3}H retained during a plasma ramp-down is removed during the next plasma ramp-up: the ^{3}H trapped during the plasma ramp-down is always retained in a 3 µm thick layer below the surface.

- After several cycles the same 4 zones can be distinguished on the simulated ^{3}H depth porfiles as the one distinguished in section 5.2.
- In case of undamaged W, due to the strong temperature gradient (inducing a gradient of the diffusion coefficient), the concentration of ^{3}H has a peak between 3 mm and 7 mm.
- Extrapolation laws have been extracted from the simulation results to estimate the depths where ^{3}H stop migrating and the amount of ^{3}H retained for high numbers of cycles. Using these extrapolation laws, it is estimated that:
    - For undamaged W, 320 cycles are required for ^{3}H to permeate all through the 1 cm thick W PFC. The quantity of ^{3}H retained is 0.045 g/m^2.
    - For damaged W, 65 000 cycles are required to do the same. The quantity of ^{3}H retained is then 160 times higher (7.5 g/m^2).

To conclude, the maximum amount of tritium retained in the W divertor target will be low in ITER compare to the safety limit assuming a exposed surface of 0.8 m^2 (estimated from scaling law obtained from current machine). However, it does not mean that the limit will not be reached in ITER since in our simulations only particular conditions are taken. If the thermal/particle fluxes changes, the temperature of the W surface may be different changing the amount of retained ^{3}H in particular in the case of undamaged W. In addition, only implanted ^{3}H are simulated here: ^{3}H trapped in deposited layers are not simulated but it has been shown that is was the major part of the D retention in JET with the ITER-like wall [156]. In order to estimate accuratly the ^{3}H retention in the entire wall, more complex simulations have to be made taking into account the different implantation conditions and the different materials (Be in the first wall of ITER that can be at the origin of co-deposition ^{3}H-Be layer).

5.4. Simulations of Tritium removal by surface heating

In the previous section, it has been seen that the W PFC can retain ^{3}H to an amount of about 7 g/m^2. Since the amount of tritium in ITER is limited to 700 g in the entire machine, in order to avoid this limit to be overpassed, Tritium need to be removed from the wall.
To control the amount of Tritium retained in the wall, several solution can be envisaged [157]:

- Plasma cleaning. ^{3}H can be removed via isotopic exchange mechanisms
- Surface heating. The plasma facing surface where ^{3}H is trapped can be heated by laser or flash lamp to remove ^{3}H.
- Oxidative methods. This method was explored for ^{3}H removal in carbon co-deposited layer: C is transformed into CO or CO_2 release the trapped ^{3}H.
- Conditioning methods. The walls are treated using RF conditioning plasmas.

In this section, the efficiency of the surface heating method is tested to see if ^{3}H can be removed with a significant amount and how it is removed.

In the simulation, to heat the plasma facing surface, the thermal flux is turned on without an implanted particle flux. Before this heating, 10 cycles are simulated to load a significant amount of ^{3}H in the W PFC. Before the heating, the 40 000 s (11 h) resting is observed. The simulation steps can then be described as followed:

- 10 cycles with the implantation/heating parameters described in section 5.1.1.
- 40 000 s (11h) of resting time.
- Surface heating: $\Gamma_{th} \neq 0$ and $\phi_{imp} = 0$. 2 cases are envisaged with a heating flux of 7.5 MW/m^2 and 10 MW/m^2. In both cases the thermal flux increases in about 20 s for numerical stability reasons.

During the surface heating, the cooling system is still turn on and the temperature of the heat sink is still 343 K:

- For a thermal flux of 7.5 MW/m^2, T_H = 1145 K and T_C = 472 K.
- For a heating flux of 10 MW/m^2, T_H = 1532 K and T_C = 537 K.

In the simulation, the surface is heated for about 7 h.

Evolution of the ^{3}H retention:

Figure 5.9 shows, for damaged and undamaged W, the evolution of the simulated ^{3}H retention with time during the three steps described previously.

For both damaged and undamaged W, the amount of ^{3}H removed during the surface heating is higher for $\Gamma_{th} = 10\ MW \cdot m^{-2}$ than for $\Gamma_{th} = 7.5\ MW \cdot m^{-2}$ because the surface temperature T_C is higher. Table 5.2 gives the amount of remaining ^{3}H in the materials after 7 h of surface heating (expressed in $^3H{\cdot}m^{-2}$ and in percentage of the ^{3}H retained before the surface heating).

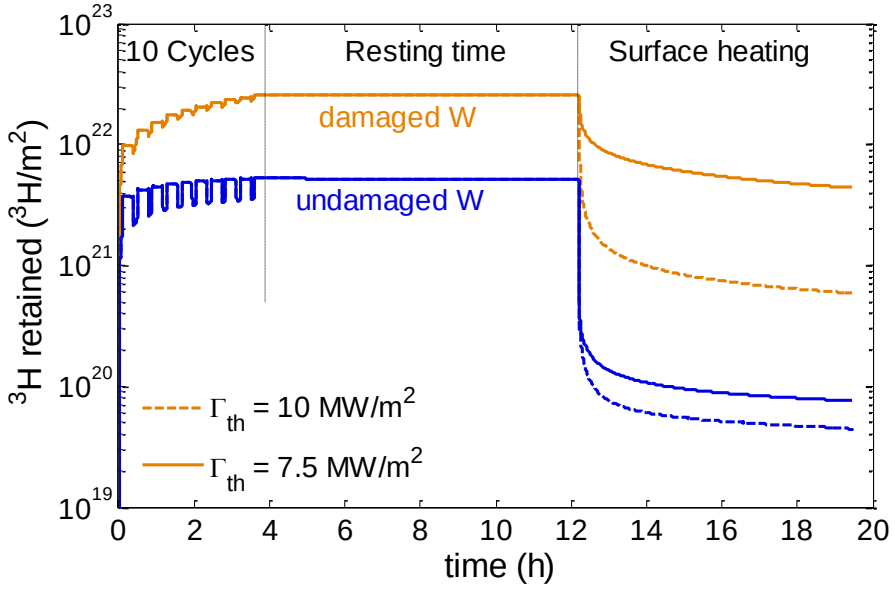

Figure 5.9. Evolution of the ^{3}H retained with time in damaged (orange) and undamaged (blue) W during 10 cycles followed by a resting time of 11 h and a surface heating with a thermal flux of 7.5 MW/m^2 (solide line) and 10 MW/m^2 (dashed line).

	Remaining ^{3}H after 7 h **Damaged W**	Remaining ^{3}H after 7 h **Undamaged W**
Γ_{th} = 7.5 MW/m^2 T_H = 1145 K	4.4×10^{21} $^3H{\cdot}m^{-2}$ 17 %	7.9×10^{19} $^3H{\cdot}m^{-2}$ 1.5 %
Γ_{th} = 10 MW/m^2 T_H = 1532 K	5.9×10^{20} 3H·m^{-2} 2.3 %	4.4×10^{19} $^3H{\cdot}m^{-2}$ 0.9 %

Table 5.2. Amount of ^{3}H remaining in the materials (damaged W and undamaged W) after 7 h of surface heating. This quantity is expressed in $^3H{\cdot}m^{-2}$ and in percentage of the ^{3}H retained before the surface heating.

As it can be seen on figure 5.9 and table 5.2, in case of undamaged W, both heating procedures are efficient to remove almost entirely the ^{3}H that has been retained after 10 cycles. After 7 h of

surface heating, in both case, only 1 % of the initial ^{3}H retention remains in the materials. Thus, for undamaged W, it is not required to increase to much the surface temperature to remove the ^{3}H.

On the other hands, for damaged W, there is a large difference between the surface heating at 10 MW/m^2 and the surface heating at 7.5 MW/m^2. Due to the presence of neutron-induced traps with high detrapping energies especially trap 6, there is 7.3 more ^{3}H remaining in the material after heating at 7.5 MW/m^2 than after heating at 10 MW/m^2. This indicates that, in order to remove efficiently ^{3}H from damaged W using surface heating, a very high surface temperature of about 1500 K is needed which can induced strong modification of the materials and degrade the mechanical properties of the PFC if recrystallization takes place [158, 9] (the recrystallized structure being fragile).

Looking at figure 5.9, one can see that there are at least two time scales that characterized the ^{3}H removal, especially for the undamaged W case:

- On 10 s scale, the ^{3}H retention quickly drops (by more than one order of magnitude in the case of undamaged W),
- On the hour scale, the ^{3}H retention smoothly decreases.

The presence of these two release time scales is due to the fact that first, the ^{3}H close to the surface is released and then, the ^{3}H trapped in the bulk is released.

The ^{3}H trapped near the heated surface is quickly release since the temperature is the highest there. Due to the temperature gradient, the release of ^{3}H deep in the bulk is harder than near the heated surface (the temperature is lower). In addition, a part of the detrapped ^{3}H deep in the bulk is pushed towards the cooled surface which may induced a release of ^{3}H in the cooling system during the surface heating.

Study of the simulated depth profiles:

To explain in more details how ^{3}H is removed from the W PFC during the surface heating, the simulated ^{3}H depth profiles in both undamaged and damaged W are presented on figure 5.10 for a heating flux of 7.5 MW/m^2 (a) and for a heating flux of 10 MW/m^2 (b). On this figure, the simulated ^{3}H depth profiles are shown before the surface heating and 40 min after the beginning of the surface heating.

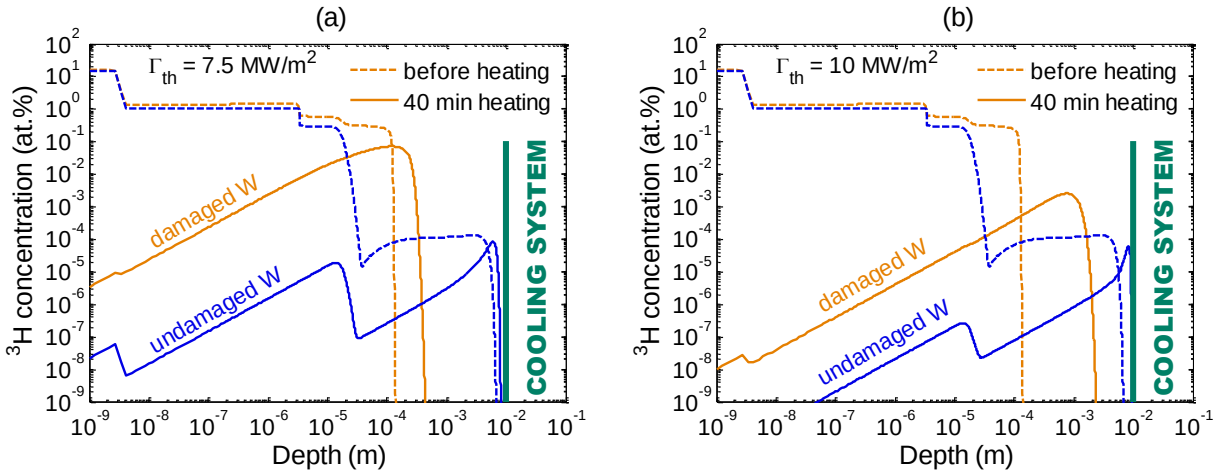

Figure 5.10. (a) Simulated ^{3}H depth profile in damaged (orange) and undamaged (blue) W after 10 cycle and before the surface heating (dashed line) and after 40 min of heating (solid line) with a heating flux of 7.5 MW/m^2.

(b) Simulated ^{3}H depth profiles in damaged (orange) and undamaged (blue) W after 10 cycles and before the surface heating (dashed line) and after 40 min of heating (solid line) with a heating flux of 10 MW/m^2.

As it is already seen on figure 5.9, it can be seen on the simulated D depth profiles that:

- The ^{3}H concentration in the materials after 40 minutes of heating is lower for 10 MW/m^2 than for 7.5 MW/m^2 thanks to the temperature difference between these two cases.
- The ^{3}H concentration in the simulated material is higher in the damaged W than in the undamaged W thanks to the high detrapping energies of the neutron-induced traps

In any cases, the ^{3}H concentration in the material after 40 min of heating has a similar shape:

- A low ^{3}H concentration near the heated surface (lower than before the heating by 6 – 9 orders of magnitude),
- The ^{3}H concentration increases with depth following the shape of the traps concentration (explaining the steps related to the zone where H-induced trap 3 is created),
- Finally, the ^{3}H concentration drops at a given depth.

Because the heated surface is the area where the temperature is the highest and since the surface acts as a sink for the diffusing ^{3}H, the ^{3}H concentration drops quickly close to the surface. Thus, as seen on figure 5.10, the ^{3}H concentration during the heating is much lower than the ^{3}H concentration before the heating in the zone near the heated surface. In this area, ^{3}H is quickly removed in few 10 seconds or few minutes.

The temperature and so the diffusion coefficient is not homogeneous in the material: they both decreases as the depth increases toward the cooled surface. This promotes the desorption toward the heated surface e.g. the major part of the ^{3}H retained in the materials is desorbed from this surface. However, as it can be seen on figure 5.10, some ^{3}H initially trapped deep in the bulk find their way toward the cooled surface since a gradient of the concentration of mobile particles is favorable for this migration. For the different cases, the depths reached after 40 min of heating and at the end of the 7 h heating phase are summarized in table 5.3.

Thermal flux	Time of heating	Depth reached by ^{3}H **Damaged W**	Depth reached by ^{3}H **Undamaged W**
	t = 0 s	140 µm	6.8 mm
$\Gamma_{th} = 7.5\ MW \cdot m^{-2}$	t = 40 min	440 µm	8.1 mm
	t = 7 h	960 µm	9.6 mm
$\Gamma_{th} = 10\ MW \cdot m^{-2}$	t = 40 min	2.2 mm	9.5 mm
	t = 7 h	3.4 mm	10 mm

Table 5.3. Depth reached for different time of heating (0, 40 min and 7 h).

This ^{3}H migration in the bulk has two major consequences:

- The entire quantity of retained ^{3}H would never be completely removed from the material by this surface heating,
- If the heating lasts long enough and if the heating flux is high enough, ^{3}H can migrate up to the cooled surface, releasing ^{3}H inside the cooling system.

In figure 5.10 and table 5.3, it can be seen that for damaged W, the ^{3}H does not migrate so deep due to the presence of the neutron-induced traps. The maximal depth reached during the heating process is few mm for the highest heating flux.

However, it is more problematic in the case of undamaged W. Even for the lowest heat flux, the ^{3}H reaches a depth close to 1 cm: some ^{3}H is dangerously close to the cooling system. And for the highest heat flux, after 7 h of heating, 10^{18} ^{3}H/m^2 have been released in the cooling system.

From the analysis of the simulated ^{3}H depth profiles, it can be said that the surface heating is quite efficient to quickly (in few minutes) remove ^{3}H from the near surface of the PFC (up to few 10 µm). However, it is not suitable for removing ^{3}H retained deep in the bulk because of the temperature gradient. In addition, the surface heating for a long period can induce a ^{3}H release into the cooling system.

Summary:

In this section, the efficiency of a method for ^{3}H removal by heating the surface by lasers of flash lamps is tested.

- In both undamaged and damaged cases, the ^{3}H is removed with two time scales:
  - In few 10 seconds/minutes: it corresponds to the desorption of ^{3}H trapped near the surface where the material is the hottest.
  - In several hours: it corresponds to the detrapping deep in the materials and the bulk.
- In case of the undamaged W, a heating flux of 7.5 MW/m^2 is as efficient as a heating flux of 10 MW/m^2.
- In case of the damaged W, a heating flux of 10 MW/m^2 helps removing much more ^{3}H from the materials: neutron-induced traps are slowly detrapped at the temperature reached with a heating flux of 7.5 MW/m^2.
- The heating surface technics seems efficient to remove the ^{3}H from the near surface: it is quick and the ^{3}H concentration drops by about 6 – 9 orders of magnitude.
- It is however not efficient at all to remove the ^{3}H trapped deep in the bulk: some ^{3}H can even migrate toward the cooling surface and ^{3}H can even be released in the cooling system.

To conclude, these simulations show that in order to remove a significant amount of ^{3}H from the wall using this technic, a thermal flux of about 10 MW/m^2 is required. Such heating flux can be achieved by laser but in this case, the area exposed is limited to few cm^2: in order to remove the ^{3}H from anywhere in the vessel, the heating has to last only few seconds and all the wall has to be scaned. In that case, the simulations shows that only the ^{3}H trapped near the surface (up to 10 µm) will be removed: this technic is probably not the best one to remove all the tritium from the wall.

5.5. Summary

In this chapter, it has been tried to estimate the amount of ^{3}H retained during realistic plasma cycles in undamaged and damaged W. To this aim, simulations of actively cooled W PFC experiencing an implanted particle flux ϕ_{imp} of ions with a given incident energy E_{inc} are undertaken. The W PFCs experience a heat flux Γ_{th} associated to the particle flux and the incident energy: the inputs of the simulations are thus E_{inc}, ϕ_{imp} and Γ_{th}.

- A plasma cycle is divided into 4 phases:
  - A 20 s-ramp-up plasma phase: the particle and heat fluxes increase from zero to the nominal value of the burning plasma phase,

    - A 380 s-burning plasma phase: during this phase, the implanted particle flux is 3×10^{23} $^3H\cdot m^{-2}\cdot s^{-1}$, the ion energy at the wall is 25 eV/^{3}H and the heat flux is 6.176 MW/m^2,
    - A 40 s-ramp-down plasma phase: the particle and heat fluxes decrease to zero,
    - A 960 s-resting time period: the heat and particle fluxes are null.
- A simple thermal model is added to MHIMS to calculate the temperature distribution inside the W PFC: during the plasma burning phase, the temperature of the plasma facing surface reaches 970 K.
- After one single cycle:
    - A sudden increase of the ^{3}H retention is observed during the ramp-down phase due to a decrease of the PFC temperature.
    - The ^{3}H retention in damaged W is 3 times higher than in undamaged W.
    - The migration depth of ^{3}H is about 40 µm in the case of damaged W and 2.5 mm in the case of undamaged W.
- Extrapolation laws can be extracted from the simulations of 40 cycles. These extrapolation laws allow to estimate the maximum retention (when ^{3}H reached the cooled surface) and the number of cycle needed to reach this value:
    - In case of undamaged W, the maximum ^{3}H retention is reached after 320 cycles and the retention is 0.045 g/m^2.
    - In case of damaged W, the maximum ^{3}H retention is reached after 65 000 cycles and the retention is 7.5 g/m^2 (160 times the retention in undamaged W case).
- Assuming that in ITER, the surface exposed to the condition used in these simulations is 0.8 m^2, the maximum retention is:
    - 0.036 g in the case of undamaged W. This amount is reached after a very short time but is three orders of magnitude lower than the 700 g safety limit of ITER.
    - 6.1 g in the case of damaged W which is two orders of magnitude lower than the 700 g safety limit of ITER.

This amount of ^{3}H retained is below the safety limit of ITER but to see if the retention in the entire wall is problematic, more complex simulations has to be made to take into account the different implantation conditions and the different materials of the wall (Be, deposited layers, W).

- A ^{3}H removal technic is finally simulated that consists on heating the PFC surface to remove thermally the ^{3}H:
    - In order to remove a significant amount of ^{3}H from W (especially damaged W), a heat flux of about 10 MW/m^2 has to be used.
    - This technics remove quickly (few 10 s) ^{3}H retained near the heated surface up to 10 µm,
    - Very hard to remove ^{3}H retained deeper in the bulk. Moreover, the heating process pushes the ^{3}H toward the cooled surface inducing a possible ^{3}H release in the cooling system.
- Since only the near surface tritium can be efficiently removed, it seems that this technic is not so good for a complete tritium removal. In addition, the high heat flux required makes this technic difficult to apply in real tokamak conditions.

6. Conclusions and perspectives

During ITER operation, high fluxes of hydrogen isotopes (HIs) constituting the fuel of the fusion reactions will interact with the plasma facing components (PFCs). The divertor is the most exposed area and in this region the PFCs are made of tungsten (W). These interactions lead to two major consequences:

- A source of outgassing cold molecules for the edge plasma that have an effect on the plasma edge physics,
- The fuel and especially the tritium retention. In ITER, the overall amount of tritium present in the entire machine is limit, for safety issue, to 700 g.

The aim of my PhD project was to determined relevant trapping parameters of fuel retention and outgassing from W by modelling different and independent experimental results. The simulated experimental results are mainly obtained by:

- Thermal desorption spectrometry experiment (TDS). It gives the temperature of desorption (and so the detrapping energies) of HIs W.
- Secondary ion mass spectrometry (SIMS). It gives the depth profiles of different species such as oxygen, carbon, tungsten oxides and HIs in W. The maximal depth achievable is about 100 nm.
- Nuclear reaction analysis (NRA) which gives the depth profiles of deuterium in W up to a depth of 7 µm.

The obtained parameters were compared to ab-initio calculations such as Density Function Theory (DFT) and Molecular Dynamics (MD) in order to try to understand the underlying physical processes.
Using the relevant parameters, a wall model was built in order to estimate the tritium retention in realistic tokamak environment.

The modelling technics used in this project is based on macroscopic rate equation model (MRE) which considers continuous concentration of HIs in the material. Two different 1-dimension models of HI in the bulk have been developed. They both considered two kinds of hydrogen isotope particles:

- The particles trapped in defects such as mono-vacancies, dislocations …,
- The mobile particles that are in interstitial position and that can diffuse between interstitial sites.

Both models used in the work are based on the diffusion/trapping model using transition state theory to address the trapping and detrapping processes and the Fick's diffusion law to express the diffusion.

The first one is a standard model widely used in the community. The second one is similar to the standard model but it includes the multi-trapping effect, a trapping process derived from DFT calculations: a defect such as a mono-vacancy can retain several HIs and the detrapping energy of the HIs inside the defect depends on the filling level of the defect.

For both models, equilibrium ratios are derived from steady-state analysis. These equilibrium ratios express the amount of particles that can be retained in a given trap for a given temperature and concentration of mobile particles. Such ratios are used to know if a trap can efficiently retain HIs or not.

Concerning the way the surface (the boundary condition) is considered in the models, two type of boundary conditions have been used:

- A simple surface model with a quick recombination of HIs,

- A more complex model that calculates the concentration of HIs on the surface and the concentration of mobile particles beneath the surface using the balance between different fluxes:
    - the incident flux of HIs as low energetic atoms
    - the direct abstraction flux: an incident atom recombines with an ad-atom on the surface
    - the desorption flux from the surface: two ad-atoms recombine forming a molecules,
    - the absorption flux from the surface to the bulk: an ad-atom enters the bulk as interstitial atom
    - the resurfacing flux from the bulk to the surface: an interstitial atom goes to the surface as ad-atom.

The first boundary condition is used in the case of ion implantations and the second more complex boundary conditions is used in the case of low energetic atom exposures that are sensitive to surface process.

Steady state analysis as well as a simple analytical model allow determining useful formulas that give simple relationship between the maximum of the concentration of mobile particles and the incident flux of ions or low energy atoms (so for both types of boundary conditions). These formulas are used with the equilibrium ratio to know if a trap can retain HIs or not for a given flux at a given temperature.

The equations of the models are numerically solved in the code MHIMS (Migration of Hydrogen Isotopes in MetalS) for the standard model and in MHIMS-R for the multi-trapping model. The core models that treat the time variation of the concentration of mobile and trapped particles can be completed by trap creation models to reproduce the ions-induced traps or/and by a thermal model to take into account a thermal gradient in an actively cooled PFC.

Firstly, simulations of single crystalline tungsten (SCW) experiments are presented. In SCW, the simulations show that the fuel retention is mainly limited by the creation of traps induced by the HI implantation. Indeed, to reproduce the experimentally observed increase of deuterium (D) retention as a function of the incident flux for a constant fluence, a trap creation model has to be used. This model is based on a balance between creation and saturation of traps.
The creation part, based on thermo-statistical model predictions, takes into account the decrease of the creation rates for concentrations of mobile particles below a critical concentration (for fluxes below a critical flux). To match the experimental results at 300 K, a threshold flux of 5×10^{17} $D\cdot m^{-2}\cdot s^{-1}$ is used which corresponds to a critical concentration corresponding to the one predicted by thermo-statistical model.
Looking at experimental SIMS depth profiles of oxygen (O), carbon (C) and deuterium, it is suggested that the trap creation process is limited also by the implantation of O and C impurities (from the background gas of the implantation chamber). Thus, the maximum amount of created traps (the saturation) corresponds to the amount of O/C impurities implanted. In the model, an ad-hoc concentration of O/C impurities is set as an input parameter to reproduce the SIMS and NRA depth profiles. This distribution can be divided into three parts:

- A near surface zone up to 20 nm with a high concentration of O/C and traps (< 1 at.%): this zone corresponds to the collision damaged generated by the O and C ions implanted in the SCW during the D implantation.

- A sub-surface zone up to 1 µm at 300 K with a medium O/C and trap concentration (> 0.01 at.%): this zone can be understood as the zone where the implanted O/C impurities diffuse.
- A bulk zone with a low O/C and trap concentration ($<10^{-3}$ at.%): this zone corresponds to the native O/C impurities present in the SCW samples.

From TDS simulations and DFT calculations, it is proposed that the traps created are first mono-vacancies with O/C impurities and HI atoms (VOH, VCH). If the amount of traps created is high, it seems that a trap mutation occurs.

As the temperature of implantation increases, the sub-surface zone extends toward the bulk. It is proposed that this extension is due to a thermally activated diffusion of O/C in the bulk: the O/C migration depth increases with temperature. From, the simulations, a diffusion coefficient of O/C is obtained that will help to determine the depth up to which the traps are created for different implantation conditions.

As suggested by the thermo-statistical model the critical concentration for trap creation also increases with the temperature. However, this critical concentration can be accurately determined from the simulation of the evolution of the D retention as a function of the flux for a constant (and low) fluence. Such data are only available at 300 K and the evolution used in the simulations is set ad-hoc to reproduce the evolution of the D retention as a function of the temperature for a constant flux.

To validate the conclusion derived from these simulations, more experimental results are required:

- The depth profiles of O and C deeper in the bulk than the 100 nm accessible with SIMS. NRA could be used. Such depth profiles are required to validate or invalidate our interpretation of the sub-surface processes, especially on the point of O/C impurities diffusion.
- The evolution of the D retention as a function of the flux for a given low fluence. This would give an accurate evolution of the critical concentration for trap creation as a function of temperature which then could be compared to the thermo-statistical.

In parallel, it could be interesting to compare the migration energy of O/C in tungsten obtained by ab-initio methods with the one extracted from these simulations. In addition, KMC simulations could be a good tool to understand how the trap mutates and what the natures of the new traps are. Finally, the creation model could be improved by taking into account the diffusion of O and C with diffusion/trapping equations rather than with ad-hoc profiles.

Secondly, simulations of poly-crystalline tungsten (PCW) experiments are presented. For these simulations, the standard model is used because the approach is more an engineer approach. The purpose is to find the relevant mean trapping parameters of fuel retention in W to use them in a tokamak wall model. Such model would be able to estimate the tritium retention during tokamak operation as well as provide a model to calculate the molecular outgassing flux of HI in plasma edge codes. A simple trap creation model is added to the standard model to take into account the observation made from the simulations of SCW experiments.

From the simulation of a TDS spectrum obtained on PCW samples that only experience low energy D ion implantation, three traps are determined: two intrinsic traps with low detrapping energies (GB, dislocations and Fe impurities) and one extrinsic traps corresponding to the ions-induced traps (VOH and VCH). These three traps accurately reproduce the evolution of the D retention with the fluence and the implantation temperature. Thus, these three trapping

parameters are accurate to estimate the tritium retention in undamaged W i.e. W which is not exposed to the 14.1 MeV neutrons produced by the fusion reactions.

To predict the effect of the 14.1 MeV fusion neutrons, PCW samples can be irradiated by heavy ions with high energy to create a localized damaged zone in the sample. From the simulations of TDS spectra obtained on such damaged PCW samples, three higher detrapping energies are determined in addition to the three detrapping energies characteristic of undamaged W. These detrapping energies are associated to jogged dislocations, dislocation loops and cavities created during the heavy ion damaging. These trapping parameters are accurate to estimate the tritium retention in W damaged by 14.1 MeV neutrons.

The current model has a very simple representation of the different traps: a defect is only represented by a single detrapping energy. The next step to add physics to the model would be to use the multi-trapping model for each defect with the distribution of detrapping energies given by DFT. To accurately represent the broaden distribution of detrapping energies of the GBs, a continuous distribution could be use since it is not possible to have the DFT distribution of detrapping energies for each type of GBs.

Another improvement that could be added to the model is the creation, the motion and the mutation/annihilation of the traps and the effects of the HIs on these three processes. Thus, the model would be able to simulate the trap formation and mutation during a simultaneous irradiation of neutrons and HIs as in a real tokamak environment.

Finally, the effect of Helium ashes should be added to the model since Helium can be present in the wall from three sources: the fusion reactions, the α-decay of the transmutation products in the wall and the β-decay of tritium.

Using these trapping parameters, the tritium implantation in 1-cm-thick actively cooled W PFC during realistic tokamak cycle is simulated. Two cases are considered: the undamaged W (2 intrinsic traps and 1 ions-induced trap) and the damaged W (2 intrinsic traps, 1 ions-induced trap and 3 neutrons-induced traps).

The inputs of the simulations are the evolution of the implanted particle flux, the incident energy ions and the associated thermal flux that heat the plasma facing surface of the PFC. In order to calculate the gradient of temperature in the actively cooled PFC, a thermal model is added to the MHIMS code. A 1400 s ITER cycle is then simulated. It is composed of a plasma ramp-up during which the particle and the associated thermal fluxes increase up to the nominal value in 20 s. A plasma burning phase follows for 380 s during which the particle and heat fluxes are constant. Then, the particle/heat fluxes decrease in 40 s during the plasma ramp-down phase. Finally, a resting time of 960 s is simulated. During the plasma burning phase, the implanted flux is 3×10^{23} $m^{-2}\cdot s^{-1}$, the ion energy is 25 eV/D and the heat flux is 6.176 MW/m^2 which corresponds to what would experience the divertor target. In these conditions, the plasma facing surface temperature rises up to 970 K.

In the results of the simulation of one cycle, it is observed that the tritium retention is 3 times higher for damage W than for undamaged W. In addition, during the plasma ramp-down phase, due to the decrease of the temperature, a sudden increase of the tritium retention is observed. The tritium atoms retained during this phase do not reached more than 3 µm but during the plasma burning phase, the retained tritium atoms migrate up to 40 µm for damaged W and up to 2.5 mm for undamaged W.

In the results of the simulations of 40 cycles, it is observed that the tritium retained during the plasma ramp-down phase is quickly removed from the PFC during the next plasma ramp-up phase due to the increase of the temperature. If one considers only the tritium retention during the

plasma burning phase, the amount of tritium retained in undamaged tungsten is 10 times smaller for undamaged W than for damaged W.

From the simulation of 40 cycles, extrapolation laws are extracted to estimate the tritium retention as well as the migration depth for a greater number of cycles. The maximum of tritium retention, i.e. when the tritium migration depth is 1 cm, is reached after only 320 cycles for undamaged W and after 65 000 cycles for damaged W. Considering that the surface exposed to such flux in ITER will be about 0.8 m^2, the maximum amount of tritium retained is 0.036 g for undamaged W and 6.1 g for damaged W. Thus the damaged W will retain 160 times more tritium that undamaged W. However, tritium will reach the cooling system (inducing possible permeation) after only 32 days of operation for undamaged W compared to about 30 years of operations for damaged W (considering 10 cycles per day and 200 days of operation per year). This can be problematic if the tritium is release in the cooling system.

In both cases, the tritium retention in the W divertor targets, the most exposed area to the particle/heat fluxes, will be below the 700 g ITER safety limit. However, the surface considered represents only 0.1 % of all the plasma facing surfaces: the other part of the W divertor as well as the Be first wall can also interact with lower heat/particle fluxes and so retained tritium. In addition, tritium can be retained in Be eroded from the first wall and deposited in layers on the W divertor. Consequently, in order to make a good estimation of the overall tritium inventory in the ITER plasma facing surface, more complex simulations are needed that take into account the variety of exposed materials as well as the different exposition conditions (particle/heat flux, ion energy).

Finally, after simulating the trapping of tritium after several cycles, a removal technics that consists on heating the surface of the PFC has been tested. From the simulations it can be concluded that in order to remove a significant amount of tritium, a heat flux of about 10 MW/m^2 is needed especially for damaged W (due to the neutrons-induced traps with high detrapping energies). Even in this case, only the tritium atoms near the surface (up to about 10 µm) are quickly removed in few tens of seconds/minutes. Indeed, the tritium atoms retained deeply in the bulk are released on the hours scale or even worst: they are pushed toward the cooling system inducing a possible permeation of tritium.

Figure table

Table list

References

[1] J. Wesson, Tokamaks, Oxford science publications.

[2] H.-S. Bosch and G. M. Hale, *Nucl. Fusion 32, No. 4,* 1992.

[3] J. D. Lawson, "Some criteria for a power producing thermonuclear reactor," *Proc. Phys. Soc. B 70/6,* 1957.

[4] CCFE, "Culham science for fusion energy.," [Online]. Available: http://www.ccfe.ac.uk/.

[5] J. Roth, E. Tsitrone, A. Loarte et al., *J. Nucl. Mater. 390-391,* pp. 1-9, 2009.

[6] E. Tsitrone, C. Brosset, B. Pegourié et al., *Nucl. Fusion 49,* p. 075011, 2009.

[7] R. A. Causey, *J. Nucl. Mater. 300,* pp. 91-117, 2002.

[8] H. Pastor, "Propriétés du tungstène et de ses alliages," *Techniques de l'ingénieur, Métaux et alliages, matériaux magnétiques et multimatériaux,* 1985.

[9] E. Lassner and W.-D. Schubert, Tungsten: Properties, Chemistry, Technology of the Element, Alloys, and Chemical Compounds, New York: Plenum, 1999.

[10] J. F. Ziegle, M. D. Ziegler and J. P. Biersack, *Nucl Instrum. Methods Phys. Res. B 268,* pp. 1818-23, 2010.

[11] C. S. Becquart and C. Domain, *Phys. Rev. Lett. 97,* p. 196402, 2006.

[12] C. S. Becquart and C. Domain, *J. Nucl. Mater. 385,* pp. 223-227, 2009.

[13] E. Bernard, R. Sakamoto, N. Yoshida et al., *J. Nucl. Mater. 463,* pp. 316-319, 2015.

[14] R. P. Doerner, M. J. Baldwin and P. C. Stangeby, *Nucl.Fusion 51,* p. 043001, 2011.

[15] G. S. Was, Fundamentals of Radiation Material Science, Metals and Alloys, Springer, 2007.

[16] H. Iida, V. Khripunov, L. Petrizzi and G. Federici, "ITER Nuclear Analysis Report G," DDD 2 W 0, 2004.

[17] M. R. Gilbert and J. C. Sublet, *Nucl. Fusion 51,* p. 043005, 2011.

[18] J. Roth and K. Schmid, *Phys. Scr. T145,* p. 014031, 2011.

[19] I. Takagi, R. Imade, Y. Ikegami et al., *J. Nucl. Mater. 417,* pp. 564-567, 2011.

[20] O. V. Ogorodnikova, *J. Appl. Phys. 118,* p. 074902, 2015.

[21] M. A. Pick and K. Sonnenberg, *J. Nucl. Mater. 131,* pp. 208-220, 1985.

[22] R. Kirchheim, *Progress in Materials Science 32,* pp. 261-325, 1988.

[23] S. Glasstone, K. Laidler and H. Eyring, The Theory of Rate Processes, New York: McGraw-Hill, 1941.

[24] R. Bisson, S. Markelj, O. Mourey et al., *J. Nucl. Mater. 467,* pp. 432-438, 2015.

[25] O. V. Ogorodnikova, J. Roth and M. Mayer, *J. Nucl. Mater. 313-316,* pp. 469-477, 2003.

[26] M. Poon, R. G. Macaulay-Newcombe, J. W. Davis et al., *J. Nucl. Mater. 307-311,* pp. 723-728, 2002.

[27] M. Poon, A. A. Haasz, J. W. Davis et al., *J. Nucl. Mater. 313-316,* pp. 199-203, 2003.

[28] C. Grisolia, E. Hodille, J. Chene and et al, *J. Nucl. Mater. 463,* pp. 885-888, 2015.

[29] R. Frauenfelder, *J. Vac. Sci. Technol. 6,* p. 388, 1969.

[30] A. Manhard, K. Schmid, M. Balden et al., *J. Nucl. Mater. 415,* pp. S632-S635, 2011.

[31] J. E. Whitten and R. Gomer, *Surf. Sci. 409,* pp. 16-26, 1998.

[32] T.-U. Nahm and R. Gomer, *Surf. Sci. 375,* pp. 281-292, 1997.

[33] D. L. Adams, L. H. Germer and J. W. MAY, *Surf. Sci. 22,* pp. 45-68, 1970.

[34] P. W. Tamm and L. D. Schmidt, *J. Chem. Phys. 51,* p. 5352, 1969.

[35] K. G. Tscherisich, J. P. Fleischhauer and H. Schuler, *J. Appl. Phys. 104,* p. 034908, 2008.

[36] E. A. Hodille, L. B. Begrambekov, J. Y. Pascal et al., *Inter. J. Hydrog. Energy 39,* pp. 20054-20061, 2014.

[37] C. Grisolia and A. Grosman, *J. Nucl. Mater. 187,* pp. 74-79, 1992.

[38] S. Markelj, I. Cadez, P. Pelicon et al., *Nucl. Instrum. Methods Phys. Res. B 25 (9),* p. 989, 2007.

[39] H. T. Lee, A. A. Haasz, J. W. Davis et al., *J. Nucl. Mater 360,* pp. 196-207, 2007.

[40] M. Mayer, "SIMNRA user's quide," Tech. Rep. IPP 9/113, MAx-Planck-Institut für Plasmaphysik, Garching, 1997.

[41] S. Markelj, A. Zaloznik, T. Schwarz-Selinger et al., *J. Nucl. Mater. 469,* pp. 133-144, 2016.

[42] M. Poon, R. G. Macaulay-Newcombe, J. W. Davis and A. A. Haasz, *J. Nucl. Mater. 337-339,* pp. 629-633, 2005.

[43] M. Poon, A. A. Haasz and J. W. Davis, *J. Nucl. Mater. 374,* pp. 390-402, 2008.

[44] V. K. Alimov, M. Mayer and J. Roth, *Nucl. Instrum. Methods Phys. Res. B 234,* pp. 169-175, 2005.

[45] J. P. Roszell, J. W. Davis, V. K. Alimov et al., *J. Nucl. Mater. 438,* pp. S1084-S1087, 2013.

[46] A. El-Kharbachi, J. Chêne, S. Garcia-Argote et al., *Inter. J. Hydrog. Energy 39,* pp. 10525-10536, 2014.

[47] V. K. Alimov, J. Roth, R. A. Causey et al., *J. Nucl. Mater. 375,* pp. 192-201, 2008.

[48] W. Wang, J. Roth, S. Lindig et al., *J. Nucl. Mater. 299,* pp. 124-131, 2001.

[49] A. Manhard, U. v. Toussaint, T. Dürbeck et al., *Phys. Scr. T145,* p. 014038, 2011.

[50] M. H. J. 't Hoen, M. Balden, A. Manhard et al., *Nucl. Fusion 54,* p. 083014, 2014.

[51] E. Bernard, R. Sakamoto, N. Yoshida et al., *J. Nucl. Mater. 463,* pp. 316-319, 2015.

[52] A. Zaloznik, S. Markelj, T. Schwarz-Selinger et al., *Phys. Scr. T167,* p. 014031, 2016.

[53] A. Van Veen, H. A. Filius, J. De Vries et al., *J. Nucl. Mater. 155-157,* pp. 1113-1117, 1988.

[54] P. E. Lhuillier, M. F. Barthe, P. Desgardin et al., *Phys. Status Solidi C 6, No. 11,* pp. 2329-2332, 2009.

[55] A. Debelle, M. F. Barthe and T. Sauvage, *J. Nucl. Mater. 376,* pp. 216-221, 2008.

[56] P. Alnot, A. Cassuto and D. A. King, *Surf. Sci. 215,* pp. 29-46, 1989.

[57] P. W. Tamm and L. D. Schmidt, *J. Chem. Phys. 52,* p. 1150, 1970.

[58] K. O. E. Henriksson, K. Vörtler, S. Dreißgacker et al., *Surf. Sci. 600,* pp. 3167-3174, 2006.

[59] O. V. Ogorodnikova, S. Markelj and U. v. Toussaint, *J. Appl. Phys. 119,* p. 054901, 2016.

[60] N. Juslin, P. Erhardt, P. Traeskelin et al., *J. Apl. Phys. 98,* p. 123520, 2005.
[61] P. A. Redhead, *Vacuum 12,* p. 203, 1962.
[62] P. W. Tamm and L. D. Schmidt, *J. Chem. Phys. 54,* p. 4775, 1971.
[63] R. DiFoggio and R. Gomer, *Phys. rev. B, Vol. 25, No 6,* pp. 3490-3511, 1982.
[64] A. Nojima and K. Yamashita, *Surf. Sci. 601,* pp. 3003-3011, 2007.
[65] D. F. Johnson and E. A. Carter, *J. Mater. Res., Vol. 25, No. 2,* pp. 315-327, 2010.
[66] K. Heinola and T. Ahlgren, *Phys. Rev. B 81,* p. 073409, 2010.
[67] P. Ferrin, S. Kandoi, A. Udaykumar Nilekar and M. Mavrikakis, *Surf. Sci. 606,* pp. 679-689, 2012.
[68] A. Moitra and K. Solanki, *Comp. Mater. Sci. 50,* pp. 2291-2294, 2011.
[69] G.-H. Lu, H.-B. Zhou and C. S. Becquart, *Nucl. Fusion 54,* p. 086001, 2014.
[70] A. Sieverts and E. Jurisch, "Platin, Rhodium und Wasserstoff," *Ber. Dtsch. Chem. Ges. vol. 45, issue 1,* pp. 221-229, 1912.
[71] K. Heinola and T. Ahlgren, *J. Appl. Phys. 107,* p. 113531, 2010.
[72] N. Fernandez, Y. Ferro and D. Kato, *Acta Mater. 94,* pp. 307-318, 2015.
[73] Y.-L. Liu, H.-B. Zhou and Y. Zhang, *J. Alloys Compd. 509,* p. 8277, 2011.
[74] G. Benamati, E. Serra and C. H. Wu, *J. Nucl. Mater. 283-287,* pp. 1033-1037, 2000.
[75] B. Zajec, V. Nemanic and C. Ruset, *J. Nucl. Mater. 412,* pp. 116-122, 2011.
[76] C. H. Skinner, A. A. Haasz, V. K. Alimov et al., *Fusion Sci. Technol. 54,* p. 891, 2008.
[77] T. Tanabe, *Phys. Scr. T159,* p. 014044, 2015.
[78] G. A. Esteban, A. Perujo, L. A. Sedano et al., *J. Nucl. Mater. 295,* pp. 49-56, 2001.
[79] T. Ikeda, T. Otsuka and T. Tanabe, *J. Nucl. Mater. 415,* pp. S684-S687, 2011.
[80] T. Ikeda, T. Otsuka and T. Tanabe, *Fusion Sci. Techno., Vol. 60, N° 4,* pp. 1463-1466, 2011.
[81] A. P. Zakharov, V. M. Sharapov, E. I. Evko et al., *Fi. Khim. Mekh. Mater. 9 (2),* p. 29, 1973.
[82] T. Otsuka, T. Hoshihira and T. Tanabe, *Phys. Scr. T138,* p. 014052, 2009.
[83] T. Otsuka, M. Shimada, R. Kolasinski et al., *J. Nucl. Mater. 415,* pp. S769-S772, 2011.
[84] Y.-L. Liu, Y. Zhang, G.-N. Luo et al., *J. Nucl. Mater. 390-391,* pp. 1032-1034, 2009.
[85] C. Wert and C. Zener, *Phys. Rev., vol. 76, n°8,* p. 1169, 1949.
[86] A. D. Quastel, J. W. Davis, A. A. Haasz et al., *J. Nucl. Mater. 359,* pp. 8-16, 2006.
[87] J. P. Roszell, A. A. Haasz and J. W. Davis, *J. Nucl. Mater. 415,* pp. S641-S644, 2011.
[88] J. P. Roszell, J. W. Davis and A. A. Haasz, *J. Nucl. Mater. 429,* pp. 48-54, 2012.
[89] V. K. Alimov, J. Roth and M. Mayer, *J. Nucl. Mater. 337-339,* pp. 619-623, 2005.
[90] R. Sakamoto, T. Muroga and N. Yoshida, *J. Nucl. Mater. 220-222,* pp. 819-822, 1995.
[91] K. Tokunaga, M. Takayama, T. Muroga et al., *J. Nucl. Mater. 220-222,* pp. 800-804, 1995.
[92] V. K. Alimov, B. Tyburska, M. Balden et al., *J. Nucl. Mater. 409,* pp. 27-32, 2011.
[93] P. J. Wiseman and P. G. Dickens, *J. Solid State Chem.,* vol. 6, p. 374, 1973.
[94] R. D. Bringans, H. Höchst and H. R. Shanks, *Surf. Sci. 111,* pp. 80-86, 1981.

[95] M. H. J. 't Hoen, B. Tyburska-Püschel, K. Ertl et al., *Nucl. Fusion 52,* p. 023008, 2012.
[96] Z. Tian, J. W. Davis and A. A. Haasz, *J. Nucl. Mater. 399,* pp. 101-107, 2010.
[97] M. Shimada, G. Cao, Y. Hatano et al., *Phys. Scr. T145,* p. 014051, 2011.
[98] S. Lindig, M. Balden, V. K. Alimov et al., *Phys. Scr. T145,* p. 014039, 2011.
[99] V. K. Alimov, W. M. Shu, J. Roth et al., *J. Nucl. Mater. 417,* pp. 572-575, 2011.
[100] A. A. Haasz, J. W. Davis, M. Poon et al., *J. Nucl. Mater. 258-263,* pp. 889-895, 1998.
[101] V. K. Alimov, B. Tyburska-Püschel, S. Lindig et al., *J. Nucl. Mater. 420,* pp. 519-524, 2012.
[102] M. Miyamoto, D. Nishijima, Y. Ueda et al., *Nucl. Fusion 49,* p. 065035, 2009.
[103] O. V. Ogorodnikova, T. Schwarz-Selinger, K. Sugiyama et al., *J. Apll. Phys. 109,* p. 013309, 2011.
[104] M. J. Baldwin, R. P. Doerner, W. R. Wampler et al., *Nucl. Fusion 51,* p. 103021, 2011.
[105] Y. Hatano, M. Shimada, T. Otsuka et al., *Nucl. Fusion 53,* p. 073006, 2013.
[106] M. H. J. 't Hoen, M. Mayer, A. W. Kleyn et al., *Nucl. Fusion 53,* p. 043003, 2013.
[107] H. Watanabe, N. Futagami, S. Naitou et al., *J. Nucl. Mater. 455,* pp. 51-55, 2014.
[108] S. Markelj, O. V. Ogorodnikova, P. Pelicon et al., *Phys. Scr. T159,* p. 014047, 2014.
[109] Y. M. Gasparyan, O. V. Ogorodnikova, V. S. Efimov et al., *J. Nucl. Mater. 463,* pp. 1013-1016, 2015.
[110] B. Tyburska, V. K. Alimov and O. V. Ogorodnikova, *J. Nucl. Mater. 395,* pp. 150-155, 2009.
[111] O. V. Ogorodnikova and V. Gann, *J. Nucl. Mater. 460,* pp. 60-71, 2015.
[112] M. Toulemonde, W. Assmann, C. Dufour et al., *Mat. Fys. Medd. Kong. Dan. Vid. Selsk. 52,* p. 263, 2006.
[113] L. Ciupinski, O. V. Ogorodnikova, T. Plocinski et al., *Nucl. Instrum. Methods Phys. Rev. B 317 A,* pp. 159-164, 2013.
[114] X.-S. Kong, Y.-W. You, Q. F. Fang et al., *J. Nucl. Mater. 433,* pp. 357-363, 2013.
[115] K. Heinola, T. Ahlgren, K. Nordlund et al., *Phys. Rev. B 82,* p. 094102, 2010.
[116] Y.-W. You, X.-S. Kong, X.-B. Wu et al., *AIP advances 3,* p. 012118, 2013.
[117] W. Xiao and W. T. Geng, *J. Nucl. Mater. 430,* pp. 132-136, 2012.
[118] H.-B. Zhou, Y.-L. Liu, S. Jin et al., *Nucl. Fusion 50,* p. 025016, 2010.
[119] D. Terentyev, V. Dubinko, A. Bakaev et al., *Nucl. Fusion 54,* p. 042004, 2014.
[120] K. Ohsawa, F. Nakamori, Y. Hatano et al., *J. Nucl. Mater. 458,* pp. 187-197, 2015.
[121] L. Sun, S. Jin, H.-B. Zhou et al., *J. Phys. Condens. Matter 26,* p. 395402, 2014.
[122] Y. Liu, T. Ahlgren, L. Bukonte et al., *AIP Advances 3,* p. 122111, 2013.
[123] X.-C. Li, X. Shu, Y.-N. Liu et al., *J. Nucl. Mater. 408,* pp. 12-17, 2011.
[124] P. M. Piaggi, E. M. Bringa, R. C. Pasianot et al., *J. Nucl. Mater. 458,* pp. 233-239, 2015.
[125] Y. Yu, X. Shu, Y.-N. Liu et al., *J. Nucl. Mater. 455,* pp. 91-95, 2014.
[126] U. von Toussaint, S. Gori, A. Manhard et al., *Phys. Scr. T145,* p. 014036, 2011.
[127] T. Oda, D. Zhu and Y. Watanabe, *J. Nucl. Mater. 467,* pp. 439-447, 2015.

[128] K. Ohsawa, J. Goto, M. Yamakami et al., *Phys. Rev. B 82*, p. 184117, 2010.

[129] U. von Toussaint, T. Schwarz-Selinger and K. Schmid, *J. Nucl. Mater. 463*, pp. 1075-1079, 2015.

[130] J. Roth, T. Schwarz-Selinger, V. K. Alimov et al., *J. Nucl. Mater. 432*, pp. 341-347, 2013.

[131] O. V. Ogorodnikova, J. Roth and M. Mayer, *J. Appl. Phys. 103*, p. 034902, 2008.

[132] K. Schmid, V. Rieger and A. Manhard, *J. Nucl. Mater. 426*, pp. 247-253, 2012.

[133] A. Manhard, "Deuterium inventory in tungsten after plasma exposure: a microstructural survey," PhD Thesis, Universität Augsburg, 2011.

[134] J. Guterl, R. D. Smirnov, S. I. Krasheninnikov et al., *Nucl. Fusion 55*, p. 093017, 2015.

[135] K. Heinola, T. Ahlgren, E. Vainonen-Ahlgren et al., *Phys. Scr. T128*, pp. 91-95, 2007.

[136] T. Ahlgren, K. Heinola, K. Vörtler et al., *J. Nucl. Mater. 427*, 2012.

[137] A. Hu and A. Hassanein, *J. Nucl. Mater. 446 (1-3)*, pp. 56-62, 2014.

[138] K. Schmid, U. von Toussaint and T. Schwarz-Selinger, *J. Appl. Phys. 116*, p. 134901, 2014.

[139] A. E. Gorodetsky, A. P. Zakharov, V. M. Sharapov et al., *J. Nucl. Mater. 93-94*, pp. 588-593, 1980.

[140] A. McNabb and P. K. Foster, *Trans. Metal. Soc. AIME 227*, p. 618, 1963.

[141] E. A. Hodille, X. Bonnin, R. Bisson et al., *J. Nucl. Mater. 467*, pp. 424-431, 2015.

[142] O. V. Ogorodnikova, in *A. Hassanein (Ed.), Hydrogen and Helium Recycling at Plasma Facing Materials*, NATO Science Series, 2001, p. 7.

[143] C. Garcia-Rosales, P. Franzen, H. Planck et al., *J. Nucl. Mater. 233-237*, pp. 803-808, 1996.

[144] A. C. Hindmarsh, "ODEPACK, A Systematized Collection of ODE Solvers," *Scientific Computing*, pp. 55-64, 1983.

[145] K. Radharkrishnan and A. C. Hindmarsh, Description and Use of LSODE, the Livermore Solver for Ordinary Differential Equations, LNLL report UCRL-ID-113855, 1993.

[146] E. A. Hodille, Y. Ferro, N. Fernandez et al., *Phys. Scr. T167*, p. 014011, 2016.

[147] K. Schmid, *Phys. Scr. T167*, p. 014025, 2016.

[148] S. Markelj, A. V. Ogorodnikova, P. Pelicon et al., *Appl. Surf. Sci. 282*, pp. 478-486, 2013.

[149] X. Li, Y. Liu, Y. Yu et al., *Plasma Sci. Tech. Vol. 17, No. 6*, p. 524, 2015.

[150] C. H. Lee, *Nature 203*, p. 1163, 1964.

[151] T. Engel, H. Niehus and E. Bauer, *Surf. Sci. 52*, pp. 237-262, 1975.

[152] T. Casper, Y. Gribov, A. Kavin et al., *Nucl. Fusion 54*, p. 013005, 2014.

[153] J. Denis, B. Pégourié, J. Bucalossi et al., *Phys. Scr. T167*, p. 014073, 2016.

[154] C. Sang, X. Bonnin, M. Warrier et al., *Nucl. Fusion 52*, p. 043003, 2012.

[155] T. Eich, A. W. Leonard, R. A. Pitts et al., *Nucl. Fusion 53*, p. 093031, 2013.

[156] K. Heinola, A. Widdowson, J. Likonen et al., *J. Nucl. Mater. 463*, pp. 961-965, 2015.

[157] A. Loarte, B. Lipschultz, A. S. Kukushkin et al., *Nucl. Fusion 47*, pp. S203-S263, 2007.

[158] M. Wirtz, G. Cempura, J. Linke, G. Pintsuk and I. Uytdenhouwen, *Fusion Eng. Des. 88*, pp. 1768-1772, 2013.

Etude de l'implantation du deutérium dans les composés face au plasma constituants du tokamak ITER

Lors de l'opération d'ITER, des flux importants d'isotopes d'hydrogène (HI) constituant le fuel interagissent avec les composants face au plasma (CFP) de la machine. Dans le cas du Tungstène (W) composant le divertor qui est la zone la plus exposée aux interactions plasma paroi, le flux incident est implanté et diffuse ensuite dans le corps du matériau entrainant un piégeage du fuel. Pour des raisons de sureté, l'inventaire de Tritium retenu dans les parois d'ITER est limité. De plus, le dégazage du fuel depuis les parois vers le plasma, lors des opérations plasma peut avoir un impact sur le contrôle global du plasma.
Le but de cette thèse est d'abord de déterminer les paramètres de piégeages du fuel dans le W (énergies/températures de dépiégeage, concentrations de pièges) grâce à la modélisation de résultats expérimentaux. Ces simulations de résultats expérimentaux montrent que l'implantation d'HIs dans le W peut induire, sous certaines conditions, la formation de lacunes contenant des impuretés. En plus de ce piège induit par l'implantation d'ions, 2 pièges intrinsèques sont présents dans le W. Ces 3 pièges retiennent les HIs jusqu'à 700 K. Enfin, il est montré que le W endommagé par des ions lourds ou des neutrons contient des dislocations, des boucles de dislocations et des cavités retenant les HIs jusqu'à 1000 K.
Après avoir déterminé ces paramètres de piégeages des HIs dans le W, la rétention des HIs durant l'opération d'ITER est estimée. Lors de cette opération, la température des CFP W atteint environ 1000 K. Les simulations montrent donc que la rétention dans les CFPs non endommagé est bien plus faible que dans le cas d'un CFP endommagé.

Mots clés : tungstène, tokamak, isotopes d'hydrogène, rétention du fuel, modélisation

Study and modeling of the deuterium trapping in ITER relevant materials

During ITER operation, important flux of Hydrogen Isotopes (HIs) constituting the fuel interact with the plasma facing components (PFC) of the machine. In the case of tungsten (W) making the divertor which is the most exposed area to the plasma wall interaction, the incident flux can be implanted and diffuse inside the bulk material inducing a trapping of the fuel. To safety issue, the tritium inventory retained in ITER's PFC is limited. In addition, the outgassing of the fuel during plasma operation can impact the edge plasma control.
The aim of this PhD project is first to determined relevant trapping parameters of the fuel in W (detrapping energies/temperatures and trap concentrations) by modelling experimental results. The simulations of experimental results shows that under specific condition, the HI implantation can induce the formation of mono-vacancies containing impurities. In addition to this induced trap, 2 intrinsic traps are present in W. This 3 traps retain HIs up to 700 K. Finally, it has been shown that the damaged W by heavy ions or neutrons contains dislocations, dislocation loops and cavities that can trap HIs up to 1000 K.
After determining the fuel retention properties of W, the HIs retention during ITER operation is estimated. During this operation, the PFC temperature reaches around 1000 K so the simulations show that the damaged W retains much more HIs than the undamaged W.

Keywords: Tungsten, tokamak, hydrogen isotopes, fuel retention, modeling